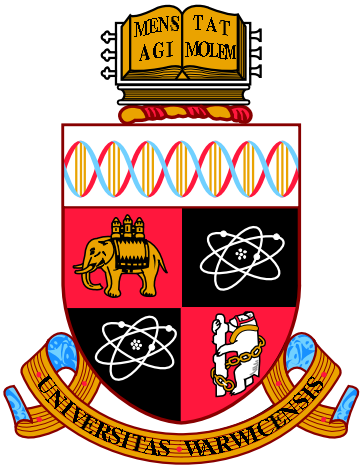


# Observations of Exoplanetary Systems at X-ray Wavelengths

by

**George William King**

**Thesis**

Submitted to the University of Warwick

for the degree of

**Doctor of Philosophy**

**Department of Physics**

October 2019

# Contents

# List of Tables

# List of Figures

# Acknowledgments

I feel very fortunate and privileged for the opportunities I have had in my life to date. I wish to give my thanks to those who helped make my PhD so enjoyable, and this thesis possible.

First and foremost, I would like to thank my supervisor, Prof. Peter Wheatley, whose guidance over the past few years has been crucial to the undertaking the work contained in this thesis. This would simply not have been possible without all of your help.

To my family, especially my parents: thank you for your encouragement in following my passions, and for not dissuading me in favour of getting a proper job. To my Dad, thank you for imparting me with your interest in space, which, like your interest in cricket, I have duly taken to the extreme.

To all of my fellow students past and present with whom I have shared my time at Warwick over the last few years: thank you for all of the cake, board games, pub quizzes, interesting (if not always wholesome) lunchtime conversations, and the steady provision of procrastination opportunities. I'm sorry for the constant bombardment of obscure TV references, and rambling on about politics so much.

To my undergrad peeps: thank you for your continued friendship, even if we don't see each other much these days. In particular, my thanks to Hasini for all her emotional support and leftie discussions down the years.

To everyone with whom I've played cricket with, in particular the University's Staff and Postgrad team: thank you for giving me the opportunity to continue enjoying my other main passion in life, and helping me to de-stress.

Last, but not at all least, to Ares: you are such an awesome person, and the best officemate I've ever had. Thank you so much for all your love and cuddles through writing this. I am immensely grateful to have you in my life every day.

# Declarations

I declare that the work presented in this thesis is my own except where stated, and has not been submitted to any other academic institution for any other degree or qualification. The research was undertaken at the University of Warwick in the period October 2015 to April 2019, under the supervision of Prof. Peter Wheatley.

This work includes material previously published in journals, as follows:

- Section 2.4 and Chapter 3 are based on the paper "The XUV environments of exoplanets from Jupiter-size to super-Earth" as published in MNRAS 478, 1193 (2018).
- The work on $\pi$ Men c in Chapter 4 is based on the paper "The XUV irradiation and likely atmospheric escape of the super-Earth $\pi$ Men c" as published in MNRAS 484, L49 (2019). Note the work on HD 219134 in this chapter has not yet been submitted to any journal.
- In addition, the introduction (Chapter 1) makes use of material from both of the published papers listed above.

I also acknowledge the following contributions:

- The data reduction and subsequent light curve and spectral analysis of the GJ 3470 and HD 149026 data in Chapter 3 were performed by Michael Salz.
- Peter Wheatley aided in the interpretation of the results presented in Chapters 3 through 7, and provided Fig. 6.3.
- Additional co-authors, provided feedback and suggestions on the manuscripts of the two published works.

# Abstract

For planets with very small semi-major axes, the implications of residing so close to a star can be wide ranging. One of the most pertinent is the effect of the X-ray and extreme ultraviolet stellar emission, which can drive significant escape of material from close-in planets' upper atmospheres. For some smaller planets, the escape processes are sufficient to substantially evolve, and in some cases completely remove, any H/He envelope they were born with.

In my first study, I derive new empirical relations in order to perform the necessary extrapolation of the X-ray emission to the unobservable EUV energy band. In addition to inferring the properties of the XUV environment of the six planets in the sample and estimating their current mass loss rates, I make the first successful detection of a planet transit with the Optical Monitor on *XMM-Newton* for the hot Jupiter WASP-80b. The resulting near ultraviolet transit depth shows a hint of being shallower than is seen at visible wavelengths.

The photoevaporation valley is one of the observed effects of escape processes on the exoplanet population. I consider planets from two nearby systems that lie either side of this valley to investigate how XUV irradiation has affected each, both now and in the past.

I investigate planets from the young open cluster Praesepe, where significant XUV irradiation is still ongoing. All of the planets in that study lie close to either the photoevaporation valley, or the other main population feature caused by photoevaporation: the Neptunian desert. I assess their past, present and possible future atmospheric evolution.

The final two studies concern the same system. HD 189733 hosts the closest transiting hot Jupiter to Earth. Using one of the largest collections of *XMM-Newton* observations for any late-type star, I make the first unambiguous detection of a planet transit at X-ray wavelengths. The deep transit reveals a large region of escaping planetary material leading the planet in its orbit. Finally, I investigate stellar activity from the system, predominately in the context of past claims of star-planet interactions. I identify new flares in the system, including some emanating from the previously-assumed-quiet wide stellar companion, and observe long-term variation possibly associated with a Solar-like activity cycle. However, I find no evidence of enhanced X-ray activity phased with the planet's orbit, and that evidence for the spinning up of star A by the planet is much weaker than previously claimed.

# Abbreviations

| | | | |
|---|---|---|---|
| **DEM** | Differential Emission Measure | **ppm** | Parts per million |
| **DSS** | STScI Digitized Sky Survey | **PSF** | Point Spread Function |
| **EM** | Emission Measure | **RV** | Radial Velocity |
| **EUV** | Extreme Ultraviolet | **SPI** | Star-Planet Interactions |
| **FIP** | First Ionisation Potential | **XUV** | X-ray and Extreme Ultraviolet |
| **FUV** | Far Ultraviolet | au | Astronomical unit, $1.496 \times 10^8$ km |
| ***HST*** | *Hubble Space Telescope* | $M_\oplus$ | Earth mass, $5.972 \times 10^{24}$ kg |
| **ISM** | Interstellar Medium | $R_\oplus$ | Earth radius, 6 378 km |
| **MUV** | Mid Ultraviolet | $M_J$ | Jupiter mass, $1.898 \times 10^{27}$ kg |
| **NIR** | Near Infrared | $R_J$ | Jupiter radius, 71 492 km |
| **NUV** | Near Ultraviolet | $M_\odot$ | Solar mass, $1.989 \times 10^{30}$ kg |
| **OM** | Optical Monitor | $R_\odot$ | Solar radius, 695 700 km |

# Chapter 1

# Introduction

*This is the human race calling from the Milky Way*
*We are highly evolved fish from near Alpha Centauri*
*We crawled out of the mud, waited our brains and blood*
*And we're only just opening our eyes*

– Will Varley - *Is Anyone Out There?*,
from the album *Postcards From Ursa Minor*, 2015

For thousands of years, humans have stared out into the night sky and wondered about our place in the Universe. Yet, it is only in the last couple of decades that we have begun to understand the planetary systems associated with other stars. Thirty years ago, despite several claims of detections of planets around other stars, the only confirmed planets known were those in the Solar System. In the time since, over 3500 confirmed discoveries of exoplanets have been made[1], and the pace shows no signs of slowing down, with several new facilities for planet detection recently commissioned or planned for the near future. That number of 3500 exoplanets is however dwarfed by the staggering number of stars in the Milky Way Galaxy and galaxies in the observable universe; both are thought to be in the region of a few hundred billion. If each of those stars has on average just one planet, something thought to be true for the Milky Way (Cassan et al., 2012), there are some $10^{22}$ planets in the observable universe. We truly are only just opening our eyes to the vast array of planets the Universe has for us to find.

The first detection of an exoplanet around a main sequence star like the Sun, 51 Peg b, was made by Mayor and Queloz (1995). As with many brand new

[1]See the NASA Exoplanet Archive: `https://exoplanetarchive.ipac.caltech.edu/`

fields of scientific discovery, we have found numerous objects we did not expect to find, based naively on the architecture of our own planetary system. These have included Jupiter-sized planets on very short orbits ("hot Jupiters", of which 51 Peg b is an example), an abundance of planets with sizes between Earth and Neptune that have no Solar System analogue (often referred to as "super-Earths"), and very tightly packed multi-planet systems all with short orbits. Indeed, selection biases have dictated that the vast majority of planets known to date have very short orbits. As I will discuss throughout this work, residing very close to your host star is something that can have profound consequences for your atmosphere, as a result of the impingent X-ray and extreme ultraviolet radiation.

## 1.1 Exoplanet detection and characterisation

In this section, I discuss the methods of exoplanet detection. I give a short description of all the common methods, followed by a longer explanation of the transit method; all of the systems I present observations for in the following chapters host transiting planets.

### 1.1.1 Detection methods

The first confirmed discovery of planets around a star other than the Sun orbit a very different kind of star. Pulsars are a type of neutron star whose magnetic and spin axes are misaligned, such that the beam of intense electromagnetic radiation they emit comes into and out of view during each of their very fast rotations (e.g. Bell Burnell, 2017). The three-planet system around PSR B1257+12 was discovered through fluctuations in the pulse arrival time from their pulsar host (Wolszczan and Frail, 1992; Wolszczan, 1994). The pulsar and each planet orbit their common centre of mass, and so along the line of sight the pulsar appears to rock back and forth in a regular, periodic manner. The effect of light travel time differences causes fluctuation in the pulse arrival time. Despite being the first successful method, only a further 11 pulsar planets have been discovered in almost three decades since (Perryman, 2018, pg. 105). This paucity is likely linked to complex formation conditions (Martin et al., 2016).

The aforementioned 51 Peg b was uncovered by studying the radial velocity (RV) of the host star over time. Again, this is caused by the motion of star and planet about their common centre of mass. In order to study the periodic shifts, one must take precise stellar spectra, sampling over a substantial temporal baseline in order to sufficiently map out the full orbit of the planet. Back at the time of

the 51 Peg b discovery, the precision of the radial velocities was on the order of $15\,\mathrm{m\,s^{-1}}$. However, with spectrographs like HARPS, we are now able to regularly achieve $1\,\mathrm{m\,s^{-1}}$ (e.g. Mayor et al., 2009; Lanotte et al., 2014; Motalebi et al., 2015). The next generation of spectrographs, such as ESPRESSO which is in the process of being commissioned on the Very Large Telescope (VLT), and those planned for the Extremely Large Telescope (ELT) in the next decade (e.g. HIRES), will hope to push down towards $10\,\mathrm{cm\,s^{-1}}$, corresponding to the RV signal induced by an Earth-like planet around a Sun-like star.

RV discoveries dominated the first decade or so of exoplanet detections after 51 Peg b. The method has since been vastly exceeded in terms of new discoveries with the advent of precise ground-based photometric surveys and, in particular, space-based missions, both targeting transiting planets (I discuss this method in detail in Section 1.1.2, below). RV observations of planetary systems remain vital however, as the dynamical information they contribute (i.e. the mass of the planet multiplied by the sine of the inclination of the orbital planet to the line of sight) is very complementary to the geometric information provided by transits.

A few other detection methods have also been successfully employed, if less prolifically. Direct imaging of planets has been performed for a small number of objects, but this has tended to be those with larger angular separations from their host. Unsurprisingly, this method has favoured large planets with orbital semi-major axes of typically tens of AU. It also requires planets that are young enough to still be hot and luminous. Among the best known results to date is the HR 8799 system, which hosts four super-Jupiter planets with semi-major axes between 14 and 68 au (Marois et al., 2008, 2010).

Microlensing involves a foreground planetary system acting as a gravitational lens for a background star. The method is most sensitive to projected separations of a few of au (Wambsganss, 1997). The signal amplitude is also largely independent of planet mass, making the method an attractive one for discovering Earth-mass planets. However, the same is not true of the detection probability (Perryman, 2011, pg. 101). Moreover, it is difficult to perform follow up observations of the systems, as the lens and lensed systems are not resolvable following the microlensing event.

Like RVs, astrometry involves searching for tiny periodic changes due to reflex motion. However, in this case, the change of interest is in the star's position on the sky as opposed to along the line of sight. The ultra-precise positioning required means that no planet has successfully been discovered yet via this method, though a few detections of known planets have been made with *HST* (e.g. Benedict et al., 2002, 2006). The nominal five-year mission of *Gaia* is expected to yield some

$21,000 \pm 6000$ (mainly giant) planets through this method, though. This rises to $70,000 \pm 20,000$ if extended to ten years (Perryman et al., 2014).

### 1.1.2 The transit method

By far the most prolific method of exoplanet detection to date is transits. This is a geometric phenomenon that relies on the alignment of the planet's orbital plane with the line of sight direction of the host star from the Solar System. As a result, the planet transits across the stellar disc and blocks out a small fraction of its light. Exoplanets that transit their star do so every orbit, such that the dip in stellar brightness occurs at regular intervals. This is in contrast to the sporadically observed transits of Mercury and Venus in our own Solar System, as in that case the Earth's motion around the Sun makes the perfect alignment unlikely on any given orbit.

That is not to say that the chance of alignment of any given planet is high. In the limit of the planet radius, $R_{\rm p}$, being much smaller than the radius of its star, $R_*$, the geometric transit probability is given by (Borucki and Summers, 1984)

$$P(Transit) = \frac{R_*}{a}, \tag{1.1}$$

where $a$ is the semi-major axis. Thankfully, nature has been kind to us. Unlike in the Solar System, our search for exoplanets has revealed an abundance of planets with small orbital separation right from the very beginning. 51 Peg b's semi-major axis of 0.0527 au was a major surprise at the time of its discovery, especially for such a large planet. It had long been thought that such large planets had to form beyond the snow line, the transition point where many volatile species condense to form solid ices. The location of the snow line is estimated to be at 3 au for a Sun-like star (e.g. Martin and Livio, 2012). An increase in solid material beyond this point was thought to allow larger planetary cores to form than within the warmer inner regions of a protoplanetary disc. Substantial accretion of gas could subsequently occur for these larger cores (e.g. Pollack et al., 1996). The most popular explanation for hot Jupiters has been migration inwards after their formation beyond the snow line. Mechanisms proposed include interaction with the gas disc (e.g. Lin et al., 1996), and perturbation by a binary star companion via the Kozai-Lidov mechanism, driving a high eccentricity which is then damped through tides (e.g. Fabrycky and Tremaine, 2007). We now know that planets in general with semi-major axes several times smaller than Mercury's 0.3781 au are very common indeed, and although hot Jupiters in particular are rarer, they are relatively easy to find. This is one of the

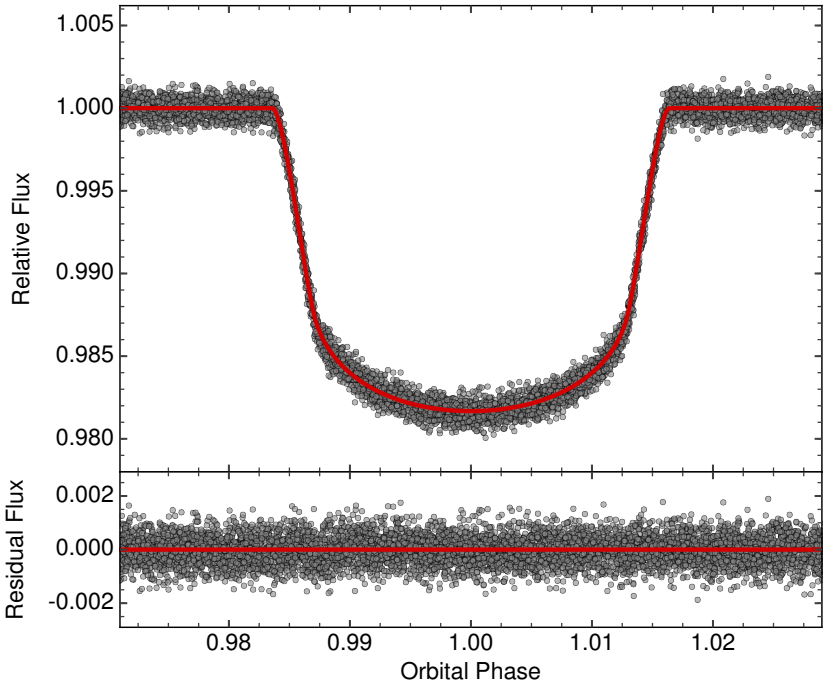


Figure 1.1: An example of phase-folded transit light curve for hot Jupiter WASP-55b. The data are from follow up observations made during Campaign 6 of the *K2* mission. Figure taken from Clark et al. (2018).

main reasons that the multitude of transit surveys undertaken over the past decade and a half have been a viable means of searching for exoplanets. Furthermore, the size, short periods, and large expanded gaseous envelopes of hot Jupiters have meant they have proved the best targets for atmospheric studies.

When a planet is seen to transit, a number of otherwise unobservable characteristics of the system become perceptible. Perhaps of greatest note is the radius of the planetary body, which is linked to the depth of the transit, $\delta$. In the case of negligible limb-darkening, this is given by

$$\delta = \left(\frac{R_{\rm p}}{R_*}\right)^2 . \tag{1.2}$$

Stellar limb-darkening is the non-uniform brightness of a star, wherein the intensity of emitted light appears dimmer towards the edges of the disc. The effect is caused by the optical thickness of the photospheric plasma. Towards the edge of the disc, the angle between the line of sight and normal to the stellar surface is greater, and so the distance below the surface where an optical depth of one is reached is smaller. (Note an optical depth of one is where the distance travelled by

a photon through the plasma is equal to the mean free path.) In turn, this means the plasma at that depth is cooler and so appears dimmer. Several formulations of limb-darkening laws have attempted to model the effect in terms of a function of a parameter $\mu = \cos\theta$, where $\theta$ is the angle between the line of sight to the observer and the normal to the stellar surface at some point. In fitting my WASP-80b NUV transit in Chapter 3, I apply the quadratic formulation (Manduca et al., 1977):

$$\frac{I(\mu)}{I(1)} = 1 - u_1(1-\mu) - u_2(1-\mu)^2, \tag{1.3}$$

where $I$ is the intensity of the observed emission for some value of $\mu$. The variables $u_1$ and $u_2$ are referred to as limb-darkening coefficients. While these are often fitted as part of the transit model, it is also common to use theoretically-derived values from stellar atmosphere models (e.g. Claret and Bloemen, 2011), as I do in Chapter 3. Other formulations of limb darkening laws include linear, square root and non-linear (e.g. Claret, 2000), each with their own set of coefficients. In a planet transit context, limb-darkening acts to smooth out what would otherwise be a box-like appearance into something more akin to a U-shape. Thus, a typical light curve of a star during the transit of a hot Jupiter (as seen from space), folded on its orbital period looks like that in Fig. 1.1.

As a purely geometric effect, transits typically cannot provide the dynamical information in order to yield a mass measurement; the main exception being where transit-timing variations are detectable (e.g. Agol and Fabrycky, 2018). In a similar vein, RVs cannot determine the radius of a planet. Thus, the best characterised planets to date are those that both transit their star and are amenable to RV follow up. Furthermore, the calculations for many of the planetary characteristics of interest depend on the star in some way. As such, accurate stellar characterisation is also crucial to obtaining accurate planetary and orbital parameters.

Like all exoplanet detection methods, transit searches suffer from several selection effects. For a transit survey, a full analysis by Haswell (2010, pg. 65) shows strong selection effects in favour of larger planets ($R_p^3$), smaller semi-major axes ($a^{-7/4}$), more luminous host stars ($L_*^{3/2}$), and a weaker effect favouring smaller stars ($R_*^{-5/4}$). These biases highlight how much easier it is to detect a hot Jupiter than an Earth-like planet. Indeed, the first planets found to transit were hot Jupiters. HD 209458b was discovered first in RVs, before follow up photometry revealed a clear, repeatable transit dip (Charbonneau et al., 2000; Henry et al., 2000). Since then, over 3500 planets have so far been observed to transit their star, according to the NASA Exoplanet Archive. I briefly outline some of the main transit surveys

that have driven the explosion in transit discovery over the past two decades, below.

### Ground-based surveys

Since the detection of HD 209458, several ground-based searches for new transiting planets have been initiated. These typically monitor thousands of stars simultaneously, and together with the contributions from space outlined below, have led to a new era in transit detection dominance within the exoplanet field.

*OGLE* provided the first new discovery via a transit detection (Konacki et al., 2003), while the most prolific to date have been *SuperWASP* (Pollacco et al., 2006) and *HAT/HAT-South* (Bakos et al., 2002, 2004). The vast majority of these new discoveries have been Jupiter or Saturn-sized objects on short orbits, providing some of the best targets for follow up characterisation. More recently, *KELT* (Pepper et al., 2007) has found a number of ultra-hot Jupiters around A- and F-type stars (e.g. Gaudi et al., 2017; Johnson et al., 2018), while *NGTS* (Wheatley et al., 2018) aims to push down to smaller planets than previously possible for Solar-like stars from the ground, with some success already (West et al., 2018). M dwarfs have become particularly attractive targets for ground-based surveys, owing to the fact that transit signals are larger than for Solar-like stars with the same planet size, and that the "habitable zone" around such stars is much closer to them. *MEarth* (Nutzman and Charbonneau, 2008) has successfully discovered three Earth/super-Earth-sized planets (e.g. Berta-Thompson et al., 2015), though perhaps the most interesting exoplanetary system discovered to date is the compact TRAPPIST-1 system, in which seven Earth-sized planets orbit an ultra-cool dwarf star only slightly more massive than a brown dwarf (Gillon et al., 2016, 2017a).

### Space-based surveys

Space-based observatories have provided unprecedented numbers of detections of exoplanets. *CoRoT* was the first dedicated space-based transit searcher (Auvergne et al., 2009), but it is *Kepler* (Borucki et al., 2010), and its repurposed mission *K2* (Howell et al., 2014), that have truly revolutionised the field. Over 2600 planets have been identified from their data and subsequently confirmed (or statistically verified), with a similar number of candidates still outstanding, according to the NASA Exoplanet Archive. This haul is well over half of the total known exoplanet population, and includes a large number of Earth, super-Earth and sub-Neptune-sized planets. Using its discoveries, detailed studies of the planet population across a sizeable area of parameter space have been possible for the first time (e.g. Fressin

et al., 2013; Winn, 2018). As part of this, features such as those thought to be driven by photoevaporation, which I discuss further in Section 1.2.4, have been discovered.

One of the limitations of the *Kepler* planets is that they tend to orbit quite distant, dim stars, making follow up characterisation to determine their masses or atmospheric compositions difficult. *K2* and the recently launched *Transiting Exoplanet Survey Satellite* (*TESS*; Ricker et al., 2015) both target(ed) brighter stars, identifying candidates more amenable to further studies. Looking into the future, it is hoped that *PLATO* (Rauer et al., 2014), together with the upcoming generation of high RV-precision spectrographs for telescopes like the ELT, will lead the way in providing an unprecedented sample of well-characterised rocky planets.

### 1.1.3 Transmission spectroscopy

One of the key aspects in following up discovered planets is investigating their atmospheric composition. Transiting planets are particularly good targets for this as the transit depth one detects varies as a function of wavelength. This variation is driven by the species present in any atmosphere maintained by the planet. Wavelengths associated with absorption lines of such species will cause the atmosphere to be more optically thick at those wavelengths, resulting in a slightly deeper transit. This variation of opacity with wavelength is somewhat analogous to atmospheric transmission of the Earth's atmosphere at different wavelengths (See Section 2.1, in particular Fig. 2.1).

The features are typically quite small and require a very precise measurement of $R_\mathrm{p}/R_*$. For a typical hot Jupiter around a Solar-type star, the transit absorption signal for one scale height of atmosphere is just 137 ppm (Deming et al., 2019). More generally, the magnitude of a transmission spectroscopy signal can be estimated by (Seager et al., 2009)

$$5 \times \frac{2R_pH}{R_*^2}, \tag{1.4}$$

where $H$ is the planetary scale height. In turn, $H \propto \mu^{-1}$, where $\mu$ is the mean molecular mass. Thus, the detection of an $N_2$-dominated atmosphere, like the Earth's, is more difficult than a $H_2$-dominated one. Keeping everything else constant, the difference in $\mu$ results in a signal that is 14 times smaller.

The technique of transmission spectroscopy has been used extensively over the past decade and a half. Just a couple of years after its initial discovery, HD 209458b became the first exoplanet to have its atmosphere detected; the transit depth was found to be slightly deeper in the sodium D lines than at the surrounding wavelengths (Charbonneau et al., 2002). Observations with *HST* and *Spitzer* have

led the way in characterising atmospheres, revealing a wealth of information about the variations of different planets' atmospheres, particularly for hot Jupiters. These have included the detection of elemental and molecular species, such as water and the aforementioned sodium, clouds, and Rayleigh scattering slopes (e.g. Sing et al., 2016). Some of these features have been successfully probed from the ground too, with both high (e.g. Brogi et al., 2016) and low resolution (e.g. Redfield et al., 2008; Kirk et al., 2017) spectrographs.

Where sensitivity is not high enough to measure high-$\mu$ features, the result is a flat transmission spectrum. This has proved a particular issue for measurements of super-Earths (Kreidberg et al., 2014; Morley et al., 2015, and references therein). Even where sensitivity is sufficient to uncover potential spectral features of an atmosphere, another complicating factor is clouds and hazes. Sufficiently high cloud decks can completely block out absorption features from detection, leading again to a flat transmission spectrum (e.g. Louden et al., 2017b).

## 1.2 Exoplanet evaporation

The vast majority of atmospheric studies, such as those described in Section 1.1.3 above, have tended to focus on observations at optical and/or NIR wavelengths. However, some of the most interesting results to date have been obtained by extending these principles to higher-energy regimes. Most notable is the discovery that some close-in exoplanets are evaporating. In this section, I discuss the observational evidence for evaporation, the possible mechanisms driving it, and its effects on the exoplanet population as a whole.

### 1.2.1 Observational evidence

#### Ly $\alpha$

A short time after the first exoplanet atmosphere detection by Charbonneau et al. (2002), Vidal-Madjar et al. (2003) published another study of HD 209458b in transit. Their observations, made with the Space Telescope Imaging Spectrograph (STIS) onboard *HST*, revealed a $15 \pm 4\%$ transit at wavelengths around the Ly $\alpha$ line at 1215.67 Å (see Fig. 1.2). This equates to being ten times deeper than the optically-measured transit depth. In comparison, the signal in the Charbonneau et al. (2002) study of the sodium lines was $0.0232 \pm 0.0057\%$ deeper than at surrounding wavelengths, and as such is consistent with being a source within the bound atmosphere of HD 209458b. On the other hand, the large depth in Ly $\alpha$ points to absorption from a

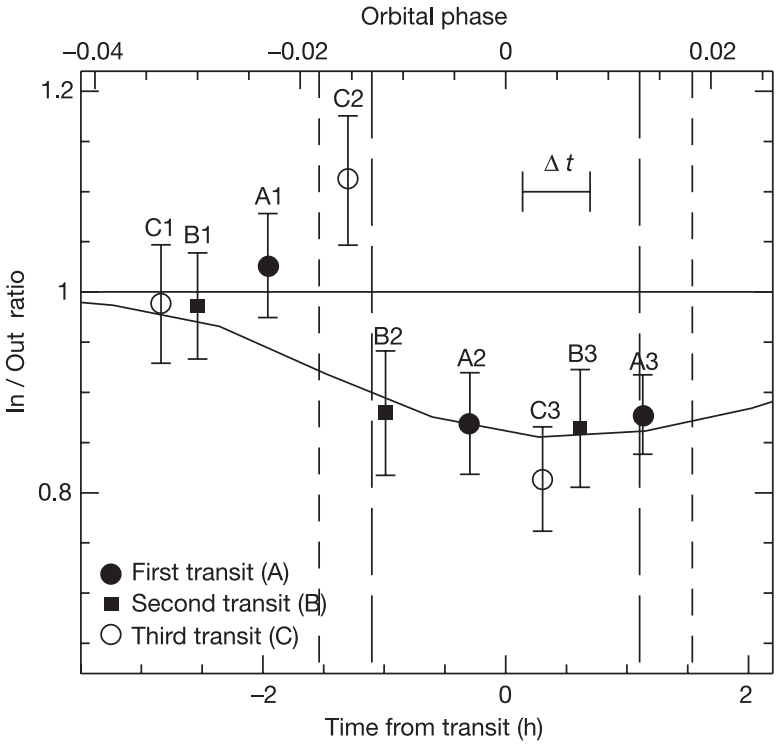


Figure 1.2: Fig. 3 of Vidal-Madjar et al. (2003), showing the deep Ly $\alpha$ transit of HD 209458 - the first evidence for evaporation from an exoplanet atmosphere.

region larger than the planet's Roche lobe. Together with the evidence for an early-ingress and late-egress, this led Vidal-Madjar et al. (2003) to conclude HD 209458b has an extended upper atmosphere of hydrogen escaping from the planet. The exact interpretation of these results have been debated as part of reanalyses in the literature (Ben-Jaffel, 2007, 2008; Vidal-Madjar et al., 2008). However, further *HST* observations at lower resolution have confirmed that the planet has a large extended hydrogen atmosphere (Vidal-Madjar et al., 2004; Ehrenreich et al., 2008; Ben-Jaffel and Sona Hosseini, 2010), even if the extent to which it is evaporating is disputed.

In Fig. 1.3, I show the Ly $\alpha$ line profile from Vidal-Madjar et al. (2003). This highlights how the core of the Ly $\alpha$ line is affected readily by ISM absorption and geocoronal emission, and why observations of this kind have to focus on the wings of the line.

HD 189733b orbits the closest and brightest star of any known transiting hot Jupiter. Observations with both the Advanced Camera for Surveys (ACS; also onboard *HST*) and STIS have revealed H I evaporation for this planet too. The 2007/2008 observations with ACS showed a 5% deep transit, twice the depth of

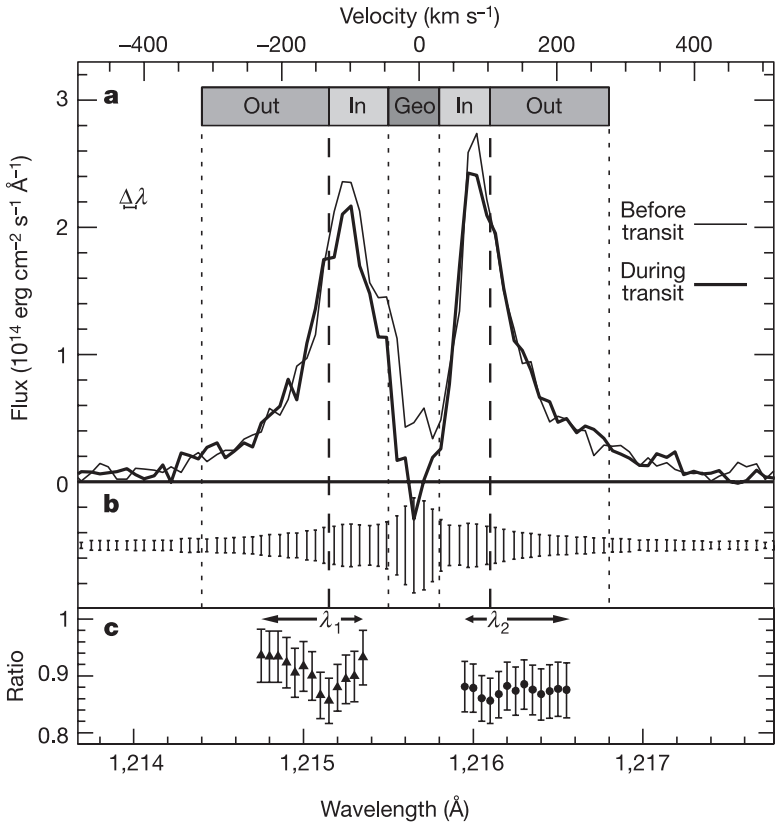


Figure 1.3: Fig. 2 of Vidal-Madjar et al. (2003), showing the profile of the Ly $\alpha$ line of HD 209458 before and during transit.

the optical transit (Lecavelier Des Etangs et al., 2010). The 2011 observations with STIS showed a much deeper transit that was almost 15% deep (Lecavelier des Etangs et al., 2012; Bourrier et al., 2013). However, a previous observation in 2010, also with STIS, showed no evidence of absorption by atmospheric hydrogen. Lecavelier des Etangs et al. (2012) suggested a possible link between the deep feature in the 2011 observations and an X-ray flare detected with *Swift*, some 9 hr before the transit. Bourrier and Lecavelier des Etangs (2013) posited that the increased absorption would be due to the flare either increasing the planetary mass loss rate or significantly changing the properties of the stellar wind at that epoch. The former scenario was disfavoured by Chadney et al. (2017), who showed that the increase in mass loss due such a flare would be insufficient to explain the large temporal variation in measured Ly $\alpha$ depth.

Similar signatures are beginning to be detected for sub-Jovian-sized planets too. GJ 436b is a warm Neptune-sized planet around a M dwarf star, and one of the closest transiting planets to Earth. Initial studies at Ly $\alpha$ with STIS hinted at an

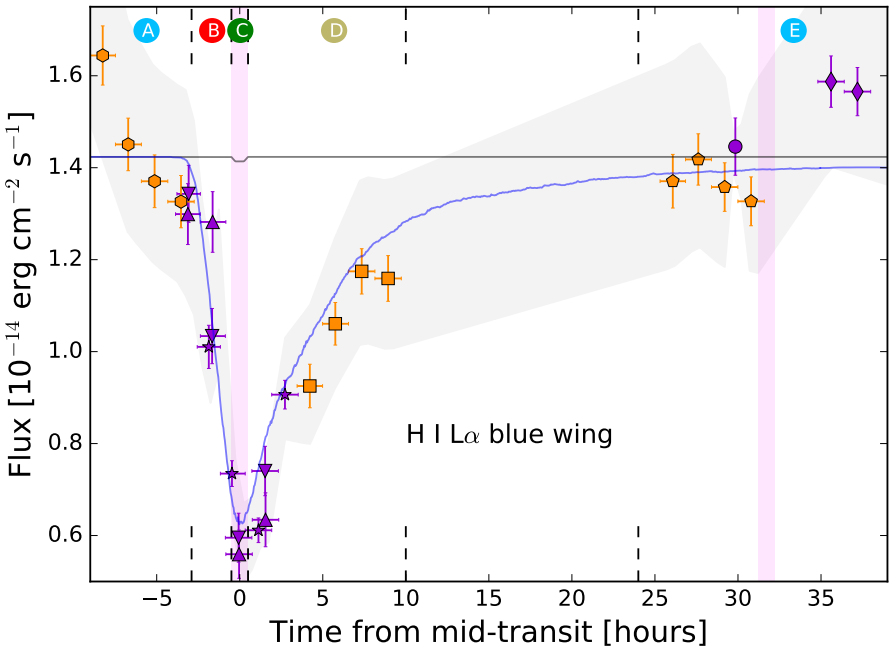


Figure 1.4: Fig. 2 of Lavie et al. (2017), showing the exceptionally deep Ly $\alpha$ transit of GJ 436b, and its long egress, lasting up to a full day after the optical transit. The two sets of points correspond to different observation epochs. The blue and black lines are the Ly $\alpha$ and optical transit models, respectively.

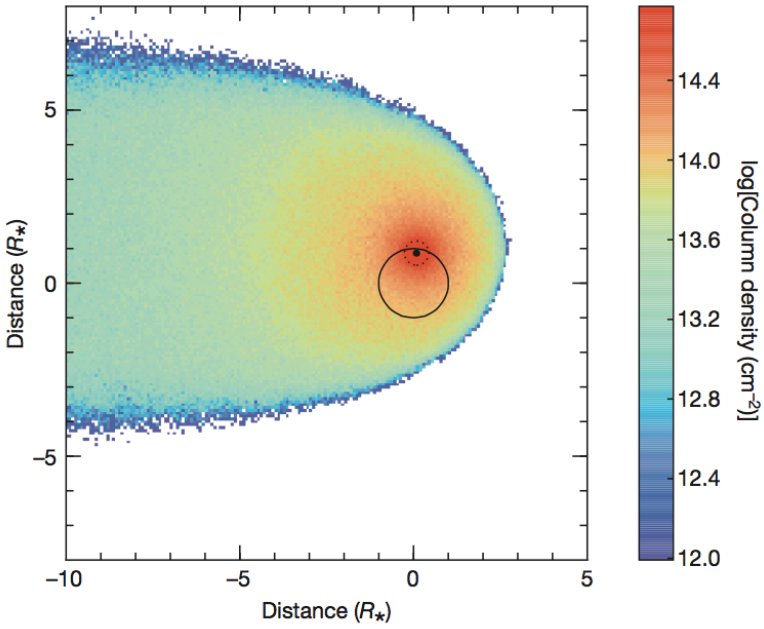


Figure 1.5: Fig. 3 of Ehrenreich et al. (2015), depicting the scale of the planetary tail of GJ 436b. Colours show the cloud density. The small black dot is the planet, the dotted circle around it is its Roche lobe, and the solid black circle is the star.

extended hydrogen envelope, but an inaccurate ephemeris affected the analysis of Kulow et al. (2014). The following year, using a reanalysis of the first observation, and two new STIS visits, Ehrenreich et al. (2015) discovered the full extent of the absorption feature. Despite an optical transit depth of just 0.69%, they found the Ly $\alpha$ transit to be exceptionally deep in the blue wing, at $56.3 \pm 3.5\%$. Furthermore, Lavie et al. (2017) obtained new observations probing the length of the long egress hinted at by Ehrenreich et al. (2015). As I display in Fig. 1.4, their blue wing light curve showed that the egress lasts anywhere between 10 and 24 hr after the optical transit. The blue model curve on that figure is that calculated with the EVaporating Exoplanets (EVE) code by Bourrier et al. (2016). The interpretation of the feature is a huge comet-like tail of material extending out behind the planet across a significant portion of its orbit. The scale of this cloud is shown in Fig. 1.5.

GJ 3470b is another warm Neptune, of similar size to GJ 436b, but somewhat denser. It also orbits an M dwarf, and with a similar orbital separation. Also like GJ 436b, it shows deep Ly $\alpha$ transits; Bourrier et al. (2018a) observed transits some $35 \pm 7\%$ and $23 \pm 5\%$ deep in the blue and red wings of the line, respectively. The signature also extended up to 3 hr before and after the centre of the optical transit, and was relatively similar in all three visits.

A few other planets have had observations at Ly $\alpha$ in order to probe possible hydrogen escape. Investigations by Bourrier et al. (2017a) for the super-Earth HD 97658b suggested that it does not have an extended, evaporating hydrogen atmosphere, in contrast to predictions of observable escaping hydrogen, due to the dissociation of steam. Possible explanations include a relatively low XUV irradiation, or a high-molecular weight atmosphere. A similar non-detection for 55 Cnc e had previously been found by Ehrenreich et al. (2012). In that case, complete loss of the atmosphere down to a rocky core has not been ruled out. That study of 55 Cnc did however suggest the possibility of an extended hydrogen atmosphere for planet b. That planet is not seen to transit optically, but the detection of Ly $\alpha$ absorption suggests the inclination may be edge-on enough that an extended atmosphere partially transits. Finally, a study of Kepler-444 showed strong variations in the Ly $\alpha$ line that could arise from hydrodynamic escape of the atmosphere (Bourrier et al., 2017c), while Ly $\alpha$ emission has been detected for TRAPPIST-1 (Bourrier et al., 2017b) and the search for evaporation signatures is ongoing.

### Heavier species

Evidence for atmospheric escape also extends to lines of other elements. Deep carbon, oxygen and silicon features have been detected for HD 209458b, and interpreted

as originating in the extended atmosphere surrounding the planet (Vidal-Madjar et al., 2004; Linsky et al., 2010; Schlawin et al., 2010), the species having been entrained in a hydrodynamically escaping flow (see Section 1.2.2). Some other detections for Si IV (Schlawin et al., 2010) and Mg I (Vidal-Madjar et al., 2013) have been more marginal, while the Si III detection has since been found to be likely due to stellar variability (Ballester and Ben-Jaffel, 2015).

For HD 189733b, a similar O I detection has been made, together with a tentative transit detection in C II showing a possible early-ingress (Ben-Jaffel and Ballester, 2013). Pre-transit absorption in the optical is also possibly present in FUV lines of S III and N V (Bourrier et al., 2013, Bourrier et al., in prep).

Outside of the interest in detecting other species in extended atmospheres, these observations of metal lines can be useful out to larger distances than Ly $\alpha$. The neutral and ionised metal lines in the UV do not suffer interstellar absorption to the same extent, and so absorption from extended atmospheres can be detected for systems much further away than possible with Ly $\alpha$. WASP-12b, residing $432 \pm 6$ pc from Earth (Gaia Collaboration et al., 2018), is such a system. *HST* observations by Fossati et al. (2010) and Haswell et al. (2012) revealed deeper transits consistent with an overfilling Roche lobe in the NUV at wavelengths corresponding with resonance lines of a long list of metals, including Fe and Mg. The observations also show a possible early ingress that has been suggested to originate from a bow shock in front of the planet. See Section 6.6.2 for a further discussion of the early ingress in the context of my findings for the X-ray transit of HD 189733b.

### Helium

Seager and Sasselov (2000) first predicted strong atmospheric absorption in a particular absorption line of helium at 10830 Å, associated with a metastable triplet state of the element. Moutou et al. (2003) attempted to detect atmospheric absorption in this line for HD 209458b, but only succeeded in placing an upper limit on the feature. Oklopčić and Hirata (2018) recently emphasised the possibility of exploiting the feature for detecting escaping atmospheres, and shortly afterwards Spake et al. (2018) successfully used Wide Field Camera 3 (WFC3) onboard *HST* to detect $0.049 \pm 0.011\%$ extra absorption in a 98 Å-wide bin around the line for hot Jupiter WASP-107b. The detection allowed the authors to estimate the mass loss rate lies between $10^{10}$ and $3 \times 10^{11}\,\mathrm{g\,s^{-1}}$. A number of other successful detections of extended/evaporating atmospheres using this method have followed in recent months, as I describe below.

One of the major advantages of this He line over both Ly $\alpha$ and most UV

metal lines for detecting extended atmospheres is that one does not have to use space-based observations. From the ground, the CARMENES instrument has led the way. CARMENES has the additional advantage over *HST* of being a high-resolution spectrograph, meaning the line is resolved. WASP-69b (Nortmann et al., 2018) and HAT-P-11b (Allart et al., 2018) have both had large extended atmospheres detected in this way. The finding for the Neptune-sized HAT-P-11b is particularly exciting as it proves the technique can be used for sub-Jovian-sized planets. Analysis of *HST* observations additionally made it the first planet for which a photoevaporation signature has been detected from both the ground and space (Mansfield et al., 2018). The signature for WASP-107b has also since been detected from the ground (Allart et al., 2019). A CARMENES detection for HD 189733b by Salz et al. (2018) is interesting as the extra absorption is only indicative of a 0.2 $R_{\rm p}$ He layer, in contrast to the large escape features seen for other species. The authors suggest that this does not contradict the findings at other wavelengths for the planet; rather, the absorption in the He line does not probe the same layers of the atmosphere.

Five other systems have had non-detections of extended atmospheres reported: WASP-12 (Kreidberg and Oklopčić, 2018), HD 209458, KELT-9 & GJ 436 (Nortmann et al., 2018), and GJ 1214 (Crossfield et al., 2019). Assessing the detections so far, Oklopčić (2019) noted that the four planets that have detections so far are in orbit around K stars, while the five with non-detections are around stars of other stellar types (both earlier and later than K). They also note that this finding is in line with their expectations from theory, with detections most likely for high-EUV and low-MUV emitting stars, due to the ability of those photons to ionise the ground and metastable states, respectively.

### Balmer lines

The final wavelengths with evidence for evaporation from exoplanets to date is the H $\alpha$ and H $\beta$ Balmer lines. Yan and Henning (2018) analysed two transit observations by CARMENES of KELT-9b, finding an extra 1.15% excess absorption in the H $\alpha$ line, giving an effective radius very close to the size of Roche lobe, implying significant atmospheric escape. Follow up observations with the Large Binocular Telescope by Cauley et al. (2019) showed the H $\alpha$ signature with a consistent depth to Yan and Henning (2018), and also revealed a slightly smaller (0.70% excess absorption) but similar feature in the H $\beta$ line.

### 1.2.2 Evaporation mechanism

With substantial evidence that the atmospheres of some close-in planets are undergoing significant evaporation, in this section I explore some of the theoretical explanations for the underlying mechanisms at play. In short, I will explain why the escape is thought to be driven by X-ray and EUV emission (together, XUV) and not the considerably higher flux at optical wavelengths.

#### Jeans escape

Jeans escape (Jeans, 1925; Chamberlain, 1963) is a thermal process related to the tail of the Maxwell-Boltzmann distribution. This occurs in the uppermost regions of planets whose atmospheres are generally tightly bound by gravity. This region, termed the exosphere, has a lower boundary: the exobase. The location of this point relates to where the density of atmospheric particles is small enough that the collisional mean free path is larger than the pressure scale height of the atmosphere. The Jeans parameter, $\lambda$, is a way of describing the rate of the loss of particles and corresponds to the ratio of the gravitational potential and the thermal energies of a gas particle. This can be written as

$$\lambda = \left( \frac{v_{\rm es}}{v_{\rm mp}} \right)^2 , \tag{1.5}$$

where $v_{\rm es}$ and $v_{\rm mp}$ are the escape and most probable velocities of an exospheric gas particle. In the Jeans escape regime, where $v_{\rm es} >> v_{\rm mp}$ (and thus $\lambda >> 1$), the vast majority of gas particles are too slow to escape. Only those at the highest speeds in the tail of the Maxwell-Boltzmann distribution can successfully escape the atmosphere. Furthermore, as $v_{\rm mp} \propto (1/\sqrt{m})$, where $m$ is the mass of the gas particle, lighter species are more susceptible to escape than heavier ones. This is one reason why Earth's atmosphere, for instance, is now dominated by heavy elements and molecules, such as $N_2$ and $O_2$, and not $H(_2)$ or He.

#### Hydrodynamic escape

When $\lambda \lesssim 1$, it is clear from Equation 1.5 that the most probable gas particle speed is about equal to or greater than the escape velocity, meaning that a large proportion of the gas particles in the upper atmosphere are susceptible to escaping the planet's gravity. In practice, Öpik (1963) determined that hydrostatic equilibrium ceases to apply for $\lambda < 1.5$ (monatomic gases) or 2.5 (diatomic gases; but see also, for example Volkov et al., 2011), and the exosphere becomes unstable to significant mass loss.

In this case, relatively large amounts of atmospheric material can flow off the planet in bulk. Unlike Jeans escape, the outflowing material in the hydrodynamic case is collisional. As such, lighter species can, in this case, drag heavier species along with them as part of the flow, or even be the main constituent of it (e.g. Seager, 2010, pg. 77). This process of hydrodynamic escape is similar to the description of the Solar wind by Parker (1963).

XUV photons deposit large amounts of energy in the upper layers of the atmospheres of close-in planets through photoionisation processes, heating the exosphere to temperatures up to around 10,000 K (e.g. Schneider et al., 1998; Coustenis et al., 1998; Lammer et al., 2003). Compton scattering has also been considered in some models of exospheric heating (e.g. Cecchi-Pestellini et al., 2006), given its comparable cross-sections to photoionisation at higher X-ray energies (Yan et al., 1998). Fig. 1.6 highlights the much larger contribution to the exospheric heating by the energetic XUV photons compared to the much larger flux of photons at optical wavelengths. The dot-dashed line shows the contribution to the exospheric heating by the radiative effective temperature, a proxy for the heating by optical/IR photons, and which dominates the bolometric flux. The solid lines are the contribution by XUV photons at various stellar ages, as the X-ray luminosity changes as the star ages (see Section 1.3.5). As can be seen, XUV heating meets the condition for hydrodynamic escape at all ages, while the heating by optical photons is always at least an order of magnitude too low to meet this condition, even for hot Jupiters. XUV photons are thus thought to be the driving force behind the hydrodynamic atmospheric escape from close-in atmospheres.

An important distinction to make is between the terms "blow-off" and "boil-off". Blow-off is a term generally applied to describe the (XUV-driven) hydrodynamic escape of material, as described above (although there are other uses of the term - see e.g. Catling and Kasting, 2017, pg. 134). "Boil-off" is specifically a process that occurs for low-mass planets with small orbital separations during a short phase after the dispersion of the protoplanetary disc, but before the onset of meaningful XUV photoevaporation. At that epoch, powerful hydrodynamic escape of a large proportion of the gas envelope accreted while in the disc can ensue (Stökl et al., 2015; Owen and Wu, 2016; Ginzburg et al., 2016; Fossati et al., 2017). This is possible because of the relatively low surface gravities of these planets as they exit the disc; they were able to capture and retain this material in the disc phase, but not after its dispersal. Driven by the cooling of the inner layers, the outer layers of the atmosphere become unbound, and the planets contract quickly during this period (e.g. Owen and Wu, 2016).

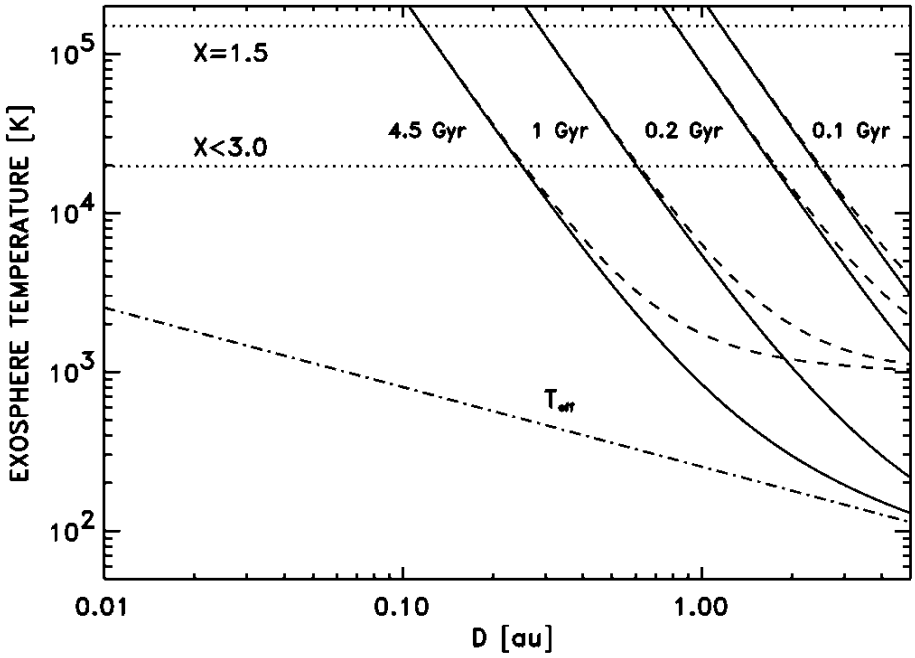


Figure 1.6: Fig. 1 of Lammer et al. (2003), highlighting how the XUV heating (solid lines), but not the optical heating (dot-dashed line), reaches the condition for hydrodynamic escape (dotted lines - also see text). X is used in place of $\lambda$ here.

Interaction of the hydrodynamically escaping material with the stellar wind is able to form the comet-like tails (Schneider et al., 1998), as have been observed for planets like GJ 436b (Ehrenreich et al., 2015; Lavie et al., 2017). However, one of the puzzling questions that remain in explaining the evaporation observed is related to the high velocities of the escaping material. The hydrodynamic escape theory suggests gas velocities in the outflow should be transonic (e.g. Parker, 1963; Yelle, 2004; Murray-Clay et al., 2009; Owen and Jackson, 2012). For a typically assumed gas temperature of $10^4$ K, this speed is about $10\,\mathrm{km\,s^{-1}}$, an order of magnitude lower than that for which significant absorption in the blue wing of the Ly $\alpha$ line is often observed (e.g. Ehrenreich et al., 2015; Bourrier et al., 2018a). A couple of approaches have attempted to tackle this problem. The first is to consider Energetic Neutral Atoms (ENAs). These result from charge exchange of the escaping hydrogen with protons from the stellar wind, and their formation where the stellar wind meets the escaping material could result in the supersonic speeds observed (e.g. Holmström et al., 2008; Ekenbäck et al., 2010; Tremblin and Chiang, 2013; Odert et al., 2019). ENAs have previously been observed in the Solar System planetary atmospheres (e.g. Brinkfeldt et al., 2006; Galli et al., 2008). An alternative explanation is that

the high velocities are driven by radiation pressure. Studies of these processes have shown them both to be a viable explanation (e.g. Bourrier and Lecavelier des Etangs, 2013; Ehrenreich et al., 2015; Beth et al., 2016).

### The role of X-ray vs. EUV

An important question to try and answer is whether X-rays or EUV are more important in driving the evaporation. This is perhaps just as pertinent a question for the observer as it is the theorist, since the EUV emission must be reconstructed from other wavelengths, as I discuss in Section 2.1.1. Therefore if it is relevant, it is important that our methods of estimating the EUV flux from the observations we make at those other wavelengths are also sound (see Section 3.4.4).

Various theoretical studies have modelled the heating contributions of only X-rays (e.g. Cecchi-Pestellini et al., 2006; Penz et al., 2008a), only EUV (e.g. Yelle, 2004; Murray-Clay et al., 2009), and a combination of both (e.g. Cecchi-Pestellini et al., 2009; Owen and Jackson, 2012; Koskinen et al., 2013). Cecchi-Pestellini et al. (2009) found an energetic cross-over, where EUV heating dominated in the uppermost parts of the atmosphere where the column density is lower, while X-rays penetrate deeper into the atmosphere and thus dominate those layers. X-rays are able to do this as the absorption cross sections of atmospheric species at those wavelengths are a few orders of magnitude smaller than for EUV photons. Owen and Jackson (2012) found two regimes present in their results. The evaporation starts off X-ray driven, before switching to be EUV driven when the X-ray luminosity, $L_{\mathrm{X}}$, drops below some threshold. The reason for this is due to the position of the ionisation front with respect to the (possible) sonic point in the flow. If the ionisation front is below the sonic point in the planet's atmosphere the flow is EUV driven; the flow is X-ray driven if the ionisation front is instead above.

A study by Owen and Wu (2013), building on the Owen and Jackson (2012) model, found that EUV contributes only 10% of the total lifetime mass loss. However, both of those studies make the assumption that the value of the EUV luminosity, $L_{\mathrm{EUV}}$ is identical to $L_{\mathrm{X}}$, and couple their evolution as such. In the context of the reconstruction method I derive in Chapter 3, I find that this is not necessarily the case. In particular, see Section 5.6.1 where I investigate the time evolution of EUV compared to X-rays under my assumed reconstuction method. That said, Kubyshkina et al. (2018a) point out that because X-rays can penetrate deeper than EUV, they can still provide a significant proportion of the heating to the atmosphere, even when the flux is much lower than the EUV.

While it seems from these theoretical studies that EUV might be more im-

portant when the overall XUV flux is lower, no definitive picture exists of exactly where each of the two wavelength ranges is important. In the face of this uncertainty, I assume X-ray and EUV to be of equal importance in the following chapters. By giving the values of $L_{\rm X}$ and $L_{\rm EUV}$ separately though, I leave the results open for possible reanalysis in the future if it becomes clear that one of the wavelengths indeed is more dominant.

### 1.2.3 Modelling mass loss

Numerous attempts have been made at modelling the mass loss from close-in planets undergoing hydrodynamic escape. I outline these attempts below.

#### Energy-limited evaporation

One of the simplest, yet effective, ways of estimating the mass loss from close-in atmospheres is the energy-limited method. In this method, one assumes that the energy input, $E$, to the system goes into removing mass from the atmosphere at some efficiency. The energy input that goes to removing mass per unit time is just the sum of the X-ray and EUV flux, $F_{\rm XUV}$, multiplied by an efficiency parameter, $\eta$, and the area, $A = \pi R_{\rm XUV}^2$, it is incident upon. Here, $R_{\rm XUV}$ is the average altitude at which the XUV photons are absorbed, and can be expressed simply as

$$R_{\rm XUV} = \beta R_{\rm p}. \tag{1.6}$$

This energy input drives a mass loss per unit time, $\dot{M}_{\rm En}$, from a gravitational potential given by $GM_{\rm p}/R_{\rm p}$. One can then equate the gravitational potential energy to the input XUV heating:

$$\frac{GM_{\rm p}\dot{M}_{\rm En}}{R_{\rm p}} = \beta^2 \eta \pi F_{\rm XUV} R_{\rm p}^2. \tag{1.7}$$

In addition to rearranging Equation 1.7 to find an equation for the mass loss rate, I also include the Roche lobe correction factor, $K$, added by Erkaev et al. (2007), given by

$$K = 1 - \frac{3}{2\xi} + \frac{1}{2\xi^3}, \tag{1.8}$$

where $\xi = R_{\rm RL}/R_{\rm p}$. In turn, $\xi$ can be approximated by $(\delta/3)^{1/3}\lambda$ where $\delta = M_{\rm p}/M_*$, and $\lambda = a/R_{\rm p}$. This extra factor accounts for the fact that one does not have to put in sufficient energy to lift the escaping mass to infinity, rather it need only be lifted to the Roche lobe height, $R_{\rm RL}$, in order to become unbound to the atmosphere.

Putting this altogether, the final version of the energy-limited mass loss rate equation is (Watson et al., 1981, though without the $K$ factor)

$$\dot{M}_{\rm En} = \frac{\beta^2 \eta \pi F_{\rm XUV} R_{\rm p}^3}{GKM_{\rm p}}. \tag{1.9}$$

Note that I follow the approach of Salz et al. (2016a), outlined in their footnote 1, in using a $\beta^2$ factor (Watson et al., 1981; Lammer et al., 2003; Erkaev et al., 2007) instead of a $\beta^3$ factor (e.g. Baraffe et al., 2004; Sanz-Forcada et al., 2010). Equation 1.9 has been applied by numerous past studies to calculate mass loss rate estimates for various planets (e.g. Lecavelier Des Etangs, 2007; Sanz-Forcada et al., 2011; Salz et al., 2015a; Louden et al., 2017a; Wheatley et al., 2017).

The value of $\eta$ for a given system has been the subject of much discussion (e.g. Shematovich et al., 2014; Louden et al., 2017a, and references therein), with estimates and adopted values often varying considerably from study to study (e.g. Penz et al., 2008b; Murray-Clay et al., 2009; Owen and Jackson, 2012). A canonical choice of 0.15 has been widely used previously in the literature (Watson et al., 1981; Tian et al., 2005; Ehrenreich and Désert, 2011; Salz et al., 2015a; Erkaev et al., 2016; Kubyshkina et al., 2018a), and numerous other studies have used similar values (Lammer et al., 2009; Sanz-Forcada et al., 2011; Wheatley et al., 2017; Owen and Wu, 2017). These values are in agreement with the findings of theoretical studies such as Owen and Jackson (2012) and Shematovich et al. (2014), and thus I adopt 0.15 as my default assumption when applying the Equation 1.9 in Chapters 3, 4 and 5. Despite this, $\eta$ should still be regarded as uncertain though, and in Chapter 3 I also apply two further assumptions of $\eta$. The first is using the results of the hydrodynamic simulations performed by Salz et al. (2016a). They infer planet-specific estimates of $\eta$ and $\beta$ for a small sample of interesting planets, including all those I consider in my sample in Chapter 3. The final assumption I use, $\eta = 0.01$, is adopted as a lower limit to the likely mass loss efficiency, and hence mass loss rates. This is motivated by observational constraints from contemporaneous measurements of the XUV irradiation and resulting mass loss detected through Ly $\alpha$ absorption in individual systems (e.g. Ehrenreich and Désert, 2011; Ehrenreich et al., 2015).

The energy-limited assumption has limitations. Examples include the uncertainty in $\eta$ (as discussed above) and $\beta$, as well as a lack of a direct way of determining whether the escape is indeed hydrodynamic from Equation 1.9, or rather in the Jeans regime (Owen, 2018). On that latter point, however, one could calculate the Jeans parameter (Equation 1.5). The energy-limited method has also been suggested to over-, and occasionally under-, estimate mass loss rates, particularly for low mass

planets (Kubyshkina et al., 2018a, and references therein). Despite the limitations though, the advantage of the method is in its relative simplicity, particularly following observations of the host star's X-ray emission.

### Simulations

There have been several attempts to model hydrodynamically-driven mass loss of various planets through numerical simulations (e.g. Yelle, 2004; Tian et al., 2005; Murray-Clay et al., 2009; Owen and Jackson, 2012; Kurokawa and Kaltenegger, 2013; Bourrier et al., 2016; Owen and Alvarez, 2016; Salz et al., 2016b; Kubyshkina et al., 2018a). These consider more detail of the physical processes at play. Thus, simulations like these can provide complementary insight to approximations like the energy-limited method, and can potentially provide a more thorough and accurate picture of the mass loss processes in general or in specific system(s), if well motivated.

As part of the results of some of these studies, other regimes of mass loss have been identified, in addition to energy-limited. Murray-Clay et al. (2009) concluded that the energy-limited formation, where most of the energy goes into $PdV$ work, was only valid for relatively low EUV fluxes ($F_{\rm EUV} \lesssim 10^4$ erg s$^{-1}$ cm$^{-2}$). At higher fluxes, the flow is "recombination-limited", where there is an equilibrium between photoionisation and recombination, and more of the input energy is lost to radiative cooling processes. The transition between the two is set by the recombination and flow timescales (Owen and Alvarez, 2016). Owen and Alvarez (2016) additionally identified a third regime, which they term "photon-limited", wherein the mass loss rate is set by the flux of XUV photons. This occurs when the recombination timescale is long, but the potential of the planet is relatively shallow; thus, it is applicable for low mass/density planets. The physical interpretation of this regime is that each incident photon drives the escape of only a single atom.

As I mentioned above, in Chapter 3 I make use of the values of $\eta$ and $\beta$ from Salz et al. (2016a) for my sample. The study investigates where energy-limited, and indeed hydrodynamic, escape breaks down due to the atmospheres being too tightly bound, finding a transition region where the heating efficiency declines rapidly. The simulations they perform couple photoionisation using the CLOUDY code, with the hydrodynamics code *PLUTO*, which they describe in Salz et al. (2015b). In Salz et al. (2016b), where they apply the code to 18 close-in planets, some of the mass loss rates they calculate seem a little high compared to observational studies, especially for GJ 436b and HD 97658b. In Section 3.6.3, I too find mass loss rates that seem high, compared to observations, when I use their efficiencies.

The simulations by Kubyshkina et al. (2018a), using a hydrodynamic code

based on that described in Johnstone et al. (2015), produce a grid of models for low-mass ($< 40\,M_{\oplus}$), hydrogen-dominated atmospheres. Their resulting mass loss estimates give reasonable agreement to the few observationally constrained results that they compare to. As part of their study, they also produced a tool that can be used to interpolate within the confines of their grid of models, thus allowing the application of their results to low-mass planets in general. I apply this interpolator tool in Chapters 3, 4 and 5 to yield mass loss estimates alongside those calculated via Equation 1.9 for the energy-limited method. Furthermore, in a follow up paper (Kubyshkina et al., 2018b), they provided an analytic approximation to their simulations, which also gives reasonable results for higher mass planets too. There are, however, some limitations of their work that one should bear in mind when I apply the interpolator tool in following chapters. Firstly, they assume a single X-ray and single EUV wavelength for all of the incident flux in each energy range, when in reality XUV spectra and opacity can be extremely wavelength dependent. The interpolator tool additionally interpolates XUV flux across four and a half orders of magnitude with only three points. Finally, like many other studies, including my own, they also assume a single, constant value for the efficiency, $\eta$, taking the canonical 0.15.

### 1.2.4 Effects of mass loss on the exoplanet population

Knowing that close-in exoplanets are subject to significant evaporation, an obvious question to ask is can the mass loss over a planet's lifetime deplete its atmosphere sufficiently to significantly change it? Despite some earlier suggestions to the contrary (Lammer et al., 2003; Baraffe et al., 2005; Penz et al., 2008a), it is thought that hot Jupiters will only lose at most a few percent of their total mass over their lifetime, and so are stable to substantial evaporation (Yelle, 2004; Lammer et al., 2009; Murray-Clay et al., 2009; Owen and Jackson, 2012). Given that a large fraction of these planets are made up of a H/He envelope, losing this much mass is unlikely to change the planet's appearance too much. This inference is corroborated by other investigations into whether hot Jupiters are evolutionarily linked to other, smaller, close-in planets using, for example, metallicity arguments (Winn et al., 2017).

In contrast, smaller planets have been found to be susceptible to extreme atmospheric evolution; in some cases, complete stripping down to the planetary core is possible (see the photoevaporation valley section, below). Evidence for this has been uncovered by looking at the exoplanet population as a whole and identifying regions of the parameter space with a dearth of planets. I outline two such regions below, both thought to possibly result from photoevaporation processes. Both are

of relevance to some of the planets I explore in Chapters 4 and 5.

### Neptunian desert

It has been suggested that Neptune-sized planets may be susceptible to losing a significant portion of their mass through escape processes (e.g. Baraffe et al., 2006; Owen and Jackson, 2012; Wu and Lithwick, 2013). Indeed, a dearth of intermediate-sized planets at short orbital periods, dubbed the "Neptunian desert", has emerged (Szabó and Kiss, 2011; Beaugé and Nesvorný, 2013; Helled et al., 2016; Lundkvist et al., 2016; Mazeh et al., 2016; Owen and Lai, 2018). The effect is observed in both the mass-period and radius-period planes, and has been attributed to photoevaporation (Kurokawa and Nakamoto, 2014). Mazeh et al. (2016) showed the region to be roughly triangular-shaped, and derived empirical relations for the boundaries. I show the region in both planes of interest in Fig. 1.7.

Recently, Owen and Lai (2018) used numerical, hydrodynamic mass loss models, coupled with the stellar evolution code MESA (Paxton et al., 2011, 2013, 2015), to show that photoevaporation can explain the lower boundary. However, both this study and Ionov et al. (2018) suggest the upper boundary may extend too high up in both planes of interest for photoevaporation processes to be the sole origin of the desert. In contrast, the models of Kurokawa and Nakamoto (2014) can explain the upper boundary with photoevaporation. They adopt their $\eta$ value from Kurokawa and Kaltenegger (2013) of 25%, which, while high, is similar to the planet-specific values of $\eta$ for some (but not all) of the low mass planets modelled by Salz et al. (2016a). However, I find in Section 3.6.3 that the mass loss rates calculated with the Salz et al. (2016a) efficiencies also seem a little high compared to observational constraints. Owen and Lai (2018) suggest the upper boundary's origin may instead be related to the tidal disruption barrier for planets migrating inwards by high-eccentricity excitation; only planets above a certain mass and radius are able to circularise at a given orbital period. This process had previously been discussed in the context of the Neptunian desert by Matsakos and Königl (2016). The lower boundary determined by Owen and Lai (2018) for these tidal processes is similar to that predicted for photoevaporation. However, the region of parameter space in which high eccentricity migration followed by tidal circularisation can occur for these smaller, lower-mass planets is relatively small.

It is likely that both mechanisms each play a role in carving out the desert, but their relative contributions could be tested by finding a sizeable sample of very young planets. XUV photoevaporation is thought to be strongest in the first 100 Myr or so (see Section 1.3.5), whereas the tidal origin could occur on a timescale of up

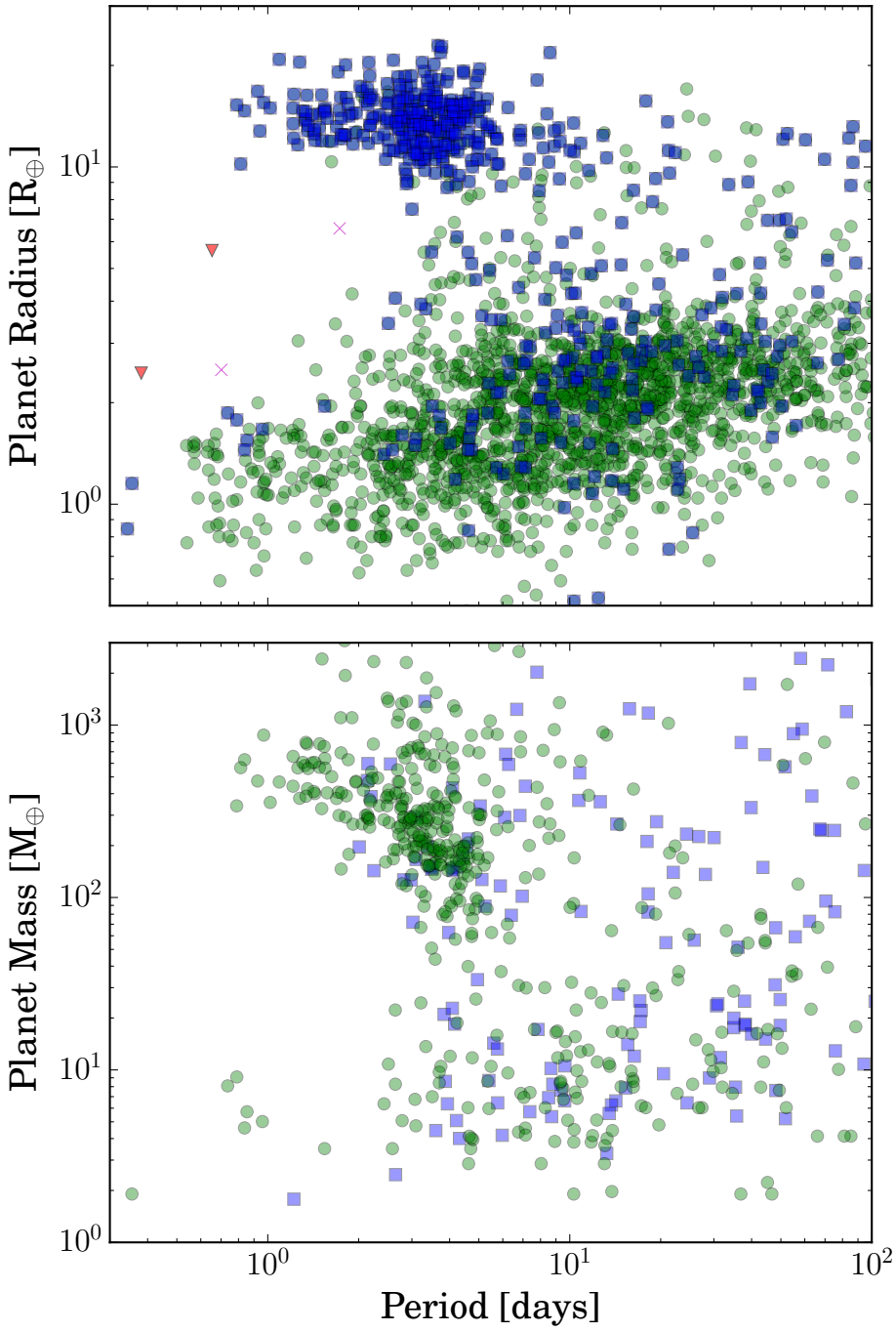


Figure 1.7: Fig. 1 of Owen and Lai (2018), showing the Neptunian desert. Shown in the radius-period plot (top), are planets with mass measurements (squares), other confirmed planets (circles), possible eclipsing binaries (crosses), and disintegrating rocky planets where the plotted radius is the dusty cometary tail size (triangles). Shown in the mass-period plot (bottom) are planets with mass measurements (circles), and $M_{\rm p} \sin i$ measurements (squares).

to perhaps a Gyr.

Finally, a recent paper by Szabó and Kálmán (2019) noted possible dependencies of the exact location of the desert on various stellar parameters ($T_{\rm eff}$, metallicity etc.), but their sample is taken from the NASA Exoplanet Archive, and as such many systematics may exist between the different surveys providing results to the database. A study with a sample whose parameters were more homogeneously determined is required to confirm their results.

### The photoevaporation valley

A study by Fulton et al. (2017) as part of the California Kepler Survey (CKS) uncovered evidence for a deficit in the number of planets with radii between 1.5 and 2.0 $\rm R_{\oplus}$. The discovery of the feature, which I display in Fig. 1.8, was made possible by the homogeneous determination of precise stellar parameters for the host stars of over 2000 planets from the original *Kepler* mission. Plotting the effect in radius-period space is a potentially powerful tool for probing composition, as I discuss below. A follow up study by Fulton and Petigura (2018), factoring in the *Gaia* DR2 results, reveals a possible dependence of the radius gap on stellar mass, with both peaks shifting to lower radii for lower mass stars.

Owen and Wu (2017) interpreted the gap to be an observational manifestation of the photoevaporation of planets with small planetary envelopes down to bare cores, while Lehmer and Catling (2017) also concluded that the feature is plausibly the result of XUV-driven escape. This "photoevaporation valley" had been previously predicted (Owen and Wu, 2013; Lopez and Fortney, 2013; Jin et al., 2014; Chen and Rogers, 2016). I display the simulated result of Owen and Wu (2017) in radius-period space in Fig. 1.9. The population of planets just above the valley remain stable to further evaporation, and have H/He envelopes that are just a few percent by mass. Also plotted on Fig 1.9 is a prediction of the biggest planet that can be a stripped core, though its exact position is sensitive to the heating efficiency.

Analysis of a smaller sample of planets by Van Eylen et al. (2018), using asteroseismology for the derivation of the stellar properties, showed evidence of both a negative slope in radius-period space and a clean break with few or no planets existing in the gap. The latter of these is suggestive of a homogeneous core composition across their sample. The exact position of the gap in radius and the gradient of the slope in radius-period space is indicative of the composition of the planets (Owen and Wu, 2017; Jin and Mordasini, 2018). A recent study by Martinez et al. (2019) performs a reanalysis of the CKS data, and reveals further evidence of a slope; their slope agrees with that from Van Eylen et al. (2018).

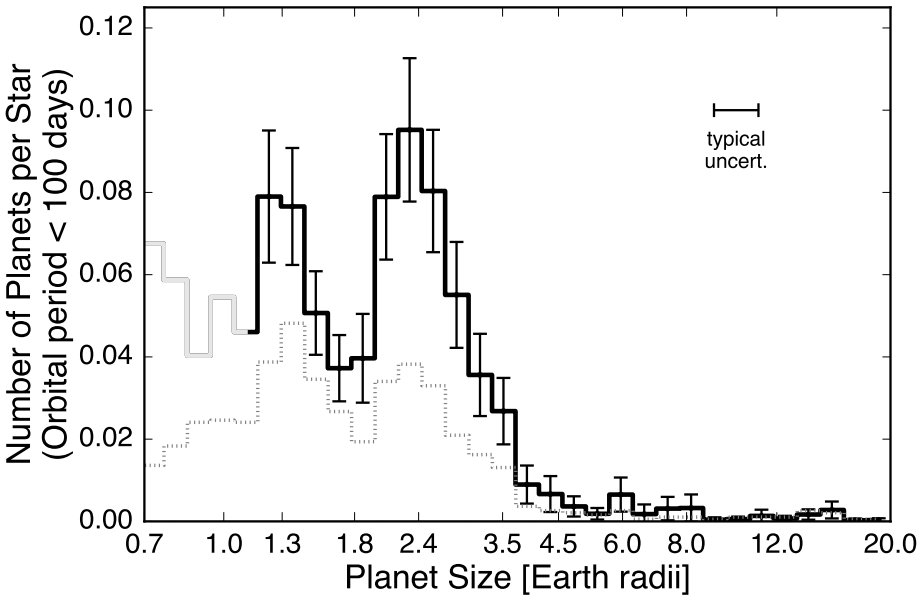


Figure 1.8: Top panel of fig. 7 of Fulton et al. (2017), showing the radius gap in the *Kepler* planets. The light grey region below 1.14 $R_\oplus$ suffers from low completeness. The histogram plotted in the dotted grey line is the same distribution of planet radii uncorrected for completeness

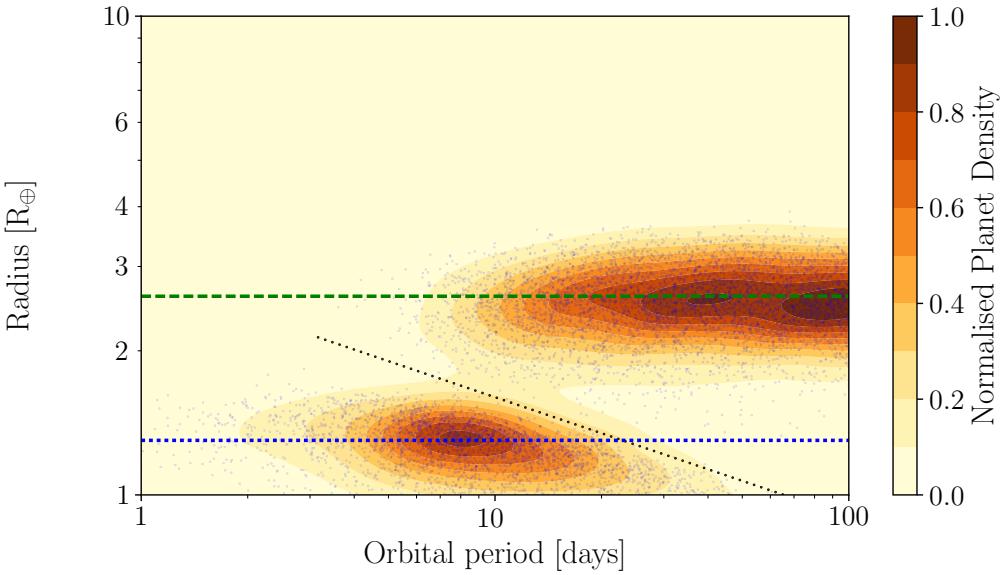


Figure 1.9: Left panel of fig. 5 of Owen and Wu (2017), giving their final simulated sample in radius-period space. The green dashed and blue dotted horizontal lines give the positions of the two peaks in radii (2.6 and 1.3 $R_\oplus$). The dotted black line is their analytic result for the size of the most massive planet that can be stripped bare as a function of period, marking the lower boundary of the valley.

Additionally, the study finds that the gap's position and slope are consistent with a photoevaporation origin, as well as a population whose core compositions are Earth-like. The conclusion favouring rocky cores over icy ones was also reached by Owen and Wu (2017) and Jin and Mordasini (2018).

As for the Neptunian desert, above, if photoevaporation is indeed the origin of the valley, then it is at early times (the first few 100 Myr; see Section 1.3.5) that the valley is carved out (e.g. Lehmer and Catling, 2017; Owen and Wu, 2017). This makes the discovery of more young planets particularly desirable, in order to probe the theory further.

An alternative scenario for the origin of the gap has also been explored. Ginzburg et al. (2018), following on their work from Ginzburg et al. (2016), determine that the feature can also be explained by "core-powered" mass loss. This is the same mechanism that has also been described as "boil-off", which I explained in Section 1.2.2. Gupta and Schlichting (2018) also come to the same conclusion that core-powered mass loss can create the radius-period valley, though they do state that their work does not necessarily rule out photoevaporative processes being relevant as well, and that more work is required to determine which, if either, is the dominant process.

## 1.3 Stellar coronae

As described in Section 1.2, we know that the atmospheres of close-in planets are evaporating, and we believe the escape is being driven by XUV photons. But how do stars emit these high-energy photons that impinge on the planetary atmospheres, and that we observe? Further, how does this emission change and vary through a star's life? I aim to outline the answers to these questions in this section, by discussing the coronae of stars.

What we think of as the "surface" of the Sun is the top of the photosphere. Above this lies its atmosphere, composed of two main regions: the chromosphere and the corona. The chromosphere lies immediately above the surface, stretching out for about a 1000 km or so. The temperature increases steadily across this region, such that its upper edge it is almost 10,000 K. Emission lines dominate the observed spectrum, with some used as activity indicators, given the region's strong links with magnetic activity, similar to that I describe for the corona, below. An example of this is the Mount Wilson S-index (Vaughan et al., 1978), which is based on observations of the Ca H & K lines at the boundary between UV and visible light.

Above the chromosphere is a thin transition region where the temperature

rises very quickly, leading into the corona. The corona is an extended region of very hot ($> 10^6$ K) yet relatively tenuous plasma. Exactly why the corona is so much hotter than the photosphere remains an open question, though it appears to be strongly related with the magnetic field lines that stretch out into the region from the photosphere, with possible heating by magnetic reconnection. Optically, the corona of the Sun is visible during a total Solar eclipse, but the region is also a strong emitter of X-rays. In fact, the X-ray photons from all late-type stars are thought to originate in their coronae.

X-ray emission from the Solar corona has been known for almost 80 years (theoretically by Edlén 1943; observationally by Burnight, 1949). In Fig. 1.10 I display an image of the Sun in X-rays. The Sun appears rather uniform in brightness at optical wavelengths, a few starspots/faculae and limb darkening effects aside. However, in X-rays this is not the case, with the emission being dominated by active regions, many of which appear as coronal loops. Coronal active regions such as these are intimately linked to both the chromosphere, and to features like starspots in the photosphere through magnetic fields. Note also that the emission also appears particularly bright around the limb of the photospheric disc. This is a result of the emission being optically thin, and thus appearing brightest when looking along the greatest column density of coronal plasma. This is relevant in Chapter 6 when exploring the X-ray transit of HD 189733b, and results in a W-shaped transit profile being expected at those wavelengths (e.g. Llama and Shkolnik, 2015; Marin and Grosso, 2017). The minima of the two dips should occur as the planet passes across onto and off of the photospheric stellar disc, where one looks along the greatest column density of this coronal plasma.

### 1.3.1 X-ray generation

The X-ray emission of late-type main sequence stars (FGKM, as well as late A stars) likely results from the heating of the corona through the deposition of large amounts of magnetic energy (for a review of late-type coronae, see Güdel, 2004). The exact conversion of the magnetic energy into heat is as yet unsolved, and referred to as the "coronal heating problem" (see, for a review, e.g. Klimchuk, 2006). Once heated, the generation of X-ray photons in the corona is driven by a few processes. There biggest contribution is from line emission (bound-bound) of the many highly ionised species present (see Section 1.3.2 for more). In addition, there is also a contribution from continuum emission that is predominantly the result of thermal Bremsstrahlung (free-free), though recombination events (free-bound emission) can

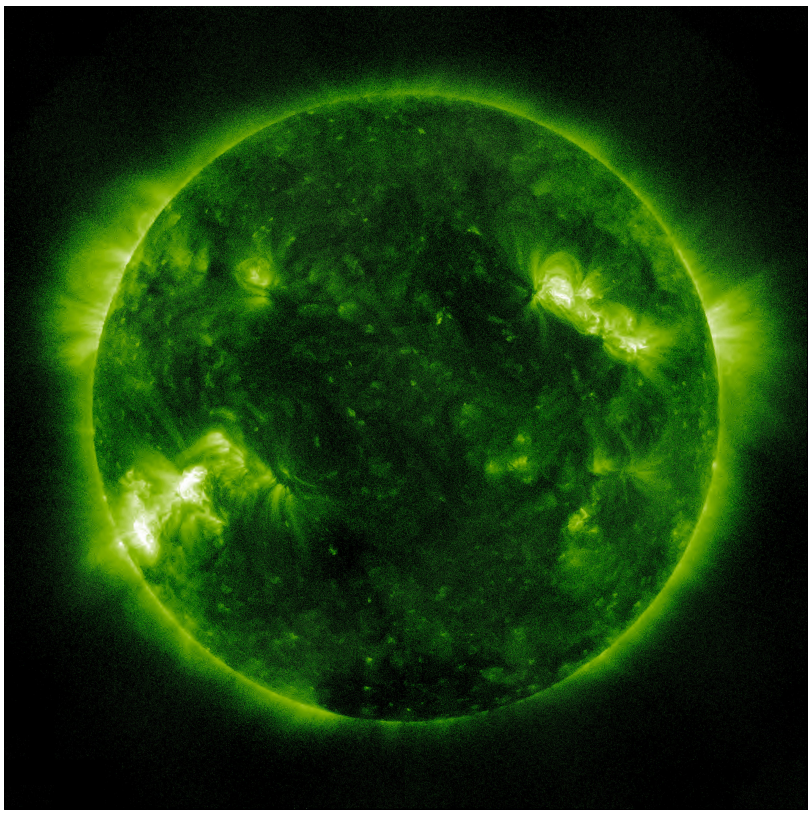

Figure 1.10: An image of the Sun in X-rays, taken in April 2011 using the 94 Å filter of the Solar Dynamics Observatory's Atmospheric Imaging Assembly. *Credit: NASA/Goddard Space Flight Center Scientific Visualization Studio*

also be important if the plasma temperature is low[2] ($kT \approx 0.1\,\mathrm{keV}$).

The source of this magnetic energy is theorised to be through the action of a dynamo within the convection zones of these stars, converting the kinetic energy associated with convection and rotation of the plasma into magnetic energy. The dynamo regenerates and sustains the magnetic field through a star's life, though, as we will see later (Section 1.3.5), the activity of a star does decrease through its time on the main sequence. Perhaps the best model to date is the $\alpha$–$\omega$ dynamo (see, for a review, e.g. Charbonneau, 2010; Cameron et al., 2017). The $\omega$ effect is the much better understood of the two mechanisms. In essence, differential rotation acts to wind up the magnetic field, converting an initially poloidal field into a toroidal one with many kinks. These kinks often become the sites of various activity-related phenomena such as sunspots, flares etc. Knowledge of differential rotation at the Solar surface has existed for almost four centuries - Christoph Scheiner noted as

[2]See description at: http://www.atomdb.org/Physics/rrc.php

early as 1630 that equatorial sunspots move faster than those closer to the poles. Helioseismic results showed that this differential rotation pervades only about 30% into the Sun. This is the location of the base of the convective zone at its interface with the radiative zone (e.g. Duvall et al., 1986; Dziembowski et al., 1989), often referred to as the tachocline (Spiegel and Zahn, 1992). Below this point, the Sun is thought to rotate as if a solid body (e.g. Brown and Morrow, 1987; Dziembowski et al., 1989). The magnetic field may well be anchored at, or close to, this point. The mechanism that returns the field to a poloidal state is more controversial than the $\omega$ effect. The $\alpha$ effect, first described by Parker (1955), explains the return to a poloidal field as related to the effect of the Coriolis force on rising plasma in the convection zone. This acts to twist both the plasma and the magnetic field lines pervading through the region, while the overall mechanism requires the accumulation of the effect across many convection cells.

Given the link of the mechanism of the dynamo with the base of the convection zone, one may wonder whether fully convective dwarf stars with $M_* \lesssim 0.35$–$0.4$ (type later than M3–M4, e.g. Limber, 1958; Dorman et al., 1989; Chabrier and Baraffe, 1997; Jao et al., 2018) show coronal emission that is also Solar-like. In these stars, the convection zone extends throughout the star, and so there is no tachocline within them as there is no radiative zone to interface with. However, observations of such stars (and even down towards the brown dwarf regime) have revealed strong activity signatures across the electromagnetic spectrum that are possibly magnetic in origin (e.g. Delfosse et al., 1998; Rutledge et al., 2000; Berger et al., 2001; Mohanty and Basri, 2003; Jackson and Jeffries, 2010). Furthermore, they have been shown to follow the same activity-rotation relationships (see Section 1.3.5) exhibited by partially convective stars in both the saturated (Wright et al., 2011; Stelzer et al., 2016) and unsaturated (Wright and Drake, 2016; Wright et al., 2018) X-ray regimes (defined in Section 1.3.5), as well the corresponding relationships for chromospheric activity (Mohanty and Basri, 2003; Newton et al., 2017; Astudillo-Defru et al., 2017). This implies that either the tachocline is not as important as thought in the dynamo of partially convective stars, or that alternative dynamo processes (for instance, the turbulent $\alpha^2$-dynamo - see e.g. Durney et al. 1993) in fully convective stars happen to produce similar short and long-term signatures to the Solar-like dynamo.

At the higher mass end, main sequence stars of type mid-A and earlier cease to have a convection zone at a temperature of around 8250 K, due to them being fully radiative. A few hundred ROSAT sources are positionally coincident with bright A-type stars (Schröder and Schmitt, 2007), however there are only a handful of unambiguous detections of X-rays from main sequence (all mid-to-late) A stars.

Many of the A stars associated with ROSAT sources are binaries where the X-rays are being produced by late-type companions, and as-yet-undiscovered late-type companions could be responsible for many or all of the rest (Schröder and Schmitt, 2007). Measurements of up to this temperature limit (e.g. Günther et al., 2012; Robrade and Schmitt, 2009) and stringent upper limits on hotter stars (e.g. Schmitt, 1997; Pease et al., 2006) show a decrease in $L_{\rm X}/L_{\rm bol}$ up to the fully radiative boundary, followed by a sharp drop below the sensitivity of observations to date. This agrees with both models of stellar structure (e.g. Ulmschneider et al., 1996; Kupka and Montgomery, 2002) and FUV observations by *FUSE*, which suggest chromospheric activity turns off at $T_{\rm eff} \approx 8300\,{\rm K}$ (Simon et al., 2002; Neff and Simon, 2008).

The lack of X-rays persists only as far as late-B stars. O and early-B stars do emit X-rays, albeit through a different mechanism. The emission is thought to emanate from within unstable regions of their radiatively-driven winds, allowing shocks to form (e.g. Lucy and White, 1980). The resulting emission is mostly thermal in nature (Güdel and Nazé, 2009), soft, and typically adheres to $L_{\rm X}/L_{\rm bol}\sim 10^{-7}$ (Pallavicini et al., 1981; Berghoefer et al., 1997). These stellar types are not relevant to my work, so I do not discuss them further.

### 1.3.2 Coronal X-ray spectra

X-ray spectra can be a powerful probe of the composition of coronae, particularly at high resolution, as is shown in Fig. 1.11, which displays high-resolution spectra taken with the Reflection Grating Spectrometers (RGS) onboard *XMM-Newton* for a sample of Solar-like stars (taken from Telleschi et al., 2005). The coronae of late-type stars tend to be at characteristic temperatures of a few million degrees. The result of such temperatures is that the bulk of quiescent stellar X-ray photons for these stars have energies below about 2 keV.

Early surveys with *Einstein* revealed a correlation between the average temperature, $\bar{T}$, and the observed X-ray luminosity, $L_{\rm X}$ (e.g. Vaiana, 1983; Schrijver et al., 1984; Schmitt et al., 1990). More recent studies with the current generation of X-ray telescopes have found the relationship to be described by (Telleschi et al., 2005)

$$L_{\rm X} \propto \bar{T}^{4.05\pm0.25}, \tag{1.10}$$

or, in terms of the surface X-ray flux, $F_{\rm X}$ (Johnstone and Güdel, 2015)

$$\bar{T} \propto F_{\rm X}^{0.26}. \tag{1.11}$$

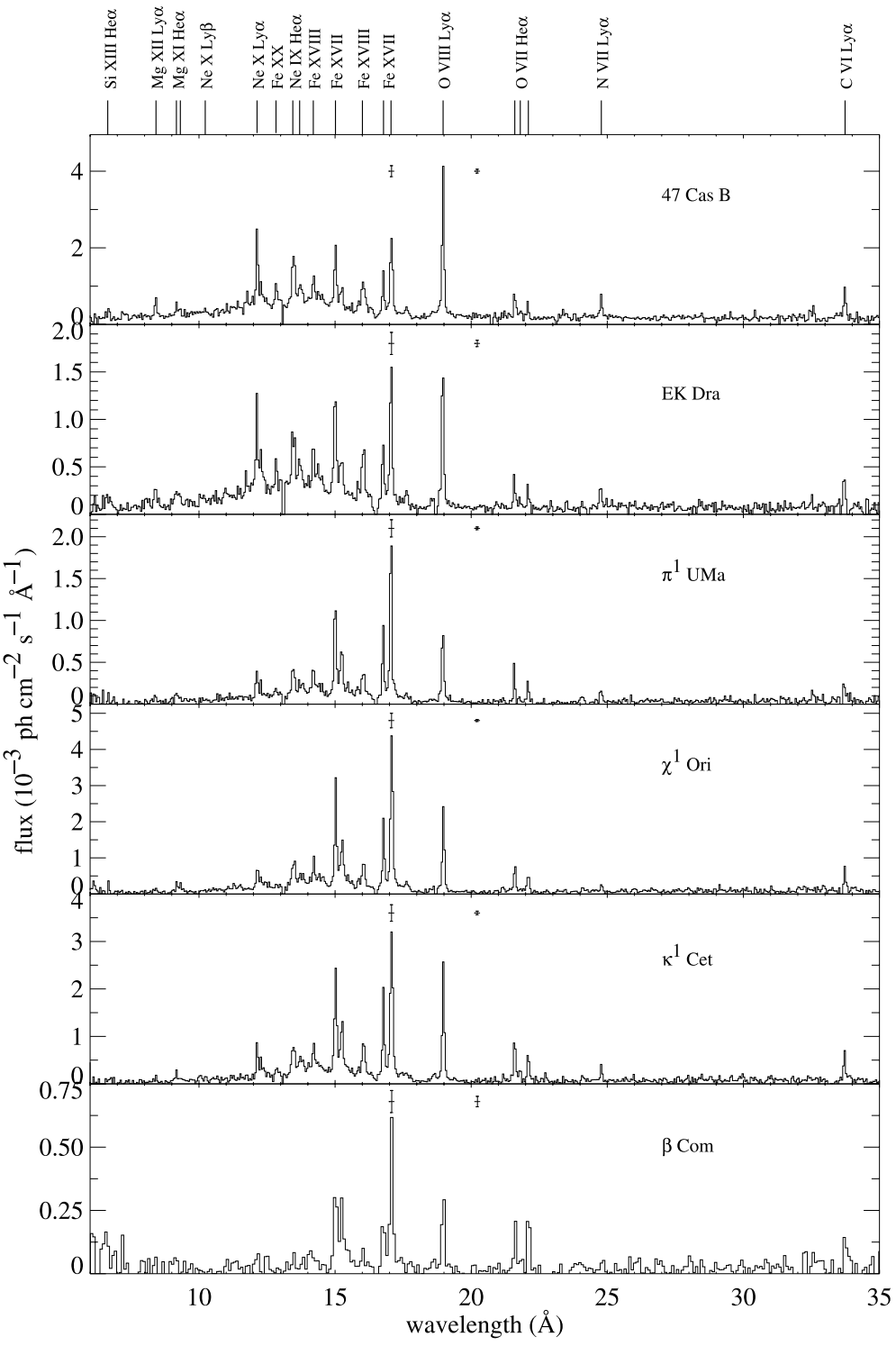


Figure 1.11: Fig. 1 of Telleschi et al. (2005), plotting high-resolution spectra taken with *XMM-Newton* RGS for a sample of Solar-like stars, co-added across both spectrographs. Wavelengths of various species are indicated across the top of the plot.

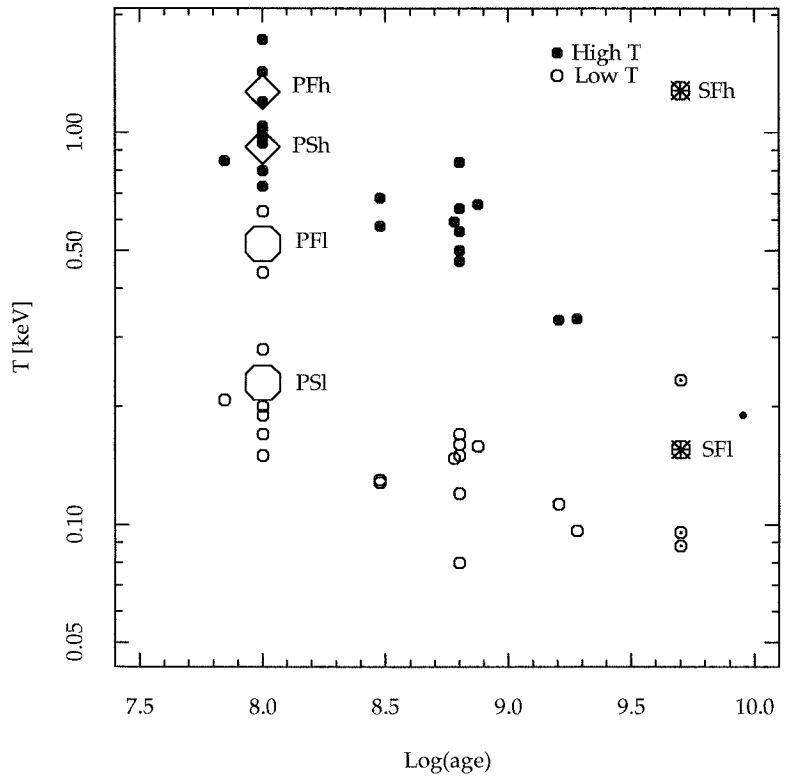


Figure 1.12: Fig. 25 of Favata and Micela (2003), showing the high (solid circles) and low (open circles) temperature components from a two temperature fit to stars of various ages.

As I will discuss in Section 1.3.5, younger stars typically exhibit higher $L_{\rm X}$. In the context of the empirical relations with $\bar{T}$, this implies that such stars have a higher coronal temperature, something that manifests itself in harder X-ray spectra than observed for older field stars. As an example, Fig. 1.12, reproduced from Favata and Micela (2003), plots the high and low temperature components for two-temperature fits to spectra for stars in the Hyades and Praesepe as well as the field. Both components are hotter for the younger stars.

As a further example, one can compare the X-ray spectra from my observations in Chapters 3 and 5. In the spectra for the 800 Myr Praesepe stars (Fig. 5.3), in particular K2-100, the bump in the emission around and just below 1 keV dominates the spectra. Contrast that with those for the field stars (Fig. 3.3), in particular GJ 436, HAT-P-11, and HD 97658 where the emission is very soft indeed. Though the increase just below 1 keV is present to varying degrees, the feature is not nearly as pronounced.

This rise in emission just below 1 keV is typically the most obvious contri-

bution of line emission to the spectra of late-type stars, and is chiefly produced by L-shell emission, photons generated by bound-bound transitions to the n=2 energy level, of highly ionised Fe. There are also contributions from highly ionised O and Ne K-shell emission – transitions to the n=1 energy level. This is another thing that is highlighted by Fig. 1.11.

### The FIP effect

The first ionisation potential (FIP) effect is related to the abundances of particular species in the corona of a star, compared to their abundance in the photosphere. Pottasch (1963) identified that Mg, Si, and Fe all had higher abundances in the Solar corona than in the photosphere. These elements all have low FIP values ($< 10\,\mathrm{eV}$). Conversely, high FIP elements such as C, N, O, and Ne are observed to exhibit very little enhancement in abundance in the corona, and in some cases are actually less abundant than in the photosphere (e.g. Laming, 2015, and references therein).

For other stars, examination of the FIP effect has only been possible in the last couple of decades with missions such as *EUVE*, *XMM-Newton*, and *Chandra*, with the advent of sensitive grating X-ray spectrographs. An increasing number of stars have now had their coronal abundances measured at high enough precision to assess the FIP effect for them. As a means of being quantitative, the FIP effect is often assessed using the FIP bias, $F_{\mathrm{bias}}$. This is given by

$$F_{\mathrm{bias}} = \log_{10}\left(\frac{\mathrm{X}}{\mathrm{Fe}}\right)_{\mathrm{cor}} - \log_{10}\left(\frac{\mathrm{X}}{\mathrm{Fe}}\right)_{\mathrm{phot}}, \tag{1.12}$$

where X is the abundance of the high FIP species being tested. The two terms correspond to the ratios of the species compared to Fe in the corona and photosphere, respectively. A final $F_{\mathrm{bias}}$ value is often obtained by averaging across multiple high FIP species, as I do in Section 7.4.3 for HD 189733A. Note that I use the Solar photospheric abundances from Asplund et al. (2009) throughout this work.

Collating literature values together, table 2 of Wood et al. (2012) demonstrates that G and early K stars typically have negative values of $F_{\mathrm{bias}}$, indicative of a FIP effect present. As stellar spectral type gets later, the strength of the FIP effect decreases. However, for both M dwarfs and young, active K stars, $F_{\mathrm{bias}}$ is positive, implying that the high FIP elements are more enhanced than the low FIP ones. This is usually referred to as an inverse FIP effect, or sometimes IFIP. An additional means of assessing the FIP effect is to consider the ratio of the coronal abundances of Ne and Fe. Table 2 of Wood et al. (2012) demonstrates a good correlation between this and $F_{\mathrm{bias}}$.

### 1.3.3 Stellar X-ray flares

The first detection of a Solar flare remains one of the most powerful known to date, as witnessed in visible light by Carrington (1859) and Hodgson (1859), and since dubbed the "Carrington Event". Since then, many flares have been observed across the electromagnetic spectrum for many other stars, as well as the Sun. The first flares detected from another star in X-rays were for YZ CMi and UV Ceti, as observed by the *Astronomical Netherlands Satellite* (Heise et al., 1975).

The mechanism (see e.g. reviews by Benz, 2008; Güdel and Nazé, 2009; Benz and Güdel, 2010) by which flares occur is the release of a huge amount of magnetic energy built up over time by the magnetic dynamo. The release occurs due to reconnection of the magnetic field, thereby returning to a less energetic state. The excess energy accelerates accelerates electrons nonthermally along the magnetic field down towards the photosphere. However, the electrons typically interact with plasma in the chromosphere, collisionally transferring the bulk of their energy into heating the surrounding plasma. These processes fill and expand existing coronal loops, from which large amounts of the energy are finally released into space via radiative cooling processes. Given the close link of these processes with the magnetic dynamo, it follows that more active stars (i.e. young, fast rotating stars - see Section 1.3.5) tend to exhibit more flares.

The energy release can be very large indeed. The Carrington Event is estimated to have released $10^{32}$ erg of energy (Tsurutani et al., 2003), a few percent of the total bolometric emission of the Sun each second. But this is far from the largest flares witnessed. Flares identified from stars as part of the *Kepler* mission have been seen to have energies up to $10^{37}$ erg (Wu et al., 2015), or possibly even $10^{38}$ erg (Van Doorsselaere et al., 2017). In X-rays, flares are regularly observed to outshine the rest of the coronal emission (see, for example Fig. 7.11), while the most extreme events can achieve X-ray luminosities of $10^{32}\,\mathrm{erg\,s^{-1}}$ (Testa, 2010; Pye et al., 2015). In addition to examining the energy properties of individual flares, the large scale survey of flares using the 2XMM serendipitous source catalogue by Pye et al. (2015) determine X-ray flare rates, both in terms of their overall frequency and as a function of energy.

Though there remains a nonthermal component to the final flare emission (through nonthermal Bremsstrahlung and gyrosynchrotron processes), an example Solar flare spectrum in fig. 2 of Benz and Güdel (2010) (adapted from Grigis and Benz, 2004) highlights that this only contributes a substantial fraction of the emission at much higher energies than I consider in this work. The overwhelming contribution to the soft X-rays remains thermal emission. The vast majority of Solar

flares show a hardening of the emission in the hard X-rays (Parks and Winckler, 1969; Kane and Anderson, 1970, see also e.g. Benz, 2008). In the softer X-rays I consider in this work, a hardening of the spectrum is also often visible (e.g. Reale et al., 2001; Telleschi et al., 2005; Pillitteri et al., 2014; Pye et al., 2015, see also the 2011 *Swift* flare for HD 189733 in Section 7.3.2). This is useful to me in Chapter 7 where I search the *Swift* data of HD 189733 for additional flares.

### 1.3.4 X-ray activity cycles

The Sun is well known to exhibit an 11 year activity cycle. This was first discovered back in the middle of the 19th Century by Schwabe (1844), using the still often used method of counting the number of sunspots visible on the Solar disc. Fig. 1.13 plots the variation of the sunspot number across the last six Solar cycles. At Solar minimum almost no spots are visible, whereas tens are present at Solar maximum.

The Solar cycle can be well understood as the time it takes for one full period of the $\alpha$–$\omega$ effect - i.e. the magnetic field goes from poloidal to toroidal and back to poloidal again. Solar maximum coincides with maximal magnetic activity within a cycle, occuring when the field lines have been tightly wound by the $\omega$ effect. This creates an abundance of kinks in the magnetic field such that many active regions pervade from the surface into the corona. Strictly speaking, the complete cycle actually is 22 years. Sunspots always come in pairs of opposite polarity where the magnetic field lines emerge above the photosphere, and descend back down into it. According to Hale's polarity law, the polarity of the leading spots on the two hemispheres is opposite, and they alternate each cycle (Hale et al., 1919; Hale and Nicholson, 1925).

The cycle is present in activity indicators and fluxes across the electromagnetic spectrum, including X-ray flux. In Fig. 1.14, I plot the daily X-ray flux averages in the 0.2–2.4 keV energy band for the Sun, observed between 2002 and 2014. This makes use of the same *TIMED/SEE* data I use in Chapter 3 to investigate extrapolation to EUV. A more detailed discussion of the *TIMED/SEE* data is presented there. Judge et al. (2003) determined that the difference between Solar minimum and maximum if measured in the *ROSAT* band (0.1–2.4 keV) would be about a factor of six. Though for a slightly different band, Fig. 1.14 corroborates this inference.

All this begs the question: what about other stars? Do they exhibit Solar-like activity cycles? Detection requires high quality, preferably homogenous observations spread out across a long baseline, and any big gaps in the data can make the inference of cycles tough. Chromospheric observations can be made from the ground, so

[4] `http://sidc.be/silso`

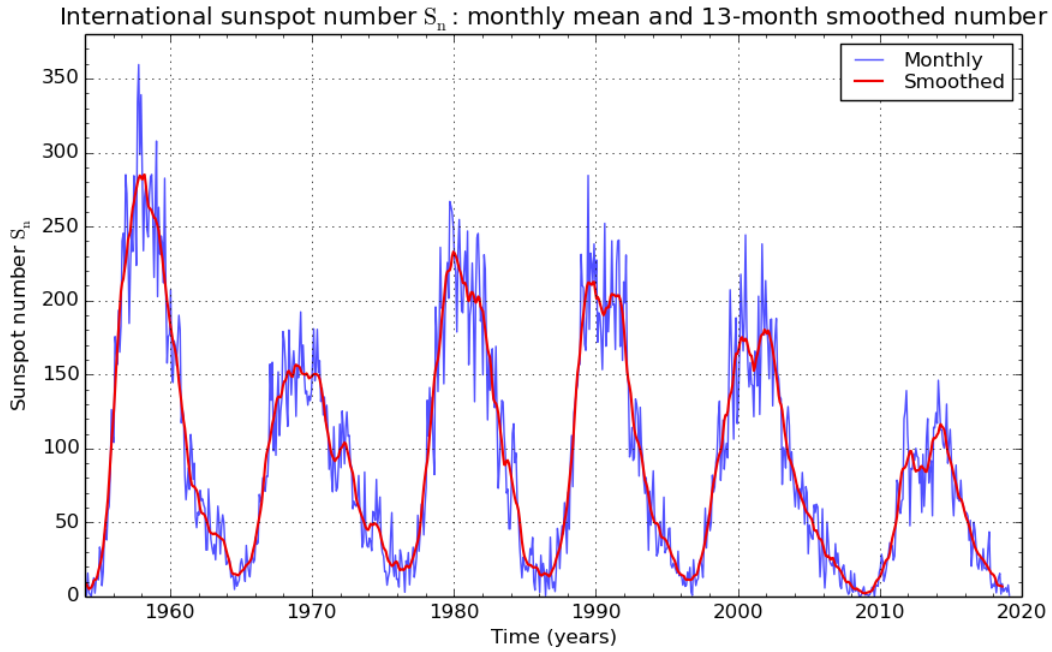


Figure 1.13: Sunspot number over the last six 11-year Solar cycles, displayed as monthly means (blue) and smoothed with a 13 month window (red). Additional variation on both short timescales and from cycle to cycle is also visible. *Credit: SILSO graphics*[4]*, Royal Observatory of Belgium*

.

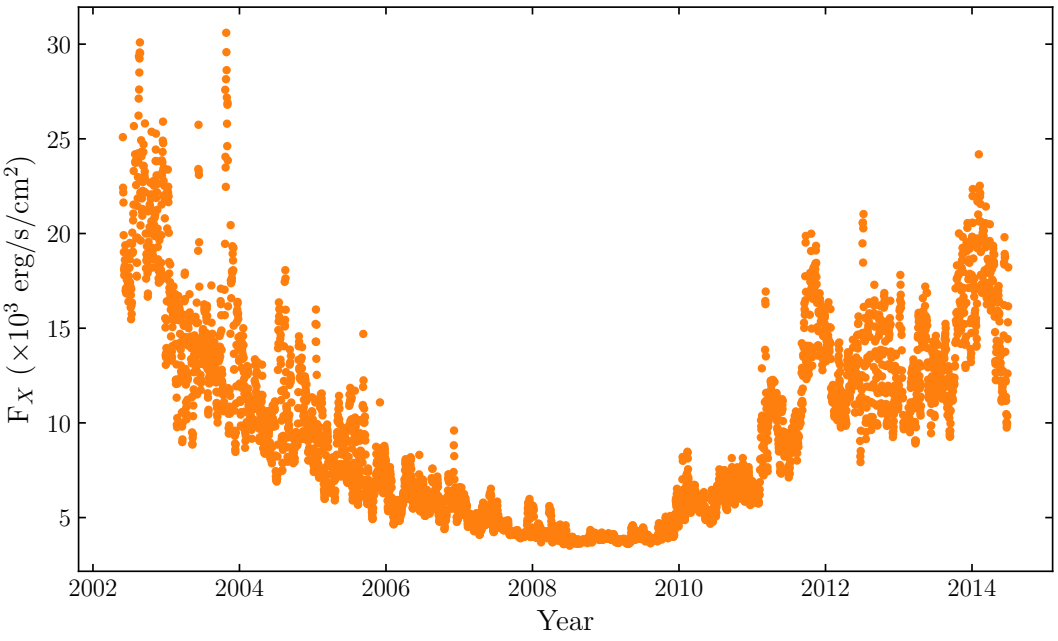


Figure 1.14: Daily X-ray flux averages for the Sun, as observed by the *TIMED/SEE* mission. Fluxes are for the 0.2–2.4 keV band.

long term observing campaigns are much easier to perform. Indeed, chromospheric activity cycles have been inferred for numerous stars from the Mount Wilson programme (Wilson, 1978; Baliunas et al., 1995). X-ray observations must be made from space (see Section 2.1). As such, long term, well-sampled programmes are very difficult, due to the relative scarcity of total observing time available to the community at these wavelengths. However, a small handful of stars now have coronal activity cycles claimed with varying robustness: 61 Cyg A (Hempelmann et al., 2006; Robrade et al., 2012), $\alpha$ Cen A/B (Ayres et al., 2008; Ayres, 2009; Robrade et al., 2012; Ayres, 2014), HD 81809 (presumed primary star A; Favata et al., 2008; Orlando et al., 2017; Egeland, 2018), $\iota$ Hor (Sanz-Forcada et al., 2013), Proxima Cen (Wargelin et al., 2017), $\tau$ Boo (Mittag et al., 2017), HR 1099 (Perdelwitz et al., 2018). These results show a range of periods: $\tau$ Boo's cycle may be as short as just four months, much shorter than the Solar cycle; conversely, HR 1099's X-ray data is best fit by a 21.2 yr cycle. In addition, Wargelin et al. (2017) find a correlation between the cycle amplitude and Rossby number (a proxy for activity level; see Section 1.3.5). In Chapter 7, I present long baseline observations of HD 189733A that show evidence of long term variation akin to an activity cycle.

### 1.3.5 X-ray relationships with age and rotation

The strength of the magnetic fields of a star, and thus its activity level, appear intimately linked to its rotation, as first observed by Skumanich (1972). The rotation period of stars is seen to increase through a star's lifetime, while the activity drops. In this section I explore the relationships observed for X-rays with age and rotation.

The magnetic braking of stars is a process first suggested by Schatzman (1962). In this process, ionised material is first captured by the magnetic field of the star. The captured material continues to corotate with the star until it is ejected into space as part of their wind. As this happens, the material retains its angular momentum, meaning it is lost to the star. Over time, this mechanism is thought to accumulate enough to explain the observed increase in rotation period, and resulting decrease in activity.

The decline in X-ray activity does not occur throughout the star's lifetime, however. During the first 100 Myr of a star's life on the main sequence, the (average) X-ray emission remains roughly constant even though the star is spinning down. This period is usually referred to as the "saturated" regime. Only after this epoch does the activity begin to decrease with the increasing rotation period. This latter regime, which operates for the remainder of the star's main sequence lifetime, is usually referred to as the "unsaturated" regime. Furthermore, a phenomenon

known as "supersaturation" has also been proposed, where in the very fastest rotators ($v_{\rm rot} \gtrsim 100\,{\rm km\,s^{-1}}$), the coronal activity is seen to decline a little below the saturation level (Randich et al., 1996).

The physical cause of saturation is currently unknown, though a few theories exist that attempt to explain it. The magnetic dynamo itself may saturate such that no further magnetic energy is produced past a certain point (e.g. Gilman, 1983). Alternatively, saturation may be driven by the speed of rotation. Theories along those lines include suppression of coronal loops by centrifugal forces (Jardine and Unruh, 1999) or saturation of the coronal filling factor (e.g. Vilhu, 1984).

I now describe some studies that have aimed to characterise these relationships in empirical formulae. I further compare results from my analyses to some of these relations on multiple occasions in the following chapters.

**Empirical relations: Rotation**

In the saturation regime, the X-ray luminosity, $L_{\rm X}$, of young stars is such that (Vilhu, 1984; Vilhu and Walter, 1987)

$$\frac{L_{\rm X}}{L_{\rm bol}} \approx 10^{-3}, \tag{1.13}$$

where $L_{\rm bol}$ is the bolometric luminosity.

In the unsaturated regime, various power law relationships have been proposed. Using results from *Einstein*, a seminal paper by Pallavicini et al. (1981) inferred the first empirical relationship between X-rays and rotation. They found a link between the X-ray luminosity $L_{\rm X}$ and the projected rotational velocity $v \sin i$ of the form

$$L_{\rm X} \propto (v \sin i)^2. \tag{1.14}$$

This further implies $L_{\rm X}$ is proportional to the inverse square of the rotation period, $P_{\rm rot}$. Several studies have since verified this relation (e.g. Maggio et al., 1987; Wood et al., 1994), while Pizzolato et al. (2003) derived a set of relations of the form

$$L_{\rm X}, \frac{L_{\rm X}}{L_{\rm bol}} \propto P_{\rm rot}^{-2}, \tag{1.15}$$

using data from *ROSAT*. Stars were split into bins based on their $B-V$ colour and mass, with separate proportionality constants and values of $P_{\rm sat}$ for each bin. Here, $P_{\rm sat}$ is the rotation period past which the emission ceases to be saturated. Further, Pizzolato et al. (2003) also confirmed a relationship with Rossby number, $R_{\rm o}$, for late-type stars with different convection properties. $R_{\rm o}$ is defined as the ratio of $P_{\rm rot}$

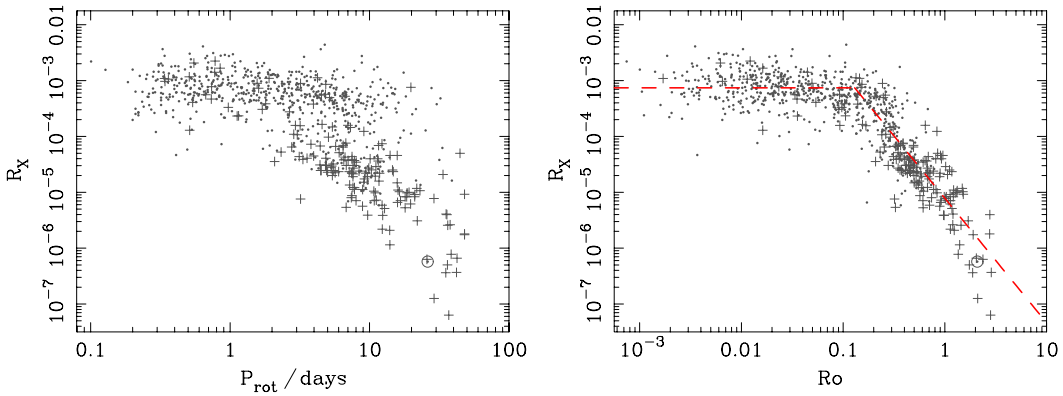


Figure 1.15: Fig. 2 of Wright et al. (2011), showing their sample plotted as a function of $P_{\rm rot}$ (left panel) and $R_{\rm o}$ (right panel). Their best fitting relation is plotted on the right panel. Their variable "$R_{\rm X}$" is $L_{\rm X}/L_{\rm bol}$.

and $\tau$, the convective turnover time (Noyes et al., 1984).

Wright et al. (2011) built on the work of Pizzolato et al. (2003) by formulating a set of relations, this time in $V-K$ bins, for this link between $L_{\rm X}/L_{\rm bol}$ and $R_{\rm o}$. Their sample in terms of both $P_{\rm rot}$ and $R_{\rm o}$ is plotted in Fig. 1.15. The relationship with $R_{\rm o}$ is noticeably tighter, although significant scatter still remains: up to an order of magnitude each way. This highlights the importance of making observations for individual objects of interest. Instead of the canonical value of $R_{\rm o}^{-2}$, the best fit power law obtained by Wright et al. (2011) is steeper: $R_{\rm o}^{-2.7}$, with the saturated threshold occurring for $R_{\rm o} = 0.13$. This steep slope implies a decrease in differential rotation as stars spin down (Testa et al., 2015), something that is incompatible with measurements from *Kepler*, which suggests differential rotation is only very weakly dependent on $P_{\rm rot}$ (Reinhold et al., 2013). Wright et al. (2011) additionally empirically estimated values for the convective turnover time for each $V-K$ bin. In two follow up papers (Wright and Drake, 2016; Wright et al., 2018), the authors extend their relations to fully convective M dwarf stars, which appear to follow the same relationship as partially convective stars. Stelzer et al. (2016) and González-Álvarez et al. (2019) additionally investigated the activity-rotation relations for M dwarfs, although the latter study did not consider the relationship with $R_{\rm o}$. I compare my results to the Wright et al. (2011) relations in Chapters 3, 4, and 5.

**Empirical relations: Age**

Although the slowing rotation is the driver behind the decrease in activity, there also exist relationships of X-ray emission with stellar age. Several studies have investigated this relationship (e.g. Micela et al., 1985; Güdel et al., 1997; Feigelson et al., 2004; Preibisch and Feigelson, 2005; Telleschi et al., 2005; Jackson et al., 2012; Booth et al., 2017).

The most up to date study with a large sample is Jackson et al. (2012), which uses data predominately from *ROSAT*, but also with *XMM-Newton* and *Chandra* contributions. They split their sample into seven $B-V$ bins, and for each bin derive a relationship of the form

$$\frac{L_{\rm X}}{L_{\rm bol}} = \begin{cases} \left(\frac{L_{\rm X}}{L_{\rm bol}}\right)_{\rm sat}, & \text{for } t < \tau_{\rm sat}. \\ Ct^{-x}, & \text{for } t > \tau_{\rm sat}. \end{cases} \tag{1.16}$$

where $t$ is the age of the star, $(L_{\rm X}/L_{\rm bol})_{\rm sat}$ is the value of $L_{\rm X}/L_{\rm bol}$ during saturation, $\tau_{\rm sat}$ is the length of the saturation epoch, $C$ and $x$ are variables that are found for each bin. $(L_{\rm X}/L_{\rm bol})_{\rm sat}$ and $\tau_{\rm sat}$ are also found for each bin separately. The bluest bins have a lower saturation level, at around $10^{-4}$ as opposed to $10^{-3}$, possibly because of the much greater $L_{\rm bol}$ for those stars. This is particularly relevant for K2-100, which I investigate in Chapter 5, as it falls into one of these bluest bins. Given the scale of this study, spanning a relatively wide range of colours, where an X-ray-age relationship is required in the following chapters, it is Jackson et al. (2012) that I default to.

Booth et al. (2017) more recently used a small sample of 14 stars older than 1 Gyr (with well-constrained age measurements) to infer a slope for the power law of -2.80. For comparison, the power law exponents in Jackson et al. (2012) are between -1.09 and -1.40, depending on which bin is considered, although all of the stars in their sample are younger than 1 Gyr. This points to a possible steepening of the relationship for stars older than 1 Gyr. The implication of that would be a steepening of the rotation-activity relationship, but in the following chapters I find $L_{\rm X}/L_{\rm bol}$ for some older stars that imply a slightly shallower slope than Wright et al. (2011), perhaps also implying a shallower activity-age relationship.

## 1.4 Star-planet interactions

In Chapter 7, I investigate possible signatures of star-planet interaction (SPI) between HD 189733b and its host. First suggested by Cuntz et al. (2000), SPI refers

to the enhancement of stellar activity due to the interaction of planets with their host stars predominately by means of tides or magnetic fields, and is presumed only detectable for hot Jupiters.

Through tides, it is thought that planets might be able to spin up their host star. The proposed mechanism for this is related to the fact that many host stars rotate slower than it takes their hot Jupiter planet to orbit them. This produces a lag of the tidal bulge raised by the planet on the star, akin to the lag of the slowly orbiting Moon behind the high tide on the faster-spinning Earth. The gravitational pull on this bulge by the planet would then transfer angular momentum to the star, allowing it to maintain a quicker rotation, and so a higher activity level, through its main sequence lifetime than would otherwise be possible. In the magnetic scenario, the magnetospheres of the star and planet interact with one another, causing reconnection events that induce a higher activity level in the region of the corona magnetically connected to the planet. This would manifest itself in as fluctuations in activity indicators that would appear to be phased with the planet's orbit. A paper by Rubenstein and Schaefer (2000) speculated this scenario could be the reason why superflares with substantially more energy than seen in any Solar flare are present on some Solar analogues.

In describing these mechanisms, Cuntz et al. (2000) pointed to the example of close stellar binary systems such as RV CVn variables, where there is plentiful observational evidence (e.g. Ayres and Linsky, 1980; White et al., 1990; Catalano et al., 1996) that the coronal/chromospheric emission of the stars can be enhanced by their interaction with each other.

For planets, various claims of SPI have been made in the past two decades. Several planets have had observations of Ca H & K lines, which probe chromospheric activity, that show hints of phasing with the orbital period of the planet and not the rotational period of the star (Shkolnik et al., 2003, 2005, 2008). Similar phasing has also been claimed at other wavelengths from optical to X-ray (Walker et al., 2008; Pagano et al., 2009; Pillitteri et al., 2011, 2014, 2015; Scandariato et al., 2013; Maggio et al., 2015). In terms of the spinning up of stars, Brown et al. (2011) investigated this possibility for WASP-18b and WASP-19b, two planets thought to be spiralling in towards their respective stars. For more stable systems, both HD 189733b and CoRoT-2b have been identified as possible candidates for spinning up their hosts (Pont, 2009). Both systems have wide binary companions, and Poppenhaeger and Wolk (2014) presented observations of both in X-rays that suggested the host stars to be more active than would be expected from the activity of the companion. I give a more detailed description of the claims of tidal and magnetic SPI for HD 189733b

and its host star in the introduction of Chapter 7, as well as a critical assessment of both based on new data from *Swift* and *XMM-Newton*.

## 1.5 Goals of my work

In Chapters 3 through 7, I present the results of various investigations into planet-hosting stars using X-ray observations, primarily taken with *XMM-Newton*, but also with some data from *ROSAT* and *Swift*. During the analyses I describe, I aimed to achieve a number of things:

- Investigate the high-energy environment experienced by close-in planets of different sizes around different stellar types. As I describe in the following chapters, the full range of planets in the systems I look at in this work is diverse in this sense.
- Investigate the high-energy environment of planets that lie close to the Neptunian desert or photoevaporation valley in radius-period or mass-period space. In Chapter 4, I analyse observations of planetary systems hosting planets either just above or below the photoevaporation valley. In Chapter 5, my small sample includes planets close to both features.
- Investigate young, transiting planets in X-rays. The vast majority of known transiting planets orbit old field stars. The Praesepe open cluster, which hosts the four planets I consider in Chapter 5, is about 800 Myr.
- Unambiguously detect a planet transit in X-rays (see Chapter 6). While this is very tough to do because of the low count rates (see Chapter 2), extending the principle of transmission spectroscopy to X-rays could provide another method of directly probing the escaping material and its composition. Assessing the transit at wavelengths driving the escape, and avoiding some of the drawbacks of Ly $\alpha$ investigations (i.e. no substantial ISM absorption; able to probe lower velocity gas) are some of the attractive prospects of these wavelengths.
- Further investigate previous claims of SPI between HD 189733b and its host by analysing various activity signatures such as flares emanating from the system (see Chapter 7).
- Provide a more appropriate means of extrapolating to the unobservable EUV band for the current generation of X-ray instruments, many of which do not push down to the lower energy limit of the *ROSAT* X-ray band. In Chapter 3, I extend the method of Chadney et al. (2015) to other choices of energy bands.

# Chapter 2

# Methods

## 2.1 X-ray astronomy

$N_2$ and $O_2$ molecules readily absorb X-rays in the upper atmosphere via the photoelectric effect, making the Earth's atmosphere opaque at these wavelengths, as highlighted in Fig. 2.1. While this blocking of harmful ionising radiation is crucial for life on Earth, it means that X-ray astronomy has to be conducted from space.

Observationally, X-ray astronomy has its origins in the aftermath of the Second World War. The first X-ray observations were made using sounding rockets based heavily on V-2 rocket technology. Over a decade elapsed between the detection of X-rays from the Sun (Burnight, 1949), and the first detection from an extrasolar source (Sco-X1; Giacconi et al., 1962). Through the 1970s, the first satellites dedicated to X-ray astronomy were launched, culminating in the first facility with the ability to image in X-rays, *Einstein* (Giacconi et al., 1979). For a full history of early X-ray astronomy missions, I refer the reader to a review by Bradt et al. (1992). *ROSAT* performed what remains the most sensitive all-sky survey in soft X-rays in the early 1990s (Voges et al., 1999; Boller et al., 2016). ASCA, another mission from the 1990s, was the first mission to carry a CCD imager (Tanaka et al., 1994). The three currently operational telescopes capable of soft X-ray observations are *Chandra* (Weisskopf et al., 2000), *XMM-Newton* (Jansen et al., 2001), and *Swift* (Gehrels et al., 2004). All were launched around the turn of the millennium, and also all employ CCD imaging cameras (see Section 2.1.3).

The challenge of X-ray astronomy goes beyond the cost and difficulty of going to space. The count rates involved in X-ray observations of late-type stars are typically very low compared to optical and infrared. A look at the typical values of $L_{\rm X}/L_{\rm bol}$ (e.g. Section 1.3.5) will explain why. Even the brightest coronal sources

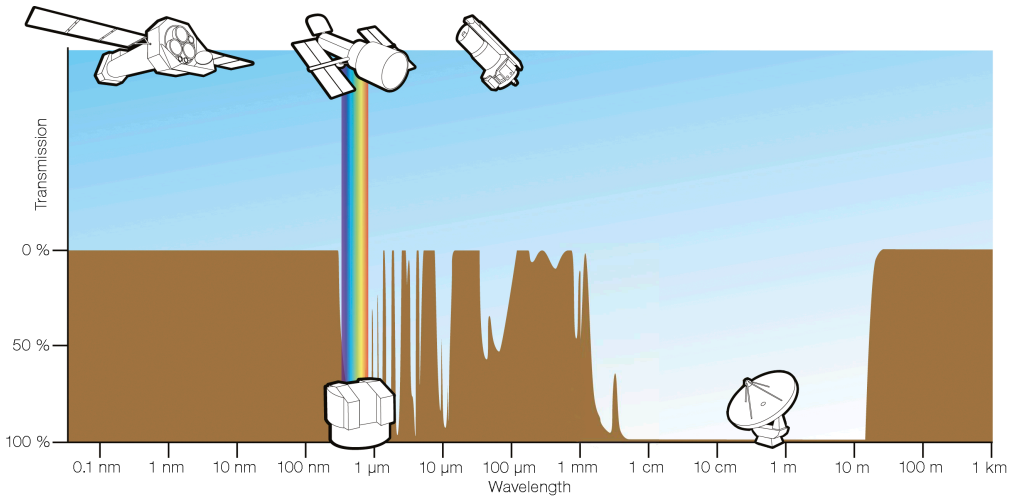


Figure 2.1: Schematic showing the transparency of Earth's atmosphere as a function of wavelength. The telescope silhouettes are (l–r): *XMM-Newton*, *HST*, VLT, *Spitzer*, and the Very Large Array (VLA). *Credit: ESA/Hubble (F. Granato).*

in the saturation regime have X-ray luminosities over 3 orders of magnitude smaller than their optical/IR emission, while many field stars are up to 7 or 8 orders of magnitude dimmer in X-rays. The brightest X-ray source I investigate in this work, HD 189733, has a quiescent observed count rate of around only $0.3\,\mathrm{s}^{-1}$ using the most sensitive soft X-ray instrument to date (*XMM-Newton*'s EPIC-pn).

There is one main advantage of the low count rates, however. At optical wavelengths, one must decide whether to perform imaging or spectroscopy, such is the flux of photons. Consequently, either spatial or spectral information must be thrown away. In X-ray astronomy, the low count rates mean that individual photons are able to be measured, meaning that both spatial and spectral information can be readily recorded for each event.

### 2.1.1 Effects of the ISM

The interstellar medium has a couple of effects on my work. Perhaps most relevant to my work, is its effect on EUV wavelengths. As discussed in Section 1.2.2, EUV may be just as important as X-rays for driving atmospheric escape. However, the EUV emission of stars other than the Sun is not possible to measure at the current epoch, for two closely-linked reasons. Firstly, photons at these wavelengths are readily absorbed by hydrogen in the ISM, similar to the missing core of the Ly $\alpha$ line in the observations described in Section 1.2.1. This makes the detection of EUV from

anything but the nearest stars very difficult. Secondly, in this context, it should be no surprise that there are no currently operational non-Solar EUV telescopes, and there has not been since *EUVE* (Bowyer and Malina, 1991) deactivated in 2001. To highlight the difficulty in detecting sources in EUV, consider the number of catalogued objects from the EUV all-sky survey by *EUVE* compared to the contemporaneous *ROSAT* all-sky survey in X-rays. The updated *ROSAT* catalogue contains some 135,000 detected sources (Boller et al., 2016), some two orders higher than catalogued by *EUVE* (Bowyer et al., 1996). Thus, for almost all sources, the EUV emission must be reconstructed, typically done from X-ray (e.g. Sanz-Forcada et al., 2011; Chadney et al., 2015, Chapter 3) or Ly $\alpha$ (Linsky et al., 2014). I provide a much more detailed discussion of EUV reconstruction in Section 3.4.4, where I also derive new empirical relations for estimating the EUV emission from X-rays by updating the method of Chadney et al. (2015).

In X-rays, of the systems that I investigate, only the Praesepe planets at a distance of about 190 pc lie far enough from Earth for ISM absorption to be very important. Absorption by the ISM has a negligible effect for nearby sources, but for completeness, I include a term to take account of ISM absorption in all spectral fits, using the TBABS model (Wilms et al., 2000).

### 2.1.2 X-ray telescopes

It is hard to focus X-rays down to a point in order to image them. Being so much more energetic, X-ray photons would be absorbed rather than reflected by an optical mirror at normal incidence. As such, focusing in X-rays is best performed at grazing incidence, taking advantage of total external reflection, wherein the X-rays are reflected with only small absorption losses. Wolter (1952) described three configurations to achieve successful focusing of X-rays. Modern X-ray telescopes use configuration I, which reflects the incoming X-rays twice: once off a parabolic mirror, and then off a hyperbolic one, which shortens the focal length. Modern telescopes also typically use sets of nested mirrors in order to maximise the collecting area.

What is the spatial resolution of X-ray telescopes? According to the Rayleigh criterion, the best possible angular resolution, $\theta$, at a wavelength $\lambda$ using a telescope with an aperture of diameter $D$ is given by

$$\theta = 1.22\frac{\lambda}{D}. \tag{2.1}$$

In theory, the short wavelengths associated with X-ray photons should mean that far superior angular resolution should be possible than at optical wavelengths. In

practice though, the quality and precision of the positioning and alignment of the mirrors limits the resolution to be about as good as possible with optical telescopes. To get to the diffraction limit in X-rays, the optics would have to be accurate down to the atomic level. The plate scale and pixel size are roughly matched to the quality of the optics. With units of arcsec $\mathrm{mm}^{-1}$, plate scale, $p$, is given by

$$p = \frac{206265}{f}, \tag{2.2}$$

where $f$ is the focal length of the telescope in mm. For the detection of enough photons, $f$ must be relatively large for an X-ray telescope, given the very small deflections associated with the requirement of grazing incidence. Putting very long telescopes into space is prohibitive for cost and logistical reasons. *Chandra*, which has the best angular resolution of any X-ray telescope to date, has a focal length of 10 m[1], giving it a plate scale of 20.6 arcsec $\mathrm{mm}^{-1}$. Multiplying this by the pixel size of its ACIS camera, 24 $\mu$m, results in $\theta = 0.5$ arcsec resolution. For *XMM-Newton*, $f = 7.5$ m, and $p = 27.5$ arcsec $\mathrm{mm}^{-1}$. Its EPIC-pn camera has a position resolution of 120 $\mu$m, resulting in $\theta = 3.3$ arcsec resolution[2]. The PSF of EPIC-pn is worse than this, with a half energy width of 16.6 arcsec[3]. This is relevant when trying to split up the three close sources in the aperture of HD 189733 in Section 6.3. I give specific details of the telescopes I have used data from in this work in Section 2.2.

### 2.1.3 Detectors

In this section, I describe the main principles behind the two types of detector used to collect the data I analyse in this work: proportional counters and CCDs. Other types of X-ray detectors have also been used for astronomy - e.g. crystal scintillators and microchannel plates - but I do not discuss them any further here.

#### Proportional counters

Proportional counters were first used for X-ray astronomy in the 1960s, and were by far the most popular choice of detector right up until the 1990s with *ROSAT*. A typical proportional counter is a box filled with noble gas, together with a wire(s) running through the gas that acts as an anode. In the event of an X-ray entering the chamber, it will travel a short distance before interacting via the photoelectric effect, ionising one of the gas atoms and creating a free electron. The initial photoelectron

[1]For *Chandra* specifications see `http://chandra.harvard.edu/about/specs.html`.
[2]See `https://www.cosmos.esa.int/web/xmm-newton/technical-details-epic`
[3]See `https://heasarc.nasa.gov/docs/xmm/uhb/onaxisxraypsf.html`

can emerge from the atom with a substantial proportion of the incoming X-ray photon's energy, and create many electron-ion pairs from other atoms in the gas. Meanwhile, fluorescence from the original ionised atom creates a new, lower energy photon which can photoionise another atom. The process repeats until almost all of the original energy is converted into an electron cloud which drifts towards the anode wire where the charge can be collected and measured. The relationship between the energy of the incoming photon and the measured charge is roughly linear (a more detailed explanation can be found in Bradt, 2003, pg. 133).

In their most basic form, proportional counters do not record spatial information about the incoming X-ray. However, more complex designs can incorporate the detection of the photon's position of origin on the sky. For instance, the position sensitive proportional counters (PSPC) on *ROSAT* had grids of anodes and cathodes, some of which were used for positioning, and some for measuring the energy of the original photon[4]. The positioning in such proportional counters can be done by measuring the proportion of charge collected at each anode (Bradt, 2003, pg. 137).

### CCDs

Charge-coupled devices (CCDs) have revolutionised astronomy at energies from X-rays to IR over the past few decades. Typically, a layer of p-doped Si less than a mm thick is topped by an even thinner layer (perhaps just a few $\mu$m thick) of n-doped Si in order to create a pn-junction. This is split into regular rows of pixels, which each may also be as small as a few microns in size. Each pixel has three electrodes. During an exposure, one of these is set to have a high positive potential, compared to the other two. Incoming photons excite electrons, via the photoelectric effect, from the valence band of the p-doped Si across the band gap into the conduction band of the n-doped Si, and are collected up in the potential well of the electrode. The charge that becomes trapped is proportional to the number of incoming photons. During read out, the potential applied to each electrode is varied, in order to move the charge along the rows and columns to an amplifier and then an analogue-to-digital converter, where the charge in each pixel is converted to a number of counts that can be recorded for that pixel in that exposure. If too much charge enters one pixel, the potential is filled, allowing charge to spill into the surrounding pixels. This is called saturation. Up until a point slightly below saturation, the response of a pixel to incoming photons is to a great extent linear.

In the case of an X-ray observation, each incoming photon liberates many

[4]See the ROSAT User's handbook, section 3. Can be found at `https://heasarc.gsfc.nasa.gov/docs/rosat/ruh/handbook/node48.html`

electrons, as in a proportional counter. As mentioned above, the low count rates of X-ray sources mean that individual photon energies can be measured. The number of liberated electrons is proportional to the incoming energy. However, to take advantage of the low count rate in this way, the exposures must be short, such that single events within pixels can be recorded separately. "Pile-up" occurs when more than one photon is detected in the same exposure within the same pixel, and the information on the energies of the photons is lost.

## 2.2 Telescopes used

In this section, I describe the three telescopes and their various instruments that I have used data from for this work.

### 2.2.1 *ROSAT*

Launched in 1990, *ROSAT* operated throughout the majority of the following decade. At the beginning of the mission, *ROSAT* performed what remains the most sensitive soft X-ray all-sky survey, almost thirty years later. The rest of the mission consisted of pointed observations, more akin to the observational strategy of *XMM-Newton* and *Chandra*, where most of the observing time is reserved for approved proposals by the astronomical community.

*ROSAT*'s main X-ray Telescope (XRT) used the Wolter I configuration, and had a focal length of 240 cm. Four instruments were carried onboard, two of which were identical. Neither the High Resolution Imager (HRI) or the Wide Field Camera (WFC), a separate EUV telescope attached to the side of the spacecraft, were used in this study, and so I do not discuss them further. The other instruments were the two Position Sensitive Proportional Counters (PSPCB and PSPCC), which were attached to the XRT along with the HRI. PSPCC was the main instrument in the all-sky survey, but was destroyed towards the end of the survey. The reserve PSPCB performed the rest of the observations made with the PSPC detectors, including the three observations of $\pi$ Men analysed in Chapter 4. The PSPC detectors were sensitive in the energy range 0.1–2.4 keV.

Generally speaking, *ROSAT*'s sensitivity has been surpassed by *Chandra* and, especially, *XMM-Newton*. However, for bright sources with very soft spectra archival *ROSAT* data can provide similar or higher count rates to *XMM-Newton*, because *ROSAT* was sensitive down to lower energies than *XMM-Newton*. $\pi$ Men, which I analyse *ROSAT* observations of in Chapter 4, is such a source.

### 2.2.2 *XMM-Newton*

The European Space Agency's *XMM-Newton* is a currently operational telescope, optimised for sensitivity and spectral resolution (Jansen et al., 2001). It contains three identical X-ray telescopes, each in Wolter I configuration. Each is mounted with one of the three European Photon Imaging Cameras (EPIC). Two of these are the Metal Oxide Semi-conductor (MOS) CCDs, while the other is the pn CCDs. Two of the telescopes are additionally mounted with identical Reflection Grating Spectrometers (RGS), used for high spectral resolution observations, where individual spectral lines can be observed. I do not use RGS data in this work. Finally, a separate small 30 cm aperture telescope is mounted to the front of the satellite, and is used for optical/NUV observations. All of the instruments are operated simultaneously.

As mentioned in Section 2.1.2, *XMM-Newton* has a maximum spatial resolution of 3.3 arcsec with the EPIC-pn. NASA's *Chandra* telescope can resolve sources down to 0.5 arcsec. However, what *XMM-Newton* lacks in this comparison, it makes up for with its increased sensitivity. EPIC-pn is able to attain higher count rates, and so higher signal-to-noise light curves and spectra. This is useful for investigating faint, single-star systems. The one object I have looked at that would have benefited from *Chandra*'s superior spatial resolution would have been HD 189733, where the PSFs of both stellar components of the system and a third background source all overlap. However, in Chapter 6, my aim is to detect the X-ray transit of the primary star's hot Jupiter planet. In pursuit of this goal, the *XMM-Newton* superior sensitivity meant it was the better telescope to use, especially since I was able to mitigate for the overlapping PSFs (see Section 6.3).

#### EPIC-pn

The EPIC-pn is the most sensitive of the three EPIC CCDs, owing to its superior quantum efficiency, particularly in soft X-rays, and is the primary instrument used in this thesis; all five science chapters contain analysis of EPIC-pn data. The camera consists of 12 separate rectangular CCDs of identical size in a $2\times6$ arrangement on a single silicon wafer. In Fig. 2.2, I give the effective area of the *XMM-Newton* detectors as a function of wavelength. The curves were calculated by taking the product of the effective area of the telescope with the quantum efficiency of the CCD (the fraction of number of incident photons actually detected by the CCD as a function of wavelength). This figure highlights the sensitivity of EPIC-pn over the other instruments. The curves do not take into account the effect of the various

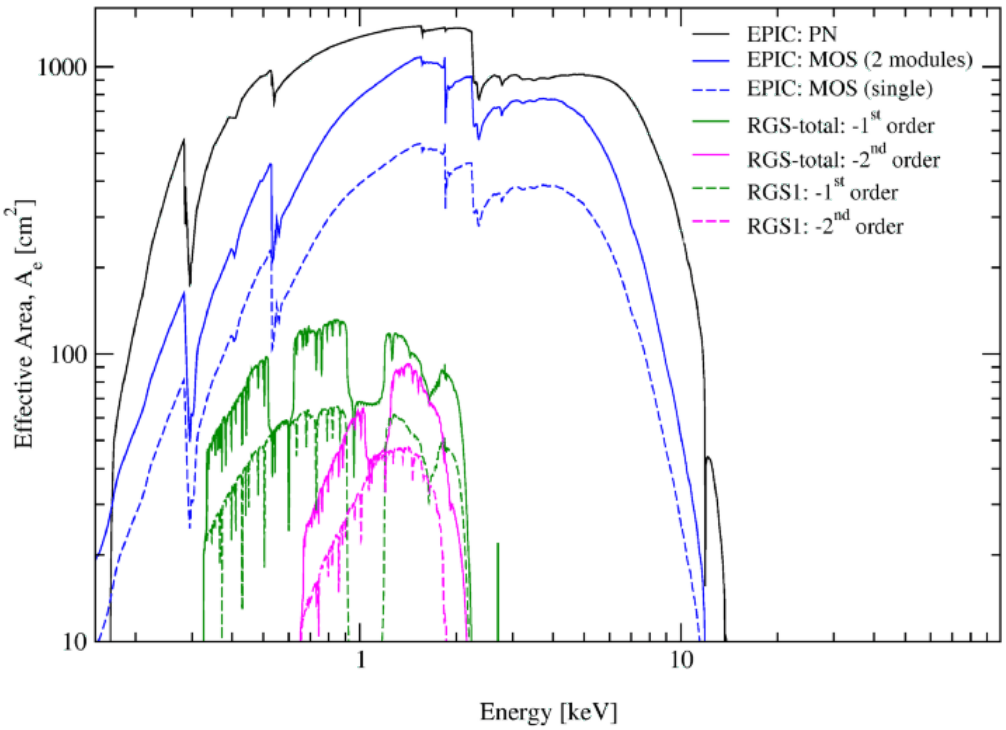


Figure 2.2: Effective area of the *XMM-Newton* detectors. Reproduction of fig .12 from the *XMM-Newton* Users Handbook[6]. *Credit: European Space Agency - XMM-Newton Science Operations Centre.*

optical blocking filters, which are described below. Fig 2.2 also shows that EPIC-pn can reach as soft as about 0.15 keV.

EPIC-pn can be operated in one of six science modes, offering differing window sizes and time resolution. In this work, I use the full frame and small window modes. The former is the default mode, offering use of the full chip at a time resolution of 73.6 ms. The latter uses a small region of only one of the CCDs, but at a smaller time resolution of 5.7 ms, making it useful for brighter objects as a way of trying to avoid pile-up. It was also used for the HD 189733 observations in Chapters 6 and 7 to avoid the need to use the medium blocking filter, and therefore preserve the soft response. One disadvantage is the increased dead time lost to readout. Small window mode has a live time percentage of 71.0%, compared to 99.9% for full frame mode.

One of three optical blocking filters is also used for the pn camera: thin, medium or thick. These are necessary because the EPIC CCDs are also sensitive to

[6] `https://xmm-tools.cosmos.esa.int/external/xmm_user_support/documentation/uhb/XMM_UHB.html`

optical, IR and UV photons, which can contaminate the observations. For example, these photons can affect the energy measurement of incident X-ray photons, as well as the detection of faint sources. The filter acts to mitigate most or all of negative effects that would otherwise result. However, the thicker filters also reduce the X-ray count rate of sources, by blocking out some of these photons too. The choice of filter is based upon the optical wavelength brightness of the target object. All of the observations analysed in this work used either the thin or medium filters.

EPIC-pn observations can be badly affected by soft proton flares. The protons are typically about 100 keV in energy, and the factors dictating their occurrence and intensity are complex. Walsh et al. (2014) provides a comprehensive review of the factors relating to the occurrence of soft proton flares, as well as their impact across the first decade of *XMM-Newton* observations. Best practice dictates that times associated with proton flares should be filtered out when analysing the data, especially spectra, as the flares can affect the accuracy and reliability of results by reducing the signal-to-noise due to the additional background they introduce.

### EPIC-MOS

Identical EPIC-MOS cameras are mounted on two of the telescopes onboard *XMM-Newton*. Each MOS camera consists of seven CCDs, with one in the centre and six placed around the outside, and each is sensitive down to about 0.2 keV. Two CCDs of EPIC-MOS1 have been rendered unusable for scientific observations though, in events likely attributable to micrometeorite impacts.

As can be seen from Fig. 2.2, both EPIC-MOS cameras together are about half as sensitive as EPIC-pn, depending on wavelength. Two factors affect the MOS-cameras' sensitivity. Firstly, a portion of the incident photons in those telescopes are redirected to the RGS instruments that are also mounted on them. Second, the back-illuminated nature of the pn CCDs is a major factor in the superior quantum efficiency over the front-illuminated MOS cameras, particularly at the soft end. To illustrate this point, one can compare fig. 5 of Strüder et al. (2001) for the pn to fig. 6 of Turner et al. (2001) for the MOS cameras.

The MOS cameras have four science modes available, each similar to one of the pn modes. All of the MOS observations in this work use the full frame mode, which has a time resolution of 2.6 s. The same three optical blocking filters are available for MOS. Also like EPIC-pn, the MOS cameras are also regularly affected by the soft proton issue, although some flares appear less intense in the MOS cameras than the pn. The relative effect for each MOS camera is typically similar, though.

#### Optical Monitor

The Optical Monitor (OM) is a small 30 cm aperture telescope onboard *XMM-Newton* that makes observations at visible/NUV wavelengths, simultaneous with the X-ray observations.

The OM has two main scientific operating modes: imaging and fast. In image mode, time resolution is sacrificed in order to make gains in the size of the field of view. Exposures of length greater than 800 s are combined into a mosaic around the target position of the observation. The fast mode provides time resolution down to 0.5 s, but only within a small window around the main target position of the observation, 22×23 pixels in size. When fast mode is used, one also obtains an image mode product, but not in mosaic form and thus with a smaller field of view.

The OM can be used with either a broadband photometric filter (V or B optically, or U, UVW1, UVM2, UVW2 in the NUV, in descending wavelength), or a grism. Throughout this work, only the NUV filters are used, in order to take advantage of the rare space-based UV capabilities of the OM. In Chapter 3, I detect a NUV transit of WASP-80b using the UVW1 filter. However, the red leak of that filter, combined with the red late-K/early-M-type spectrum of WASP-80 means that the data is essentially dominated by the equivalent of the U band (See Fig. 3.7). Note also that in analysing those data, I investigated in detail the reduction of OM fast mode data for precision photometry. This is presented in Section 2.4.

### 2.2.3 *Swift*

*Swift* is a NASA telescope, designed primarily for the observation of gamma-ray bursts. As its name suggests, the observing strategy of *Swift* is geared toward very fast follow up of these transient events once one is detected. *Swift* has simultaneous, multi-wavelength coverage of gamma-rays, X-rays and the NUV/optical. The gamma-ray and NUV/optical telescopes are the Burst Alert Telescope (BAT) and the Ultraviolet/Optical Telescope (UVOT), the latter of which is somewhat analogous to the OM on *XMM-Newton*. In this work, I only make use of the X-ray Telescope (XRT; Burrows et al., 2005).

Like the other modern X-ray telescopes, the XRT uses Wolter I mirror configuration. Related to its low Earth orbit, *Swift* observes in snapshots because it can only observe for part of its orbit, similar to *HST*. The XRT uses a camera very similar to the two MOS cameras on *XMM-Newton*, described above, meaning it can observe down to energies around 0.3 keV. *Swift* is therefore not the best choice for fainter sources with soft spectra, hence the very marginal detection of $\pi$ Men

in Chapter 4. *Swift* is however much more useful in Chapter 7, where I use data spread across nine years to investigate flares and activity for the planet host star HD 189733, which is brighter in X-rays.

## 2.3 X-ray data reduction & analysis

In this section, I describe the basic processes behind the reduction and analysis of the X-ray data I present in the following science chapters. My analyses make extensive use of the HEASoft[7] package. *XMM-Newton* additionally has its own reduction/analysis software called the Scientific Analysis System[8] (SAS).

The main output from the processing of the raw X-ray data, done onboard the telescope and once the data has been received back down on the ground, is an event file. This lists each detected X-ray photon (and charged-particle contaminant event), together with its timestamp, channel number (which can be converted into energy), and position on the CCD it was detected. Together with the astrometric solution contained in the file, the latter can easily be converted into an actual RA/dec on the sky. Often, a pattern will also be attached to each event; with so many electrons being liberated, the associated charge may not just collect in one pixel, but can instead be spread across several. The pattern describes how the the X-ray events are split between pixels. One can filter out patterns that are less likely to have been caused by genuine X-ray events, and instead the result of something else - perhaps a cosmic ray, for example.

With an event file obtained, the next step, should highly accurate timing be required, is to perform a barycentric correction. This shifts the timestamps associated with each event from the local rest frame of the telescope to the barycentre of the Solar System. By removing the effects of light travel time associated with the motion of the Earth around the Sun, this allows comparisons between observations, or to a particular ephemeris for a transit. The correction process requires an orbit file that describes the position of the Earth at a particular time.

For *XMM-Newton*, there is at this point an extra step, relating to the soft proton flares I described in Section 2.2.2. The event file should be tested for periods of flaring particle background, by checking for time periods where the overall hard X-ray ($> 10$ keV) count rate is above some threshold. If this is found to be the case, those times can be filtered out of the event file.

The event file is then in a state where scientific products, such as light curves

[7] See `https://heasarc.gsfc.nasa.gov/docs/software/heasoft/`

[8] See `https://www.cosmos.esa.int/web/xmm-newton/sas`

or spectra can be extracted by filtering the file with source and background regions. In order to do this, one usually extracts an image from the event file. Visual inspection can help to determine quickly whether a source has been detected or not, and aids in the placing of background regions away from other sources. Extraction of light curves, spectra etc is performed by an event-selecting program. For *XMM-Newton*, this is EVSELECT (part of SAS), while for *ROSAT* and *Swift* I used XSELECT, part of HEASOFT. Both of these programs are able to perform event list filtering, as well the extraction of light curves, spectra etc. For light curves, these programs bin the data in time to a user-defined bin size. For spectra, these programs collect the events into their respective channel numbers. This is converted into energy only when a spectral response file is applied, typically in a fitting program such as XSPEC (see Section 2.3.1).

A few more steps are required before the products are ready to use, including background correction, for example. For *XMM-Newton* data, SAS has a task EPICLCCORR which take a source and background light curve, performs the background correction, as well as a few other corrections for bad pixels, vignetting etc. For the spectra, the response of the detector as a function of energy must be quantified. This is usually done through a redistribution matrix file (rmf). Additionally, an ancillary response file (arf) quantifies both the effective area of the telescope, filter and detector, as well as the quantum efficiency of the detector. For *XMM-Newton*, the source, background, rmf and arf can be combined using the SPECGROUP command. This additionally rebins the spectra with a user-specified minimum counts per bin.

For *XMM-Newton* OM data, SAS has preset reduction chains for each of its observing modes, which can be used to obtain basic scientific products. For image mode data, OMICHAIN produces images, as well as detecting sources, which are listed in an output source list file with count rates (raw and background corrected), and position on the sky. For fast mode data, a time series will also be output, with a default time binning of 10 s. A barycentric correction can be applied to this time series, following its production. The outputs from both chains are produced on an exposure-by-exposure basis. I describe my findings for the best way to perform precision photometry using the fast mode data for detecting transits in Section 2.4.

### 2.3.1 xspec

For examining and fitting X-ray spectra, I use the HEASOFT program XSPEC throughout this work. XSPEC can take an input source spectrum and correct it with both a background spectrum and the response files (rmf/arf). One can read in multiple spectra for the same objects, perhaps taken with different instruments (pn and

MOS, for instance), or at different epochs. The model parameters described below can be linked across these different spectra during fitting.

XSPEC has many built in models and variants that can be used to fit the spectra. I employ APEC models throughout this work, except where I briefly use CEMEKL as a comparison in Section 3.4.3. The fitting process can be conducted using a range of fit statistics. Where my spectra have high enough signal-to-noise that I can bin to a minimum of 25 counts per bin, the uncertainties on the data should be Gaussian enough that I can use $\chi^2$. Where this is not the case, I employ the C-statistic (Cash, 1979) to account for the low numbers of counts per bin. Like $\chi^2$, this is a log likelihood function, which is maximised in order to perform parameter estimation. However, unlike $\chi^2$, the data are assumed Poissonian rather than Gaussian, and thus this likelihood statistic may be applied to situations where the count rate is low and uncertainties are typically asymmetric. Except where stated, I adopted Solar abundances from Asplund et al. (2009).

As part of the model, I also include a multiplicative term for the interstellar absorption. The TBABS model (Wilms et al., 2000) I employ takes a single variable: the column density of H I along the line of sight to the system. Given the nearby nature of almost all of my systems of interest, only in Chapter 5 for the more distant systems in Praesepe do I leave this as a parameter to be fitted. Even in this case, I limit this to be a maximum based on the total Galactic H I value along that line of sight (See Section 5.4.2).

The APEC models I employ are for an optically-thin plasma in collisional ionisation equilibrium, meaning that the ionisation balance is not evolving in time through the effect of some outside influence. The model assumes that the plasma is thermal, in which the electron velocity distribution is Maxwellian, and considers both a continuum element and line element to the emission. In XSPEC, a basic APEC model is described by four parameters: a characteristic temperature, a global value for the abundances of the most important elements (with respect to their Solar photospheric value), a redshift (not relevant for my work as I am considering only Galactic sources), and a normalisation. This normalisation parameter is given by, in cgs units,

$$\mathrm{Norm} = \frac{10^{-14}}{4\pi \left[D_{\mathrm{A}}(1+z)\right]^2} \int n_{\mathrm{e}} n_{\mathrm{H}} dV, \tag{2.3}$$

where $D_{\mathrm{A}}$ is the angular diameter distance to the source and $z$ is the redshift. In the case of galactic sources, $D_{\mathrm{A}}(1+z)$ is just the distance, $d$, to the source. At this

point, I will define the emission measure (EM):

$$\mathrm{EM} = \int n_{\mathrm{e}} n_{\mathrm{H}} dV, \tag{2.4}$$

where $n_{\mathrm{e}}$ and $n_{\mathrm{H}}$ are the electron and hydrogen ion number densities, respectively, and $V$ is the volume of the plasma. The case of $n_{\mathrm{H}} \approx n_{\mathrm{e}}$ is often considered, as this reduces the number densities terms to $n_{\mathrm{e}}^2$. Equation 2.4 is for the EM at a particular temperature, and the associated X-ray flux is directly proportional to the EM multiplied by a temperature dependent emissivity or line cooling function. Putting together Equations 2.3 and 2.4, we can reduce the normalisation parameter down to

$$\mathrm{Norm} = \frac{10^{-14}}{4\pi d^2}\ \mathrm{EM}. \tag{2.5}$$

Therefore, given a fitted value of the normalisation, Equation 2.5 can be rearranged to give an estimate of the emission measure associated with that temperature component of the model. In reality, plasmas are not isothermal, and so in the general case where one does not wish to approximate with components that have a single characteristic temperature, a distribution of EM with temperature is required. Such a distribution is often referred to as a differential emission measure (DEM), defined by

$$\mathrm{DEM} = n_{\mathrm{e}} n_{\mathrm{H}} \frac{dV(T)}{d\ln T}. \tag{2.6}$$

In the case of APEC, which calculates the model for a single characteristic temperature, multiple temperature components can be added together to approximate to the continuous range of temperatures present.

The strength of the continuum and, especially, the line emission in the APEC model is affected by the abundances. In the most basic APEC case, there is a single multiplicative factor for all elements compared to their Solar values. More complex APEC variants in XSPEC, "VAPEC" and "VVAPEC", both give the extra option of changing the abundances of some of the elements individually, as opposed to in bulk as in the main APEC model. I use VAPEC for the high signal-to-noise spectra for HD 189733A in Chapter 7, allowing me to free up elements relevant to the FIP effect (see Section 1.3.2). Each time an APEC model is generated, the emissivity of each individual line, as well as the continuum, is considered based on the parameters of the model (temperature, abundances, emission measure) and combined to form the full spectrum of that APEC component.

With a model fitted, the quality of the fit can be examined both through the fit-statistic and the built-in "goodness" command, which performs a Monte-Carlo

assessment of the goodness of fit for a user-specified number of realisations of the model. Following this, one of the main points of interest is to obtain the X-ray flux associated with the model, and XSPEC has a command "flux" to determine this. As I have included a term for interstellar absorption, this output number is the X-ray flux measured after this absorption. In order to determine the unabsorbed flux, I then set the H I column density to zero, and recalculate the flux without refitting the model.

For the determination of uncertainties on both the parameters of the model and the X-ray flux, XSPEC has a built-in Markov-Chain Monte Carlo (MCMC) sampler which can produce many realisations of the model. The chain can be run with a chain length and burn-in specified by the user. The output is a sample chain of the various model parameters, and this can be used in conjunction with the "error" command to obtain values for the uncertainties on both these parameters and the X-ray flux associated with the model. I give a brief introduction to MCMC methods in Section 2.5.

## 2.4 Data reduction & analysis of XMM-Newton OM fast mode

In assessing the OM data for WASP-80 (see 3.5.2), I noticed the outputs from the standard SAS analysis chains for the image and fast mode data, OMICHAIN and OMFCHAIN, respectively, did not fully agree with each other. Fig. 2.3 highlights the differences between the shape of the image mode light curve (red circles) and fast mode light curves (green squares and pink triangles; where the green squares are from the per-exposure source lists accompanying the fast mode light curve, and the pink triangles represent the fast mode time series binned to the same cadence, both from OMFCHAIN). The most obvious differences are the jump after the first two points and drop down before the last two points.

My hypothesis for the cause of the discrepancy between the image and fast mode chains was that this was due to the different source apertures employed. OMICHAIN uses 12 pixel radii apertures for the image mode data, but OMFCHAIN uses only 6 pixel radii regions because of the small size of the fast mode window. Unfortunately, I could not test this hypothesis using the analysis chains. The aperture size used by OMICHAIN is unable to be modified, and although the sizes employed by OMFCHAIN are customisable, the fast mode window is far too small for apertures with a radius of 12 pixels to be used. Therefore, to test my hypothesis, I instead analysed the data using a standard photometry code.

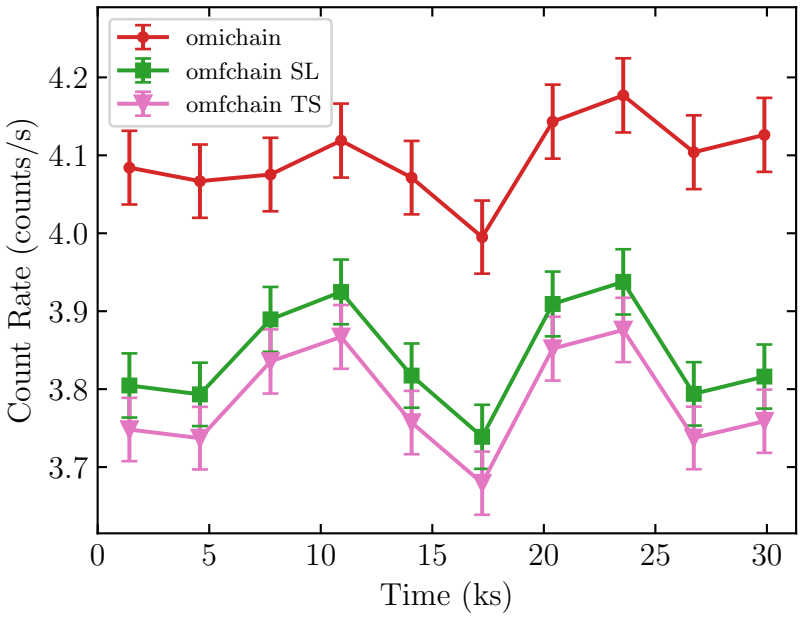


Figure 2.3: Comparison of the *XMM-Newton* Optical Monitor light curves for WASP-80. The image mode data reduced by OMICHAIN is shown by the red circles. Two fast mode light curves from the OMFCHAIN outputs are displayed: one taken from the source list (SL) for each overall exposure (green squares), the other from the time series (TS) binned to the same cadence (pink triangles).

I performed aperture photometry on the image mode data using the AUTOPHOTOM routine, part of the PHOTOM package (Eaton et al., 2009) from the STARLINK project (Currie et al., 2014). This was done using source aperture radii of 12 and 6 pixels. These light curves, along with the raw light curves from the OMICHAIN and OMFCHAIN, are displayed in Fig. 2.4. My 12 pixel aperture extraction using AUTOPHOTOM (shown as cyan up-pointing triangles) is in excellent agreement with the OMICHAIN light curve (red circles), and my 6 pixel aperture AUTOPHOTOM extraction is very similar in shape to the raw OMFCHAIN time series. This confirms my hypothesis that the main difference between OMICHAIN and OMFCHAIN can be attributed to the different extraction radii. However, there is a slight difference in the 6 pixel aperture light curves towards the middle of the observation, which points to a second effect (there is also an offset similar to that seen between the two OMFCHAIN outputs in Fig. 2.3).

I believe this second effect is the result of the source moving in the fast mode window, causing the extraction aperture to extend a little beyond the fast mode window for these exposures. This is highlighted in Fig. 2.5, which shows two fast mode window exposures: '401' and '007'. The former is unaffected by this issue,

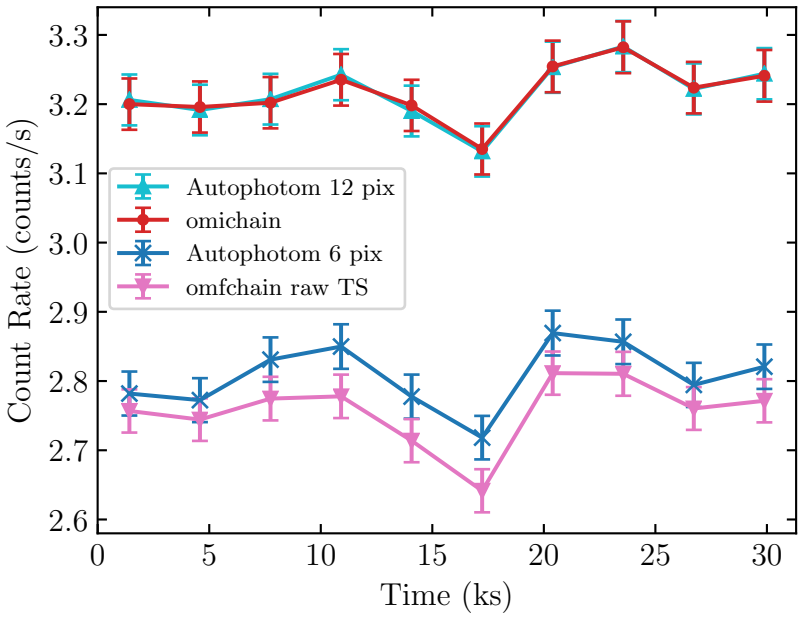


Figure 2.4: Comparison of the raw OMICHAIN (red circles) and OMFCHAIN time series (pink down-pointing triangles) with AUTOPHOTOM analyses using 12 (cyan up-pointing triangles) and 6 (blue crosses) pixel radii apertures. This shows the main difference between OMICHAIN and OMFCHAIN light curves is due to the different extraction radii used.

whereas the latter is the worst afflicted. The points with a greater offset in the fast mode comparison in Fig. 2.4 correspond to the exposures where the PSF runs into the edge of the fast mode window.

I conclude that the differences in shape I see in Fig. 2.3 can be understood as primarily resulting from the different aperture sizes used, with a further, smaller contribution from the source aperture running into the sides of the fast mode window. Therefore, I feel justified in correcting fast mode data from OMFCHAIN by the corresponding image mode data from OMICHAIN. Taking the ratio of the image mode data to the fast mode time series binned to the same cadence (i.e. the ratio of the red and pink light curves in Fig. 2.3) provides a suitable correction. Each individual time bin in my analysis in Section 3.5.2 was therefore multiplied by this ratio, as calculated for the corresponding exposure.

## 2.5 Bayes Theorem and MCMC

During parameter uncertainty estimation in XSPEC and transit light curve fitting, I implement Markov-Chain Monte Carlo (MCMC) methods. The main idea behind

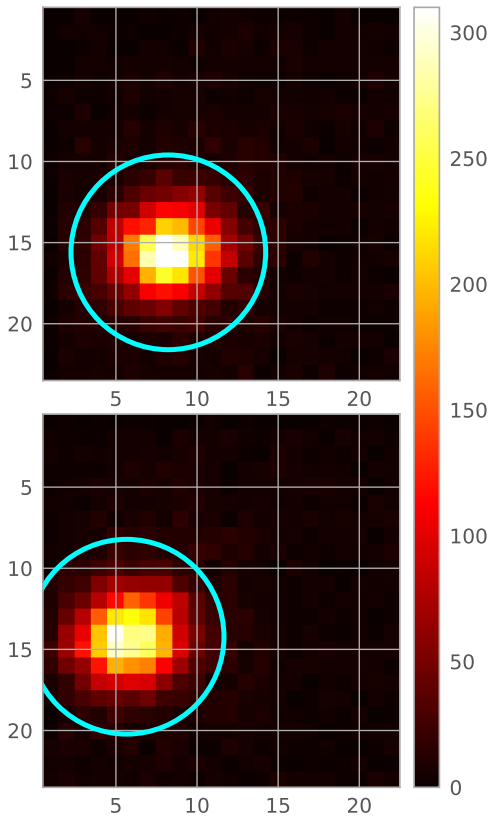


Figure 2.5: Comparison of two fast mode exposures, and how the source position within the window changes. For exposure 401 (top panel), the omfchain aperture used to extract the time series, overplotted in cyan, remains fully within the window. However, the aperture runs into the side of the window in exposure 007 (bottom panel), causing a small discrepancy with the corresponding image mode data when a same-sized aperture is used.

MCMC is to explore the parameter space for the variables within a model that one wishes to fit to some data in order to find the high probability areas of the space, and allow estimation of the values of the model parameters and their uncertainties..

MCMC is a Bayesian method, and so is based upon Bayes theorem:

$$P(A|B) = \frac{P(B|A)P(A)}{P(B)}. \tag{2.7}$$

$P(A|B)$ (the probability of A being true, given B is true) is referred to as the posterior, $P(B|A)$ (the probability of B being true, given A is true) the likelihood, $P(A)$ (the probability of A being true) the prior, $P(B)$ the evidence (the probability

of B being true). As an illustrative example of Equation 2.7, consider the following[9]: *A patient goes to see a doctor. The doctor performs a test with 99% reliability - that is, 99% of people who are sick test positive and 99% of the healthy people test negative. The doctor knows that only 1% of the people in the population are sick. Now the question is: if the patient tests positive, what are the chances the patient is sick?*

In this example, event A refers to having the disease, and event B refers to a positive test for the disease. Let us assume we have a population of 10,000 people, and work through the problem with Equation 2.7. We are interested in $P(A|B)$ which is the probability of a person having the disease, given they test positive. We know that $P(A)$, the probability of having the disease, is 0.01 (i.e. 100 of our population), and that $P(B|A)$, the probability of a positive test given the person has the disease, is 0.99 (i.e. 99 of our population). Analytically, the probability of a positive test, $P(B)$, is

$$P(B) = P(A)P(B|A) + P(\bar{A})P(B|\bar{A}). \tag{2.8}$$

$P(\bar{A})$ is the probability of being healthy, as we must also take into account the healthy individuals that give a false positive test. In addition to our 99 sick people that test positive, 1% of our 9900 healthy individuals, another 99 persons, would also test positive. Therefore, $P(B) = 198/10,000 = 0.0198$. Plugging in our values into Equation 2.7, we see that

$$P(A|B) = \frac{0.99 \times 0.01}{0.0198} = 0.5, \tag{2.9}$$

meaning there is only a 50:50 chance that someone testing positive actually has the disease. This is a rather surprising result when intuitively one might have said the answer would be much higher. Clearly, those false positive tests are hampering the effectiveness of the test.

How is this equation used in the context of MCMC sampling? At each point in the MCMC chain, new values for each parameter, $x_{i+1}$, in some model are proposed through some random jump away from the previous values, $x_i$. Equation 2.7 is assessed for both sets of model parameters and the results compared. Taking the ratio of the two posteriors:

$$R = \frac{P(B|A(x_{i+1}))}{P(B|A(x_i))} \times \frac{P(A(x_{i+1}))}{P(A(x_i))} \tag{2.10}$$

[9]E.g. from `https://www.scientificamerican.com/article/what-is-bayess-theorem-an/`

allows the often tricky to calculate $P(B)$ term to be cancelled out. $R$ can be used to compare the two sets of model parameters in terms of their relative goodness of fit to the data. Various prescriptions have been implemented to determine the acceptance/rejection of the new parameters $x_{i+1}$. As an example, consider the Metropolis-Hastings algorithm (Metropolis et al., 1953; Hastings, 1970). In this case, one accepts the new parameters $x_{i+1}$ if $R > 1$, and $x_{i+1}$ becomes the new $x_i$. This ensures the chain does not get stuck in low-probability areas of the parameter space. Alternatively, if $R < 1$ the new parameters are accepted with probability $R$, else $x_i$ remain the current parameters and a new $x_{i+1}$ is tested against these same parameters in the next step. This latter probabilistic acceptance ensures that the MCMC chain does not get stuck in the areas of very high probability and can instead well sample the full parameter space.

Typically, one takes thousands of steps to explore the parameter space. At each step, the current parameters $x_i$ are appended to the chain, such that after $N$ steps each parameter has $N$ values in the chain. However, this chain usually takes some time to find the best area of the parameter space and begin to fully explore it. The chains are said to have converged at this point. The early part of the chain pre-convergence is referred to as the "burn-in", and the first $N_{\rm burn}$ steps of this chain are usually thrown away before estimating parameters. Visual inspection of the chains can help determine at which point the chains have successfully converged. Following the throwing away of the burn-in, the remaining $N_{\rm sample}$ steps of the chain can be used for parameter and uncertainty estimation. One method of performing this takes the median samples as the best-fit value for each model parameter, and the 16th and 84th percentiles as the limits of the 1-$\sigma$ region. Note that estimating the values in this way is only strictly applicable if the sample distributions are Gaussian.

For running MCMC in this work, XSPEC has a built-in MCMC sampler for exploring the parameter space around a spectral model fit. This permits estimation of the uncertainties on both the fit parameters and the flux associated with the model. When I fit transit light curves for WASP-80b in the NUV (Section 3.5.2) and HD 189733 in X-rays (Section 6.4.3), I use the EMCEE code, a Python implementation of MCMC by Foreman-Mackey et al. (2013) that allows the user to employ a number of parallel walkers that simultaneously explore the parameter space.

# Chapter 3

# The XUV environments of exoplanets from Jupiter-size to super-Earth

## 3.1 Introduction

As I have discussed in Section 1.2.2, X-ray and EUV photons are thought to be the driving force behind atmospheric mass loss from close-in planets. Direct measurements of the X-ray irradiation incident upon planets can be highly informative as regards the possible rate of such mass loss. This is particularly the case for planets which have had both their radius and mass measured, as it allows one to estimate the mass loss rate through prescriptions such as the energy-limited equation (equation 1.9).

However, in order to make the best estimates of mass loss using the observations, it is also important to consider the unobservable EUV emission too. In Chapter 1, I discussed previous attempts to estimate this from X-ray emission (Sanz-Forcada et al., 2011; Chadney et al., 2015), rotational velocity (Lecavelier Des Etangs, 2007; Ehrenreich and Désert, 2011), Ly $\alpha$ (Linsky et al., 2014), and full Differential Emission Measure recovery (Louden et al., 2017a).

Several studies have previously used X-ray observations of known planet-hosting stars, taken with both past and current telescopes, to investigate the high-energy environments experienced by close-in planets (e.g. Kashyap et al., 2008; Poppenhaeger et al., 2010; Sanz-Forcada et al., 2011; Ehrenreich et al., 2015; Salz et al., 2015a; Louden et al., 2017a; Wheatley et al., 2017). *XMM-Newton* is perhaps the best X-ray telescope available for making observations to characterise relatively

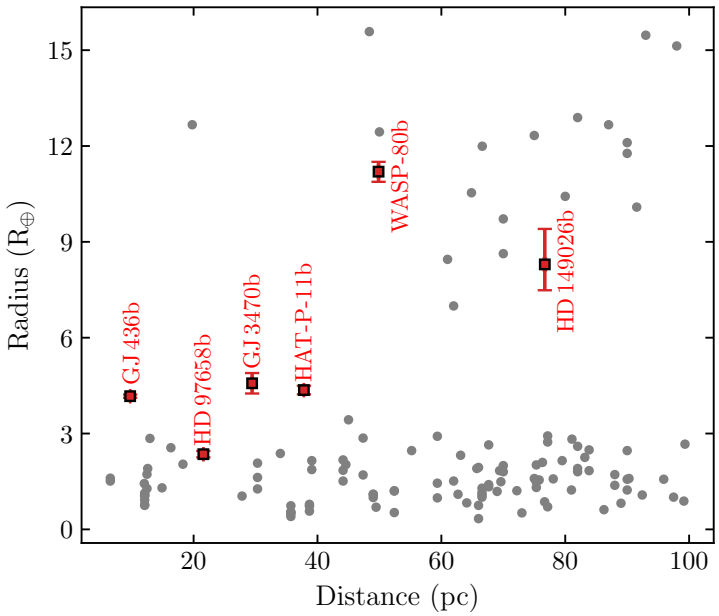


Figure 3.1: Distances and radii of all known transiting planets within 100 pc of Earth. The six planets in my sample are shown as red squares. Other planets are shown as grey circles. Data taken from NASA Exoplanet Archive.

nearby planet-hosting stars. While its inferior spatial resolution compared to *Chandra* means it is not so good for host stars in close binaries, the effective area of its EPIC-pn camera is unrivalled at soft energies down to about 0.2 keV.

In this Chapter, following on from Salz et al. (2015a)'s investigations into hot Jupiters, I probe the high-energy environments of planets ranging from Jupiter-size down to super-Earth using observations taken with *XMM-Newton* in 2015. All six planets in the sample orbit their parent star with a period <10 d. Unlike some previous studies with larger samples (Sanz-Forcada et al., 2011), my sample also only contains stars hosting transiting planets. In order to reconstruct the unobservable EUV emission, I improve upon the work of Chadney et al. (2015) by deriving a new set of relations from Solar *TIMED/SEE* data that are applicable to the standard bands of the current generation of X-ray instruments. Finally, I also exploit the rare capabilities of the Optical Monitor on *XMM-Newton* to detect the transit of WASP-80b in the NUV.

## 3.2 Sample

My sample of six systems is made up of six of the closest known transiting planets to Earth, and is listed in Table 3.1. Fig. 3.1 shows all known transiting planets within

100 pc, and highlights the objects in this sample. Each of the planets occupies a scarcely populated area of this parameter space. For the giant planets, the sparsity is an intrinsic characteristic of the exoplanet population. The lack of increase in super-Earth-sized planets at larger distances, however, is a selection effect, due to the difficulty in detecting the smaller transits of such planets. Together with the results of past observations with *XMM-Newton* and *ROSAT* for some of the sample, the proximity of these systems means that all of the stars were predicted to exhibit sufficient X-ray flux for characterisation of the planet's XUV irradiation.

Table 3.1 outlines the properties of each planetary system investigated. I note that the values for HD 149026 from Southworth (2010) differ substantially from those of Carter et al. (2009), and that this also affects my mass loss analysis in Section 3.6.3.

GJ 436b, GJ 3470b, and HAT-P-11b are the three closest transiting Neptune-sized planets. Only one other confirmed transiting planet within 100 pc, K2-25b, has a radius between 3 and 5 $R_\oplus$, and it was discovered after these observations were taken. HD 149026 is one of just a few exoplanets within 100 pc with its radius between that of Neptune and Saturn. At the time of observation, HD 97658b was the second-closest, and orbited by far the brightest star ($V = 7.7$ mag) of any known planet of its size. This has since been surpassed by $\pi$ Men c, for which I analyse archival observations in Chapter 4. Though its importance is less obvious from Fig. 3.1, WASP-80 represents one of only three transiting hot Jupiters in orbit around a late K/early M-type star.

In addition to the favourable X-ray characterisation potential, four of the systems (GJ 436, HAT-P-11, HD 97658, and WASP-80) were also chosen in order to explore their near ultraviolet (NUV) transit properties with the Optical Monitor (OM) on *XMM-Newton*.

## 3.3 Observations

The six planet hosts were all observed with the European Photon Imaging Camera (EPIC) on *XMM-Newton* in 2015. Table 3.2 provides details of the observations in time, duration and orbital phase, as well as the adopted ephemerides. Observations were taken with the OM concurrently, cycling through different filters for GJ 3470 and HD 149026. For the other four objects, a single filter was used in fast mode in an attempt to detect transits in the ultraviolet.

Table 3.1: System parameters for the six transiting exoplanet host stars I observed with *XMM-Newton*.

| System | Spectral Type | $V$ (mag) | $d$ (pc) | Age (Gyr) | $R_*$ ($R_\odot$) | $T_{\rm eff,*}$ (K) | $P_{\rm rot}$ (d) | $R_{\rm p}$ ($R_\oplus$) | $M_{\rm p}$ ($M_\oplus$) | $\log g$ (cm/s$^2$) | $P_{\rm orb}$ (d) | $a$ (au) | $e$ | $T_{\rm eff,\,p}$ (K) |
|---|---|---|---|---|---|---|---|---|---|---|---|---|---|---|
| GJ 436 | M2.5V | 10.6 | 9.7560 | 6 | 0.437 | 3585 | 44.09 | 3.96 | 23.42 | 3.15 | 2.644 | 0.0287 | 0.153 | 740 |
| GJ 3470 | M1.5V | 12.3 | 29.446 | 1–4 | 0.568 | 3600 | 20.7 | 4.74 | 13.9 | 2.76 | 3.337 | 0.0369 | 0 | 620 |
| HAT-P-11 | K4V | 9.5 | 37.806 | 5.2 | 0.752 | 4780 | 29.33 | 4.80 | 25.74 | 3.05 | 4.888 | 0.0513 | 0.2646 | 880 |
| HD 97658 | K1V | 7.7 | 21.575 | 9.7 | 0.741 | 5170 | 38.5 | 2.40 | 7.55 | 3.17 | 9.489 | 0.080 | 0.078 | 760 |
| HD 149026 | G0IV | 8.1 | 76.70 | 1.2 | 1.290 | 6147 | 11.5 | 6.84 | 113.15 | 3.37 | 2.876 | 0.0429 | 0 | 1600 |
| WASP-80 | K7-M0V | 11.9 | 49.86 | 0.1 | 0.571 | 4145 | 8.5 | 10.97 | 171.0 | 3.18 | 3.068 | 0.0346 | $<$0.07 | 800 |

References: GJ 436: All parameters from Knutson et al. (2011) except $d$ (*Gaia* DR2: Gaia Collaboration et al., 2018), age and $T_{\rm eff,*}$ (Torres, 2007), $P_{\rm rot}$ (Bourrier et al., 2018b), and $M_{\rm p}$ (Southworth, 2010). GJ 3470: All from Awiphan et al. (2016), except $d$ (*Gaia* DR2) and $P_{\rm rot}$ (Biddle et al., 2014). HAT-P-11: $R_*$, $M_{\rm p}$, and $T_{\rm eff,\,p}$ from Bakos et al. (2010), $R_{\rm p}$, $P_{\rm orb}$, $a$, and $e$ from Huber et al. (2017a,b), $d$ from *Gaia* DR2, age from Bonfanti et al. (2016), $P_{\rm rot}$ from Béky et al. (2014). HD 97658: All from Van Grootel et al. (2014), except $d$ (*Gaia* DR2), age (Bonfanti et al., 2016), $P_{\rm rot}$ (Henry et al., 2011), $R_{\rm p}$ and $P_{\rm orb}$ (Knutson et al., 2014). HD 149026: All from Southworth (2010) ($P_{\rm rot}$ from $v \sin i$), except $d$ (*Gaia* DR2), and $T_{\rm eff,*}$ (Sato et al., 2005). WASP-80: All from Triaud et al. (2015) ($P_{\rm rot}$ from $v \sin i$), except $d$ (*Gaia* DR2), $P_{\rm orb}$ (Mancini et al., 2014).

Table 3.2: Details of my *XMM-Newton* observations.

| Target | ObsID | PI | Start time (TDB) | Exp. T (ks) | Start – Stop phase | Transit phase | PN filter | OM filter(s) | Ref. |
|---|---|---|---|---|---|---|---|---|---|
| GJ 3470 | 0763460201 | Salz | 2015-04-15 03:13 | 15.0 | 0.838 – 0.890 | 0.988 – 1.012 | Medium | U/UVW1/UVM2 | 1 |
| WASP-80 | 0764100801 | Wheatley | 2015-05-13 13:08 | 30.0 | 0.944 – 1.065 | 0.986 – 1.014 | Thin | UVW1 | 2 |
| HAT-P-11 | 0764100701 | Wheatley | 2015-05-19 13:13 | 28.5 | 0.967 – 1.035 | 0.990 – 1.010 | Thin | UVW2 | 3 |
| HD 97658 | 0764100601 | Wheatley | 2015-06-04 04:35 | 30.9 | 0.980 – 1.019 | 0.994 – 1.006 | Medium | UVW2 | 4 |
| HD 149026 | 0763460301 | Salz | 2015-08-14 19:19 | 16.7 | 1.009 – 1.077 | 0.977 – 1.023 | Medium | UVM2/UVW2 | 5 |
| GJ 436 | 0764100501 | Wheatley | 2015-11-21 01:40 | 24.0 | 0.949 – 1.063 | 0.992 – 1.008 | Thin | UVW1 | 6 |

Start time and duration are given for EPIC-pn.

References for the ephemerides: (1) Biddle et al. (2014); (2) Triaud et al. (2013); (3) Huber et al. (2017b); (4) Knutson et al. (2014); (5) Carter et al. (2009); (6) Lanotte et al. (2014).

The data were reduced using the Scientific Analysis System (SAS 15.0.0) following the standard procedure, as outlined on the 'SAS Threads' webpages[1]. The EPIC-pn data of all systems except HD 97658 show elevated high-energy background levels at some points in the observations. To minimise loss of exposure time, I raised the default count rate threshold for time filtering due to high-energy events ($> 10$ keV) by a factor of two compared to the standard value. Background filtering does not affect the results, except for HAT-P-11. High background (exceeding this higher threshold) was observed at numerous epochs in the HAT-P-11 data, as often seen in *XMM-Newton* due to Solar soft protons (Walsh et al., 2014). Although the size of the uncertainties were not significantly changed by filtering, a 10 per cent increase in the best fit flux values were obtained with the filtered dataset. The results presented here use the filtered dataset in the spectral fitting process and subsequent analysis, however the light curve for HAT-P-11 presented in Section 3.4.1 uses the unfiltered dataset in order to avoid large gaps.

### 3.3.1 Nearby sources

HD 149026 is not known to be a double star system (Raghavan et al., 2006; Bergfors et al., 2013), but STScI Digitized Sky Survey (DSS) images show a nearby star at 20 arcsec distance north-east of HD 149026. The source is also present in 2MASS images (Skrutskie et al., 2006) and my OM data. In the multi-epoch DSS images HD 149026 displays a proper motion of 3.651 arcsec measured over a time period of 40 years (Raghavan et al., 2006). The nearby source is not co-moving, hence, I identified it as a background source.

DSS and 2MASS images contain a source 8 arcsec away from HAT-P-11. This object was identified as KOI-1289 by the *Kepler* mission, and later found to be a false positive due to a blended signal from HAT-P-11[2]. KOI-1289 is 4.6 mag fainter than HAT-P-11 in the B band, and 6.3 mag fainter in the R band (Cutri et al., 2003; Høg et al., 2000; Monet et al., 2003). This is consistent with my findings: KOI-1289 is barely detected in OM. Comparison of the OM positions of both objects to their respective J2000 positions (Cutri et al., 2003; van Leeuwen, 2007) reveals proper motion in different directions at different rates, and are thus not co-moving.

WASP-80 also has a much fainter star located nearby (9 arcsec), as discussed in section 3.1 of Salz et al. (2015a). They identify it as a background 2MASS source, 4 mag dimmer than WASP-80.

[1] `http://www.cosmos.esa.int/web/xmm-newton/sas-threads`

[2] Flagged as a false positive on the MAST Kepler archive: `https://archive.stsci.edu/kepler/`. Inspection of the light curves reveal a transit signal with the same period as HAT-P-11.

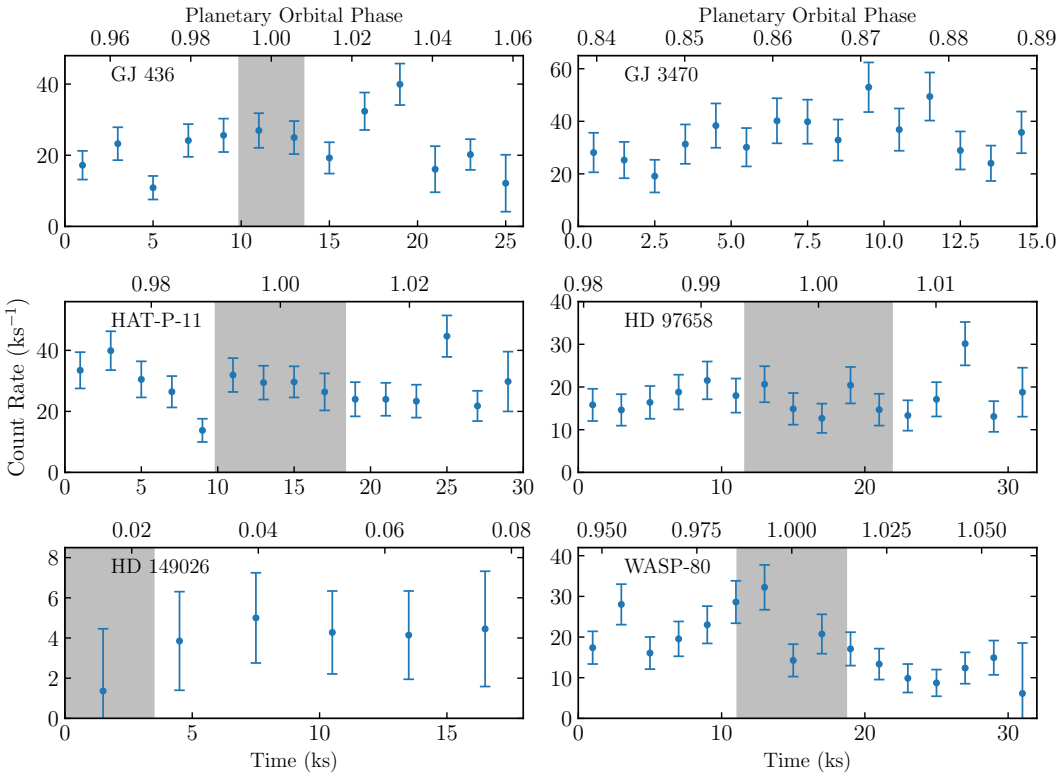


Figure 3.2: Background corrected X-ray light curves of the six targets. The count rate is the sum of the three EPIC detectors. The areas shaded in grey are the planetary transits (1st to 4th contact) in visible light. Time in each case is that elapsed from the beginning of the observation, as listed in Table 3.2.

In all four cases, the detected X-rays are centred on the exoplanet host star, and there is no evidence for X-rays from the nearby object. They were therefore neglected in the following analysis.

## 3.4 X-ray analysis and results

An X-ray source was detected within 1.5 arcsec of the expected position of each target star. 15 arcsec radius extraction regions were used for all sources, with multiple circular regions on the same CCD chip used for background extraction, located as close to the source as possible beyond 30 arcsec.

### 3.4.1 X-ray light curves

I analysed the light curves of the targets for two primary purposes. Firstly, I checked for strong stellar flares that could bias the measurements of the quiescent X-ray flux.

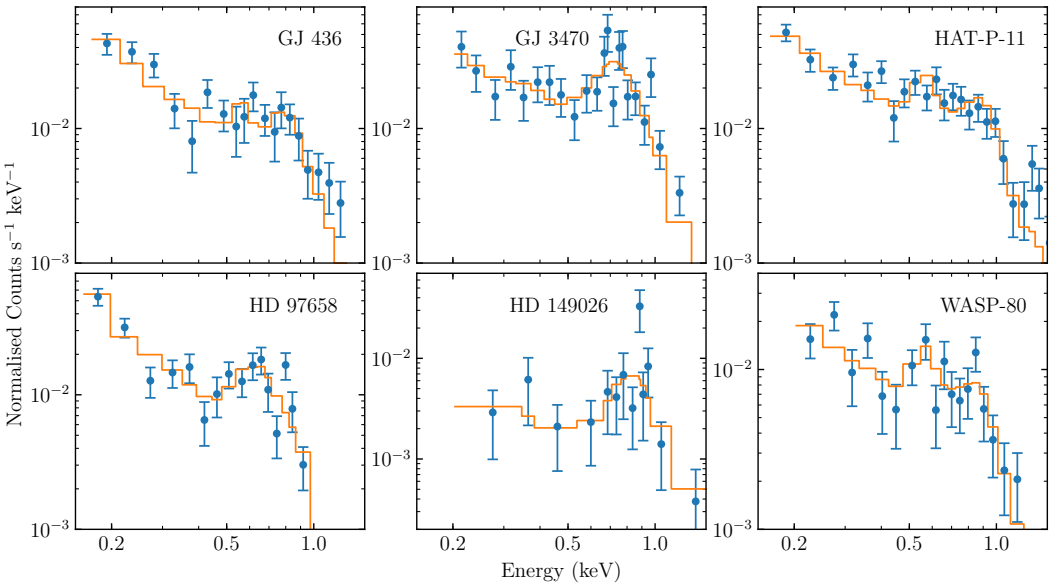


Figure 3.3: EPIC-pn X-ray spectra for the six targets. Unlike in the main analysis, the spectra are binned to a lower resolution to aid inspection. The background-corrected count rates are shown by the points with errorbars, with the histogram representing the fitted two-temperature APEC model.

Second, as shown in Table 3.2, four of the observations coincide with full planetary transits, and a fifth contains partial transit coverage. I examined the light curves for evidence of planetary transit features.

Figure 3.2 displays the background corrected light curves, coadded across the three EPIC detectors. The count rate of HD 149026 is too low to detect any variability, though a large flare would likely have been detectable, had one occurred. Of the other five observations, GJ 436 and WASP-80 show temporal variability at the 3-$\sigma$ level when tested against a constant, equal to the mean count rate. HAT-P-11 also exhibits variation, with a significance just below 3-$\sigma$. However, no strong flares are detected in any of the data, and none of the five observations covering a transit show any convincing evidence of transit features in their light curves.

### 3.4.2 X-ray spectra

I analysed the unbinned, background corrected spectra in XSPEC 12.9.0 (Arnaud, 1996). Accordingly, I used the C-statistic in my subsequent model fitting (Cash, 1979). The errors on my fitted parameter values were determined using XSPEC's error command, with confidence intervals of 68 per cent.

I fitted APEC models for optically-thin plasma in a state of collisional ion-

isation equilibrium (Smith et al., 2001). In all cases with this model, a single-temperature fit can be rejected at 95 per cent confidence, using a Monte Carlo technique to assess the goodness of fit. I therefore performed fits with two temperature components, which gives a good fit for all six datasets. The abundances were fixed to solar values (Asplund et al., 2009). Additionally, I included a term for the interstellar absorption, making use of the TBABS model (Wilms et al., 2000). I set the H I column density for GJ 436 and HD 97658 to the values found by Youngblood et al. (2016). For the other four objects I follow the approach of Salz et al. (2015a), who fixed the H I column density to the distance of the system multiplied by a mean interstellar hydrogen density of $0.1\,\mathrm{cm}^{-3}$ (Redfield and Linsky, 2000). I note that this estimate applies only to the Local Interstellar Cloud, and is not strictly applicable for lines of sight that contain other interstellar clouds. Redfield and Linsky (2008) showed that lines of sight to nearby stars varied around the average $N_\mathrm{H}$ value by about a factor of three. I found that changing $N_\mathrm{H}$ by a factor of three in either direction only changes the best fit measured fluxes by a few percent, well within the measured uncertainties.

The APEC-fitted EPIC-pn X-ray spectra are shown in Fig. 3.3. These have been binned to lower resolution to aid visualisation. The X-ray fluxes at Earth for the directly observed 0.2 – 2.4 keV band, $F_{\mathrm{X},\,\oplus}$, are shown in Table 3.3. To obtain the unabsorbed fluxes, I changed the H I column density to zero on the fitted model and reran the flux command. Since the error command cannot be run without refitting the model, I scaled the uncertainties so as to keep the percentage error constant between the absorbed and unabsorbed fluxes. Treating the errors in this way is valid here as the low column densities result in the flux change after setting the column density to zero is negligible.

### 3.4.3 X-ray fluxes

Most commonly used energy ranges for X-ray fluxes in the literature are conventions resulting from the passbands of various observatories. The ROSAT band (0.1 – 2.4 keV; 5.17 – 124 Å) is one of the most widely employed. However, this band is not so easily applied to data from the current generation of X-ray observatories: the effective area of *XMM-Newton's* EPIC pn and *Chandra's* ACIS-S both decline quickly below 0.25 keV. Thus, extrapolations to the ROSAT energy range must be made. As highlighted in Bourrier et al. (2017a) and Wheatley et al. (2017), while the fluxes obtained in XSPEC are usually seen to be consistent with one another in directly observed bands, the fluxes when extrapolating down to 0.1 keV can disagree significantly between models.

Table 3.3: Results from my X-ray and EUV reconstruction analyses. The results given are for the X-ray range 0.2 – 2.4 keV, and corresponding EUV range 0.0136 – 0.2 keV. The X-ray fluxes at Earth are the APEC modelled values.

| System | $kT$ keV | $N_{\rm H}$ ($a$) | EM ($b$) | $F_{\rm X,\,\oplus}$ ($c$) | $L_{\rm X}$ ($d$) | $L_{\rm EUV}$ ($d$) | $F_{\rm XUV,\,p}$ ($e$) | $F_{\rm XUV,\,1\,au}$ ($e$) | $L^{\dagger}_{{\rm Ly}\alpha}$ ($d$) | $F^{\dagger}_{{\rm Ly}\alpha,\oplus}$ ($c$) | $F_{{\rm Ly}\alpha,\oplus}$ ($c$) |
|---|---|---|---|---|---|---|---|---|---|---|---|
| GJ 436 | $0.12 \pm 0.01$<br>$0.61 \pm 0.08$ | 1.1 | $0.19 \pm 0.3$<br>$0.048^{+0.007}_{-0.006}$ | $2.91^{+0.16}_{-0.27}$ | $0.332^{+0.019}_{-0.030}$ | $2.95^{+0.24}_{-0.34}$ | $1380^{+100}_{-150}$ | $1.16^{+0.12}_{-0.16}$ | 3 | 27 | $20^{*}, 21^{\S}$ |
| GJ 3470 | $0.09 \pm 0.03$<br>$0.35^{+0.06}_{-0.03}$ | 8.9 | $1.7^{+4.1}_{-0.9}$<br>$1.0^{+0.2}_{-0.2}$ | $4.5^{+0.2}_{-0.9}$ | $4.67^{+0.21}_{-0.93}$ | $14.6^{+2.2}_{-4.1}$ | $5000^{+700}_{-1100}$ | $6.9^{+0.8}_{-1.6}$ | 13 | 13 | – |
| HAT-P-11 | $0.16 \pm 0.01$<br>$0.81^{+0.12}_{-0.06}$ | 12 | $2.7 \pm 0.2$<br>$0.91^{+0.11}_{-0.10}$ | $3.58^{+0.17}_{-0.21}$ | $6.13^{+0.29}_{-0.37}$ | $22.1^{+2.4}_{-2.7}$ | $3560^{+320}_{-350}$ | $10.0^{+0.9}_{-1.0}$ | 35 | 21 | – |
| HD 97658 | $0.044^{+0.013}_{-0.008}$<br>$0.24 \pm 0.1$ | 2.8 | $15^{+16}_{-10}$<br>$0.56 \pm 0.06$ | $2.92^{+0.16}_{-0.78}$ | $1.63^{+0.09}_{-0.43}$ | $11.1^{+1.1}_{-3.3}$ | $700^{+60}_{-190}$ | $4.5^{+0.4}_{-1.3}$ | 22 | 39 | $42^{\ddagger}, 91^{\S}$ |
| HD 149026 | $0.09^{+0.41}_{-0.06}$<br>$0.71^{+0.14}_{-0.09}$ | 24 | $2.3^{+148.6}_{-2.3}$<br>$1.7^{+0.4}_{-0.2}$ | $0.84^{+0.01}_{-0.21}$ | $5.81^{+0.07}_{-1.45}$ | $37^{+4}_{-11}$ | $8200^{+900}_{-2000}$ | $15.1^{+1.6}_{-3.8}$ | 52 | 7.5 | – |
| WASP-80 | $0.15 \pm 0.02$<br>$0.73 \pm 0.09$ | 19 | $3.6^{+2.8}_{-2.0}$<br>$1.1^{+0.9}_{-0.6}$ | $1.78^{+0.11}_{-0.16}$ | $5.30^{+0.32}_{-0.48}$ | $16.1^{+2.1}_{-2.6}$ | $6420^{+650}_{-790}$ | $7.6^{+0.8}_{-1.0}$ | 28 | 9.4 | – |

$a$ $10^{18}\,{\rm cm}^{-2}$ (column density of H)
$b$ $10^{50}\,{\rm cm}^{-3}$
$c$ $10^{-14}\,{\rm erg\,s}^{-1}\,{\rm cm}^{-2}$ (at Earth, unabsorbed)
$d$ $10^{27}\,{\rm erg\,s}^{-1}$
$e$ ${\rm erg\,s}^{-1}\,{\rm cm}^{-2}$
$^{\dagger}$ Estimated using the relations between EUV and Ly $\alpha$ fluxes at 1 au in Linsky et al. (2014).
$^{*}$ As reconstructed from observation by Bourrier et al. (2016).
$^{\ddagger}$ As reconstructed from observation by Bourrier et al. (2017a).
$^{\S}$ As reconstructed by Youngblood et al. (2016).

I investigated the extrapolation discrepancy between the APEC model and CEMEKEL, the second model used by Bourrier et al. (2017a) and Wheatley et al. (2017). The latter is a multi-temperature plasma emission model, wherein the emission measure as a function of temperature is described by a power law (Schmitt et al., 1990; Singh et al., 1996). The TBABS term accounting for interstellar absorption was applied in the same way as for the APEC model, above. For HD 97658, the CEMEKL model yields a flux in the 0.2 – 2.4 keV band of $\left(2.90^{+0.15}_{-0.24}\right) \times 10^{-14}\,\mathrm{erg\,s^{-1}\,cm^{-2}}$, in good agreement with the APEC value of $\left(2.92^{+0.16}_{-0.77}\right) \times 10^{-14}\,\mathrm{erg\,s^{-1}\,cm^{-2}}$. However, when extrapolated down to 0.1 keV, the CEMEKL value, $1.34 \times 10^{-13}\,\mathrm{erg\,s^{-1}\,cm^{-2}}$, was almost four times lower than the corresponding APEC value of $5.3 \times 10^{-13}\,\mathrm{erg\,s^{-1}\,cm^{-2}}$. Similar, but smaller, differences were also observed for the other objects. These originate from the different temperature-emission measure distribution assumptions of the models. For this reason, I chose to extrapolate directly from the observed X-ray fluxes to the full XUV band, rather than taking a two-step method of extrapolating to the *ROSAT* band and then the EUV.

### 3.4.4 EUV reconstruction

EUV fluxes of stars must be reconstructed using other spectral ranges. Salz et al. (2015a) compared three such methods, finding them to differ by up to an order of magnitude in active stars. However, Chadney et al. (2015), hereafter C15, presented a new empirical method of reconstructing the EUV flux from the measured X-ray flux. This method shows a better agreement with stellar rotation-based and stellar Ly $\alpha$ luminosity-based reconstructions (Lecavelier Des Etangs, 2007; Linsky et al., 2014) than the X-ray-based method of Sanz-Forcada et al. (2011).

C15 analysed observations of the Sun, deriving a power law relation between the ratio of EUV to X-ray flux and the surface X-ray flux. This method seems physically well motivated, relating the fluxes at the stellar surface, thereby implicitly taking the local conditions of this region into account. Indeed, their result agrees well with synthetic spectra for a small number of nearby, K and M dwarf stars, as generated from coronal models. These synthetic spectra, in turn, agree with EUVE measurements within the uncertainties.

The C15 relation adopts the ROSAT band. Accordingly, they define the EUV band as 0.0136 – 0.1 keV (124 – 912 Å). As discussed in section 3.4.3, this definition does not transfer well onto the current generation of X-ray telescopes. To apply the C15 relation to observations by either *XMM-Newton* or *Chandra*, one must perform two extrapolations. The first estimates the missing X-ray flux down to 0.1 keV, which I have shown to be uncertain by a factor of a few. The second occurs

in applying the relation itself. Given the model-dependence on the first of these steps highlighted above, it would be preferable to derive a new set of relations that allow direct extrapolation from the observed band to the rest of the XUV range in a single step. By reperforming the C15 analysis with different boundaries, I derived new such relations that are more applicable to current instruments.

### Derivation of new X-ray-EUV relations

The data used by C15 comes from the ongoing *TIMED/SEE* mission (Woods et al., 2005). One of the primary data outputs of the mission is daily averaged Solar irradiances, given in 10 Å intervals from 5 – 1945 Å. I integrated the fluxes up to the Lyman limit (0.0136 keV, 912 Å), splitting the data into X-ray and EUV bands either side of some defined boundary. Here, I used a range of boundary choices to produce my set of relations.

Using only the C15 sample (30 May 2002 – 16 November 2013), I was able to replicate their relation exactly, but I have the benefit of extra data. However, I noticed that some of the most recent observations appear to be offset from the rest of the data (see Fig. 3.4). This offset is likely a result of instrument degradation, which is not yet properly accounted for in the recent data (private communication with the TIMED/SEE team). Therefore, I chose to cut off all data past 1 July 2014, where the data start to show significant differences to older observations.

Additionally, I noticed that the errorbars in the merged file of all observations did not match those in the individual daily files. This bug was kindly fixed by the mission team. It seems that the data used by C15 had the same problem, so I also update C15's relation for the 0.1 keV boundary.

Fig. 3.5 shows the solar *TIMED/SEE* data and fluxes from the comparison synthetic stellar spectra, plotted for three of the boundary choices. The residuals of the single power law fit reveal a trend. As the choice of boundary energy is increased, the log-log plot increasingly deviates from linear. A more complex function may be justified when solely considering the solar data. However, this would have proved less robust when extrapolating the relation to higher flux levels in active stars. I obtained synthetic spectra for a sample of nearby stars: $\epsilon$ Eri from the X-Exoplanets archive[3], and the spectra for AD Leo and AU Mic presented in C15. Using these, a single power law fitted to the solar data agrees well with the comparison stars. During this comparison process, I also found that unweighting the solar data actually provided a slightly better fit with regard to the comparison stars across the choice

[3]Available at `http://sdc.cab.inta-csic.es/xexoplanets/jsp/homepage.jsp`. See also Sanz-Forcada et al. (2011).

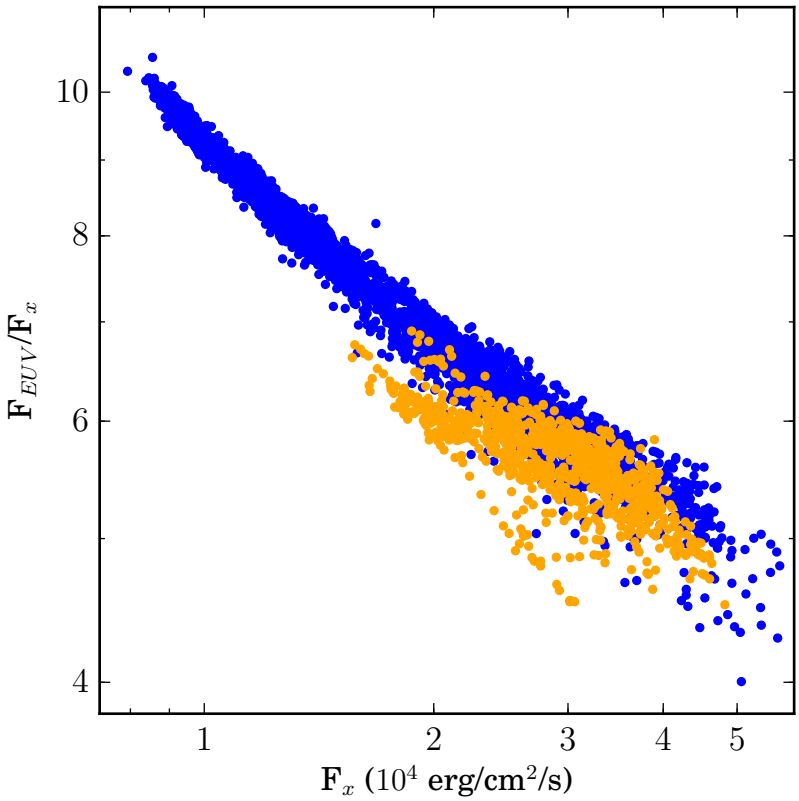


Figure 3.4: An updated version of fig. 2 of C15: the ratio of the EUV flux to X-ray flux plotted against the X-ray flux for a boundary energy of 0.1 keV. The C15 sample (30 May 2002 – 16 November 2013) is shown in blue, and data from 17 November 2013 to 21 July 2016 are shown in orange.

of boundary energies.

Given the choice of a single power law, each relation takes the form

$$\frac{F_{\rm EUV}}{F_{\rm X}} = \alpha \, (F_{\rm X})^{\gamma} \, , \tag{3.1}$$

where $F_{\rm EUV}$ is the flux in the extrapolated band, from 0.0136 keV up to the chosen boundary, and $F_{\rm X}$ is the flux in the observed band, from the boundary up to 2.4 keV. The exception to this is the 0.124 keV boundary which, as per convention, extends the observed band to 2.48 keV. As in C15, these fluxes are those at the stellar surface. The values of $\alpha$ and $\gamma$ are given in Table 3.4 for each of the five boundary choices. As highlighted in Table 3.4, each of the boundary energies were chosen to correspond to the observational band of an X-ray satellite, or a widely-used choice in the literature. I also include two further relations for going directly from the 0.2 – 2.4 keV band to the 0.0136 – 0.1 keV and 0.0136 – 0.124 keV EUV bands.

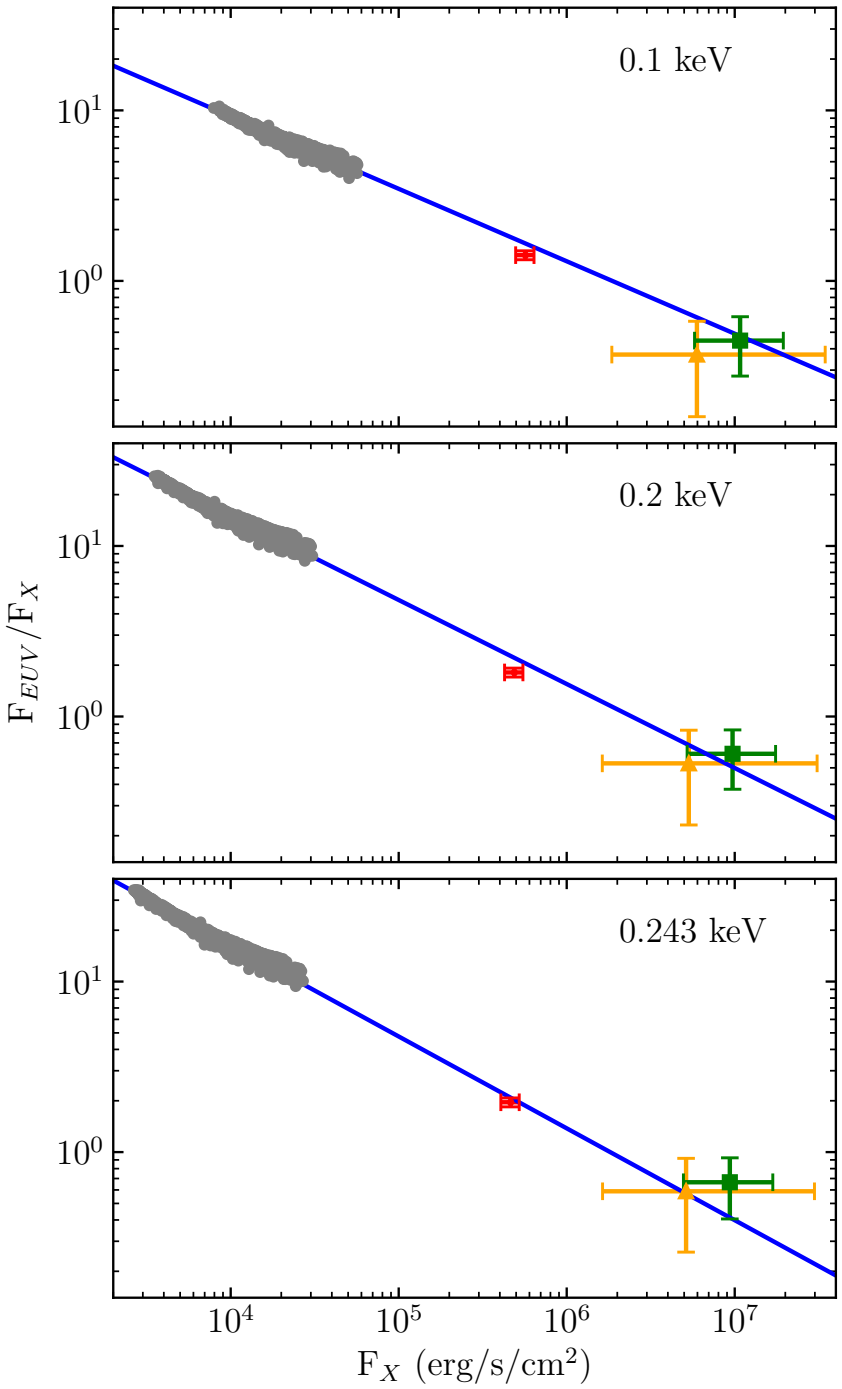


Figure 3.5: Solar *TIMED/SEE* data plotted for three of the new boundary energy choices: 0.1 keV/124 Å (top), 0.2 keV/62 Å (middle), and 0.243 keV/51 Å (bottom). Fluxes for the comparison stars are plotted as follows: $\epsilon$ Eri - red circle; AD Leo - orange triangle; AU Mic - green square.

Table 3.4: Best fitting power laws to be used in conjunction with equation 3.1 for each choice of boundary energy. See Sect. 3.4.4.

| # | X-ray range | | EUV range | | $\alpha$ | $\gamma$ | Relevant Satellite |
|---|---|---|---|---|---|---|---|
| | (keV) | (Å) | (keV) | (Å) | † | | |
| 1 | 0.100 – 2.400 | 5.17 – 124 | 0.0136 – 0.100 | 124 – 912 | 460 | -0.425 | *ROSAT* (PSPC) |
| 2 | 0.124 – 2.480 | 5.00 – 100 | 0.0136 – 0.124 | 100 – 912 | 650 | -0.450 | None, widely-used (5 – 100 Å) |
| 3 | 0.150 – 2.400 | 5.17 – 83 | 0.0136 – 0.150 | 83 – 912 | 880 | -0.467 | *XMM-Newton* (pn, lowest) |
| 4 | 0.200 – 2.400 | 5.17 – 62 | 0.0136 – 0.200 | 62 – 912 | 1400 | -0.493 | *XMM-Newton* (pn, this work), *XMM-Newton* (MOS), *Swift* (XRT) |
| 5 | 0.243 – 2.400 | 5.17 – 51 | 0.0136 – 0.243 | 51 – 912 | 2350 | -0.539 | *Chandra* (ACIS) |
| 6 | 0.200 – 2.400 | 5.17 – 62 | 0.0136 – 0.100 | 124 – 912 | 1520 | -0.509 | *XMM-Newton* (Obs. to ROSAT EUV) |
| 7 | 0.200 – 2.400 | 5.17 – 62 | 0.0136 – 0.124 | 100 – 912 | 1522 | -0.508 | *XMM-Newton* (Obs. to 5 – 100 Å band) |

† $\mathrm{erg\,s^{-1}\,cm^{-2}}$

Table 3.5: OM results for GJ 3470 and HD 149026.

| Filter | Central $\lambda$ (Å) | Flux $10^{-15}\,\mathrm{erg\,s^{-1}\,cm^{-2}\,Å^{-1}}$ | Mag. |
|---|---|---|---|
| | | *GJ 3470* | |
| U | 3440 | $3.66 \pm 0.07$ | 14.9 |
| UVW1 | 2910 | $0.49 \pm 0.24$ | 17.2 |
| UVM2 | 2310 | 1.2* | 16.4 |
| | | *HD 149026* | |
| UVM2 | 2310 | $0.10 \pm 0.02$ | 19.1 |
| UVW2 | 2120 | $0.30 \pm 0.04$ | 18.1 |

* Note that the UVM2 flux conversion introduces a factor of two error for M dwarf stars.

**Total XUV flux calculations**

Using my newly derived relations, I determine the full XUV flux at the stellar surface, at the distance of each planet, $F_{\mathrm{XUV},p}$, and at 1 au (see Table 3.3). For the zero eccentricity planets GJ 3470b and HD 149026b, I simply use the semi-major axis in Table 3.1. WASP-80b has a small upper limit on its eccentricity, so I again use the semi-major axis estimate. However, GJ 436, HAT-P-11, and HD 97658 all have non-zero eccentricities, and as such I use the time-averaged separation (see, for a discussion, Williams, 2003). Consequently, determined values of $F_{\mathrm{XUV},p}$ in these cases should also be considered time-averages. I find that HD 149026b, WASP-80b, and GJ 3470b are subject to the largest XUV irradiation. HAT-P-11b receives about half the XUV flux of HD 149026b, but still a few times more than GJ 436b and HD 97658b.

## 3.5 Optical Monitor results

Observations using the OM camera on *XMM-Newton* were taken concurrently with those of the EPIC X-ray detectors. Different observing strategies were employed for this instrument in the two separate proposals that comprised the full set of observations I describe. In both cases, however, I have taken advantage of the NUV capabilities of the OM.

### 3.5.1 GJ 3470 and HD 149026

For GJ 3470 and HD 149026, some of the ultraviolet filters were cycled through in turn during the observation period. In the case of GJ 3470, all ultraviolet filters

were employed except UVW2, that pushes furthest into the ultraviolet but is also the least sensitive. All ultraviolet filters were used for HD 149026, but the object was saturated in the U and UVW1 filters, leaving useful measurements only for UVW2 and the next bluest ultraviolet filter, UVM2.

For both objects, the measured count rates were converted into fluxes and magnitudes following the prescription of a SAS watchout page[4]. I adopted the conversions for M0V and G0V stars for GJ 3470 and HD 149026, respectively (cf. spectral types in Table 3.1). The calculated fluxes and magnitudes for each filter used for each object are summarised in Table 3.5.

### 3.5.2 Fast mode observations

The other four objects were observed in a single filter, and in fast mode, in order to probe ultraviolet variation in the source over the course of the observation. This opened up the possibility of detecting the transit in the NUV. In each case, the single filter choice was a trade off between wishing to push as far into the NUV as possible, while wanting to maintain a high enough (predicted) count rate that transit detection level precision might be possible. UVW1 was chosen for GJ 436 and WASP-80, while HD 97658 and HAT-P-11 were observed using the UVW2 filter.

The final light curves for GJ 436, HAT-P-11 and HD 97658 are shown in Fig. 3.6, and I conclude that none of these three observations detected the transit in NUV. The light curves were built by correcting the fast mode time series data from OMFCHAIN using the corresponding image mode extractions from OMICHAIN. The reasons for this were described in Section 2.4.

#### WASP-80

I identified a possible transit detection in the WASP-80 data. Again, I corrected the fast mode time series by the corresponding image mode extractions, as described in 2.4.

I modelled my time series using the TRANSIT code[5], a PYTHON implementation of the Mandel and Agol (2002) analytic transit model. To fit the model I used the MCMC sampler provided by the EMCEE package (Foreman-Mackey et al., 2013). I set Gaussian priors on the transit centre time, $a/R_*$, and the system inclination, $i$, according to the values and references in Tables 3.1 and 3.2. The prior for

[4]"How can I convert from OM count rates to fluxes", available at `https://www.cosmos.esa.int/web/xmm-newton/sas-watchout-uvflux`.

[5]Available as part of the RAINBOW package (`https://github.com/StuartLittlefair/rainbow`). Documentation can be found at `http://www.lpl.arizona.edu/~ianc/python/transit.html`.

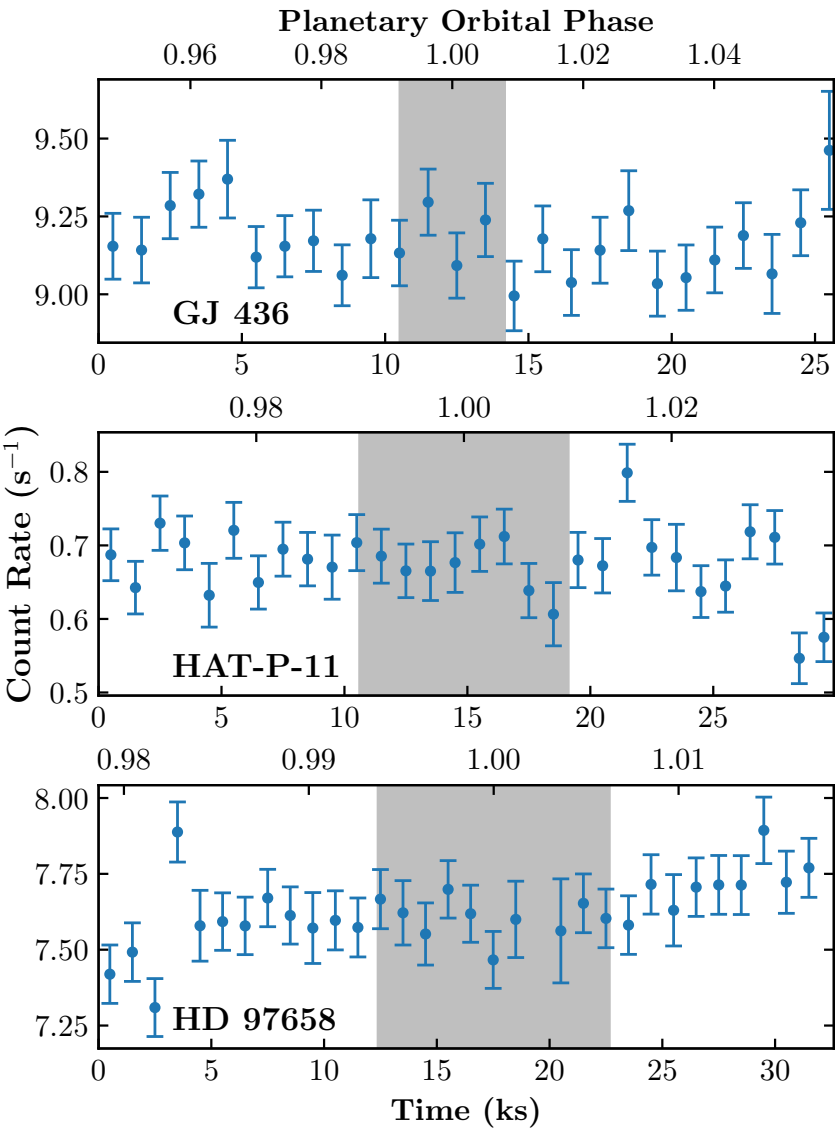


Figure 3.6: Optical Monitor light curves for GJ 436, HAT-P-11, and HD 97658, binned to 1000 s resolution. The areas shaded in grey are the planetary transits (1st to 4th contact) in visible light.

the transit centre at the epoch of my observations, $t_{\mathrm{Cen}}$, was calculated using the ephemeris of Mancini et al. (2014). $R_p/R_*$ and the out of transit count rate were allowed to vary freely with uniform priors. The latter was included to normalise the out of transit data to an intensity of unity.

I applied a quadratic limb darkening law (equation 1.3), with the coefficients fixed to those for the U band from Claret and Bloemen (2011), according to the stellar properties of WASP-80. Despite being taken with the UVW1 filter, the

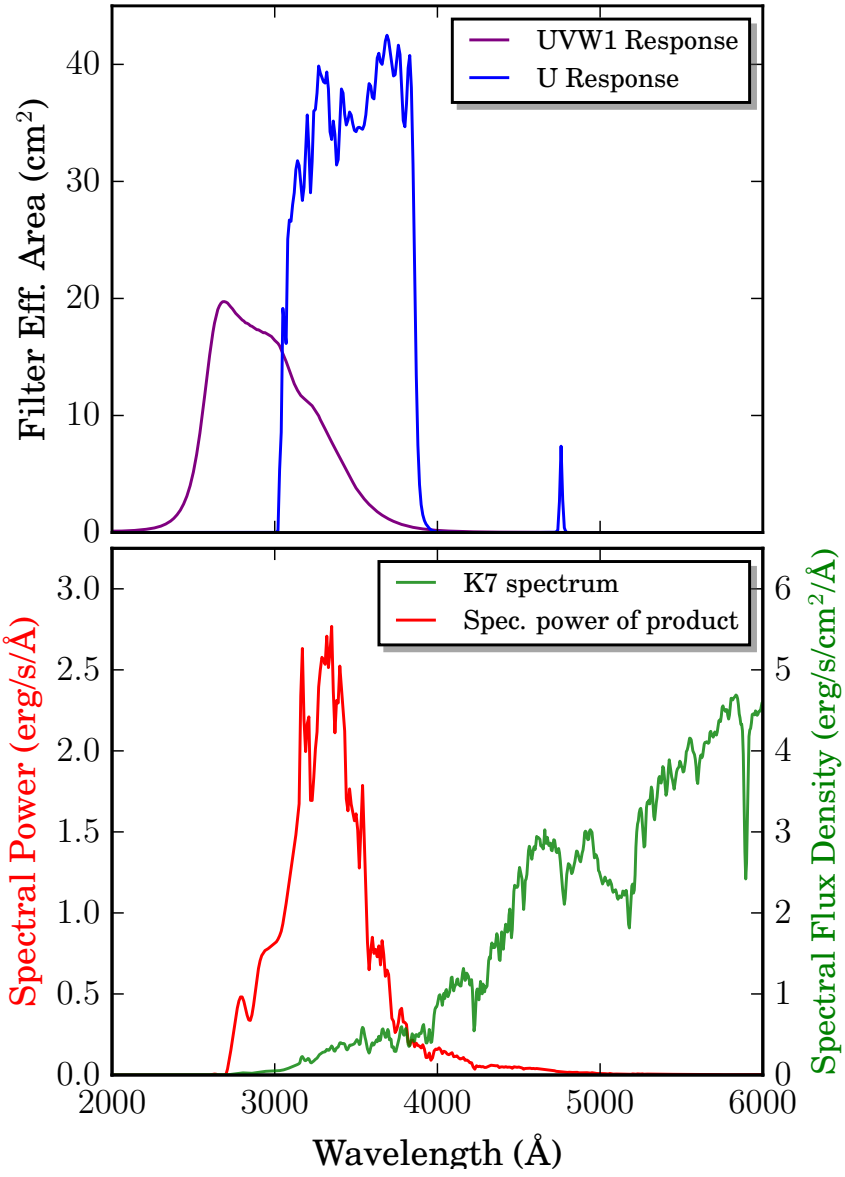


Figure 3.7: Top: Effective area of the UVW1 (purple) and U band filters on the OM camera as a function of wavelength. Bottom: Model spectrum for a K7V star, and the product of the UVW1 effective area and the K7V spectrum.

sampling of the late-K dwarf spectrum is weighted to the U band, due to the red tail of the filter. This is shown in Fig. 3.7 which plots the effective area of the OM UVW1 and U band filters, a model spectrum for a K7 dwarf star (Pickles, 1998), and the product of the UVW1 response with the model spectrum.

Fig. 3.8 displays the WASP-80 OM light curve with the best fit model and the 1-$\sigma$ credibility region, with the data binned to a lower resolution to aid the eye. The

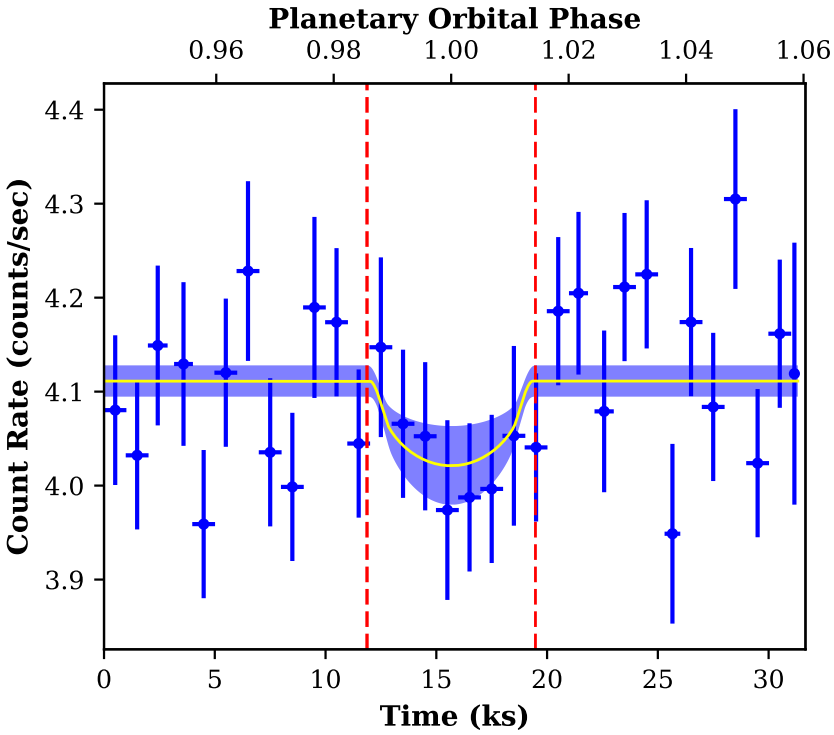


Figure 3.8: WASP-80 data binned to 1000 s bins. Overlaid is the best fit model (yellow) along with the 1-$\sigma$ confidence region (blue shaded region). The dotted red lines correspond to the first and fourth contact of the transit, as calculated from the visible light ephemeris (Mancini et al., 2014).

resulting best fit parameters for the model are given in Table 3.6. The best fitting depth is shallower than previous optical measurements, but is consistent to within 1.6-$\sigma$. My best fit $R_p/R_*$ shows some weak correlation with the out of transit count rate. The associated corner plot, made using the corner.py code (Foreman-Mackey, 2016), is shown in Fig. 3.9.

## 3.6 Discussion

### 3.6.1 X-ray Fluxes

In Section 1.3.5, I described the links that have been explored between X-ray emission and rotation period. I compare my measured fluxes to the Wright et al. (2011), hereafter W11, relations, linking $L_{\rm X}/L_{\rm bol}$ with Rossby number, $R_{\rm o}$. The larger sample of M stars considered by W11 compared to, for example, Pizzolato et al. (2003) is useful for my study, which contains two M stars and a third on the K-M type

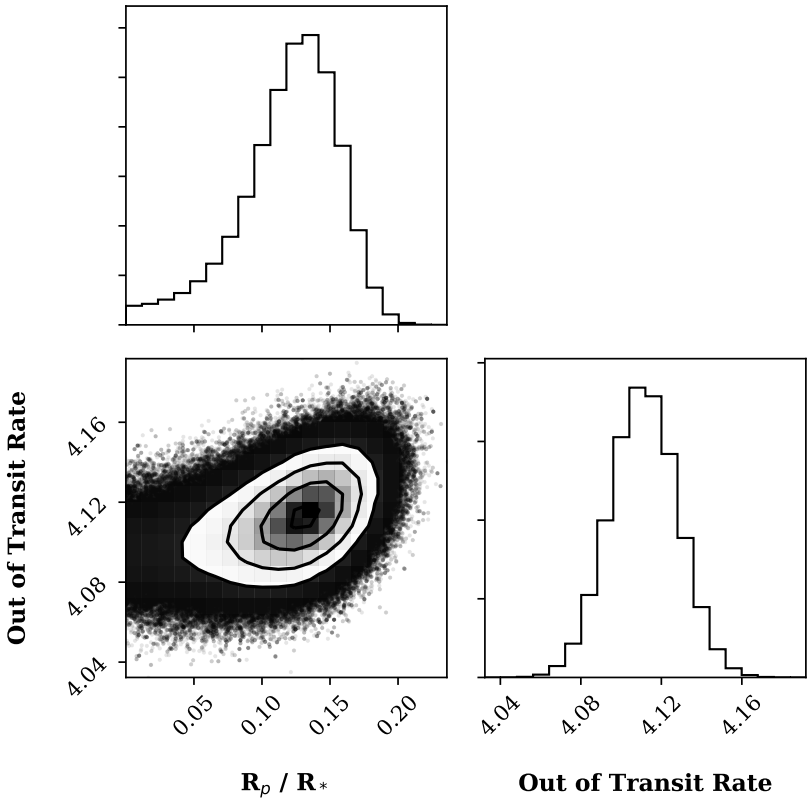


Figure 3.9: Corner plot for the WASP-80 fit showing the correlation of the out of transit count rate with $R_p/R_*$. The parameters bound by a Gaussian prior are omitted.

Table 3.6: WASP-80 near ultraviolet MCMC fit priors and results.

| Parameter | Value | Reference |
|---|---|---|
| | *Gaussian priors* | |
| $t_{\rm Cen}$ (BJD) | 2457156.21885(31) | Mancini et al. (2014) |
| $a/R_*$ | $12.989 \pm 0.029$ | Triaud et al. (2013) |
| $i$ | $89.92 \pm 0.10$ | Triaud et al. (2013) |
| | *Fixed values* | |
| u1 | 0.9646 | Claret and Bloemen (2011) |
| u2 | $-0.1698$ | Claret and Bloemen (2011) |
| | *Free, fitted parameter* | |
| $R_p/R_*$ | $0.125^{+0.029}_{-0.039}$ | *This work* |

boundary.

The X-ray emission considered in W11 is for the 0.1 – 2.4 keV ROSAT band. Examining the solar TIMED/SEE data in a similar way to the method in Section 3.4.4 with the two bands defined as 0.1 – 0.2 and 0.2 – 2.4 keV showed an approximate 1:1 ratio of flux in the two bands. I therefore doubled the flux in the observed 0.2 – 2.4 keV to estimate that in the ROSAT band. However, I added 50 per cent uncertainties in quadrature with the observed flux errors, due to the scatter of the comparison stars to the TIMED/SEE data. $L_{\rm bol}$ was evaluated using the Stefan-Boltzmann law. I note that the subgiant nature of HD 149026 means that the W11 relations, derived for main sequence stars, may not be directly applicable to the star.

Fig. 3.10 depicts my measured $L_{\rm X}/L_{\rm bol}$ against that expected from W11. W11 found a best-fitting exponent of the power law in the unsaturated regime of -2.7, a value that was inconsistent with the canonical -2 at high significance. My sample seems to point to a shallower slope, even shallower than the canonical value - a simple least squares fit to my six measurements yields a slope of -1.13. Booth et al. (2017) recently found a steeper age-activity slope for old, cool stars to previous studies. They suggested that in the context of the findings of van Saders et al. (2016), which found evidence for weaker magnetic breaking in field stars older than 1 Gyr, this could point to a steepening of the rotation-activity relationship, in contrast to my measurements. Despite the apparent shallower trend in Fig. 3.10, my measurements are in line with the scatter in the W11 sample itself, as can be seen in Fig. 3.11. The significant scatter in these activity relations underlines the need for measurements of X-ray fluxes for individual exoplanet hosts.

**GJ 436**

I compare my measured fluxes to previous studies. A summary of these comparisons can be found in Table 3.7.

GJ 436 previously had X-ray fluxes measured by Sanz-Forcada et al. (2011) and Ehrenreich et al. (2015) (hereafter E15) using the *XMM-Newton* dataset from 2008 (Obs ID: 0556560101; PI: Wheatley). The two analyses produced very different results, with the former finding the flux at Earth to be $7.3 \times 10^{-15}$ erg s$^{-1}$ cm$^{-2}$ for the 0.124 – 2.48 keV band, almost five times smaller than the $4.6 \times 10^{-14}$ erg s$^{-1}$ cm$^{-2}$ found by the latter analysis in the same energy range. I note that Louden et al. (2017a) found a similar discrepancy between their analysis and that of Sanz-Forcada et al. (2011) for an observation of HD 209458. I reanalysed the previous *XMM-Newton* dataset for GJ 436 for a more direct comparison of the fluxes, obtaining

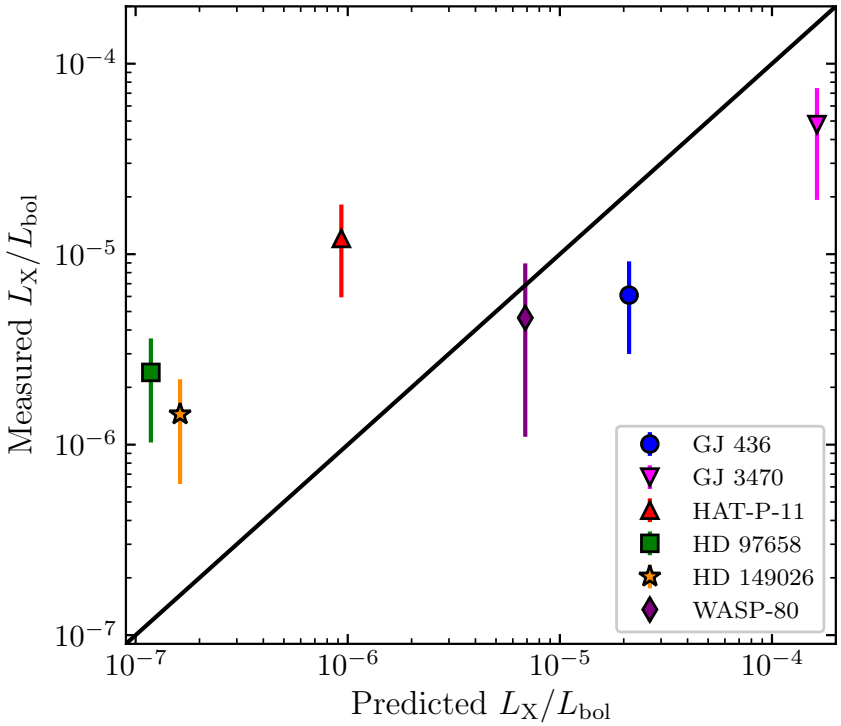


Figure 3.10: Comparison of the measured $L_X/L_{bol}$ to that expected from the relations of W11.

a flux of $\left(2.26^{+0.11}_{-0.38}\right) \times 10^{-14}\,\mathrm{erg\,s^{-1}\,cm^{-2}}$ in the 0.2 – 2.4 keV band. I therefore conclude that there was a modestly increased X-ray output at the time of the 2015 observations. GJ 436 was one of the stars whose light curve was seen to vary at the 3-$\sigma$ level in section 3.4.1. The difference in flux between the 2008 and 2015 datasets points to significant variation also on longer timescales.

E15 also found their analysis of the 2008 *XMM-Newton* observations to agree with their Chandra data in the overlapping 0.243 – 2.0 keV energy range: $1.84 \times 10^{-14}\,\mathrm{erg\,s^{-1}\,cm^{-2}}$ versus the $1.97 \times 10^{-14}\,\mathrm{erg\,s^{-1}\,cm^{-2}}$ obtained when averaging across the four Chandra datasets. I measure $\left(2.35^{+0.16}_{-0.26}\right) \times 10^{-14}\,\mathrm{erg\,s^{-1}\,cm^{-2}}$ in this slightly more restrictive band, again showing a modest increase on the 2008 *XMM-Newton* data, but also compared to the averaged 2013-14 *Chandra* data. Furthermore, I compared the emission measures of the 2015 data to the other *XMM-Newton* and *Chandra* observations using the method of E15 (The results for the other five datasets are plotted in their extended data fig. 8). For the most direct comparison, I fixed the temperatures and abundances to that found in E15 (i.e. *not* those in Table 3.3). With this method, I obtain emission measures of $9.7^{+1.3}_{-1.2}$ and $2.10^{+0.23}_{-0.22}\,\mathrm{cm^{-3}}$ for the low and high temperature components, respectively. These

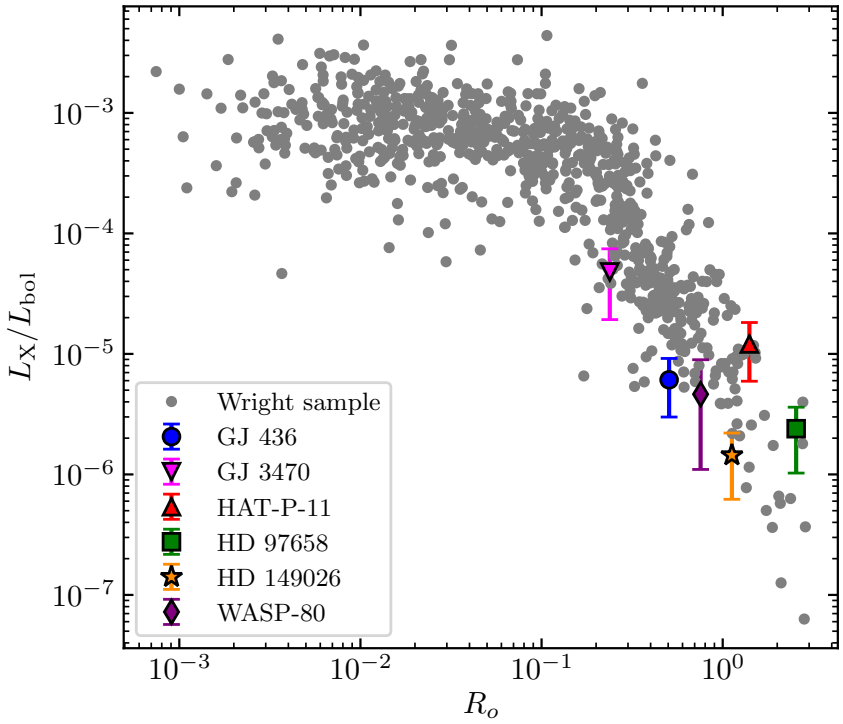


Figure 3.11: Replotting of fig. 1 of Wright and Drake (2016), itself an update of the W11 sample, with points added from my own sample.

results concur with the conclusion of E15 that there is more variation in the higher temperature component than in the soft.

I note that GJ 436 was also observed in X-rays during the *ROSAT* All-Sky Survey. Hünsch et al. (1999) reported an X-ray flux in the 0.1 – 2.4 keV band of $1.2 \times 10^{-13}$ erg s$^{-1}$ cm$^{-2}$, which is much higher than all of the other datasets. However, the revised PSPC catalog by Boller et al. (2016) suggests the GJ 436 detection is not real and should be treated as an upper limit.

### HAT-P-11

Morris et al. (2017) used Ca II H & K observations to show HAT-P-11 has an unexpectedly active chromosphere for a star of its type. My work suggests this extends to the corona too, with its measured $L_X/L_{bol}$ an order of magnitude larger than that expected from W11 (Fig. 3.10). Morris et al. (2017) also presented evidence for an activity cycle for HAT-P-11 in excess of 10 years using observations of chromospheric emission, with the star's S-index spending a greater proportion of its activity cycle close to maximum compared to the Sun. Despite this, my *XMM-Newton* observations were taken about halfway between activity maximum and minimum, and

Table 3.7: Comparison of GJ 436 and WASP-80 X-ray fluxes with previous studies, grouped by energy range.

| Dataset | Reference | Energy Range (keV) | Flux ($a$) |
|---|---|---|---|
| | *GJ 436* | | |
| 2008, *XMM* | SF11 | 0.124 – 2.48 | 0.73 |
| 2008, *XMM* | E15 | 0.124 – 2.48 | 4.6 |
| 2008, *XMM* | This work | 0.2 – 2.4 | $2.26^{+0.11}_{-0.38}$ |
| 2015, *XMM* | This work | 0.2 – 2.4 | $2.91^{+0.16}_{-0.27}$ |
| 2008, *XMM* | E15 | 0.243 – 2.0 | 1.84 |
| 2013-14, *Chandra* | E15 | 0.243 – 2.0 | 1.97 |
| 2015, *XMM* | This work | 0.243 – 2.0 | $2.35^{+0.16}_{-0.26}$ |
| *ROSAT* All-Sky Survey | H99, B16 | 0.1 – 2.4 | $< 12$ |
| | *WASP-80* | | |
| 2014, *XMM* | S15 | 0.124 – 2.48 | $1.6^{+0.1}_{-0.2}$ |
| 2014, *XMM* | This work | 0.2 – 2.4 | $1.67^{+0.12}_{0.26}$ |
| 2015, *XMM* | This work | 0.2 – 2.4 | $1.78^{+0.11}_{0.16}$ |

$a$ $10^{-14}\,\mathrm{erg\,s^{-1}\,cm^{-2}}$ (at Earth, unabsorbed)
References are: SF11: Sanz-Forcada et al. (2011); E15: Ehrenreich et al. (2015); H99: Hünsch et al. (1999); S15: Salz et al. (2015a); B16: Boller et al. (2016).

$L_\mathrm{X}/L_\mathrm{bol}$ was much larger than the W11 prediction even though the star was not close to its maximum activity level.

**WASP-80**

WASP-80 has had a previous *XMM-Newton* dataset from 2014 (Obs ID: 0744940101; PI: Salz) analysed by Salz et al. (2015a). They reported a flux at Earth of $(1.6^{+0.1}_{-0.2}) \times 10^{-14}\,\mathrm{erg\,s^{-1}\,cm^{-2}}$, in the 0.124 – 2.48 keV band. As for GJ 436, I repeated the analysis of this older dataset using the same procedure as for the new observations for a more direct comparison. The fluxes can be compared in Table 3.7. I find a flux at Earth in the slightly more restrictive 0.2 – 2.4 keV band of $(1.67^{+0.12}_{-0.26}) \times 10^{-14}\,\mathrm{erg\,s^{-1}\,cm^{-2}}$. This result is consistent with my observations at the newer epoch within the uncertainties.

### 3.6.2 EUV estimation

In section 3.4.4, I derived new empirical relations for reconstructing the EUV emission of stars from their observed X-rays, with the results presented in Table 3.3. I now draw comparisons to past applications of other methods.

For GJ 436, E15 obtained estimates of the EUV at 1 au from both the C15 X-ray and Linsky et al. (2014) Ly $\alpha$ methods, and found them to be remarkably similar. Adjusting for the new distance estimate from *Gaia*, these were 0.92 and 0.98 erg s$^{-1}$ cm$^{-2}$, respectively. In order to procure a directly comparable flux from my own measurements, I used equation 3.1 (boundary energy choice #7) from Table 3.4. This was applied to my flux measurement from the same 2008 dataset analysed by E15 (section 3.6.1). I determine an EUV flux at 1 au of $0.86^{+0.06}_{-0.17}$ erg s$^{-1}$ cm$^{-2}$, in satisfactory agreement with the values found by E15. The corresponding EUV flux value for the new 2015 dataset is $0.98^{+0.08}_{-0.12}$ erg s$^{-1}$ cm$^{-2}$.

Bourrier et al. (2016) also estimated the EUV flux using the Linsky et al. (2014) method. They determine EUV fluxes of 0.88 and 0.86 erg s$^{-1}$ cm$^{-2}$ at their two, independent epochs, in good agreement with my results from X-rays.

The MUSCLES Treasury Survey has combined observations from multiple passbands from X-ray to mid-IR to study the intrinsic spectral properties of nearby low-mass planet-hosting stars (France et al., 2016). Youngblood et al. (2016) reconstructed the EUV flux of GJ 436 in the 0.0136 – 0.1 keV band with the Linsky et al. (2014) Ly $\alpha$ method, obtaining 0.83 erg s$^{-1}$ cm$^{-2}$ at 1 au. Their results are therefore also consistent with extrapolation from the X-ray band.

The data presented here for HD 97658 (Table 3.3) were previously investigated by Bourrier et al. (2017a). Unlike here, they first extrapolated to the ROSAT band, and then used C15 to extrapolate to the EUV. They also estimate the EUV from multiple epochs of *HST* Ly $\alpha$ observations, applying the relations of Linsky et al. (2014). The results from the two methods were compatible. My direct extrapolation to the EUV from the observed X-rays obtains an XUV flux at the planet that is marginally smaller, but consistent within the uncertainties to their best estimate. The agreement with EUV estimates from Ly $\alpha$ supports the accuracy of the two methods of reconstructing the EUV emission.

### 3.6.3 Mass loss rates

I present estimated energy-limited mass loss rates for all six planets in Table 3.8, applying equation 1.9. For the value of the efficiency, $\eta$, I use three different assumptions, as discussed in Section 1.2.3, to estimate the mass loss rates corresponding to

Table 3.8: Current mass loss rate and total lifetime mass loss estimates of the six planets in my sample for different assumed sets of $\eta$ and $\beta$. The first listed $\eta$ and $\beta$ for each planet are taken from Salz et al. (2016a); the second is a canonical value of $\eta = 0.15$ and $\beta = 1$; the third provides a lower limit on the mass loss rates of these planets, motivated by Ly $\alpha$ observations.

| System | $\eta$ | $\beta$ | $\log \dot{M}_{\rm En}$ ($\rm g\,s^{-1}$) | Lifetime Loss % Const.* | J12† |
|---|---|---|---|---|---|
| | 0.275 | 1.48 | 9.8 | 0.8 | 4.3 |
| GJ 436 | 0.15 | 1 | 9.2 | 0.2 | 1.0 |
| | >0.01 | 1 | >8.0 | >0.01 | >0.07 |
| | 0.135 | 1.77 | 10.7 | 4.3 | 9.3 |
| GJ 3470 | 0.15 | 1 | 10.2 | 1.5 | 3.5 |
| | >0.01 | 1 | >9.0 | >0.1 | >0.2 |
| | 0.229 | 1.61 | 10.4 | 2.3 | 8.8 |
| HAT-P-11 | 0.15 | 1 | 9.8 | 0.6 | 2.4 |
| | >0.01 | 1 | >8.6 | >0.04 | >0.2 |
| | 0.288 | 1.75 | 9.4 | 1.7 | 3.9 |
| HD 97658 | 0.15 | 1 | 8.6 | 0.3 | 0.7 |
| | >0.01 | 1 | >7.5 | >0.02 | >0.05 |
| | 0.093 | 1.26 | 10.0 | 0.05 | 0.7 |
| HD 149026 | 0.15 | 1 | 10.0 | 0.05 | 0.7 |
| | >0.01 | 1 | >8.8 | >0.003 | >0.05 |
| | 0.100 | 1.24 | 10.3 | 0.004 | 0.06 |
| WASP-80 | 0.15 | 1 | 10.3 | 0.004 | 0.05 |
| | >0.01 | 1 | >9.2 | >0.0004 | >0.004 |

* Constant lifetime XUV irradiation rate, at the current level.

† Lifetime XUV irradiation estimated by the relations of Jackson et al. (2012).

Table 3.9: Comparison of current mass loss rate estimates for the four smallest planets in my sample using the Kubyshkina et al. (2018a) and energy-limited methods. I used the $\beta$ value reported as an output parameter by the Kubyshkina et al. (2018a) method as an input to the energy-limited calculation for a direct comparison.

| System | $\eta$ | $\log \dot{M}_{\rm Kuby}$ ($\rm g\,s^{-1}$) | $\beta$ | $\log \dot{M}_{\rm En}$ ($\rm g\,s^{-1}$) |
|---|---|---|---|---|
| GJ 436 | 0.15 | 8.9 | 1.15 | 9.3 |
| GJ 3470 | 0.15 | 10.3 | 1.27 | 10.4 |
| HAT-P-11 | 0.15 | 10.2 | 1.18 | 9.9 |
| HD 97658 | 0.15 | 9.1 | 1.48 | 9.0 |

my observed XUV fluxes. The first uses the results of Salz et al. (2015a), which not only estimated $\eta$ values for all of the planets in my sample, but $\beta$ values too. These calculations imply relatively high mass loss efficiencies, especially for lower mass planets (See, for instance, Table 3.8). I also include a more canonical choice of 0.15 and 1 for $\eta$ and $\beta$, respectively. These were the values adopted by Salz et al. (2015a), allowing direct comparison of my predicted mass loss rates with those systems. My third assumption of 1 per cent efficiency is adopted as a lower limit to the likely mass loss efficiency, and hence mass loss rates. This is motivated by the observational constraints discussed in Section 1.2.3, from contemporaneous measurements of the XUV irradiation and resulting mass loss detected through Ly $\alpha$ absorption in individual systems (e.g. Ehrenreich and Désert, 2011). For GJ 436b an efficiency as low as 0.5% has been shown to be sufficient to explain the observed strong Ly $\alpha$ absorption, if the material is completely neutral as it leaves the planet (Ehrenreich et al., 2015; Bourrier et al., 2016). For the hot Jupiter HD 189733b a similarly low lower limit of 1% is also sufficient to explain the observed absorption by H I, although a somewhat higher efficiency is likely to be needed to account for the unobserved ionised hydgrogen (Lecavelier des Etangs et al., 2012). For the super-Earth HD 97658b, upper limits on Ly $\alpha$ absorption from Bourrier et al. (2017a) suggest a mass loss efficiency that could be substantially lower than that predicted by Salz et al. (2016a), depending on the ionisation fraction of material leaving the planet. Since this fraction is poorly known, the assumed value of 1% efficiency in Table 3.8 provides a lower limit on the mass loss rates of the planets. The true efficiency is likely to be higher, and indeed a much higher mass loss efficiency is also required for HD 209458b (Louden et al., 2017a).

Following Salz et al. (2016a), the mass loss rate estimates for GJ 436b and HD 97658b exceed the values derived by modelling Ly $\alpha$ observations with the EVaporating Exoplanets (EVE) code (Bourrier et al., 2016, 2017a). The resulting mass loss estimates for the other choices of $\eta$ and $\beta$ for these planets are both lower and closer to their respective estimates from Ly $\alpha$, although the $\eta = 0.01$ results perhaps provide a slight underestimation.

Additionally, I also calculate mass loss estimates for the four smallest planets with an interpolation across the hydrodynamic models described by Kubyshkina et al. (2018a). The interpolation tool also reports an estimate of $\beta$ as an output parameter. It is important to note that the interpolator tool does not take an eccentricity input, and therefore only considers circular orbits; this is most relevant for GJ 436b and HAT-P-11b, which have $e = 0.153$ and 0.265, respectively. I then recalculated the energy-limited mass loss with the same assumptions (the simulations

also employed the canonical $\eta = 0.15$), for a direct comparison of the methods. I give the results in Table 3.9. I find that the Kubyshkina et al. (2018a) models suggest that the energy-limited method overestimates the mass loss from GJ 436b, as is also suggested when comparing to the EVE code. However, for HAT-P-11b and HD 97658b, the interpolator favours mass loss rates more in line with the Salz et al. (2016a) $\eta$ and $\beta$ values, as opposed to the canonical choice.

As discussed by Owen and Alvarez (2016) and in Section 1.2.3, EUV-driven evaporation of close-in planets can be in one of three regimes: energy-limited, recombination-limited, and photon-limited. Their numerical calculations show that the transition between the three regimes does not occur at a single point, rather over a few orders of magnitude. However, their fig. 1 allows us to determine that GJ 3470b, HAT-P-11b, and HD 97658b are likely in the region of energy-limited escape. HD 149026b and WASP-80b lie close to the transition between the energy-limited and recombination-limited regions. Note that energy conservation always applies in the planetary thermospheres, but in the case of recombination-limited escape, a larger fraction of the absorbed radiative energy is re-emitted by recombination processes, so that less energy is available to drive the planetary wind. Therefore, the recombination-limited regime exhibits lower evaporation efficiencies than the energy-limited regime. In agreement with their intermediate location close to the recombination regime, the estimates of $\eta$ for HD 149026b and WASP-80b from Salz et al. (2016a) are smaller than for the other four planets.

#### Total lifetime mass loss

Jackson et al. (2012) produced a set of relations characterising the evolution of the X-ray emission with stellar age (see Section 1.3.5). As a result, they were able to further derive relations that can be used to estimate the total X-ray emission of a star over its lifetime to date. In turn, this could be used to estimate the total mass lost from an exoplanet. This would be particularly useful to apply to close-in super-Earth and mini-Neptune-sized planets, to investigate if they could have suffered substantial or total loss of a gaseous envelope. For middle-aged systems, if this happened, it is likely to have occurred much earlier in their life when the coronal emission of their host was much greater.

I apply equation 8 of Jackson et al. (2012), together with the ages from Table 3.1, in order to estimate the lifetime X-ray output from each of the six host stars in the sample. The results are given in Table 3.8. Additionally, I consider the corresponding EUV by applying relation #1 (Table 3.4) to the estimated X-ray output at 1000 yr steps and integrating over the resulting lifetime evolution. I then

scale the results to the average orbital separation of the system's planet, and apply equation 1.9 to estimate the total mass lost over the planet's lifetime. Estimates for all three sets of choices of $\eta$ and $\beta$ are included. Also in Table 3.8 are estimates for the total percentage mass loss over the lifetime of each planet, assuming a constant XUV irradiation rate, at the current level. While I assume a constant radius across the planet's lifetime, if substantial evolution has occurred, the use of a constant radius could mask a greater total lifetime mass loss than my estimates (Howe and Burrows, 2015).

The lifetime loss results are sensitive to the assumed $\eta$ and $\beta$, as well as discrepancies between the theoretically expected $L_{\rm X}/L_{\rm bol}$ and that observed. Additionally, HD 149026's subgiant nature will affect its estimate. However, more qualitatively, the four smallest planets studied are expected to have lost a much greater percentage of their mass over their lifetime than the other two much larger planets in the sample.

Applying equation 1.9 to a planet of Neptune mass and radius with the same irradiation history as HD 97658b, I find such a planet would have lost $\sim$3.5 per cent of its mass over its lifetime. This is in contrast to closer-in planets like CoRoT-7b, which is suspected to have suffered a near-complete loss of its gaseous envelope due to intense irradiation (Jackson and Jeffries, 2010).

### 3.6.4 Ly $\alpha$ estimation

As discussed in Section 1.2.1, Ly $\alpha$ observations of highly irradiated exoplanets is an important tool to determine the extent of atmospheric evaporation. Ly $\alpha$ transits have proven successful in detecting evaporating atmospheres. Additionally, Ly $\alpha$ observations also provide a separate regime from which EUV reconstruction can be performed.

For each of the systems in my sample, I have estimated the Ly $\alpha$ output in two steps. Firstly, I used equation 3.1 (boundary relation #7) to calculate the EUV flux in the 0.0136 – 0.124 keV band. Then, I applied the relations of Linsky et al. (2014), linking Ly $\alpha$ and EUV fluxes at 1 au. By plotting the curves given by the relations, I approximated the Ly $\alpha$ flux according to the position of each systems' EUV estimation. Table 3.3 gives Ly $\alpha$ luminosity, $L_{\rm Ly\alpha}$, estimates for my six systems, and the corresponding flux at Earth, $F_{\rm Ly\alpha,\oplus}$. For GJ 436 and HD 97658, I additionally include literature values. While the results from Bourrier et al. (2016) and Bourrier et al. (2017a) for GJ 436 are remarkably consistent with my results, there is less agreement with those of Youngblood et al. (2016) for HD 97658, although their value is poorly constrained with larger errors.

My analysis suggests that the HAT-P-11 system is the best candidate for Ly $\alpha$ observations, of those that have not previously been studied in this way. I predict the star to have the largest apparent Ly $\alpha$ brightness of the three, while I estimate the planet's mass loss rate to be larger than that of GJ 436b by about a factor of three. This is largely because the observed X-ray flux is significantly higher than expected. While my $F_{\mathrm{Ly}\alpha,\oplus}$ prediction does account for interstellar absorption, the Ly $\alpha$ snapshot of WASP-80 by Salz (2015) shows that large transits could even be detected for one of the most distant systems in this sample. Hence, all of the studied systems are likely promising candidates for systematic Ly $\alpha$ transit observations, but HAT-P-11 appears to be the best suited.

### 3.6.5 WASP-80 NUV transit

The OM light curve of WASP-80 allowed us to detect the planetary transit in the near ultraviolet. My best fit $R_p/R_*$ of $0.125^{+0.029}_{-0.039}$ corresponds to a NUV transit depth of $1.6^{+0.5}_{-0.7}$ per cent, and a planet radius of $0.69^{+0.16}_{-0.22}\,\mathrm{R_J}$. In comparison, the discovery paper reported a visible light $R_p/R_*$ of $0.17126^{+0.00031}_{-0.00026}$ (Triaud et al., 2013), while Mancini et al. (2014) measured $0.17058 \pm 0.00057$, and Kirk et al. (2018) found $0.17113 \pm 0.00138$. The latter study also found little evidence of large variation in the radius of WASP-80 b's across the visible and near infrared. My results are consistent, though the best fit transit is shallower by 1.59-$\sigma$. This is perhaps a hint that the NUV transit is shallower, consistent with the single U band transit observed by Turner et al. (2017). It would be desirable to follow up with more observations in the NUV that could constrain the depth to a higher precision, particularly given the size of the uncertainties on my fitted depth.

A shallower NUV transit would not be without precedent. With ground-based observations, Turner et al. (2016) found smaller NUV (U band) transit depths for hot Jupiters WASP-1b and WASP-36b with significance 3.6-$\sigma$ and 2.6-$\sigma$, respectively. Physically, a shallower transit in NUV could result from the planet passing in front of dimmer regions of the star. The contrast between the areas of the stellar disc the planet crosses and brighter regions elsewhere would also need to be higher in the NUV than visible light for this explanation to be feasible. Unocculted faculae could possibly produce this effect. Spectral modelling of faculae have shown the contrast in intensity between the facula and elsewhere on the stellar disc is greater in the UV than in the visible and IR, as well as for regions closer to the limb of the disc (e.g. Unruh et al., 1999; Norris et al., 2017). Indeed, stellar activity in the transit light curve of WASP-52 b was interpreted by Kirk et al. (2016) as occulted faculae. WASP-80 b has a much lower impact parameter than WASP-52 b,

and so spends less time crossing regions close to the limb, making it more likely that high-contrast faculae close to the limb would go unocculted.

## 3.7 Conclusions

I have analysed *XMM-Newton* data to investigate the XUV environments of six nearby transiting planets that orbit in close proximity to their host star, ranging in size from Jupiter-size to super-Earth. For each star, I directly measure the flux in the 0.2 – 2.4 keV band by fitting a two temperature APEC model. I use a similar approach to Chadney et al. (2015) in using Solar *TIMED/SEE* data to derive a new set of relations for reconstructing the unobservable EUV emission. I use different boundary choices between the EUV and X-ray bands based on the current generation of X-ray instruments. The resulting estimates for the full XUV range of GJ 436 and HD 97658 are in good agreement with past reconstructions from X-ray and Ly $\alpha$.

With the contemporaneous measurements from the OM in the near ultraviolet, I searched for transits in the fast mode data. I successfully uncovered a transit from OM data for the first time. My resulting fit showed a best fit transit depth for WASP-80b consistent with previous studies in visible light and in the near infrared within the uncertainties. However, there is a hint that the depth could be shallower, and so I recommend further observations in the NUV to investigate more precisely the possibility of a smaller transit depth at these wavelengths.

I investigated how my measured X-ray emission, and its ratio to the corresponding bolometric luminosity, compared to that expected from the known rotation rate and estimated Rossby number of each star. I see a possible trend to slower rotating stars being brighter than expected. The scatter in these results highlights the importance of investigating systems of interest with dedicated observations.

The mass loss rate for each planet was estimated. My mass loss rates for GJ 436b and HD 97658b calculated using the efficiency and absorption radii determined by Salz et al. (2016a) appear inconsistent with analysis of Ly $\alpha$ observations. Based on my Ly $\alpha$ emission estimates, all of the stars in my sample with no prior observations at those wavelengths would be good candidates to explore. However, HAT-P-11b is best suited of those without previous extensive investigation due to their proximity to the Solar System. It has a larger predicted mass loss rate than GJ 436b or HD 97658b. Finally, I determined that the super-Earth and three Neptunes among the sample are likely to have lost a larger mass fraction over their lifetimes than the other two larger planets.

# Chapter 4

# $\pi$ Men c and HD 219134b & c: XUV irradiation either side of the photoevaporation valley

## 4.1 Introduction

The photoevaporation valley was introduced in Section 1.2.4 as one of the main possible effects of atmospheric mass loss on the observed exoplanet population. Two populations of planets are seen in radius-period space to reside either side of a region with few or no planets (Fulton et al., 2017; Van Eylen et al., 2018). The population below the valley is thought to consist of planets stripped of the H/He envelopes they formed with down to bare cores, while immediately above the valley are planets with small ($\sim$1 % by mass) H/He envelopes that are resistant to any further substantial stripping (Owen and Wu, 2017). Exploring the XUV conditions of planets in these two populations either side of the valley is therefore an effective way of probing not just the evaporative histories and resulting atmospheric evolution of small planets, but also test the photoevaporative explanation of the valley.

Searches for evaporation signatures from smaller planets have so far proved inconclusive. HD 97658b is a planet above the evaporation valley, slightly bigger than $\pi$ Men c, and with a slightly wider orbit. Observations suggested a lack of evaporating hydrogen surrounding the planet (Bourrier et al., 2017a). 55 Cnc e is another small, nearby planet, although this time below the evaporation valley and thought to be rocky. It also showed a non-detection at Ly $\alpha$ (Ehrenreich et al., 2012). Ly $\alpha$ observations of the much smaller Kepler-444 planets show variations that might be associated with hydrogen escape from its rocky planets (Bourrier et al., 2017c).

The brightness and proximity of the $\pi$ Men host star, together with the likelihood of $\pi$ Men c retaining a substantial atmosphere, presents a superb new opportunity to search for mass loss from a super-Earth and hence determine the composition of its atmosphere.

In this Chapter, I investigate the $\pi$ Men (HD 39091) and HD 219134 systems. The former hosts the first confirmed discovery from the NASA Transiting Exoplanet Survey Satellite (*TESS*; Ricker et al., 2015) mission: a $2\,R_\oplus$ planet around a $V$=5.7, G0V star residing just above the photoevaporation valley (Huang et al., 2018; Gandolfi et al., 2018). HD 219134 hosts the closest currently known transiting planets to Earth. The two closest-in planets (b & c) transit, while evidence from radial velocity (RV) investigations point to four, likely non-transiting planets at greater separation. It is the two transiting planets that I am most interested in, as both lie just below the evaporation valley with radii of about $1.5\,R_\oplus$.

### 4.1.1 The $\pi$ Men system

$\pi$ Men was already known to host a long-period, non-transiting, eccentric companion with a minimum mass of $10\,M_{Jup}$ (Jones et al., 2002). As such, the new discovery by *TESS* is designated $\pi$ Men c.

In targeting bright, nearby stars, *TESS* is identifying planets that are ideal for follow up observations and further characterisation. $\pi$ Men c will likely prove to be an important discovery, given its relatively small size and bright host. Its size is just large enough, and density just low enough, to suggest the presence of a substantial envelope of volatile material. The survival of this envelope to its present age of a few Gyr is consistent with its position above the photoevaporation valley (Huang et al., 2018; Gandolfi et al., 2018).

### 4.1.2 The HD 219134 planetary system

HD 219134 is a K3V star just $6.5325 \pm 0.0038$ pc from Earth, as measured by *Gaia* (Gaia Collaboration et al., 2018). My adopted stellar parameters are given in Table 4.1. The age of HD 219134 has been suggested to be in excess of 10 Gyr (Takeda et al., 2007; Ramírez et al., 2013; Gillon et al., 2017b), though another estimate places it at a lower figure of 6.8 Gyr (Pace, 2013). Despite its possibly old age, the star shows signs of modest chromospheric activity, with an $S$-index of about 0.25 (Vogt et al., 2015) and $\log R'_{HK}$ of -5.02 (Motalebi et al., 2015). The $S$-index, an activity indicator based on the Ca H and K lines and associated with chromospheric emission, is seen to vary appreciably between about 0.15 and 0.35 (Vogt

Table 4.1: Adopted stellar parameters for HD 219134.

| Parameter | Value | Reference |
|---|---|---|
| Spectral type | K3V | Soubiran et al. (2008) |
| $V$ | 5.57 | Oja (1993) |
| Mass ($M_\odot$) | $0.81 \pm 0.03$ | Gillon et al. (2017b) |
| Radius ($R_\odot$) | $0.778 \pm 0.005$ | Boyajian et al. (2012) |
| $T_{\rm eff}$ (K) | $4699 \pm 16$ | Boyajian et al. (2012) |
| Distance (pc) | $6.5325 \pm 0.0038$ | Gaia Collaboration et al. (2018) |
| Luminosity ($L_\odot$) | $0.2646 \pm 0.0050$ | Gillon et al. (2017b) |
| $\log g$ (dex) | $4.567 \pm 0.018$ | Gillon et al. (2017b) |
| Age (Gyr) | $11.0 \pm 2.2$ | Gillon et al. (2017b) |

et al., 2015; Johnson et al., 2016).

The initial discovery of the planets orbiting the star was reported in two papers, Vogt et al. (2015, hereafter, V15) and Motalebi et al. (2015, hereafter, M15). V15 identified six candidates (planets b, c, f, d, g, & h; in period order) from radial velocity studies at the Keck and Lick Observatories. M15 independently identified four planets (b, c, d, & e) from using radial velocity from HARPS-N, while additionally reporting the discovery of the transit of planet b from *Spitzer* data. Gillon et al. (2017b) recently showed planet c also transits its host, again discovered using *Spitzer*. Planets e and h are likely to be same object, with M15 reporting a period of $1842^{+4199}_{-292}$ d for planet e, and V15 finding planet h to have a period of $2247 \pm 43$ d. Johnson et al. (2016) detected planets b and h, while also observing low-significance signals at the periods of planets f and d. However, their $S$-index investigation identifies a periodicity at $22.83 \pm 0.03$ d likely to be of stellar origin. This is equal, within the uncertainties, to the period stated by V15 for planet f, $22.805 \pm 0.005$ d, putting the existence of this planet into question. Johnson et al. (2016) further describe an activity cycle of $4230 \pm 100$ d also to be present in the $S$-index data, similar in length to the 11 year Solar cycle.

The adopted planetary parameters are given in Table 4.2. I include planet f despite its possible false-positive nature, as further work is required to disprove its existence. I treat planets e and h as a single object, adopting the parameters from V15 because of the better period constraint, as well as its corroboration from Johnson et al. (2016).

Table 4.2: Adopted planetary parameters for the HD 219134 system. The numbers in parentheses are the uncertainties associated with the last two digits of the values.

| Planet | $P_{\rm orb}$ (d) | Transit ($\rm BJD_{TDB}$) | $a$ (au) | $e$ | $R_p$ ($\rm R_\oplus$) | $M_p$ ($\rm M_\oplus$) | $\rho_p$ ($\rho_\oplus$) | $i$ (°) |
|---|---|---|---|---|---|---|---|---|
| b | 3.092926(10) | 2457126.69913(87) | 0.03876(47) | 0 (fixed) | $1.602 \pm 0.055$ | $4.74 \pm 0.19$ | $1.15 \pm 0.13$ | $85.05 \pm 0.09$ |
| c | 6.76458(33) | 2457474.04591(88) | 0.06530(80) | $0.062 \pm 0.039$ | $1.511 \pm 0.047$ | $4.36 \pm 0.22$ | $1.26 \pm 0.14$ | $87.28 \pm 0.10$ |
| f | 22.717(15) | 2457716.31(50) | 0.1463(18) | $0.148 \pm 0.047$ | – | $> 7.30 \pm 0.40$ | – | – |
| d | 46.859(28) | 2457726.03(63) | 0.2370(30) | $0.138 \pm 0.025$ | – | $> 16.17 \pm 0.64$ | – | – |
| g | 94.2(02) | – | 0.3753(04) | 0 (fixed) | – | $> 10.8 \pm 1.3$ | – | – |
| e/h | 2247(43) | – | 3.11(04) | $0.06 \pm 0.04$ | – | $> 108 \pm 6$ | – | – |

References:
Planets b, c, f & d (Gillon et al., 2017b). The ephemerides for planets f & d are predictions from their radial velocity fits.
Planets g & e/h (Vogt et al., 2015).

**Possible stellar and brown dwarf companions**

Binary companions to planet hosting stars are of interest from an X-ray point of view because of previous studies investigating star-planet interactions by using wide binary companions as a comparison object of the same age (e.g. Poppenhaeger and Wolk, 2014). A few papers and catalogues have reported the existence of a 9.4 mag wide binary companion at 106.6 arcsec from HD 219134 (e.g. Dommanget and Nys, 2002; Eggleton and Tokovinin, 2008). This star is identified by Dommanget and Nys (2002) as BD +56 2967. Using the data reported by *Gaia* DR2 (Gaia Collaboration et al., 2018), I identify this star to be at a distance of $429.9^{+5.4}_{-5.3}$ pc, over 65 times further from Earth than HD 219134. Its proper motion is 370 times smaller. I therefore conclude this is a background object.

HD 219134 has also been identified as a possible "astrometric binary unresolved by speckle interferometry" (Hartkopf and McAlister, 1984; Hoffleit and Jaschek, 1991). The source of this identification is likely observations reported by Lippincott (1974). The paper notes the 'possibility of variable proper motion' in declination with no certainty. There is no follow up confirmation in the literature and Gatewood et al. (1992) ruled out a deviation from linear of the proper motion by more than 2.5 milliarcsec over a period of 5 yr.

Tanner et al. (2010) reported three candidate brown dwarfs within 11 arcsec, although one of these was ruled out as a non-common proper motion using archival data. *Gaia* DR2 lists only one further source within 15 arcsec of HD 219134, with a *Gaia* $G$ magnitude of 18.7. It has no parallax listed, but its $BP - RP$ colour is very similar to HD 219134, whereas one would expect a brown dwarf to be much redder.

## 4.2 Observations

### 4.2.1 $\pi$ Men

Seven pointed observations of $\pi$ Men were made with *ROSAT* between 1990 and 1998. I analysed the three observations with more than ten minutes of live exposure time. All three were made with the PSPCB detector, and they are outlined in Table 4.3. The 1991 observations contained four visits spread across one week. $\pi$ Men was also observed with *ROSAT* as part of its All Sky Survey. There are additional serendipitous observations of the system in the *Swift* archive, taken between 2015 December 31 and 2016 January 6, totalling 9.1 ks of exposure time.

The discovery papers give parameters that are in broad agreement with each other. I adopted the stellar and planetary parameters from Huang et al. (2018), and

Table 4.3: Details of the three *ROSAT* pointed observations of $\pi$ Men with exposure times greater than 10 minutes.

| Obs ID | Exp. Time (s) | Start (TDB†) | End (TDB†) |
|---|---|---|---|
| RP999998A01 | 7061 | 1991-04-18T02:12 | 1991-04-24T04:31 |
| RP999998A03 | 1408 | 1993-04-12T22:38 | 1993-04-12T23:24 |
| RP180278N00 | 856 | 1998-12-12T13:43 | 1998-12-12T13:58 |

† Barycentric Dynamic Time

Table 4.4: Planetary phase coverage of the observations of HD 219134. For planets f and d, these phases given here are expectations from their radial velocities according to the calculations of Gillon et al. (2017b).

| Planet | Phase Coverage | Transit Phase |
|---|---|---|
| b | 0.9693 – 1.1040 | 0.9936 – 1.0064 |
| c | 0.7350 – 0.7966 | 0.9971 – 1.0029 |
| f | 0.8300 – 0.8483 | 0.9965 – 1.0035 |
| d | 0.3166 – 0.3255 | 0.9975 – 1.0025 |

the positional and kinematic information provided by the second *Gaia* data release (Gaia Collaboration et al., 2018). Furthermore, the parameters should be better constrained as data from more TESS sectors is taken; $\pi$ Men is located close enough to the southern ecliptic pole that it will observed for six months during the primary mission.

All three pointed *ROSAT* observations were performed with the position of $\pi$ Men located on axis. The source was very clearly detected in the longest observations from 1991 (see the image in Fig. 4.1), only marginally detected in 1993, and detected again in 1998. I used an 80 arcsec radius extraction region for the source, and a single, large 450 arcsec region for background estimation. Extractions were performed using the XSELECT program[1].

For the *Swift* data, I employed 30 and 90 arcsec source and background regions, respectively. These were again extracted using XSELECT.

### 4.2.2 HD 219134

HD 219134 was observed for 35 ks by the European Photon Imaging Camera (EPIC) on *XMM-Newton* on 2016 June 13 (ObsID: 0784920201; PI: Wheatley). The medium optical blocking filter was employed, and the data taken in full frame mode. Simultaneous observations with the Optical Monitor (OM) were taken in fast mode using

[1] `https://heasarc.gsfc.nasa.gov/ftools/xselect/`

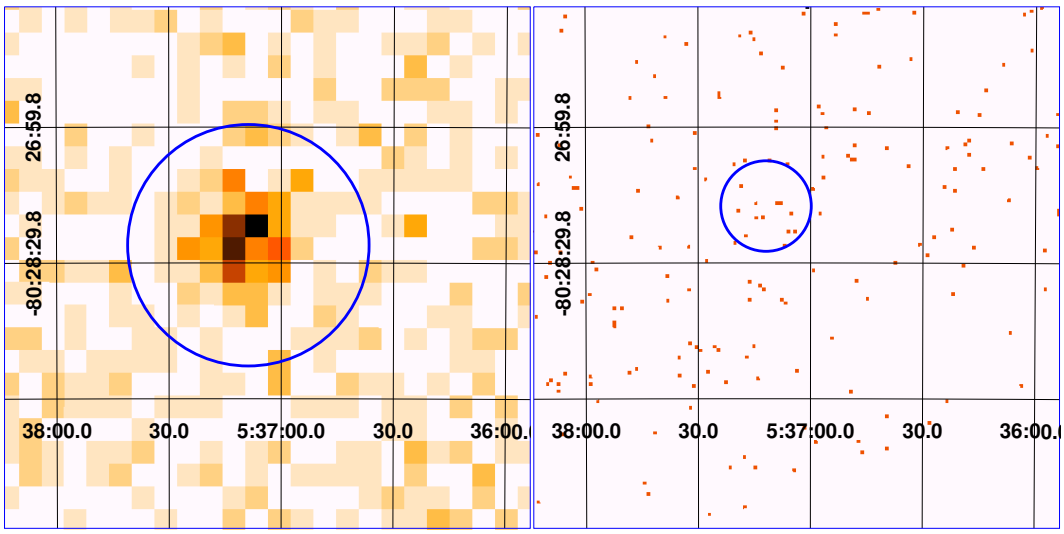


Figure 4.1: X-ray images of the 1991 *ROSAT* (left), and *Swift* data (right) for $\pi$ Men, on the same spatial scale. The blue circles depict the source extraction region used in each case. The single orange points in the right hand plot are individual X-ray photons.

the UMW2 ultraviolet filter. The phase of planets b, c, f, and d during the observations, calculated using the ephemerides in Table 4.2, are displayed in Table 4.4.

The data were reduced using the Scientific Analysis System (SAS 16.0.0) using the standard procedure[2]. The final quarter of the observations saw numerous high background peaks in the EPIC-pn camera due to Solar soft protons (Walsh et al., 2014). These time periods were filtered out of the spectral analysis. The EPIC-MOS cameras were unaffected.

## 4.3 Light curve analysis

I plotted X-ray light curves for the various observations analysed. These were searched for flares and stellar variation, as well as for evidence of transit features in the case of HD 219134b.

### 4.3.1 $\pi$ Men X-ray light curve

The *ROSAT* X-ray light curve of $\pi$ Men is plotted in Fig. 4.2, binned to one point per visit. The light curve covers the full PSPCB energy range of 0.1 – 2.4 keV,

[2]As outlined on the 'SAS Threads' webpages: `http://www.cosmos.esa.int/web/xmm-newton/sas-threads`

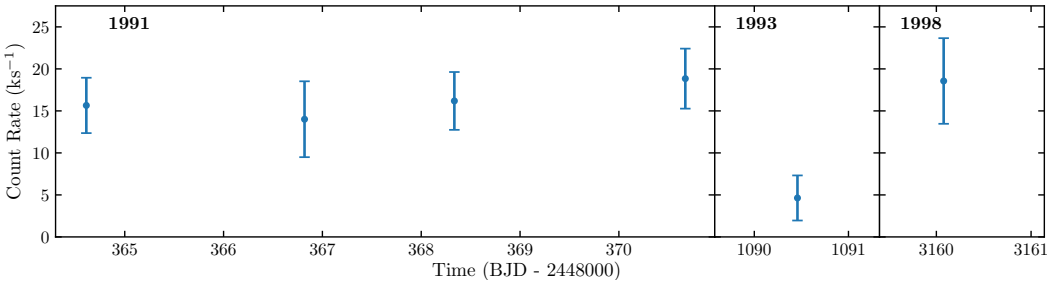


Figure 4.2: Background corrected *ROSAT* PSPCB light curve of $\pi$ Men, covering the energy range 0.1–2.4 keV.

although, as discussed in Section 4.4.1, the source is very soft with most photons detected having energies below 0.3 keV.

The single 1993 visit has a count rate considerably below that of the other visits, as suggested by the very marginal detection in that observation. The other five visits have count rates that are all consistent with one another to within 1-$\sigma$. Analysis of the All Sky Survey data by me, and that presented in the Second *ROSAT* All Sky Survey source catalogue (Boller et al., 2016), obtain a count rate ($22.9\pm6.1\,\mathrm{ks}^{-1}$), which is consistent with all of the pointed observations except the 1993 visit. I note that the 1993 visit was not made at the expected time of a planet transit.

### 4.3.2 HD 219134 X-ray light curve

Fig. 4.3 shows the X-ray light curve for HD 219134 for three energy ranges: 0.20 – 2.50 keV ('full'), 0.20 – 0.65 keV ('soft'), 0.65 – 2.50 keV ('hard'). Each panel has been coadded across all three EPIC detectors. Further, in Fig. 4.4, I split up the EPIC-pn and EPIC-MOS light curves. These two figures demonstrate that there are no strong X-ray flares from the star during the observations.

In the full light curve, there is a broad minimum in the X-ray count rate around the time of the primary transit of planet b, around phases $0.98 < \phi < 1.02$. The average count rate for the six bins in this phase range is $89.2\pm2.9\,\mathrm{ks}^{-1}$, compared to $102.3\pm2.5\,\mathrm{ks}^{-1}$across the rest of the light curve. This lower count rate could either be the result of absorption by a large cloud of gas surrounding the planet (i.e. an X-ray transit), or due to stellar variability. Unlike in Chapter 6 (see e.g. Fig 6.7), I do not have the benefit of multiple observations in this case. Averaging across many observations allows stellar variability to also be averaged over, and repeated dips increase the likelihood of them being due to absorption by planetary material. I discuss my interpretations further in Section 4.5.5, though the origin of this apparent

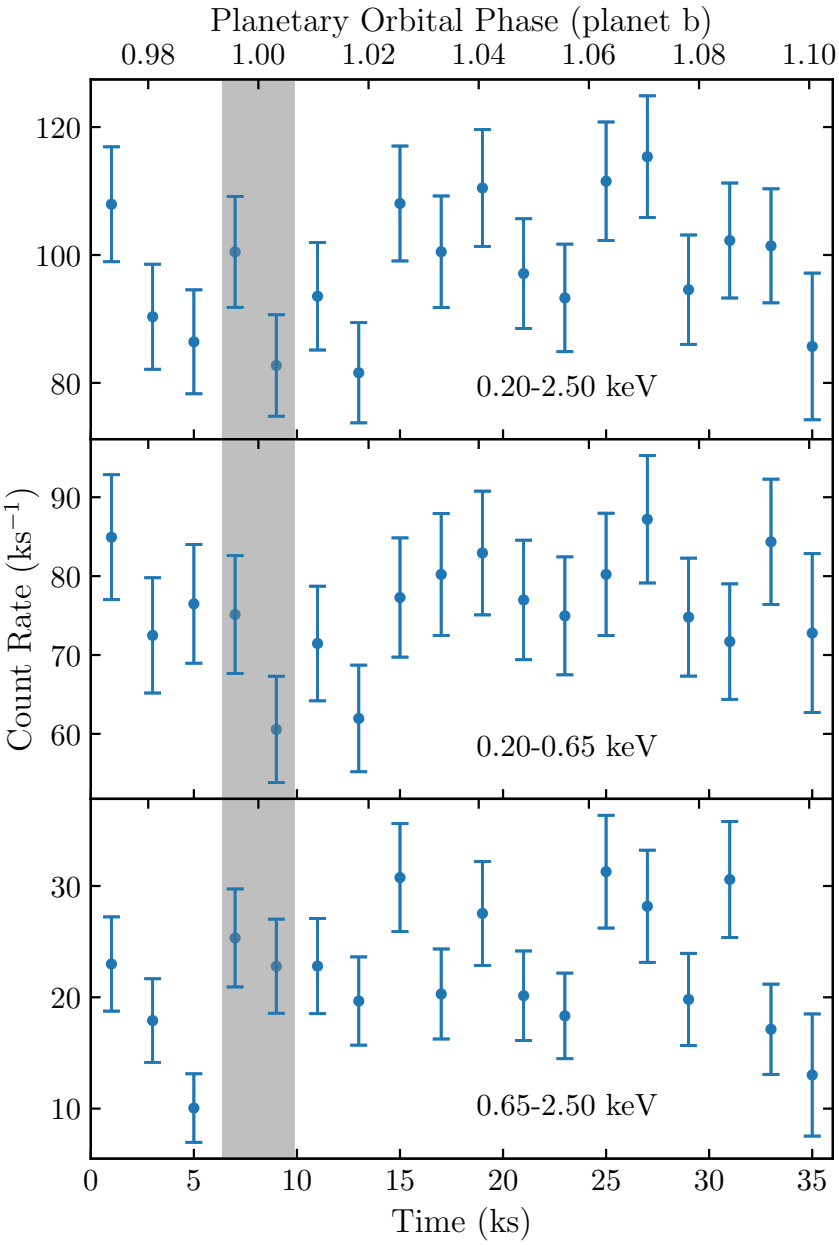


Figure 4.3: X-ray light curve of HD 219134 for three energy ranges: 0.20 – 2.50 keV (top), 0.20 – 0.65 keV (middle), and 0.65 – 2.50 keV (bottom). The count rates are the sum of all three EPIC detectors. The grey shaded regions are the duration of the planetary transit of planet b at optical wavelengths.

signal is uncertain and requires additional observations to determine either way if this is indeed genuinely related to the planetary transit, or just stellar variation.

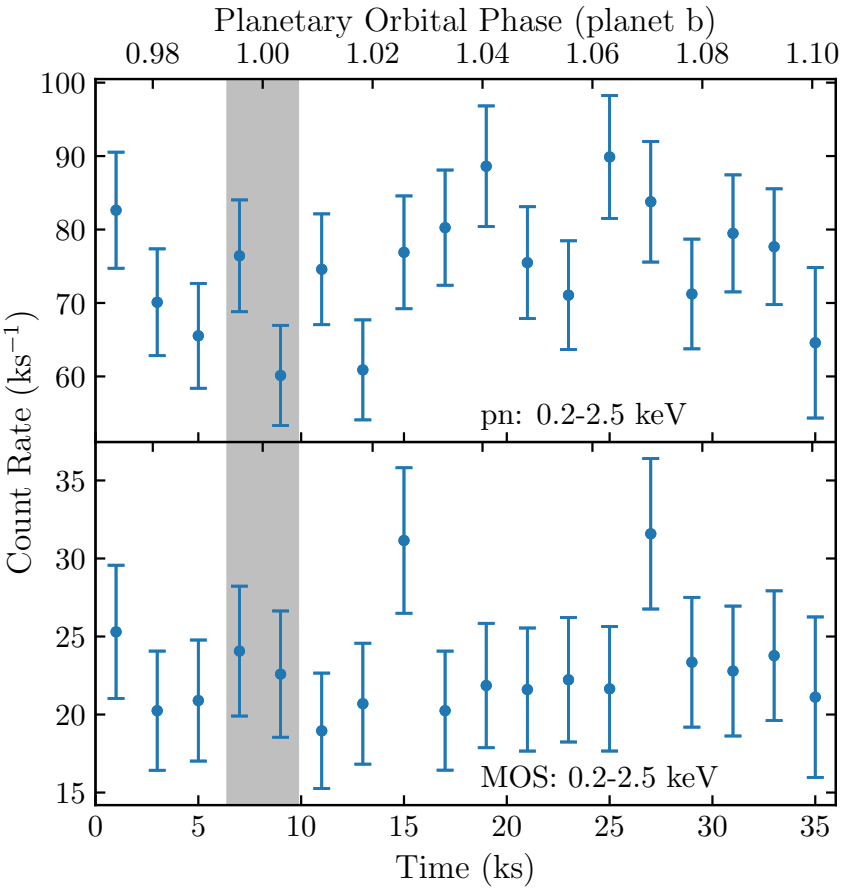


Figure 4.4: X-ray light curves of HD 219134 for the EPIC-pn (top) and EPIC-MOS (bottom) plotted separately. The count rates for the MOS plot is the sum of both MOS detectors. The grey shaded regions are as in Fig. 4.3.

### 4.3.3 HD 219134 OM UV light curve

Ultraviolet observations of HD 219134 were taken with the Optical Monitor (OM), simultaneously with the X-ray data. The UVW2 filter was used, and the data were taken in fast mode in an attempt to detect a transit of planet b.

I corrected the fast mode time series obtained from OMFCHAIN using the count rate from the corresponding image mode extractions from OMICHAIN. This is the same method I applied for my detection of the ultraviolet transit of WASP-80b in Chapter 3, and I described my motivations for correcting the data in this way in detail in the Section 2.4.

The corrected OM light curve is plotted in Fig. 4.5. The data shows an upwards trend in count rate, together with a dip at around phase 1.04–1.06 for planet b, and is not coincident with the primary transit time for any planet in the

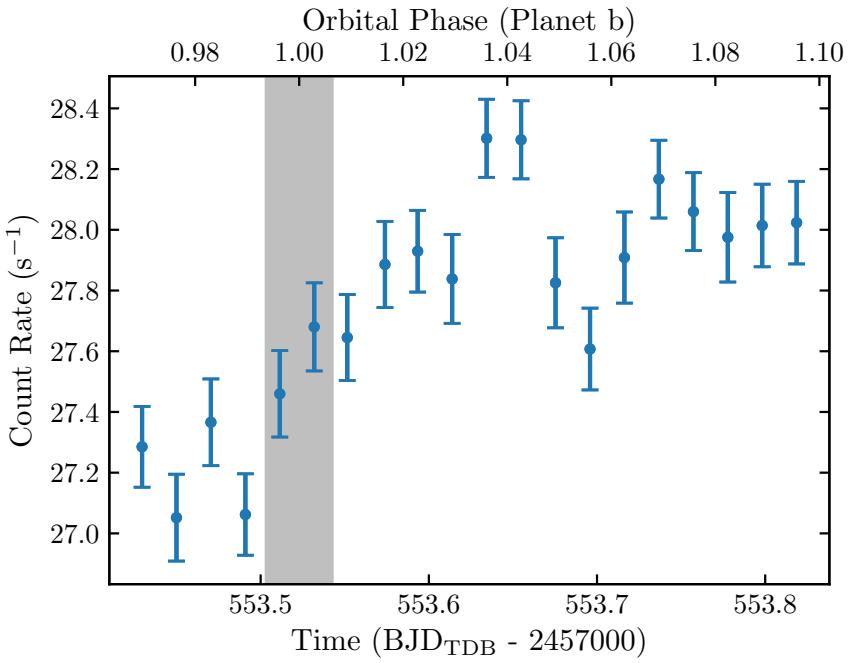


Figure 4.5: HD 219134 Optical Monitor light curve, taken using the UVW2 filter.

system. The data show no obvious transit-like signature around the correct phase for planet b. Indeed, the precision of this single observation is insufficient to have detected a transit if it were of a similar depth in the near ultraviolet to the optical transit (0.036 per cent). I can rule out all inflated depths larger than about 1 per cent that could result from significant evaporation of the planetary atmosphere.

## 4.4 X-ray spectral analysis

I display the X-ray spectra together with their best fitting models for $\pi$ Men and HD 219134 in Figs. 4.6 and 4.7, respectively.

I analysed the spectra in XSPEC 12.9.1p (Arnaud, 1996), using many of the same methods I applied to the sample of larger planets in Section 3.4.2. I modelled the coronal emission with APEC models, describing an optically-thin thermal plasma (Smith et al., 2001). A multiplicative TBABS model was also once again included in both analyses to account for interstellar absorption (Wilms et al., 2000). The value for the H I column density was then estimated using the method from Redfield and Linsky (2000), where the system's distance is multiplied by a mean density of 0.1 cm$^{-3}$. This was then removed after fitting to estimate the unabsorbed fluxes. The systems' close proximity to the Earth meant that this term's influence on the

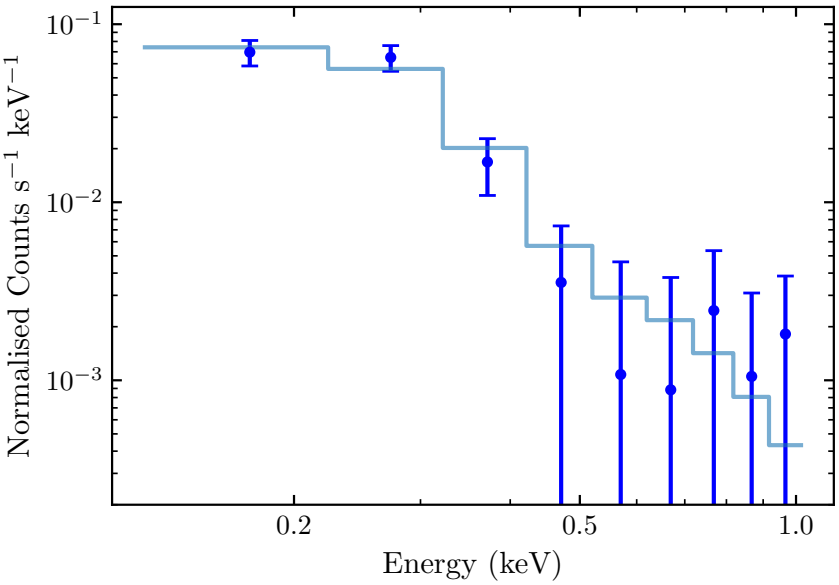


Figure 4.6: Observed X-ray spectra of $\pi$ Men from the 1991 *ROSAT* observations, displayed along with the best fit model.

fluxes in both cases is minimal. Abundances were set to Solar values (Asplund et al., 2009), as [Fe/H] was measured to be close to Solar for both $\pi$ Men ($0.08 \pm 0.03$, Ghezzi et al., 2010), and HD 219134 ($0.11 \pm 0.04$; M15). All estimates of uncertainties on my fitted parameters in XSPEC were made using a combination of the software's MCMC sampler and error command. They represent the 1-$\sigma$ level. Further details related to the spectral fitting are discussed for the two systems in turn, below.

### 4.4.1 $\pi$ Men *ROSAT* spectrum

The *ROSAT* PSPCB spectrum of $\pi$ Men is displayed in Fig. 4.6. The spectrum is very soft, and is dominated by photons with energies below 0.3 keV.

My main fit was to the 1991 data only, which has a far larger number of counts compared to the other two epochs. However, the spectrum still only required a single-temperature APEC model. The model was fitted using the C-statistic (Cash, 1979) because of the low numbers of counts in some of the higher energy bins. The best fit model parameters for the 1991 observations, together with their corresponding fluxes and luminosities, are given in Table 4.5. My analysis uses 0.1 – 2.4 keV as the X-ray band and 0.0136 – 0.1 keV as the EUV band.

My analysis of the *ROSAT* All Sky Survey data and 1998 visit revealed a similarly soft spectrum, consistent with the 1991 data.

Table 4.5: Results of the X-ray spectral analysis of $\pi$ Men, together with fluxes and corresponding planetary irradiation estimates.

| Parameter | Symbol | Value |
|---|---|---|
| Temperature | $kT$ | $0.152^{+0.029}_{-0.037}$ keV |
| Emission Measure | EM | $\left(1.10^{+0.24}_{-0.16}\right) \times 10^{50}\,\mathrm{cm}^{-3}$ |
| Unabsorbed flux at Earth | $F_{\mathrm{X},\oplus}$ | $\left(6.7^{+1.3}_{-1.2}\right) \times 10^{-14}\,\mathrm{erg\,s^{-1}\,cm^{-2}}$ |
| X-ray[a] luminosity | $L_{\mathrm{X}}$ | $\left(2.67^{+0.50}_{-0.46}\right) \times 10^{27}\,\mathrm{erg\,s^{-1}}$ |
| X-ray to bolometric lum. | $L_{\mathrm{X}}/L_{\mathrm{bol}}$ | $\left(4.84^{+0.92}_{-0.84}\right) \times 10^{-7}$ |
| EUV[b] luminosity | $L_{\mathrm{EUV}}$ | $\left(21.1^{+4.6}_{-4.3}\right) \times 10^{27}\,\mathrm{erg\,s^{-1}}$ |
| XUV[c] flux at 1 au | $F_{\mathrm{XUV,1\,au}}$ | $8.5^{+1.7}_{-1.6}\,\mathrm{erg\,s^{-1}\,cm^{-2}}$ |
| XUV[c] flux at planet c | $F_{\mathrm{XUV,c}}$ | $1810^{+350}_{-330}\ \mathrm{erg\,s^{-1}\,cm^{-2}}$ |
| XUV received (c.f. Earth) | $P_{\mathrm{XUV,c}}$ | $1930^{+390}_{-360}\,\mathrm{P_{XUV,\oplus}}$ |

[a] 0.1 – 2.4 keV (5.17 – 124 Å); [b] 0.0136 – 0.1 keV (124 – 912 Å); [c] 0.0136 – 2.4 keV (5.17 – 912 Å).

### 4.4.2 $\pi$ Men *Swift* data

The XRT instrument on *Swift* extends only down to 0.3 keV, not low enough to cover the energies where the majority of the *ROSAT* counts were detected. Inspection of the *Swift* data showed only a marginal detection of $\pi$ Men (see the image in Fig. 4.1). I measure a 0.3–2.0 keV count rate of $0.67 \pm 0.34\,\mathrm{ks^{-1}}$ across the 9.1 ks of exposure time. I estimate there to be 6 source and 3 background counts in the 30 arcsec aperture. Applying parameters from the 1991 *ROSAT* model fit gives an estimated a *Swift* XRT count rate of $0.76\,\mathrm{ks^{-1}}$, in good agreement with the data.

### 4.4.3 HD 219134 *XMM-Newton* spectra

The X-ray spectra for HD 219134 in Fig. 4.7 displays the observed spectra in each of the three EPIC cameras, together with the best fit model for the three cameras combined. The best fit spectral parameters are in Table 4.6, together with my flux and luminosity estimates.

With a large number of counts detected in the source region, I binned the spectra to a minimum of 25 counts per bin prior to fitting. Fits were made to two separate sets of the data. The first was to only the data from the EPIC-pn, while the second additionally included the data from both EPIC-MOS cameras.

For both datasets, I fitted a two-temperature APEC model. In the fit to data from all three cameras, I coupled the temperature and normalisation parameters. Initially, I included an extra constant in the model for the two EPIC-MOS cameras, to allow it to vary in intensity but not spectral shape. I found that the separate fluxes

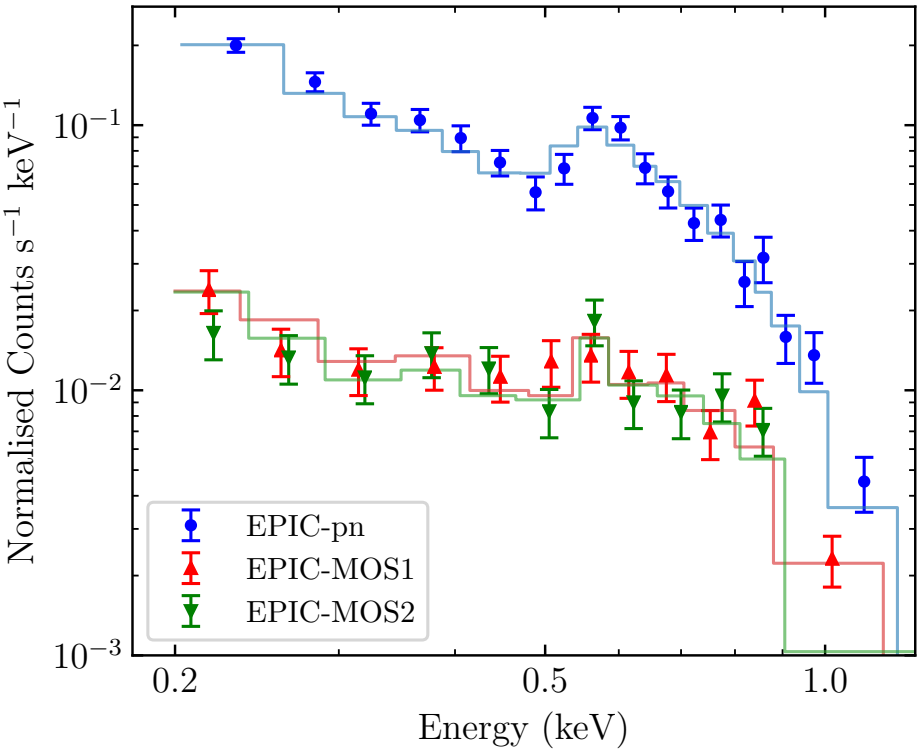


Figure 4.7: Observed X-ray spectra of HD 219134 from each of the three EPIC cameras, displayed along with their best fit model (see text and the 'pn & MOS' fit in Table 4.6 for details). The two MOS cameras have the same model, but differ slightly because of the different energy ranges spanned in each spectral bin between the two.

for the pn and MOS that this method yielded were consistent with one another, while the best-fit constant value was $0.946^{+0.046}_{-0.049}$. Therefore, I refitted the data without the constant, thereby forcing the exact same model across all three cameras. The model parameters and measured fluxes from this fit, and the separate one to only the pn data, are given in Table 4.6.

### 4.4.4 EUV estimation

I estimate the EUV emission by following the empirical relations I introduced in Section 3.4.4 (see Equation 3.1 and Table 3.4), based on the method of Chadney et al. (2015). The EUV luminosities associated with each model fit are given in Tables 4.5 and 4.6. Note that the defined X-ray and EUV bands differ slightly: the $\pi$ Men results use an X-ray/EUV boundary of 0.1 keV, whereas the HD 219134 results use 0.2 keV. This is because of the differences in the observable energies of the telescopes used to measure the two spectra. The full XUV band is the same in each

Table 4.6: Results of the X-ray spectral analysis for HD 219134, with and without the inclusion of the EPIC-MOS data in the fit. Fluxes and corresponding planetary irradiation estimates are also presented. Here, I use slightly different X-ray/EUV definitions to those in Table 4.5 because of the different observation energy range: 0.2 – 2.4 keV (5.17 – 62 Å) for X-ray; 0.0136 – 0.2 keV (62 – 912 Å) for EUV. The full XUV band remains unchanged: 0.0136 – 2.4 keV (5.17 – 912 Å).

| Parameter | pn Only | pn & MOS |
|---|---|---|
| $kT$ (keV) | $0.1010^{+0.0097}_{-0.0127}$ | $0.1064^{+0.0068}_{-0.0124}$ |
| | $0.253^{+0.028}_{-0.018}$ | $0.254^{+0.023}_{-0.015}$ |
| EM ($10^{49}\,\mathrm{cm}^{-3}$) | $5.46^{+1.50}_{-0.58}$ | $4.65^{+1.14}_{-0.26}$ |
| | $1.56^{+0.35}_{-0.34}$ | $1.54^{+0.29}_{-0.30}$ |
| $F_{\mathrm{X},\oplus}$ ($10^{-13}\,\mathrm{erg\,s^{-1}\,cm^{-2}}$)* | $1.748^{+0.102}_{-0.067}$ | $1.664^{+0.083}_{-0.044}$ |
| $L_{\mathrm{X}}$ ($10^{26}\,\mathrm{erg\,s^{-1}}$) | $8.93^{+0.52}_{-0.34}$ | $8.49^{+0.42}_{-0.22}$ |
| $L_{\mathrm{EUV}}$ ($10^{26}\,\mathrm{erg\,s^{-1}}$) | $86.1^{+6.9}_{-5.1}$ | $84.0^{+6.0}_{-3.9}$ |
| *Planetary irradiation estimates* ($\mathrm{erg\,s^{-1}\,cm^{-2}}$) | | |
| $F_{\mathrm{XUV,b}}$ | $2250^{+170}_{-120}$ | $2190^{+140}_{-100}$ |
| $F_{\mathrm{XUV,c}}$ | $790^{+58}_{-44}$ | $768^{+50}_{-34}$ |
| $F_{\mathrm{XUV,f}}$ | $155^{+12}_{-9}$ | $150^{+10}_{-7}$ |
| $F_{\mathrm{XUV,d}}$ | $59.1^{+4.4}_{-3.3}$ | $57.5^{+3.8}_{-2.6}$ |
| $F_{\mathrm{XUV,g}}$ | $24.0^{+1.8}_{-1.3}$ | $23.3^{+1.5}_{-1.0}$ |
| $F_{\mathrm{XUV,h}}$ | $0.348^{+0.051}_{-0.041}$ | $0.339^{+0.046}_{-0.034}$ |
| $F_{\mathrm{XUV,1\,au}}$ | $3.38^{+0.31}_{-0.26}$ | $3.29^{+0.28}_{-0.22}$ |

* Unabsorbed flux at Earth

case, and fluxes for this are given in the tables too, scaled to both the time-averaged orbital separation of each planet and 1 au.

## 4.5 Discussion

### 4.5.1 Stellar X-ray emission of $\pi$ Men

The measured value of $L_{\mathrm{X}}/L_{\mathrm{bol}}$ for $\pi$ Men of $(4.84^{+0.92}_{-0.84}) \times 10^{-7}$ is similar to that for the Sun in mid-activity cycle (Judge et al., 2003; Ribas et al., 2005). However, the predicted value using the X-ray-age relation of Jackson et al. (2012) is $3 \times 10^{-6}$, which is almost an order of magnitude greater. Furthermore, using the stellar rotation period of $\pi$ Men ($18.3 \pm 1.0$ d; Zurlo et al., 2018), the X-ray-rotation relation of Wright et al. (2011) predicts $5 \times 10^{-8}$, which is an order of magnitude in the other direction. These discrepancies with empirical age and rotation relations highlight

the importance of making direct observations of X-ray irradiation rates of exoplanet host stars.

The very marginal detection of the star in the 1993 *ROSAT* data is interesting given that the source is detected in the 1998 data with a substantially shorter exposure time (Tab. 4.3). The X-ray light curve in Fig. 4.2 shows that the star is clearly a variable X-ray source. I checked the orbital phase of the planet at the time of the 1993 observations and found that it did not coincide with a planetary transit. The variation is therefore stellar in origin. The consistency of the X-ray brightness across one week in 1991 perhaps indicates that the low flux in 1993 is more likely to be associated with longer timescale variations, perhaps related to a magnetic activity cycle. However, additional X-ray observation are clearly needed in order to determine the variability timescales.

I estimated the potential count rate for an observation with the EPIC-pn camera on *XMM-Newton*. Applying the best-fit spectral parameters from the fit to the 1991 data yields a count rate of $11\,\mathrm{ks}^{-1}$ with the thick optical blocking filter.

### 4.5.2 XUV output and the rotation period of HD 219134

HD 219134 was previously observed in X-rays by *ROSAT*. Schmitt and Liefke (2004) reported $\log L_\mathrm{X}$ (in $\mathrm{erg\,s}^{-1}$) of 26.85. Though no uncertainty was given for this luminosity, their count rate had a ∼40 per cent error (about 10 times larger than the error on my fluxes with *XMM-Newton*). If I double my $L_\mathrm{X}$ to account for the missing flux down to 0.1 keV, as I did in Section 3.6.1, there is a hint of increased X-ray in the *XMM-Newton* observations compared to *ROSAT*. However, the large uncertainty in doubling the flux/luminosity means that they are statistically consistent.

The rotation period of HD 219134 has been a subject of discussion in the literature. M15 explored a periodogram of the activity indicators to detect a $42.3 \pm 0.1$ d period, and estimated $v \sin i$ from their RVs to be $0.4 \pm 0.5\,\mathrm{km\,s}^{-1}$. V15 based their estimate of ∼20 d on a larger $v \sin i$ measurement of $1.8\,\mathrm{km\,s}^{-1}$ (Valenti and Fischer, 2005) and the stellar radius. Additionally, V15 argue that because the $22.805 \pm 0.005$ d period is the strongest power spectrum peak when the other planet signals are removed across their different RV datasets that the signal cannot be the result of spot modulation, and is indeed a real planet. However, (Johnson et al., 2016) detected a signal at the same period ($22.8 \pm 0.03$ d) in their S-index analysis, pointing to a stellar origin. They do not believe this to be the true rotation period, however, rather they favour a differentially rotating star where the 22.8 d period is a first harmonic of activity at higher latitudes than the origin of the 42.3 d signal reported by M15. This assessment by Johnson et al. (2016) has since been

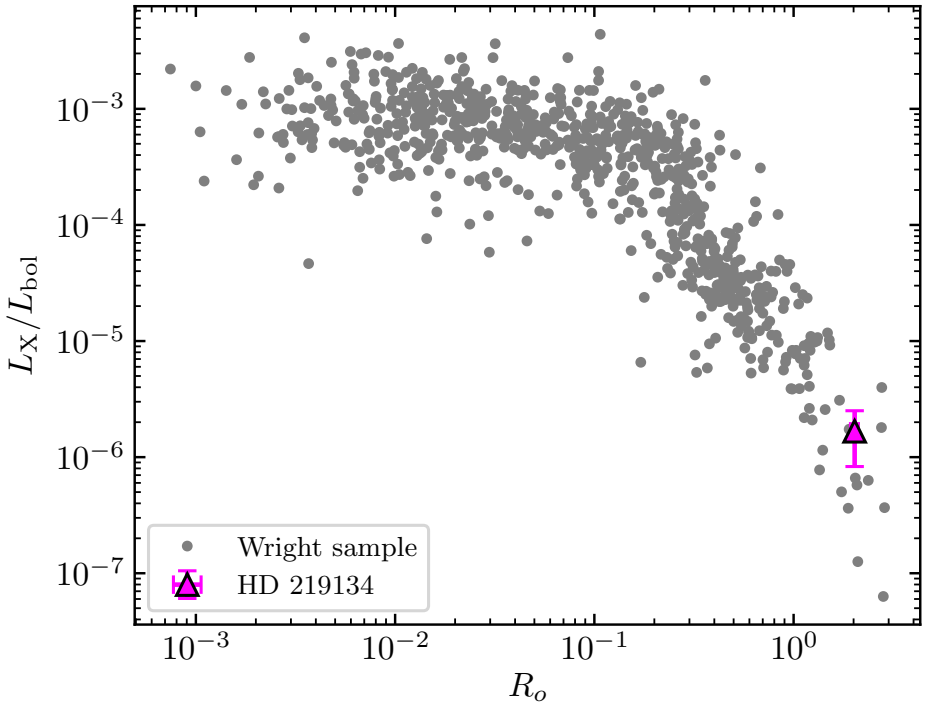


Figure 4.8: Replotting of fig. 1 of Wright and Drake (2016), with HD 219134 added.

corroborated by spectropolarimetric observations (Folsom et al., 2018).

Assuming the 42.3 d rotation period, I investigate the compatibility of my X-ray flux measurement with studies of the relationship between X-rays and rotation. Specifically, I compare my measurements to the empirical relations of Wright et al. (2011), linking $L_X/L_{bol}$ to Rossby number, $R_o$, defined as $P_{rot}/\tau$, where $\tau$ is the convective turnover time (Noyes et al., 1984). Given the 42.3 d rotation period, these relations predict $L_X/L_{bol} = 3.5 \times 10^{-7}$, whereas my measured value is $(1.67 \pm 0.84) \times 10^{-6}$. Note that for $L_{bol}$ I adjusted the luminosity given in Table 4.1 for the updated distance estimate from *Gaia* DR2. In Fig. 4.8, I plot HD 219134 with the Wright and Drake (2016) sample, itself an update of the Wright et al. (2011) sample. Despite the measured $L_X/L_{bol}$ being higher than expected, the measurement is consistent with some of the other points around it.

### 4.5.3 Atmospheric escape

I investigated XUV-driven atmospheric mass loss in the two systems. As in Chapter 3, I employ both the energy limited formulation (see Section 1.2.3), and the interpolation tool related to the grid of hydrodynamic models described in Kubyshkina et al. (2018a). The efficiency parameter, $\eta$, was taken to be 0.15 throughout the

Table 4.7: Estimates of the mass loss rate from the atmosphere of $\pi$ Men c under the different assumptions described in Sect. 4.5.3.

| Method | $\eta$ | $\beta$ | $\dot{M}$ ($\times 10^{10}$ g s$^{-1}$) | Life. Loss % Const.* | J12† | Ref. |
|---|---|---|---|---|---|---|
| Kubyshkina | 0.15 | implicit[a] | 2.8 | 8.4 | – | This work |
| Kubyshkina | 0.15 | implicit | 1.2 | 3.8 | – | Gandolfi et al. (2018) |
| Energy lim. | 0.15 | 2.67 | 1.5 | 4.7 | 18 | This work |
| Energy lim. | 0.15 | 1.00 | 0.11 | 0.36 | 3.0 | This work |

[a] $\beta$ is reported as an output parameter, with a value of 2.67.
* Constant lifetime XUV irradiation rate, at the current level.
† Lifetime XUV irradiation estimated by the relations of Jackson et al. (2012).

analysis of these systems.

### $\pi$ Men c

The mass loss rate of $\pi$ Men c was previously considered by Gandolfi et al. (2018), but using an assumed X-ray flux. Those authors also employed the interpolation grid across the Kubyshkina et al. (2018a) models. I compare my results with those Gandolfi et al. (2018) in Table 4.7, where it can be seen that my estimate using the measured XUV flux is a factor of 2.3 higher. As discussed by Gandolfi et al. (2018), such a high mass loss rate implies that $\pi$ Men c has either lost its hydrogen envelope, and now has an atmosphere dominated by heavier elements, or it must have formed with a thick hydrogen atmosphere that has only partly survived.

Also given in Table 4.7 are results of applying the energy-limited method. For the effective planet radius at which XUV radiation is absorbed, $\beta$, I made two choices. First, the value of 2.67 output by the interpolation method, above, which is appropriate for a hydrogen-dominated atmosphere. Second, a value of 1.0, corresponding to the limiting case for an atmosphere consisting of heavier species (e.g. water or methane). The energy-limited mass loss estimates are also given in Table 4.7, and I note that for the same $\beta$ the energy limited rate is within a factor 2 of the mass loss rate derived from the hydrodynamical model. As in Section 3.6.3, I use the energy-limited results to estimate the lifetime mass loss, using both a constant irradiation and an irradiation history based on Jackson et al. (2012). These results are also displayed in Table 4.7.

Table 4.8: Mass loss rates for HD 219134b & c estimated with the two different methods. Lifetime mass loss estimates are also given, using the energy-limited method.

| Planet | $\eta$ | $\beta$ | $\dot{M}_{\rm En}$ ($\times 10^8\,{\rm g\,s^{-1}}$) | $\dot{M}_{\rm Kuby}$ ($\times 10^8\,{\rm g\,s^{-1}}$) | Lifetime Loss % Const.* | J12† |
|---|---|---|---|---|---|---|
| b | 0.15 | 1.00 | 6.8 | - | 0.83 | 6.1 |
| | 0.15 | 1.56 | 17 | 5.7 | 2.0 | 14 |
| c | 0.15 | 1.00 | 2.0 | - | 0.25 | 2.1 |
| | 0.15 | 1.70 | 5.9 | 3.7 | 0.72 | 5.7 |

* Constant lifetime XUV irradiation rate, at the current level.
† Lifetime XUV irradiation estimated by the relations of Jackson et al. (2012).

**HD 219134b & c**

I present mass loss estimates for the two transiting, innermost planets in Table 4.8. I find that planets b and c have a similar energy-limited mass loss rate to that predicted for HD 97658b when the same $\eta$ and $\beta$ assumptions are made (see Chapter 3). Unlike for $\pi$ Men c, the energy-limited mass loss rates for both HD 219134b and c is slightly higher than for the Kubyshkina et al. (2018a) method. It should be noted that the Kubyshkina et al. (2018a) models apply only to hydrogen dominated atmospheres. The densities of both HD 219134b & c suggest they lack a H/He envelope, and therefore the application of the interpolation grid over those models to the planets may not be valid in their present day state. The Kubyshkina et al. (2018a) study itself did model the early lives of both planets, concluding that both would have been stripped of any hydrogen-dominated envelope they may have begun their lives with well within a few tens of Myr of their formation.

Lifetime mass loss estimates based on the energy-limited method are also given in Table 4.8. The first assumes the current mass loss rate to have been constant over the system's lifetime, whilst the second is based on the relations described by Jackson et al. (2012), including the EUV output in addition to the X-rays. Both of these methods have limitations. The constant method neglects the much greater XUV output the star would have had early in its life, though it does provide an absolute minimum value for the total lifetime loss. While the Jackson et al. (2012) relations account for high irradiation at early times, the mass loss estimates I calculate assume a constant radius across the planets' lifetime. If these planets started with a small H/He envelope that was evaporated away, they would have begun their lives bigger, and traversed across part of the evaporation valley. Nonetheless, Owen and Wu (2017) describes how a H/He envelope with an envelope mass fraction of

just a few percent is sufficient for the radius to place it the other side of the valley. If these planets traversed the valley earlier in their lives, a lifetime loss between this and 15%, as I have estimated, are reasonable for these planets.

It is interesting that the results using the $\beta$ values output by the Kubyshkina et al. (2018a) code give higher lifetime loss rates for $\pi$ Men c than for either HD 219134b or c. This could be because of the constant radius approximation, or it could suggest that $\pi$ Men c was born more massive than HD 219134.

### 4.5.4 Detecting evaporation of $\pi$ Men c

My predicted mass loss rates for $\pi$ Men c, given in Table 4.7 are substantial, with significant implications for the evolution of the planetary atmosphere. These escape rates are even higher than my XUV estimates for the Neptune-sized planet GJ 436b (see Section 3.6.3), for which ultraviolet absorption from the escaping atmosphere has been detected (Kulow et al., 2014; Ehrenreich et al., 2015). In that case, Ly $\alpha$ absorption has been observed up to 56 per cent deep during transits that last for up to 20 hours after the optical transit (Ehrenreich et al., 2015; Lavie et al., 2017). This deep absorption was found to be consistent with neutral hydrogen escape of only $(2.5 \pm 1) \times 10^8\,\mathrm{g\,s^{-1}}$ (Bourrier et al., 2015, 2016).

This favourable comparison with GJ 436b, together with a bulk density requiring a volatile envelope, suggests that atmospheric escape from $\pi$ Men c should be readily detectable using the *Hubble Space Telescope*: either at Ly $\alpha$ or wavelengths associated with heavier species. My predicted atmospheric escape for $\pi$ Men c is also greater than my estimate for HD 97658b (see Chapter 3) for which Ly $\alpha$ absorption was not detected (Bourrier et al., 2017a).

The species detected/not detected in an extended or escaping atmosphere around the super-Earth would determine the composition of the planetary atmosphere. For example, the presence of both hydrogen and oxygen would point to a $H_2O$ rich world, which is consistent with its density from Huang et al. (2018). Alternatively, hydrogen and helium detections would suggest a substantial gaseous envelope around a dense rocky core, also consistent with the density from Huang et al. (2018).

The proximity of $\pi$ Men to Earth means that the star should be bright enough in Ly $\alpha$, and the interstellar absorption low enough, for a sensitive search for escaping neutral hydrogen. Using the empirical relations of Linsky et al. (2014) linking Ly $\alpha$ and EUV fluxes, I use my EUV flux to estimate the Ly $\alpha$ flux at Earth of $\pi$ Men to be $8.7 \times 10^{-13}\,\mathrm{erg\,s^{-1}\,cm^{-2}}$. This is four times that of GJ 436 (Bourrier et al., 2016; Youngblood et al., 2016), and twice that of HD 97658 (Youngblood et al., 2016;

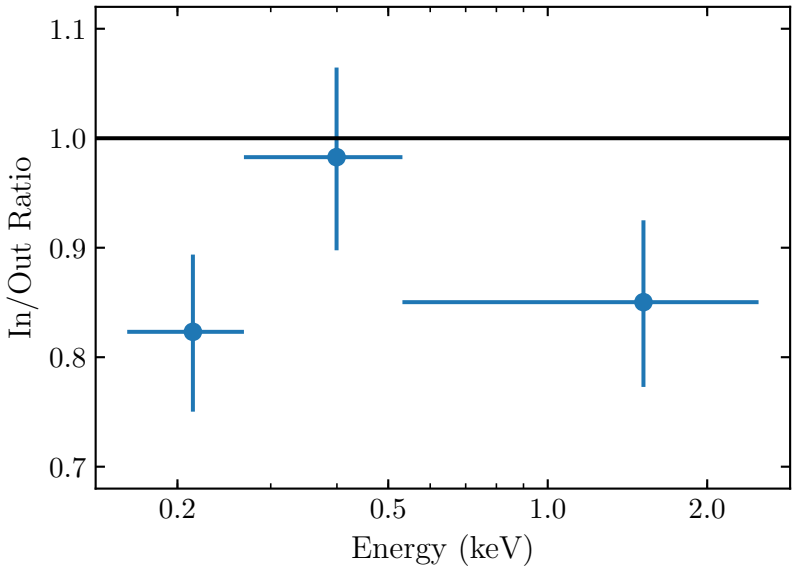


Figure 4.9: Ratio of the 'in' and 'out of transit' spectra for HD 219134 as a function of energy. See main text for phase definition.

Bourrier et al., 2017a).

Sensitive searches for other elements and ion species surrounding $\pi$ Men c can also be made. Notably, the 10830 Å helium line that was recently detected for WASP-107b (Spake et al., 2018) could be explored, as well as ultraviolet lines of carbon, oxygen, nitrogen and magnesium previously detected around hot Jupiters (e.g. Vidal-Madjar et al., 2004; Fossati et al., 2010; Linsky et al., 2010; Ben-Jaffel and Ballester, 2013).

### 4.5.5 Possible X-ray transit features

In Section 4.3.2, I presented my X-ray light curve of HD 219134, in which I highlighted a possible transit-like feature at phases concurrent with, and surrounding, the primary transit. The only previous transit detections in X-ray were for HD 189733b (see Chapter 6, and Poppenhaeger et al., 2013).

To investigate this further, I extracted separate spectra for the 'in' and 'out of transit' phases. $0.98 < \phi < 1.02$ was defined as in transit, with all other phases defined as out of transit. This was chosen because the lower count rates around the optical transit in Fig. 4.3 extends out to roughly these phases. In the case of a genuine transit, this could be due to the extended nature of the coronal emission beyond the stellar disc. Moreover, in the analysis of HD 189733b, the ingress and egress of the X-ray transit extended out as far as $\phi \approx 0.94$ and 1.04, respectively

(Chapter 6).

I split both of the in-transit and out-of-transit spectra in three energy bins, cutting the total counts up to 2.5 keV across all orbital phases roughly evenly into three. I then took the ratio of the in and out spectra for each spectral bin. The result is plotted in Fig. 4.9. There is a disparity between the in and out phases in the softest and hardest energy bins.

The depth of the possible signal here is much greater: ∼20 per cent, as opposed to the ∼8 per cent for HD 189733b. The energy dependence is different too. For HD 189733b, the transit detection was much stronger at the softer energies than harder. However, for HD 219134b here, I see that the dips either side of the visible light transit appear to be driven by different energies to each other. From the middle and bottom panels of Fig. 4.3, one can see that the low count rate between phase 1.00 and 1.02 comes primarily from the softer energies, while the low count rate around phase 0.99 is clearly driven by a particularly low hard count rate at this point of the observation. Nothing like this is seen when combining 20 primary X-ray transits of HD 189733b, and such a clear difference in shape between hard and soft energies could point to coincidentally timed drops in count rate due to correlated noise, rather than a planetary transit. As presented in Section 4.3.3, the concurrent NUV light curve shows an upward trend. It could be argued that the EPIC-pn light curve shows a slight overall upward trend as well. There are hints that downward trends of smaller amplitude in the OM light curve around 1.05–1.06 in phase and towards the end of the observation, are also manifested in the X-ray light curves. Whatever the cause of the signal, be it stellar or planetary in origin, it seems to be present at both wavelengths.

Could a planet like HD 219134b even produce such a signal? The planet's radius places it toward to low-radius end of the evaporation valley, in a regime where a planet would be thought unlikely to have a substantial H/He envelope. Indeed, the current best density estimate for the planet by Gillon et al. (2017b) suggests it is slightly denser than the Earth. Furthermore, Dorn and Heng (2018) conclude that $H_2$ dominated atmospheres are unlikely for both planets b and c, but that secondary atmospheres are possible. The same study also suggests that the gas layer of planet b must be larger than for planet c because the two do not fall on the same mass-radius curve, though it is puzzling how such a planet could be undergoing atmospheric mass loss sufficient to cause a ∼20 per cent absorption of the star's coronal emission. However, I conclude that the situation is unclear enough as to recommend further *XMM-Newton* observations to investigate if this signal is indeed related to the transit or coincidentally timed variation.

## 4.6 Conclusions

I have analysed *XMM-Newton* observations of planets either side of the evaporation valley.

$\pi$ Men c, the first confirmed exoplanet from the *TESS* mission is a super-Earth orbiting a Sun-like star of naked-eye brightness. I find that the star has a soft X-ray spectrum and an X-ray luminosity similar to that of the Sun. It is also a variable X-ray source. I show that $\pi$ Men c suffers XUV irradiation around 2000 times stronger than that of the Earth. As a consequence, the planet atmosphere is likely to be escaping at a rate greater than that readily observed for the warm Neptune GJ 436b. Furthermore, I predict that $\pi$ Men is four times brighter than GJ 436 at Ly $\alpha$. I conclude that the detection of material escaping $\pi$ Men c using ultraviolet and infrared spectroscopy presents the current best opportunity to determine the composition of a super-Earth atmosphere.

HD 219134 is the closest known system with transiting planets. A relatively bright soft X-ray source was detected at the expected position of the star. I find that the closest planet to the star, HD 219134b, receives moderate XUV flux, 1500 times stronger than Earth, and was likely highly irradiated early in its life. Both it and planet c would have been stripped of any H/He envelope at this epoch. The current mass loss rates for both planets b and c is estimated to be similar to that for HD 97658b, another close-in planet which does retain a substantial envelope. I also see hints of a transit-like dip in the count rates at times matching the primary transit of planet b, an inference supported by investigating the ratio of spectral extractions of the in and out of transit events. However, it is very possible that the variation in count rate has an alternative explanation, and so I do not claim to have detected an X-ray transit in these observations. If subsequent observations were to build further evidence supporting a $\sim 20$ per cent transit, this would present a challenge to explain how a planet that probably does not have a substantial envelope could generate such a signal.

# Chapter 5

# XUV-driven evolution of young planets in the Praesepe open cluster

## 5.1 Introduction

The XUV emission of stars is highest in the first few hundred Myr of a star's life (e.g. Micela et al., 1985; Güdel et al., 1997; Micela, 2002; Feigelson et al., 2004; Jackson et al., 2012, see also Section 1.3.5). As such it is at these times that the majority of atmospheric evaporation is thought to occur, and features like the Neptunian desert and photoevaporation valley (see Sections 1.2.4 and 1.2.4) are thought to be carved out. Thus, young planetary systems, where strong XUV irradiation is ongoing, provide the best testing ground for this theory.

The vast majority of currently known exoplanets orbit mature stars, with ages of typically a few Gyr. This is primarily because of the challenges posed by stellar activity for the current dominant discovery methods, and because the target stars of the prolific *Kepler* mission were typically old field stars, as the field of view was deliberately chosen to avoid young stellar populations (Batalha et al., 2010). However, the repurposed mission of *Kepler*, known as *K2*, has targeted a number of open clusters searching for planets around younger stars. This has led to the discovery of nine planetary candidates orbiting eight stars in Praesepe (also known as M44, or the Beehive Cluster). Four of the planets were identified as candidates in 2016 (Pope et al., 2016; Barros et al., 2016; Libralato et al., 2016). One of these, K2-95, was later the subject of papers by Obermeier et al. (2016) and Pepper et al. (2017). In the former, the object was confirmed as a planet by

combining several techniques to rule out other scenarios. Mann et al. (2017, hereafter M17) validated six planets with false positive probabilities (FPP) of less than 1 per cent, including all four previously identified candidates. The seventh candidate in their study, EPIC 211901114b, was calculated to have a 2 per cent FPP, and was considered unvalidated. Recent studies by Rizzuto et al. (2018) and Livingston et al. (2018) announced the discovery of a new two-planet system from Campaign 16.

In this chapter, I present an analysis of X-ray observations of the host stars for four of these Praesepe planets, all taken by *XMM-Newton* in 2013 and 2015. Being members of a cluster, these systems have a far more reliable age estimate than most known planetary systems, which tend to be around field stars where ages are harder to constrain. Indeed, cluster ages are often used to calibrate age determination methods for use on field stars (for a review, see Soderblom, 2010). At ∼800 Myr years old (Brandt and Huang, 2015), these planets in Praesepe are also likely more intensely irradiated at the current epoch than systems previously studied at X-ray wavelengths, and so perhaps still undergoing significant atmospheric mass loss. Moreover, the estimated radii for most of these planets is consistent with being in or close to the photoevaporation valley and/or Neptunian desert, making them an ideal testing ground for these theories of planetary atmosphere evolution.

## 5.2 My Sample

My sample consists of K2-95, K2-100, K2-101, and K2-104. The planets and their host stars are detailed in Table 5.1, where the adopted values are from M17, unless stated otherwise. All four planets reside close to the Neptunian desert, photoevaporation valley, or both. They are therefore important in the context of studying these features in the exoplanet population, particularly given their relative youth.

The four planets are plotted in radius-period space in Fig. 5.1. Also plotted are lines showing the empirical Neptunian desert (Mazeh et al., 2016), a numerical determination of the lower desert boundary (Owen and Lai, 2018, for a core mass of $11.25\,M_\oplus$), and an analytical determination of the largest planet that can be a stripped core (OW17). I follow OW17 in only plotting the latter for periods greater than 3 d. OW17 also note that the evaporation and core composition models used affect the exact scaling and vertical position of the line, respectively. Similarly, the lower desert boundary from Owen and Lai (2018) plotted is one of a set of solutions the study finds, depending the core mass and atmospheric metallicity. I refer the reader to their paper and figures within for the full range of boundary solutions they determine, some of which reside above and below the representative line plotted here.

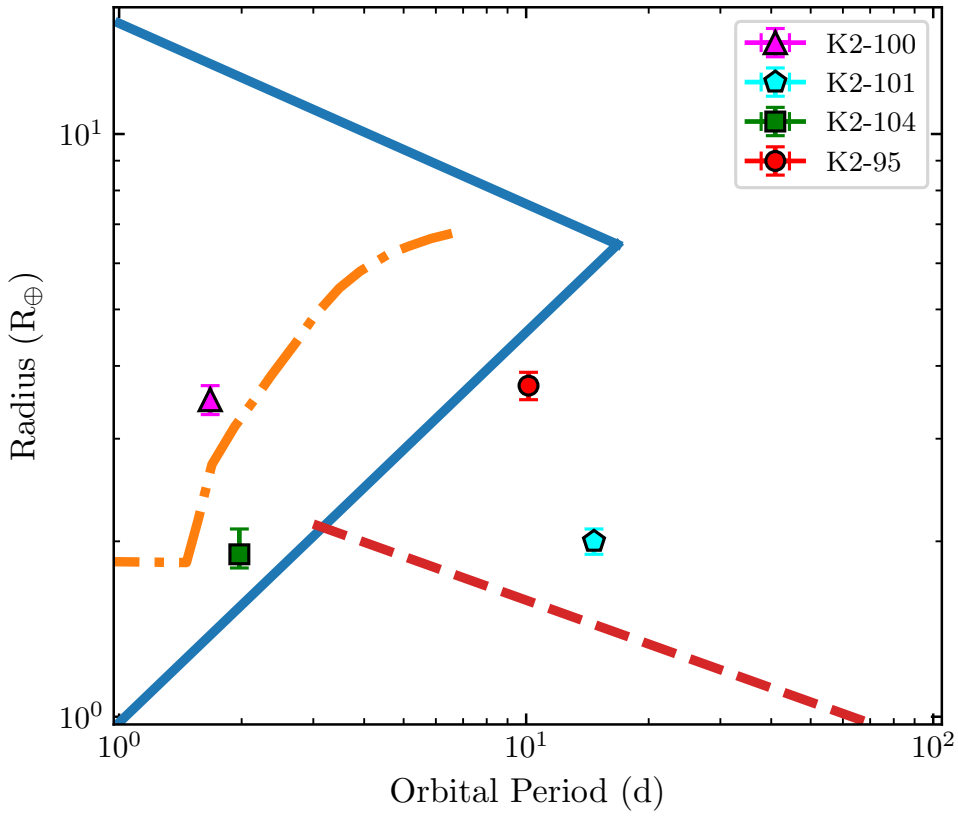


Figure 5.1: Positions of the four planets in my sample in radius-period space. The solid blue triangular region is the Neptunian desert, as empirically determined by Mazeh et al. (2016). The dashed red line corresponds to the most massive planet than can have been stripped bare at a given period, as analytically determined by OW17. The dot-dash orange line is one of the numerical solutions for the lower desert boundary determined by Owen and Wu (2017) for a core mass of 11.25 $M_\oplus$.

Fig. 5.1 highlights the proximity of the planets to evaporation features in the exoplanet population. K2-100b is seen to lie well inside the Mazeh desert. It is also inside the desert for most, though not all, solutions from Owen and Lai (2018). K2-104b also resides within the Mazeh desert. However, it lies below all the Owen and Lai (2018) solutions for the desert, and if one extrapolates the lower boundary of the evaporation valley to shorter periods it would lie below this line too, suggesting it could actually be a stripped core of a once larger planet. K2-101b intriguingly resides just a bit above the evaporation valley, and so could either retain a small envelope for the rest of its life, or could still be in process of being stripped. K2-95b's position is close to the Mazeh desert and so it is worth exploring whether it could have evolved out of this region, although the Owen and Lai (2018) solutions place it a bit further away from the desert.

Table 5.1: Parameters for the systems in my sample.

| System | Spectral Type | $V$ (mag) | $d$ (pc) | $R_*$ ($R_\odot$) | $T_{\rm eff,*}$ (K) | $P_{\rm rot}$ (d) | $R_{\rm p}$ ($R_\oplus$) | $P_{\rm orb}$ (d) | $T_0$ (†) | $T_{\rm eq}$ (K) |
|---|---|---|---|---|---|---|---|---|---|---|
| K2-95 | M2V | 17.22 | 180.7 | 0.44 | 3410 | 23.9 | 3.7 | 10.135091 | 140.74083 | 1738 |
| K2-100 | G0V | 10.52 | 190.0 | 1.19 | 6120 | 4.3 | 3.5 | 1.673916 | 144.06723 | 598 |
| K2-101 | K3V | 12.96 | 189.3 | 0.73 | 4819 | 10.6 | 2.0 | 14.677286 | 152.68135 | 780 |
| K2-104 | M1V | 16.36 | 190.2 | 0.48 | 3660 | 9.3 | 1.9 | 1.974190 | 140.38117 | 419 |

† Ephemerides are $\rm BJD_{TDB}$ - 2457000.

Parameters and ephemerides from M17 except:

$V$: K2-100 and K2-101 from APASS (Henden et al., 2012); K2-95 and K2-104 converted from SDSS g and r, using Jordi et al. (2006).

$d$: All converted from *Gaia* DR2 parallaxes.

$T_{\rm eq}$: Calculated from the M17 parameters assuming zero Bond albedo and uniform redistribution of heat

## 5.3 Observations

### 5.3.1 *XMM-Newton*

I have analysed archival *XMM-Newton* observations that together include data for the four systems introduced in Section 5.2. These observations are summarised in Table 5.2. K2-101, K2-95, and K2-104 have each been observed once, while K2-100 has been observed twice: once in 2013 when K2-104 was also within the field of view, and a second time in 2015. While the *XMM-Newton* Science Archive[1] lists an additional observation for K2-102 (ObsID: 0101440401; PI: Pallavicini), inspection of the images revealed the source to have fallen just outside the field of view of all three EPIC cameras (XMM-Newton has three co-aligned X-ray telescopes). Further, two of the objects, K2-104 and K2-95, fell on to one of the faulty CCDs of the EPIC-MOS1 camera during their respective observations. These two stars therefore only have data from EPIC-pn and EPIC-MOS2.

Only K2-95 happened to be located in the field of view of the Optical Monitor (OM). None of the observations specifically targeted these systems, and so the other objects fell outside the far smaller field of view of the OM. The K2-95 OM data were taken with the UVM2 filter.

The data were reduced using the Scientific Analysis System (SAS 16.0.0). The standard procedures were used in each case[2]. Elevated high-energy background, due to Solar soft protons (Walsh et al., 2014), affected a small proportion of each observation. These periods were filtered out during the spectral fitting and ensuing analyses. However, the unfiltered data are used to produce the light curves in Section 5.4.1, in order to avoid having gaps in them.

### 5.3.2 K2 light curves

Praesepe was observed in 2015 between April 27 and July 10 as part of campaign 5 of the *K2* mission. Three of the *XMM-Newton* observations described above were simultaneous with the *K2* observations: the 2015 observations of K2-100, K2-101, and K2-95. I analysed the spot modulation of each star in its K2 light curve, in order to determine the modulation and phase at the time of the *XMM-Newton* observations. I obtained the detrended, corrected *K2* light curves output by the EVEREST pipeline (Luger et al., 2016, 2017). These were downloaded from the Barbara A. Mikulski Archive for Space Telescopes (MAST).

[1] `http://nxsa.esac.esa.int`

[2] As outlined on the 'SAS Threads' webpages: `http://www.cosmos.esa.int/web/xmm-newton/sas-threads`

Table 5.2: Details of the *XMM-Newton* observations.

| System(s) | ObsID | PI | Start time (TDB) [a] | Exp. T (ks) [a] | Start – Stop phase [b] | Transit phase [b] | EPIC Cameras [c] | EPIC filter |
|---|---|---|---|---|---|---|---|---|
| K2-100 | 0721620101 | Agueros | 2013-10-30 11:34 | 68.8 | 0.573 – 1.057 | 0.981 – 1.019 | All | Thin |
| K2-104 | | | | | 0.241 – 0.652 | 0.987 – 1.013 | pn, MOS2 | |
| K2-100 | 0761920901 | Drake | 2015-05-06 00:36 | 59.9 | 0.662 – 1.077 | 0.981 – 1.057 | All | Medium |
| K2-101 | 0761921001 | Drake | 2015-05-09 13:13 | 50.0 | 0.957 – 0.998 | 0.995 – 1.005 | pn, MOS2 | Medium |
| K2-95 | 0761921101 | Drake | 2015-05-11 23:19 | 61.2 | 0.355 – 0.426 | 0.995 – 1.005 | All | Medium |

[a] Start time and duration are given for EPIC-pn.

[b] All ephemerides taken from Mann et al. (2017).

[c] Listing of which of the EPIC cameras' fields of view the source appears in. The three EPIC cameras are pn, MOS1, and MOS2.

## 5.4 *XMM-Newton* results

K2-100 and K2-101 were both very clearly detected at the expected position in all three EPIC cameras. Restricting the MOS2 images for K2-95 to 0.6–1.0 keV, energies expected to be bright for young objects due to Fe L-shell emission, showed an excess of counts at the expected position of the star. Using the same energy band in the pn for K2-104 revealed a marginal detection.

In analysing each observation, I employed 15 arcsec radius source regions, centred on the proper-motion-corrected positions of each system. Multiple background regions from the same CCD chip were used for background subtraction. K2-104 is close on the sky to a galaxy cluster, the outskirts of which contribute additional background to the source region. I attempted to mitigate this by placing my background regions on an arc about the centre of the galaxy cluster on the chip, such that the contamination would be similar in each background region to that in the source region.

The only target falling in the OM field of view, K2-95, was not detected in those observations using the UVM2 filter. The source detection algorithm applied by the standard reduction chain did not detect any source within 30 arcsec of the expected position of the star. Visual inspection of the images confirmed the non-detection.

### 5.4.1 X-ray light curves

I coadded the count rates across all EPIC cameras for which data were available for each of the observations. The resulting X-ray light curves are plotted in Fig. 5.2, covering the energy range 0.2–2.5 keV. Transit phases in the optical are displayed as grey shaded regions. This was searched for temporal variation in the X-ray flux, as well as for hints of transit features.

None of the observations show any strong flares, and none of the three light curves covering either a full or partial transit show any evidence of transit features. Both K2-100 datasets exhibit some variation in the count rate. The 2013 data dips down in a few places, while the 2015 data slopes down over the first 20 ks before flattening off for the rest of the observation. This is explored further in the context of the simultaneous *K2* data in Section 5.5. The other three light curves suffer from a lack of counts, making them insensitive to low amplitude variability. The points with large error bars in each of the K2-100 (2015), K2-101, and K2-95 light curves correspond to periods of elevated background and are not indicative of any genuine source variability.

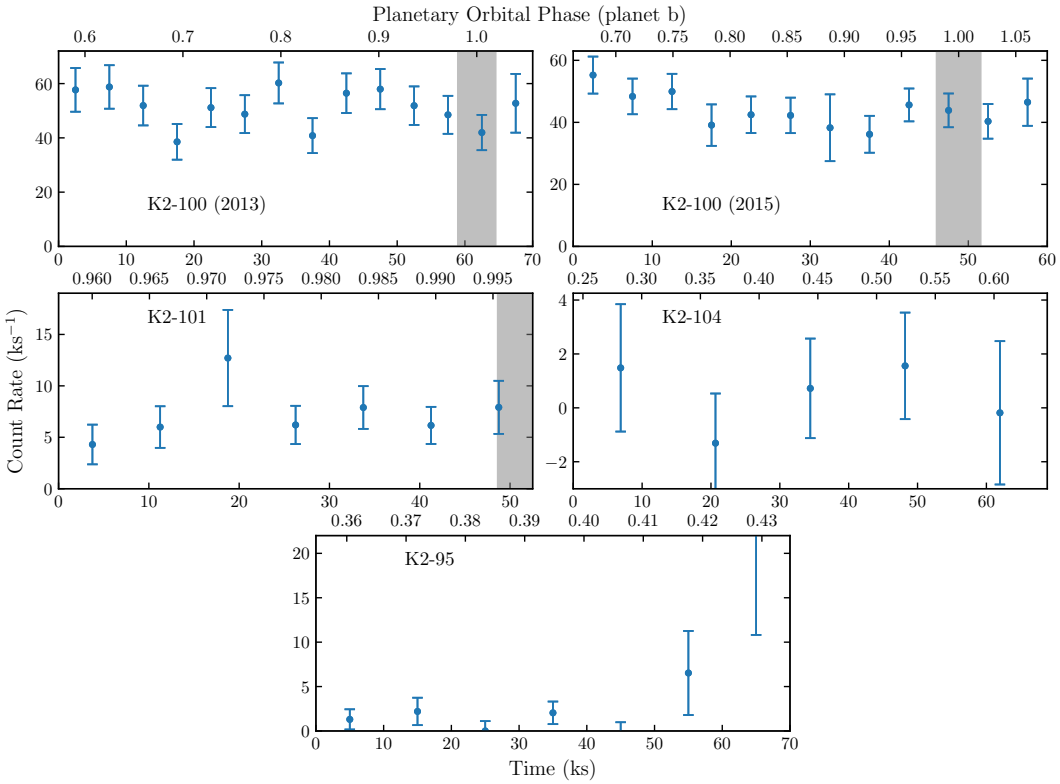


Figure 5.2: Background corrected X-ray light curves of the observations, covering the energy range 0.2–2.5 keV. The count rate is the sum of all EPIC detectors for which data were available. Areas shaded in grey are the planetary transits (1st to 4th contact) in visible light.

### 5.4.2 X-ray spectra

The X-ray spectra for each EPIC camera from each observation is displayed in Fig. 5.3. Overplotted in each case is my best fit model, as fitted using XSPEC 12.9.1p (Arnaud, 1996). For the K2-100 observations, where I had a relatively large number of counts, I binned the spectra to a minimum of 25 counts prior to fitting. This choice was unsuitable for the other three objects, all of which had a more limited number of counts, and their spectra were therefore binned to a minimum of 10 counts. Accordingly, I used the C-statistic in fitting models to these three spectra (Cash, 1979). The K2-100 analysis used $\chi^2$ as the fit statistic. Throughout my analysis, I estimated uncertainties using a combination of XSPEC's built-in MCMC sampler and error command. These values correspond to the 1-$\sigma$ (68 per cent) level, and are calculated from chains run for 100000 steps following 5000 used for burn-in. Abundances were set to Solar values (Asplund et al., 2009).

In all cases, APEC models were used to fit the spectrum (Smith et al., 2001).

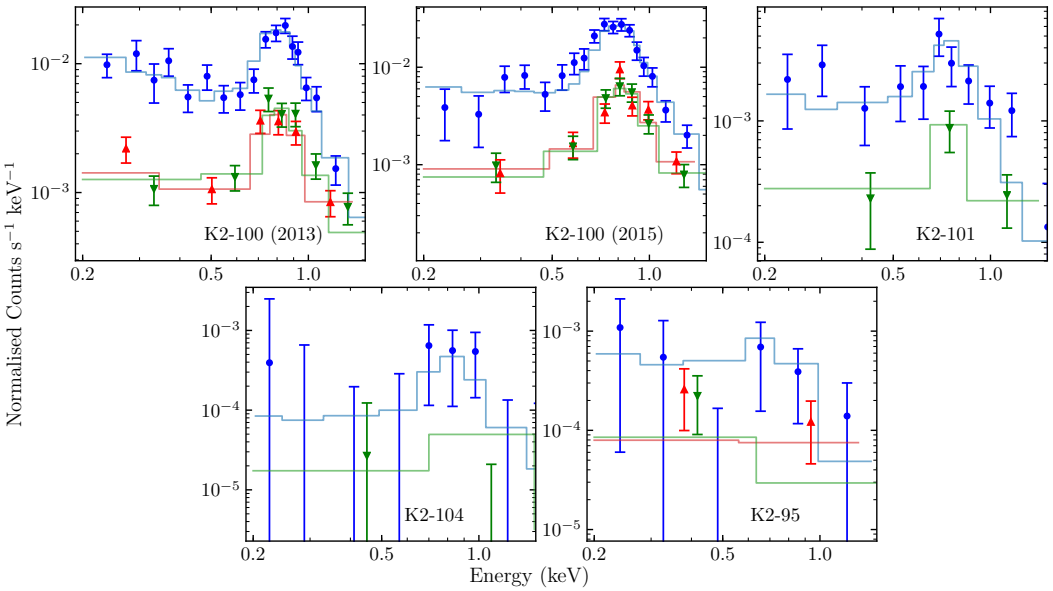


Figure 5.3: Observed X-ray spectra for each of the observations, displayed along with the best fit model. Each EPIC camera is displayed separately: EPIC-pn is shown with blue circles, EPIC-MOS1 with red up-pointing triangles, and EPIC-MOS2 with green down-pointing triangles.

For K2-100, the spectra were of good enough quality to warrant a two-temperature fit. These temperatures were forced to be equal across the two observations, but their normalisations were allowed to vary. The low count rates for both K2-104 and K2-95 meant that I had to limit the range of temperatures to be below 1.5 keV, to prevent it reaching unreasonable values.

As in Chapters 3 and 4, interstellar absorption was accounted for by including a multiplicative TBABS model term (Wilms et al., 2000). I initially performed the K2-100 fit with the hydrogen column density, $N_{\rm H}$, left free, except for a hard upper limit set to the total Galactic H I along the line of sight taken from Kalberla et al. (2005)[3]. The fit favoured a value equal to this limit ($2.74 \times 10^{20}\,{\rm cm}^{-2}$), but with a wide distribution of values stretching out to smaller $N_{\rm H}$. In order to account for the effect of the uncertainty in the column density on the X-ray fluxes, I therefore performed two final fits for each object: one with the $N_{\rm H}$ fixed to the Galactic limit, and a second with it set to the 10th percentile of the values in the chain from the MCMC run with $N_{\rm H}$ free (giving $1.45 \times 10^{20}\,{\rm cm}^{-2}$). Since the $N_{\rm H}$ is relatively unconstrained in that MCMC fit, the latter gives a plausible lower limit for its value, based on the K2-100 data. I applied these two estimates of $N_{\rm H}$ to each of the sources.

[3]This was calculated using an online HEASARC tool: `https://heasarc.gsfc.nasa.gov/cgi-bin/Tools/w3nh/w3nh.pl`.

Table 5.3: Results of the X-ray spectral analysis. The top and bottom halves correspond to the results with $N_{\rm H}$ fixed to the total Galactic H I along the line of sight and the 10th percentile of the $N_{\rm H}$ chain in a fit to the K2-100 datasets, respectively. All fluxes and luminosities are for the 0.2–2.4 keV band, except for the final three columns, which are for the 0.1–2.4 keV 'ROSAT' band. The latter all have '0.1' added in subscript to their column header.

| System | kT (keV) | EM ($a$) | $F_{\rm X}$ ($b$) | $L_{\rm X}$ ($c$) | $L_{\rm EUV}$ ($c$) | $F_{\rm XUV,\,p}$ ($d$) | $F_{\rm XUV,\,1\,au}$ ($e$) | $L_{\rm X,0.1}$ ($c$) | $\frac{L_{\rm X,0.1}}{L_{\rm bol}}$ ($\times 10^{-5}$) |
|---|---|---|---|---|---|---|---|---|---|
| | | | | $N_{\rm H}$= $2.74 \times 10^{20}$ cm$^{-2}$ | | | | | |
| K2-100 (2013) | $0.0869^{+0.0001}_{-0.024}$<br>$0.629^{+0.018}_{-0.023}$ | $174^{+420}_{-8}$<br>$68.3^{+4.3}_{-3.3}$ | $72.5^{+3.8}_{-4.0}$ | $313^{+18}_{-19}$ | $255^{+65}_{-66}$ | $162^{+20}_{-21}$ | $202^{+23}_{-24}$ | $630 \pm 320$ | $9.2 \pm 4.6$ |
| K2-100 (2015) | *As 2013* | $40^{+72}_{-15}$<br>$68.3^{+3.7}_{-3.2}$ | $47.5^{+2.2}_{-2.3}$ | $205 \pm 11$ | $206 \pm 47$ | $118^{+14}_{-16}$ | $146 \pm 17$ | $410 \pm 300$ | $6.0 \pm 3.0$ |
| K2-101 | $0.357^{+0.071}_{-0.031}$ | $16.6^{+2.3}_{-2.9}$ | $8.6 \pm 1.1$ | $36.8 \pm 4.8$ | $53 \pm 14$ | $2.61 \pm 0.43$ | $32.0^{+5.1}_{-5.2}$ | $74^{\pm}38$ | $7.6 \pm 3.9$ |
| K2-104 | $0.71^{+0.50}_{-0.54}$ | $2.0^{+3.9}_{-0.8}$ | $1.2^{+0.8}_{-0.9}$ | $5.1^{+3.5}_{-4.0}$ | $13^{+10}_{-11}$ | $10.4^{+6.1}_{-6.5}$ | $6.5^{+3.8}_{-4.2}$ | $10.2^{+6.6}_{-7.6}$ | $7.3^{+4.7}_{-5.4}$ |
| K2-95 | $0.27^{+0.78}_{-0.07}$ | $3.8^{+2.1}_{-1.8}$ | $2.1^{+0.7}_{-0.8}$ | $8.1^{+2.7}_{-3.3}$ | $15.0^{+6.7}_{-7.9}$ | $1.74^{+0.56}_{-0.60}$ | $8.2^{+2.6}_{-3.0}$ | $16^{+9}_{-11}$ | $18^{+10}_{-12}$ |
| | | | | $N_{\rm H}$= $1.45 \times 10^{20}$ cm$^{-2}$ | | | | | |
| K2-100 (2013) | $0.093^{+0.005}_{-0.031}$<br>$0.634^{+0.016}_{-0.023}$ | $99^{+307}_{-17}$<br>$66.0^{+4.3}_{-3.0}$ | $59.7^{+4.3}_{-2.6}$ | $258^{+20}_{-13}$ | $232^{+61}_{-55}$ | $140 \pm 18$ | $174^{+22}_{-20}$ | $520 \pm 260$ | $7.6 \pm 3.8$ |
| K2-100 (2015) | *As 2013* | $16^{+43}_{-7}$<br>$66.0 \pm 3.4$ | $42.3^{+2.2}_{-1.8}$ | $183^{+11}_{-9}$ | $194^{+44}_{-43}$ | $108^{+13}_{-14}$ | $134^{+16}_{-15}$ | $370 \pm 180$ | $5.4 \pm 2.7$ |
| K2-101 | $0.370^{+0.080}_{-0.032}$ | $15.5^{+2.1}_{-2.8}$ | $8.0^{+1.0}_{-1.1}$ | $34.1^{+4.3}_{-4.6}$ | $51^{+13}_{-14}$ | $2.47^{+0.40}_{-0.41}$ | $30.4^{+4.8}_{-5.0}$ | $68 \pm 35$ | $7.0 \pm 3.6$ |
| K2-104 | $0.71^{+0.52}_{-0.52}$ | $1.9^{+3.6}_{-0.7}$ | $1.1^{+0.8}_{-0.8}$ | $5.0 \pm 3.6$ | $13 \pm 10$ | $10.1^{+6.2}_{-6.0}$ | $6.3 \pm 3.9$ | $9.9^{+8.4}_{-7.4}$ | $7.0^{+6.0}_{-5.3}$ |
| K2-95 | $0.27^{+0.85}_{-0.06}$ | $3.6^{+1.7}_{-1.7}$ | $2.0^{+0.6}_{-0.8}$ | $7.7^{+2.2}_{-3.2}$ | $14.6^{+5.9}_{-7.9}$ | $1.67^{+0.50}_{-0.60}$ | $7.9^{+2.3}_{-3.0}$ | $15^{+8}_{-10}$ | $17^{+9}_{-12}$ |

*a* $10^{50}$ cm$^{-3}$ (Emission measure)
*b* $10^{-15}$ erg s$^{-1}$ cm$^{-2}$ (at Earth, unabsorbed)
*c* $10^{27}$ erg s$^{-1}$
*d* $10^{3}$ erg s$^{-1}$ cm$^{-2}$
*e* erg s$^{-1}$ cm$^{-2}$

Table 5.3 summarises the findings of my spectral analysis of each observation. The best fit temperatures and emission measures are given for both $N_{\rm H}$ values used. Estimated fluxes, luminosities and planetary irradiation levels are given for both fits to each observation. The extrapolations to the EUV were performed using the empirical relations I derived in Chapter 3, based on the method of Chadney et al. (2015). All system parameters adopted are from M17, with the exception of the distance, for which I calculate individual distances for each system using the parallaxes from Gaia DR2 (Gaia Collaboration et al., 2018).

The K2-100 data allows a comparison of the stellar X-ray output at two separate epochs. The flux is about 40-50 % higher in the 2013 data than the 2015 data. From both the spectra in Fig. 5.3 and the emission measures in Table 5.3, one can see that this change is being driven by the softest energies. The emission measures of the higher temperature component are in excellent agreement, but the 2015 emission measure for the lower temperature component is some five or six times smaller.

All the results above are for the 0.2–2.4 keV band. I also calculated fluxes for both $N_{\rm H}$ choices for each object in the 0.1–2.4 keV band in XSPEC, in order to compare to previous studies of the rotation-X-ray output relationship. These fluxes are given in Table 5.3. As I did in Chapter 3, I estimated the 0.1–2.4 keV flux by doubling the 0.2–2.4 keV flux. The values used for $L_{\rm bol}$ are those from M17, but scaled to the distances from *Gaia* DR2.

## 5.5 *K2* results

I examined the EVEREST-corrected light curves for the three stars with simultaneous *K2* and *XMM-Newton* observations. This was performed with the aim of putting the X-ray observations into the context of the optical spot modulation, including searching for correlated variability between the optical and X-ray light curves. The data are plotted in Fig. 5.4, which includes both the entire Campaign 5 light curve (left panels), and a zoomed in section (right panels) around the epoch of the *XMM-Newton* observations, which is highlighted by the blue shaded region in each panel. All three stars show obvious spot modulation in their light curves, on the order of a few per cent.

From Fig. 5.4, I can see that the K2-100 *XMM-Newton* data cover a relatively large rise in the optical light curve, on the order of about 1 per cent. For K2-101, a much shallower rise in optical flux through the X-ray observation epoch is evident in the right-hand middle panel of Fig. 5.4. However, the larger modulation amplitude

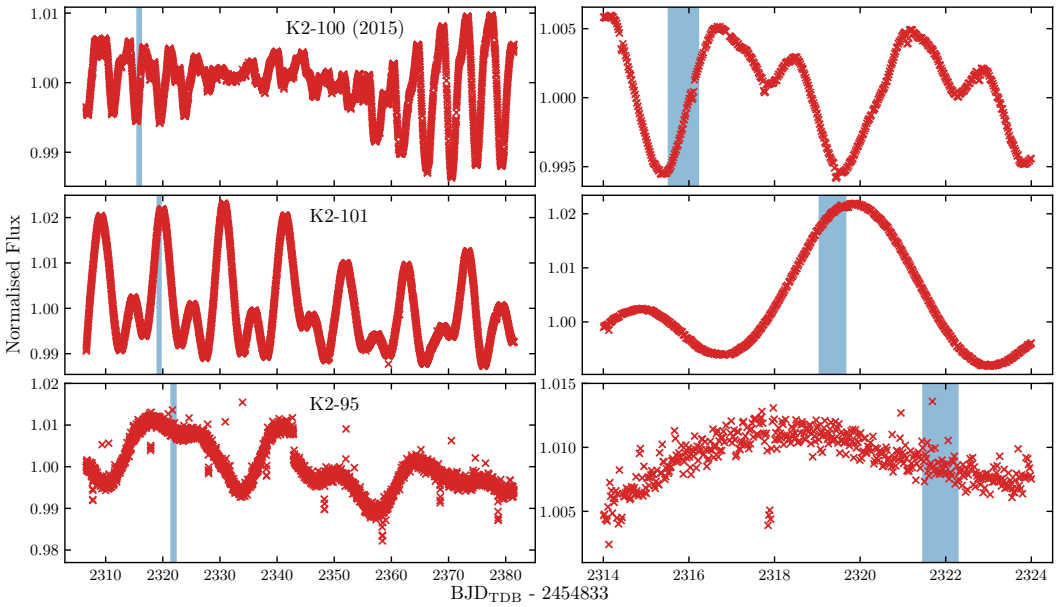


Figure 5.4: *K2* light curves, detrended and corrected by the EVEREST pipeline, for each of the three targets with simultaneous *K2* and *XMM-Newton* observations. Horizontally, the left-hand panels plot the full Campaign 5 light curves, while the right-hand panels zoom to the few days around where the simultaneous *XMM-Newton* data were taken. Vertically, the top panels are for K2-100, the middle for K2-101, and the bottom for K2-95. The blue shaded region in all panels shows the epoch of *XMM-Newton* observations for that system.

for this star (∼3 per cent versus ∼0.5–2 per cent for K2-100) means the fractional increase in the *K2* flux during the *XMM-Newton* observations is still about 0.4 per cent. The longer rotation period of K2-95 means that substantial changes in the optical flux due to spot modulation are on a timescale a little too long to be important through the length of an average *XMM-Newton* observation. K2-95 also shows numerous outliers at elevated fluxes, suggestive of frequent flaring, which is to be expected for a young, active star. Its late spectral type also means such events are more easily observed for this star than K2-100 and K2-101.

In Fig. 5.5, I replot the *XMM-Newton* light curves from Fig. 5.2, together with the simultaneous *K2* data. This highlights an increase in the optical flux of K2-100 throughout the *XMM-Newton* observation, simultaneous with a decrease in the X-ray flux followed by a plateau. Optically-dim starspots and X-ray bright coronal loops are both associated with active regions, and hence such behaviour of the X-ray and optical flux is reasonable and could be astrophysical. While K2-101 also shows a rise in optical flux through the time of the X-ray observations, albeit a smaller one fractionally, the factor of a few lower X-ray count rate likely means any

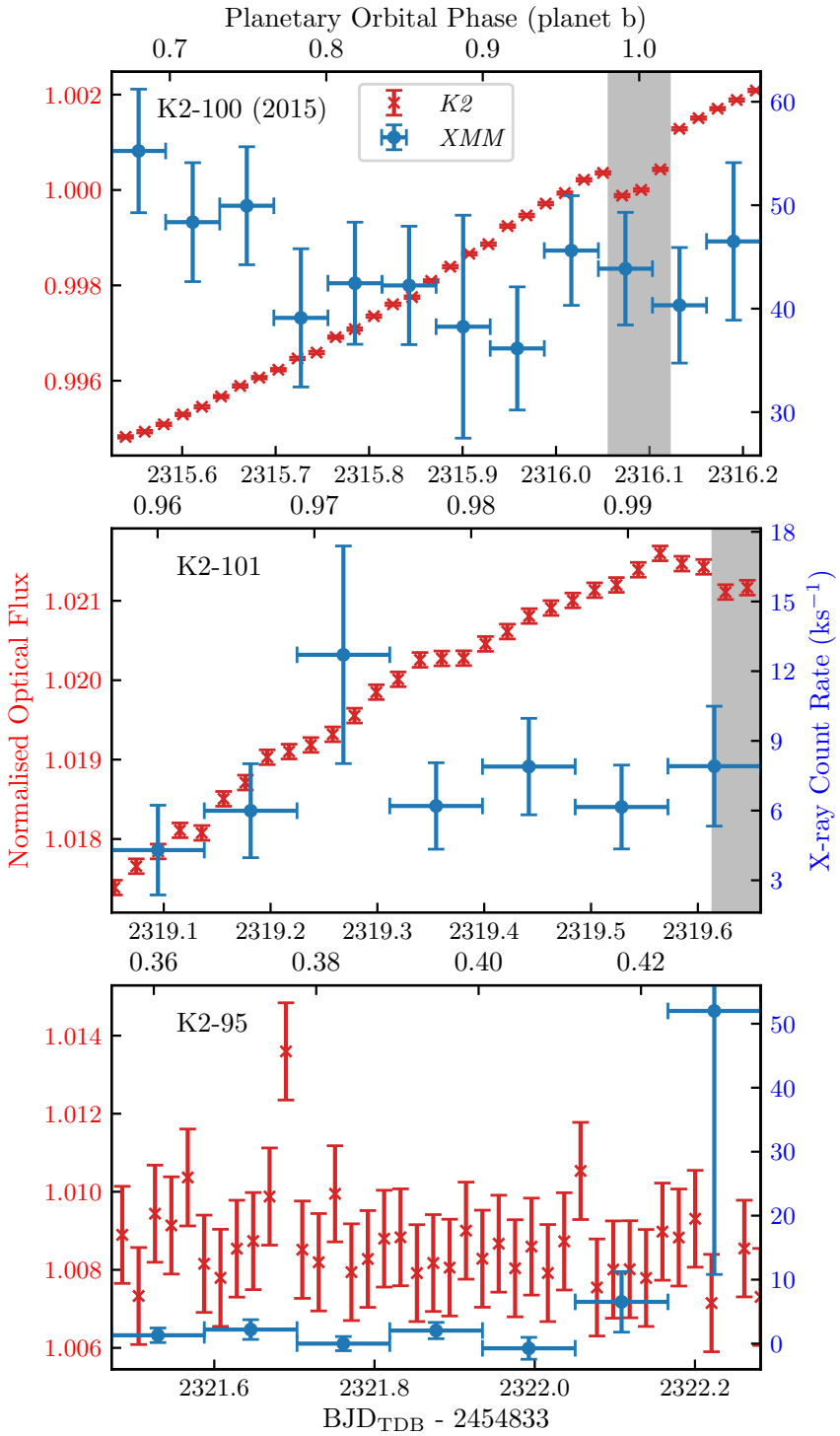


Figure 5.5: Comparison of the EVEREST *K2* and *XMM-Newton* light curves. The top, middle, and bottom panels are for K2-100, K2-101, and K2-95, respectively. The *K2* data are shown as red crosses, and the *XMM-Newton* data are the blue circles. The grey shaded regions display the optical light transit epochs.

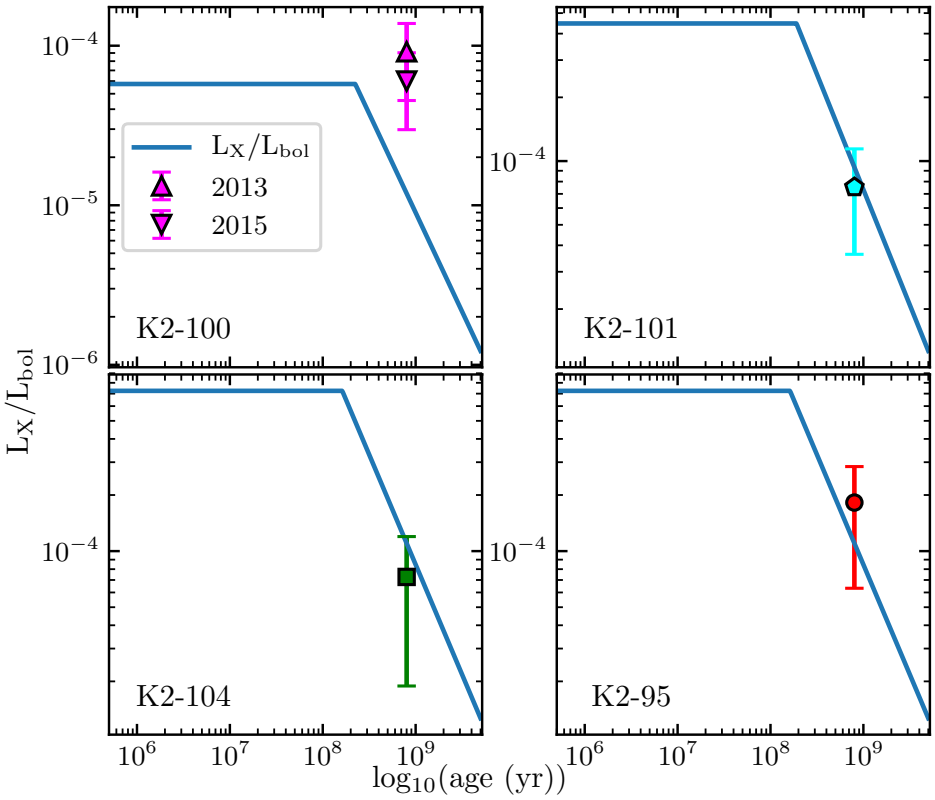


Figure 5.6: Comparison of the X-ray emission evolution of the stars in my sample, according the X-ray-age relations of J12. The measured $\log(L_X/L_{bol})$ in the 0.1–2.4 keV band are also plotted for each star.

effect on the X-ray output is too small to be seen within the uncertainties for this star.

## 5.6 Discussion

### 5.6.1 X-ray output

In section 1.3.5, I described how coronal X-ray emission reduces over a star's lifetime, as it spins down through magnetic braking, and how X-ray-age and X-ray-rotation relationships have been explored. The emission is saturated for 100 Myr or so, with $L_X/L_{bol} \approx 10^{-3}$, before falling off as a power law as the rotation period increases.

I give the $L_X/L_{bol}$ in the 0.1–2.4 keV band for each observation in Table 5.3. The values of $L_X/L_{bol}$ for this sample of host stars cluster around $10^{-5}$ to $10^{-4}$. These are all smaller, by an order of magnitude or more, than the observed saturation level at around $10^{-3}$. Therefore, the irradiation rates at the planets are now lower

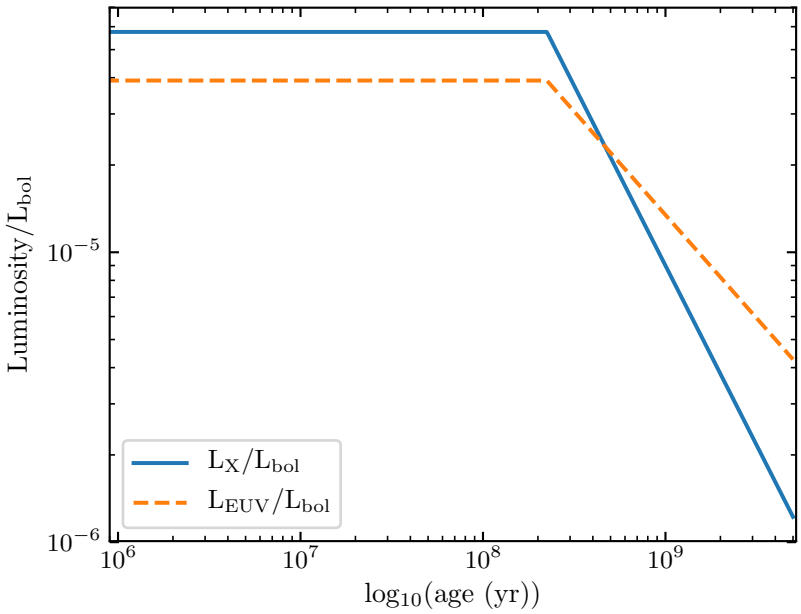


Figure 5.7: Comparison of the X-ray (blue solid line) and EUV (orange dashed line) emission evolution of K2-100. The X-ray evolution is that given by the X-ray-age relations of J12, and then extrapolated to EUV using the relations derived in Chapter 3.

than they would have been over the first few hundred Myr of their lives, but still higher than many middle-aged field stars.

Fig. 5.6 compares the estimates to the X-ray-age relations of Jackson et al. (2012, hereafter, J12). My observed values agree nicely with the relations, except for K2-100. This is likely because the saturation level for the two bluest B-V colour bins in the J12 study is substantially lower than the rest. K2-100 falls into the second bluest, where the saturation level is $\log(L_X/L_{bol}) = -4.24$, far below the canonical value of about $-3$ (see Section 1.3.5). Lower X-ray luminosity ratios for saturated stars bluer and more massive than the Sun have been found in other studies too (e.g. Pizzolato et al., 2003; Wright et al., 2011). The exact cause is unknown, but could possibly be linked to supersaturation, where at very high rotational velocities, $L_X/L_{bol}$ has been observed to decrease slightly below the saturation level (Randich et al., 1996).

I also numerically integrated J12 X-ray age relations to calculate both the total X-ray emission to date, and that still to come between now and the age of an average field star, which I take to be 5 Gyr. I applied my EUV extrapolation method from Chapter 3 at each timestep of the integration, in order to obtain estimates pertaining to the full XUV range. These values permit the calculation of

Table 5.4: Assumed masses for each planet, together with estimates of the current mass loss rate, total lifetime mass loss, and future XUV irradiation. The top and bottom values of mass loss and constant rate total lifetime loss are estimated from the 2013 and 2015 *XMM-Newton* observations, respectively.

| Planet | $M_{\rm p}^{*}$ ($M_{\oplus}$) | $\log \dot{M}_{\rm En}$ ($\rm g\,s^{-1}$) | Lifetime Loss % Const.$^{\dagger}$ | J12$^{\ddagger}$ | $\rm E_{X,f}^{\dagger\dagger}$ | $\rm E_{EUV,f}^{\dagger\dagger}$ % |
|---|---|---|---|---|---|---|
| K2-100b (2013) | $13.3^{+2.9}_{-2.8}$ | 11.4 | 6.7 | 5.0 | 34 | 58 |
| K2-100b (2015) | | 11.2 | 4.9 | | | |
| K2-101b | $6.5 \pm 2.3$ | 9.0 | 0.07 | 0.28 | 39 | 61 |
| K2-104b | $6.1^{+2.5}_{-2.4}$ | 9.6 | 0.31 | 1.5 | 33 | 58 |
| K2-95b | $14.3^{+3.0}_{-2.9}$ | 9.3 | 0.06 | 0.15 | 33 | 58 |

* Planetary mass, estimated using the mass-radius relation of Wolfgang et al. (2016).
† Lifetime to date mass loss rate, assuming a constant XUV irradiation rate in the past at the current level.
‡ Lifetime to date mass loss estimated by the relations of Jackson et al. (2012).
†† Future stellar emission from 800 Myr to 5 Gyr, estimated using the relations of Jackson et al. (2012) together with the EUV extrapolations derived in Chapter 3. Given as % of total output (past and future) to 5 Gyr.

total mass loss rates to date, as well as a comparison between the irradiation already received by these planets, and that received by the older Kepler sample, for which the evaporation valley was measured. Fig. 5.7 shows a clear dominance of EUV over X-rays for ages greater than a few hundred Myr. The estimates, in Table 5.4 reveal that a significant proportion of the irradiation is still to come, especially at EUV wavelengths where the value is over half in each case. This has possible implications for future mass loss and evolution of the planet's atmospheres.

### 5.6.2 Planetary mass loss

Using the XUV irradiation calculated in Section 5.4.2, I was able to estimate the current mass loss rate for each planet. I initially adopted the energy-limited approximation (equation 1.9), together with canonical values for $\eta$ and $\beta$ of 0.15 and 1.00 (as used in Chapters 3 and 4). None of the seven planets presented by M17 have mass measurements. Most have too faint hosts or are likely too small for radial velocity follow up to measure well constrained masses. Furthermore, each system has only a single planet detected, and so there is currently no possibility of measuring transit timing variations to infer masses. Instead, I use the mass-radius

Table 5.5: Mass loss rate estimates using the interpolation tool $\dot{M}_{\rm Kuby}$, the hydro-based approximation $\dot{M}_{\rm HBA}$, and a further application of the energy-limited formula $\dot{M}_{\rm En}$ using the output $\beta$ from the interpolation tool. The masses assumed are the same as in Table 5.4.

| Planet | $\log \dot{M}_{\rm Kuby}$ ($\rm g\,s^{-1}$) | $\beta$ | $\log \dot{M}_{\rm HBA}$ ($\rm g\,s^{-1}$) | $\log \dot{M}_{\rm En}$ ($\rm g\,s^{-1}$) |
|---|---|---|---|---|
| K2-100b (2013) | 12.6 | 1.45 | 13.4 | 11.7 |
| K2-100b (2015) | 12.6 | 1.51 | 13.3 | 11.6 |
| K2-101b | 9.5 | 1.40 | 9.2 | 9.3 |
| K2-104b | 9.6 | - | 10.4 | - |
| K2-95b | 8.8 | 1.26 | 9.0 | 9.5 |

relation and associated code[4] of Wolfgang et al. (2016) to estimate the mass of the four planets in my sample, $M_{\rm p}$. Their method is a Bayesian probabilistic model for the relation, quantifying and accounting for intrinsic scatter due to the range of compositions present, and allows for uncertainties on the parameters to be estimated. The calculated masses for each planet are given along with the resulting energy-limited mass loss rates in Table 5.4. I give two mass loss rates for K2-100b, corresponding to the 2013 and 2015 observations. These values are calculated for the $N_{\rm H} = 2.74 \times 10^{20}\,\rm cm^{-2}$ fits to the X-ray spectra. The corresponding estimates for the $N_{\rm H} = 1.45 \times 10^{20}\,\rm cm^{-2}$ fits differ by less than 20 per cent in all cases, and less than 5 per cent for K2-101, K2-104 and K2-95. This is small compared to the uncertainties, for example due to the efficiency of the mass loss processes (see Section 1.2.3).

As in Chapters 3 and 4, I also applied the interpolation tool that estimates mass loss according to the Kubyshkina et al. (2018a) models. These mass loss rates are given in Table 5.5, together with the output values of $\beta$. I then also fed the output values of $\beta$ back into the energy-limited formula, for a more direct comparison. K2-104b raised a segmentation fault on the publicly available version of the code. I was able to obtain a mass loss rate, but not a $\beta$, by contacting the authors, who ran it through their version of the code. I then also calculated the hydro-based approximation from the author's follow up paper (Kubyshkina et al., 2018b) to check if that value was sensible, given the issues. I give values calculated in this way for all of the planets in Table 5.5, for completeness. This method gives rates for K2-100b and K2-104b that are somewhat greater than the interpolator tool. As for HD 219134b and c in Chapter 4, if either of the smaller planets, K2-101b and K2-104b, do not retain a substantial hydrogen envelope, then the validity of the

[4]Their code: `https://github.com/dawolfgang/MRrelation`

Kubyshkina et al. (2018a) models for those planets is uncertain.

K2-100b is almost certainly undergoing the greatest current level of mass loss, in absolute terms, of the planets in my sample. This is owing to the combination of its relatively large radius and mass, together with its small separation from and large XUV output of its host star. If K2-104b still retains a substantial envelope, it is losing mass at only a slightly greater rate than K2-101b and K2-95, despite its much shorter orbital period and separation. For K2-101b, this is because the stellar XUV output of the star is much greater than K2-104, while K2-95b has double the radius of K2-104b, and so the XUV absorbing region is about four times as large.

The current mass loss rates calculated above can be used to inform discussion of the temporal evolution of the planets' atmospheres. Alongside my current energy-limited rate estimates in Table 5.4, I also present estimates of the lifetime mass loss. Two estimates are given: one assuming the current mass loss rates have been constant over the planets' 800 Myr lifetimes, and another using the integrated X-ray-age relations of J12 from Section 5.6.1. One would expect the former to give a lower limit estimate of the total lifetime loss, as the XUV output of the stars would have been higher in the past, especially when the emission was saturated. The lifetime mass loss estimated using the 2013 K2-100 observation's irradiation rate at a constant level gives a greater value than the J12 method. This is again because the saturation level for K2-100's B-V bin is substantially lower than all bins redder than its one. As when this method was previously applied in Chapters 3 and 4, one should also note that these mass loss estimates were calculated assuming a constant radius across the planet's life. In reality, this is something that will change as the planet reacts to the mass loss from it, especially for smaller planets where adding an envelope with a mass fraction of just a few per cent to a super-Earth-sized core can double the planet's radius (OW17).

### 5.6.3 Past and future evolution

In Section 5.6.1, I showed the majority of EUV, and almost half of the total XUV, emission from each of these stars is still to come. Under the energy-limited assumptions of mass loss, this could mean further substantial evolution of these planets' atmospheres. I discuss the possible implications of this on a planet-by-planet basis below. While reading these discussions, the reader should bear in mind that some theoretical studies have suggested that EUV heating may be less important than X-ray heating as it is less efficient at driving the mass loss, perhaps contributing less than 10 per cent of the total (Owen and Wu, 2013). On the other hand, that study and others (e.g. Owen and Jackson, 2012) have assumed the EUV emission to

have the same time evolution as the X-ray, unlike that assumed here. This assumption would lead to an underestimation of the EUV irradiation in the post-saturation regime. As I outlined in Section 1.2.2, the uncertainty in the relative importance of X-ray and EUV means I have chosen to assume they are equally important in this work.

### K2-100b

K2-100b is estimated to have lost about 5 per cent of its mass over its lifetime. A value of several per cent mass loss across the planet's lifetime seems sensible, in any case. Neptune and Uranus have been estimated to have envelope mass fractions between 5 and 15 per cent (Guillot, 1999; Helled et al., 2011, e.g.), so a lifetime mass loss much higher than the estimates here would lead one to think the planet had been totally stripped of its envelope, which it is unlikely to have been given its current radius. While there may have been considerable stripping of the planet over its 800 Myr life, it cannot have started as a Jupiter; the estimated mass loss for a Jupiter mass, Jupiter radius planet with this irradiation history is just 0.3 per cent.

The planet could now be on the desert boundary depending on its core mass, or be in thin strip in radius-period space where low mass planets (even down to $\sim 5\,M_\oplus$) can exist having undergone high-eccentricity migration (Owen and Lai, 2018). However, with the future irradiation predicted in Section 5.6.1, and the estimated mass from the Wolfgang et al. (2016) relation, K2-100b could lose as much as 5 per cent of its current mass between now and 5 Gyr, perhaps as much as was lost until now. This could be enough to evaporate it out of the desert, if indeed it is in it. Again, this estimate assumes the energy-limited approximation and a constant radius.

### K2-104b

I estimate a lifetime to date mass loss for K2-104b up to 1.5 per cent. The OW17 study indicated the difference between planets on either side of the evaporation valley to be an envelope only a few per cent the mass of the core for the planets on the larger side. Therefore, one would expect super-Earths like K2-104b to only lose, at most, on the order of 1 or 2 per cent of their mass before being stripped. My estimate is therefore consistent with this assertion. Alternatively, the planet could be a smaller core that is still losing the last part of its envelope, although one would expect a smaller core to have been stripped by this time too; I estimate a $4\,M_\oplus$ planet of the same size and irradiation history would have lost 3.5 per cent of its

mass by this age. I also predict another 1.2 per cent mass loss is possible by 5 Gyr with the irradiation still to come. However, this would be irrelevant if the planet is indeed already stripped.

#### K2-101b

K2-101b's position on the plot in Fig. 5.1 indicates it is seemingly too large for a planet at its orbital separation to have been stripped bare. Indeed, I estimate a total lifetime to date loss of less than 0.3 per cent in mass, compatible with the planet having not been fully stripped of its atmosphere, remembering that planets just above the valley have an envelope mass fraction of 1 or 2 per cent (OW17). I predict a further 0.3 per cent mass loss from now to 5 Gyr. This may or may not be enough to strip the planet, depending on the actual mass and envelope mass fraction.

#### K2-95b

K2-95b resides in a region of the parameter space where it is very likely resistant to any future evolution; I estimate just a further 0.1 per cent loss up to 5 Gyr. Its position close to, but not in, the Neptunian desert does hint at a possible past evolution out of that region. However, the small current and lifetime losses estimated suggest otherwise, pointing to a scenario where the planet has undergone very little past evolution. Starting the planet a little larger as a Neptune analogue (in both radius and mass), the lifetime loss is still just 0.12 per cent to date.

## 5.7 Conclusions

I have investigated four of the seven young planets discovered to date in the open cluster, Praesepe. X-ray analyses were performed for each of the four host stars using data taken by *XMM-Newton*, allowing us to estimate the XUV irradiation experienced by planets at the current epoch. I found that although the XUV radiation is about an order of magnitude or so below the saturated level, the stars are as expected still relatively active compared to older field stars. The X-ray observations were paired with simultaneously taken *K2* data, where possible, for further insight. For K2-100, the X-ray flux decreases and flattens off while the optical flux rises throughout, something that could result from active regions disappearing from view as the star spins.

Putting these analyses together with relationships describing how X-ray emission changes with time, and the positions of the planets with respect to evaporation

features in the exoplanet population, I have explored how the planets may have evolved in the past, and what the future may hold. I have found that about three fifths of the total EUV irradiation up to 5 Gyr is still to come, something which could possibly drive further evolution of the planet's atmospheres.

I found that K2-100b is undergoing by far the largest evaporation at the current epoch, and could have lost about five per cent of its mass over its 800 Myr life to date. K2-104b is probably a stripped core, given its XUV flux history and its current position in radius-period space. K2-101b may or may not retain the small envelope the planet likely currently holds, while K2-95b has probably seen the least evolution of the planets in the sample, and will retain almost all of its atmosphere that remains.

# Chapter 6

# The X-ray transit of HD 189733b

## 6.1 Introduction

The unambiguous detection of a planetary transit at X-ray wavelengths has the potential to probe the kind of atmospheric mass loss predicted in the previous chapters, while additionally giving information about the structure of the host star's corona.

While it has proved a powerful tool for an increasing number of exoplanets (see Section 1.2.1), probing atmospheric escape through Ly $\alpha$ observations has its limitations. Due to efficient absorption by the ISM, little to no signal from the core of the Ly $\alpha$ line reaches Earth. This means the level of absorption by planetary material at low velocities is difficult to assess at these wavelengths, unless the system has a large systemic radial velocity with respect to the Solar System.

The ionisation level of the hydrogen is also relevant. Consider two identically-sized regions of hydrogen escaping a planet: one is fully ionised, the other entirely neutral H I gas. The neutral region case could show a transit that is much deeper than that measured optically. Conversely, Ly $\alpha$ photons would pass through the ionised region uninhibited, and no transit would be measurable, save for those blocked out by the planet disc itself. As an example, fig. 11 of Lecavelier Des Etangs et al. (2010) depicts two theoretical Ly $\alpha$ transits with depths of 5 and 19% that have the same mass loss rate, but different ionisation levels. While probing other species (e.g. He, C, O) can also aid in getting around these issues, searching for transits in X-rays has the additional advantage of being the wavelengths driving the escape being investigated, as described in Section 1.2.2. The absorption in X-rays within the escaping material occurs via bound-free photoelectric processes

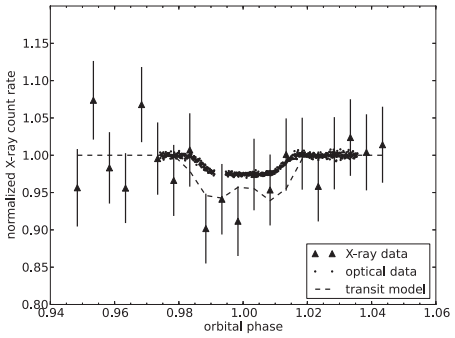


(a) All seven data sets

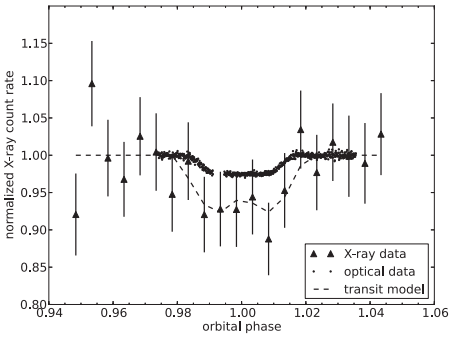


(b) Six data sets, excluding the potentially flaring *Chandra* observation

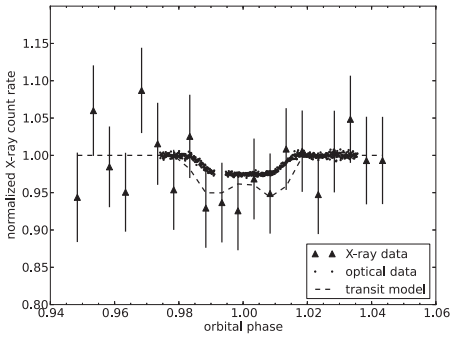


(c) Six data sets, excluding the potentially flaring *XMM-Newton* observation

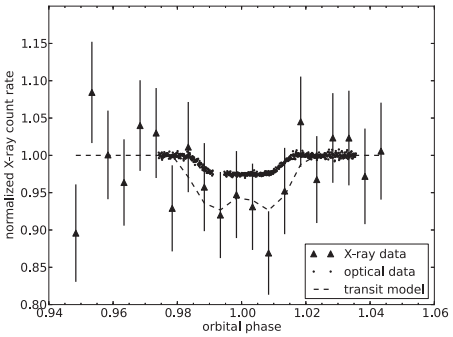


(d) Five quiescent data sets, excluding both potentially flaring observations

Figure 6.1: Fig. 8 of Poppenhaeger et al. (2013), depicting their X-ray light curves for different combinations of their seven data sets.

across many ionisation levels of the many species entrained in the flow.

To date, there is only one previous claim of the detection of an X-ray transit being successfully observed; this was for the nearby prototypical transiting hot Jupiter HD 189733b. Poppenhaeger et al. (2013) combined six *Chandra* and one *XMM-Newton* observation to probe the X-ray transit, and indeed their study uncovered a lower count rate at the time of planetary transit (see Fig. 6.1). However, the significant red noise in the data meant that neither the shape of the transit nor the depth were well-constrained. In the case of the latter, combining any six of the seven observations yielded depths ranging from 2 to 9%.

In this Chapter, I revisit this system with *XMM-Newton*, combining twenty primary transit observations spread across 8 years. By averaging across so many observations, I was able to mitigate the effects of red noise in the data, for instance from stellar activity. For the first time, I have successfully observed the expected limb-brightened or W-shaped transit profile in X-rays. Additionally, the transit has an early ingress, late egress, and is over 7% deep at its maximum extent.

## 6.2 The HD 189733 system

HD 189733 is a K1 dwarf that, at a distance of just 19.775±0.013 pc (Gaia Collaboration et al., 2018), hosts the closest known transiting hot Jupiter to Earth. The planet was initially discovered using RVs, before its transiting nature was revealed in follow-up photometric observations (Bouchy et al., 2005). Along with HD 209458b, the first transiting planet discovered, HD 189733b can be considered as one of two prototypical hot Jupiters. The brightness of their host stars (HD 189733: $V = 7.648$ Koen et al. 2010), combined with the size and transiting nature of the planets themselves, mean these are two of the best studied exoplanets to date. I give my adopted stellar and planetary parameters in Table 6.1.

In addition to the planetary-mass companion, Bakos et al. (2006) identified an M dwarf stellar companion, after they found its proper motion to be consistent with that of the planet host. The authors determined that the projected separation of HD 189733B was 216 au, with a period of roughly 3200 years.

As discussed in Chapter 1, signatures of atmospheric escape from HD 189733b have been observed with *HST* for both hydrogen at Ly $\alpha$ wavelengths (Lecavelier Des Etangs et al., 2010; Lecavelier des Etangs et al., 2012; Bourrier et al., 2013), and O I (Ben-Jaffel and Ballester, 2013). Further tentative signatures of escaping C II (Ben-Jaffel and Ballester, 2013) and H $\alpha$ (Jensen et al., 2012; Cauley et al., 2015, 2017) material could possibly be of either planetary or stellar origin instead.

For detecting X-ray transits, HD 189733b's radius, the X-ray flux of its host, and the proximity of the system to the Earth all combine to make it the single best target available. HD 209458 is two orders of magnitude dimmer in terms of X-ray flux at Earth (Louden et al., 2017a) and orbits a larger G-type star, inhibiting searches for transits in X-rays. Meanwhile, all of the known transiting planets around stars with similar X-ray flux are much smaller than HD 189733b. Given the difficulties in teasing out the transit shape and depth for HD 189733b in the Poppenhaeger et al. (2013) study, it may well be that it is the only system, or one of very few, where X-ray transit detection is possible with the current generation of X-ray telescopes.

Aside from the aforementioned *Chandra*/*XMM-Newton* transit study by Poppenhaeger et al. (2013), HD 189733 has been observed and detected in X-rays by a number of missions and studies. Kashyap et al. (2008) identified the system as detected in observations with *ROSAT* with both the HRI and PSPC instruments, as well as by the *EXOSAT* and *Einstein* missions. The papers by Pillitteri et al. (2010, 2011, 2014) identify three flares in observations with *XMM-Newton*, all occurring within a few hours of the secondary eclipse of the planet. I discuss these

Table 6.1: Adopted stellar and planetary parameters for HD 189733(b).

| Parameter | Symbol | Value | Unit | Reference |
|---|---|---|---|---|
| Stellar mass | $M_*$ | $0.823 \pm 0.029$ | ($M_\odot$) | (1) |
| Stellar radius | $R_*$ | $0.780^{+0.017}_{-0.024}$ | $R_\odot$ | (2) |
| Distance | $d$ | $19.775 \pm 0.013$ | pc | (2) |
| Planet to star radius | $R_p/R_*$ | $0.15712 \pm 0.00040$ | | (3) |
| Orbital period | $P_{orb}$ | 2.218575200(77) | d | (3) |
| Transit centre | $T_0$ | 2453955.5255511(88) | $BJD_{TDB}$ | (3) |
| Semi-maj. axis to star rad. | $a/R_*$ | $8.863 \pm 0.02$ | | (4) |
| Eccentricity | $e$ | 0 | | (5) |
| Orbital inclination | $i$ | $85.710 \pm 0.024$ | $^\circ$ | (4) |
| Impact parameter | $b$ | $0.6636 \pm 0.0019$ | | (3) |

References: (1) Triaud et al. (2009); (2) Gaia Collaboration et al. (2018); (3) Baluev et al. (2015); (4) Agol et al. (2010); (5) Bouchy et al. (2005).

further in Chapter 7. The first of these three papers identifies a background Galactic X-ray source, 1 kpc distant. Poppenhaeger et al. (2013) were able to take advantage of the superior spatial resolution of *Chandra* to separate out signatures from both HD 189733B and the background source from HD 189733A. The three form a roughly equilateral triangle on the sky, with angular separations of about 12 arcsec. I adopt the position measured by Poppenhaeger et al. (2013) for the background source ($\alpha = 300.1813^\circ$, $\delta = 22.7068^\circ$), assuming negligible proper motion given the distance of the source. There is also a series of *Swift* observations of HD 189733 taken between 2008 and 2016. I analyse these data in the context of stellar activity in Chapter 7.

### 6.2.1 Observations

I give details of the 20 observations covering primary transits of HD 189733b made by *XMM-Newton* between 2007 and 2015 in Table 6.2. I note that observation 1 from 2007 is the same *XMM-Newton* observation used in the Poppenhaeger et al. (2013) analysis. In all twenty observations, the EPIC-pn camera was operated in small window mode. This has the advantage of being able to use the thin optical blocking filter, as opposed to the medium filter normally used for a source of similar optical brightness and which would reduce the X-ray count rate. However, it also results in about 30% of the exposure time listed in Table 6.2 being lost to readout.

In Fig. 6.2, I display the phase coverage of the observations, giving the number of observations present in the data as a function of phase. I chose to filter out sections of four of the observations due to the presence of flares (see Section 6.3, be-

Table 6.2: Details of the HD 189733 *XMM-Newton* observations.

| No. | Observation IDs | Start Time (TDB) | Finish Time (TDB) | Exp. Time (s) |
|---|---|---|---|---|
| 1 | 0506070201 | 2007-04-17 14:06:31 | 2007-04-18 05:20:49 | 54858 |
| 2 | 0692290201 | 2013-05-09 20:16:00 | 2013-05-10 07:09:38 | 39218 |
| 3 | 0692290301 | 2013-11-03 07:54:13 | 2013-11-03 18:12:33 | 37100 |
| 4 | 0692290401 | 2013-11-21 00:58:40 | 2013-11-21 12:38:40 | 42000 |
| 5 | 0744980201 | 2014-04-05 05:05:20 | 2014-04-05 18:25:20 | 48000 |
| 6 | 0744980301 | 2014-05-02 01:22:25 | 2014-05-02 10:44:05 | 33700 |
| 7 | 0744980401 | 2014-05-13 01:55:22 | 2014-05-13 13:02:01 | 39999 |
| 8 | 0744980501 | 2014-05-15 09:57:00 | 2014-05-15 18:50:20 | 32000 |
| 9 | 0744980601 | 2014-05-17 14:21:12 | 2014-05-17 23:14:32 | 32000 |
| 10 | 0744980801 | 2014-10-17 16:08:26 | 2014-10-18 02:25:06 | 37000 |
| 11 | 0744980901 | 2014-10-19 20:38:36 | 2014-10-20 06:11:56 | 34400 |
| 12 | 0744981001 | 2014-10-22 01:39:14 | 2014-10-22 12:44:14 | 39900 |
| 13 | 0744981101 | 2014-10-24 06:15:47 | 2014-10-24 17:05:47 | 39000 |
| 14 | 0744981301 | 2014-11-08 20:16:34 | 2014-11-09 05:53:14 | 34600 |
| 15 | 0744981201 | 2014-11-11 00:37:26 | 2014-11-11 12:50:46 | 44000 |
| 16 | 0744981401 | 2014-11-13 06:46:05 | 2014-11-13 15:39:25 | 32000 |
| 17 | 0744980701 | 2014-11-15 09:48:00 | 2014-11-15 20:38:00 | 39000 |
| 18 | 0744981501 | 2015-04-13 02:37:23 | 2015-04-13 15:14:03 | 45400 |
| 19 | 0744981601 | 2015-04-17 12:34:55 | 2015-04-17 23:58:15 | 41000 |
| 20 | 0744981701 | 2015-04-19 19:06:26 | 2015-04-20 05:39:46 | 38000 |

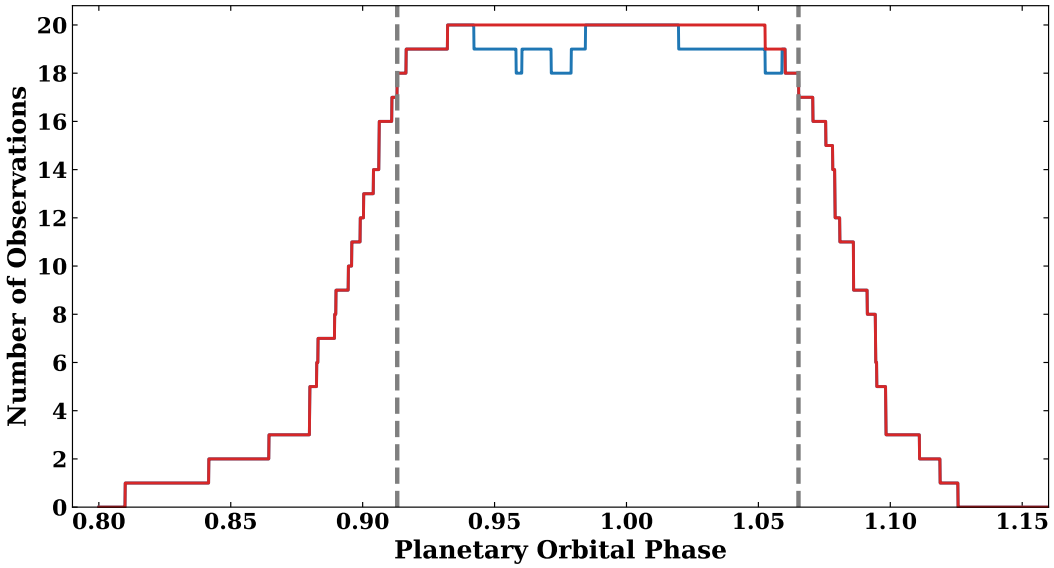


Figure 6.2: Phase coverage of the *XMM Newton* observations of HD 189733 that cover a primary transit. The red and blue lines correspond to the number of observations present at each phase before and after filtering for flares (see Section 6.2.1) in the data. The grey dashed lines are the phases considered in the main analysis.

low, and Chapter 7 for more details of the flares). The result of the filtering process on the phase coverage is also shown in Fig. 6.2 where the blue line, representing the filtered data, dips below the red line, representing the unfiltered data. In order to average over red noise in the data, I chose to focus only on the phases for which there is at least 18 of the 20 observations present after filtering. This leaves phases 0.9131 – 1.0652, and these start and end points are marked on Fig. 6.2 as grey dashed lines.

Using SAS 15.0.0, I followed the standard analysis procedures for reducing data from *XMM-Newton*. The final analysis used 15 arcsec radius source regions; however, my initial analysis to assess the level of contamination from the nearby sources used smaller 10 arcsec regions. I outline this analysis in Section 6.3.

## 6.3 Contamination

While it has the significant benefit of a higher count rate, there is one main disadvantage of using *XMM-Newton* for observations of HD 189733 compared to *Chandra*: the PSFs of HD 189733A, HD 189733B and the background source described in Section 6.2 all partially overlap. However, the spectra of the three sources in fig. 5 of Poppenhaeger et al. (2013) suggests that HD 189733A is at least an order of magnitude brighter than HD 189733B at all energies, and that the third, background

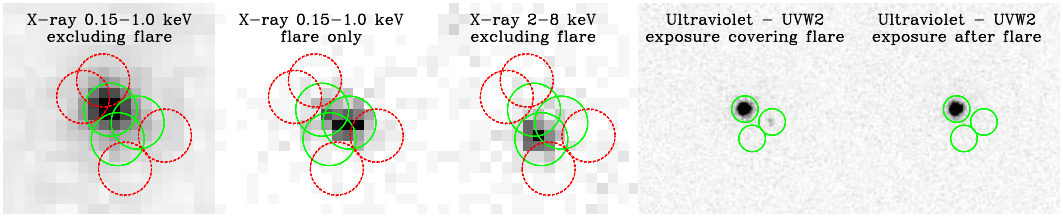


Figure 6.3: Images from observation 3 (see Table 6.2). The first three panels from the left are X-ray images taken by the EPIC-pn camera comparing different energy ranges, as well as data in and out of flare. The right-most two panels show OM images taken with the UVW2 filter during and after the flare. *Credit: P. Wheatley*

source is only relevant above about 1.2 keV.

I investigated this in my own data by performing an analysis to recover separate signals from each of the three sources, using smaller 10 arcsec source regions. I assessed the contamination by considering the contribution of each of the three sources to the PSF of the other two. This involved placing extra 10 arcsec radius extraction regions equidistant from the centre of the contaminant's PSF on the opposite side. This contribution can then be subtracted off. The first three panels on the left of Fig. 6.3 gives an example of how the regions for this process are defined. The three overlapping circles in the centre of each image are the source regions for (top to bottom) HD 189733A, HD 189733B and the background source. Each of the red regions assesses the contribution of one of the sources to the PSF of another.

Plotting the resulting light curves from this process indeed confirms the background source is irrelevant at soft energies, and HD 189733B's contribution is, at almost all times, negligible. The exception to the latter is three flares that I identify as originating from HD 189733B, instead of the planet host, on 3 November 2013, 11 November 2014, and 15 November 2014. I give an example of the resulting light curves from this contamination assessment at soft energies for the 3 November 2013 flare in Fig. 6.4. Light curves for the other two flares are depicted in Fig. 7.12, along with more discussion of the M star flares and of the implications of their detection in Section 7.4.2.

Analysing and comparing images of the X-ray and UV of the observations in different energy bands and at different times backed up these inferences. Fig. 6.3 gives an example for observation 3 (see Table 6.2). These images show that out of flare only HD 189733A is relevant at soft energies, and only the background source is relevant at harder energies. The OM images confirm that the 3 November 2013 X-ray flare was from the M star companion HD 189733B, and not the transit host. Neither of the other two M star flares are picked up definitively in the OM, however

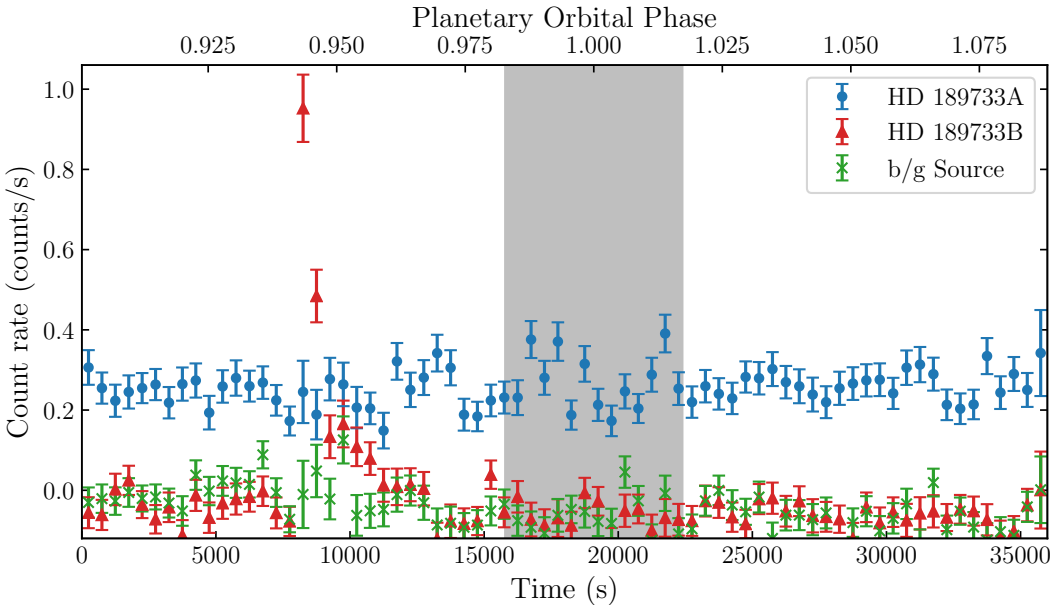


Figure 6.4: X-ray light curves for the three sources for observation 3, from 3 November 2013, extracted during the contamination assessment (see Section 6.3). The light curves cover the energy range 0.166–1.20 keV. HD 189733A, HD 189733B and the background source are depicted with blue circles, red triangles, and green crosses, respectively. The grey shaded region depicts the primary transit of HD 189733b.

their X-ray brightness was only about 60 and 40% that of the 3 November 2013 flare, and so it is possible that any flare at NUV wavelengths was much quieter too. There is a possible marginal OM detection for the 15 November 2014 flare, but this is not picked up as a detected source by OMICHAIN.

Taking all these results into consideration, I determined that a full extraction of HD 189733A using a larger 15 arcsec was able to be performed, provided I restricted the energies to be less than 1.2 keV, and removed the data around the three M star flares. During the examination of the light curves for this contamination assessment, I additionally identified a single flare from HD 189733A in the 17 May 2014 observations, which was also excluded from the final analyses. More discussion of this flare is given in Section 7.4.1, and the flare light curve is plotted in Fig. 7.11.

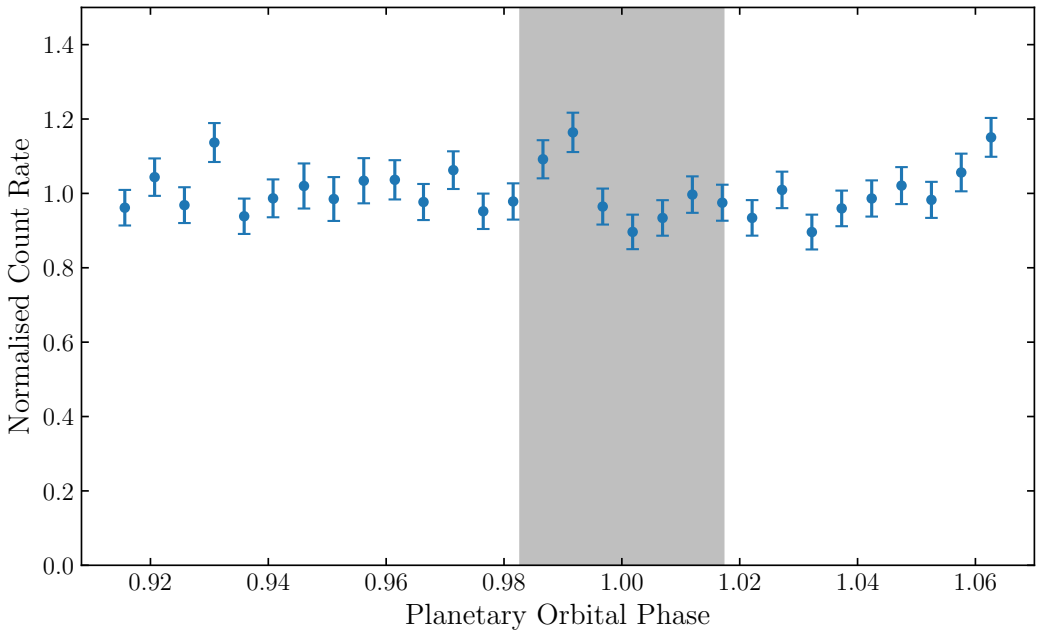


Figure 6.5: Binned X-ray light curve of HD 189733, folded on the ephemeris (Baluev et al., 2015), and averaged across the twenty observations. The energy range is 0.166–1.20 keV.

## 6.4 Light curves

### 6.4.1 Binning & visual inspection

This section focuses on the 'full' 15 arcsec extraction of the twenty observations. Following the findings of Section 6.3, above, I restrict my extractions to be within the energy range 0.166–1.2 keV, with data around the four flares removed, and focused only on phases 0.9131–1.0652. Each light curve was normalised by dividing by its average count rate, in order to remove any observation-to-observation variation in the out-of-transit baseline. I chose not to normalise to an out-of-transit phase range as it was not clear a priori what the duration of the transit would be, or whether it would be offset in time from the optical transit.

I binned the data initially into 30 equally sized phase bins. Visual inspection of the full 0.166–1.20 keV energy range revealed a rather precise light curve when averaging across all twenty observations. The light curve, shown in Fig. 6.5, does show a dip followed by a rise starting during the optical transit of the planet, but there is no unambiguous detection of the X-ray transit across this energy range.

In order to search for the transit in soft x-rays, where the strength of photoelectric absorption is expected to be strongest, I split the data into soft and hard

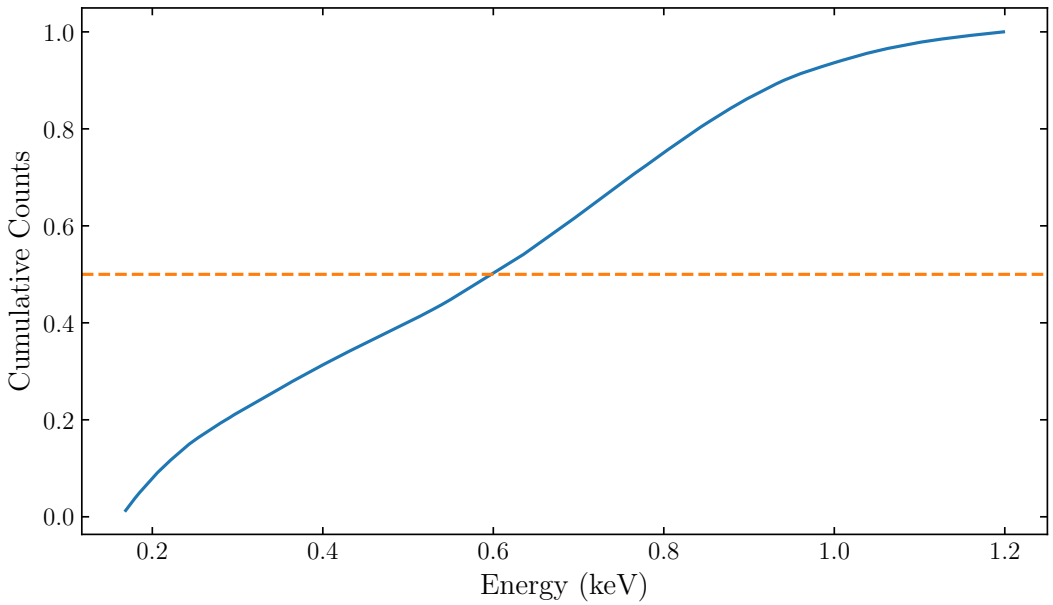


Figure 6.6: Cumulative counts plotted as a function of energy. The orange dashed line is plotted at 0.5. Where this meets the cumulative curve, it gives the energy at which the data are split into two energy bins with equal number of counts in each.

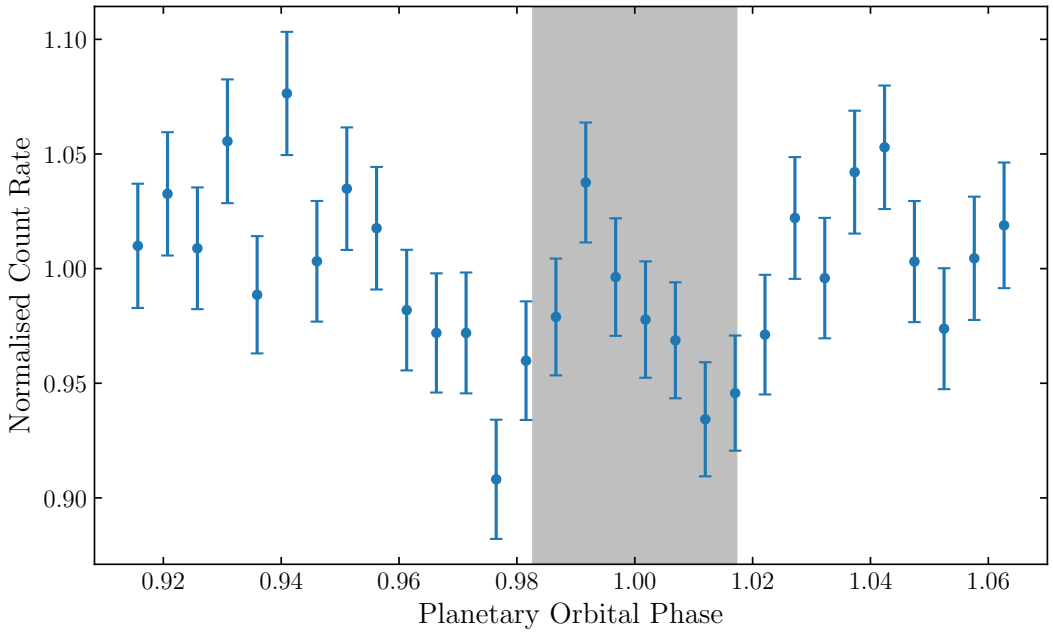


Figure 6.7: As Fig. 6.5, but for the soft band (0.166–0.60 keV) only.

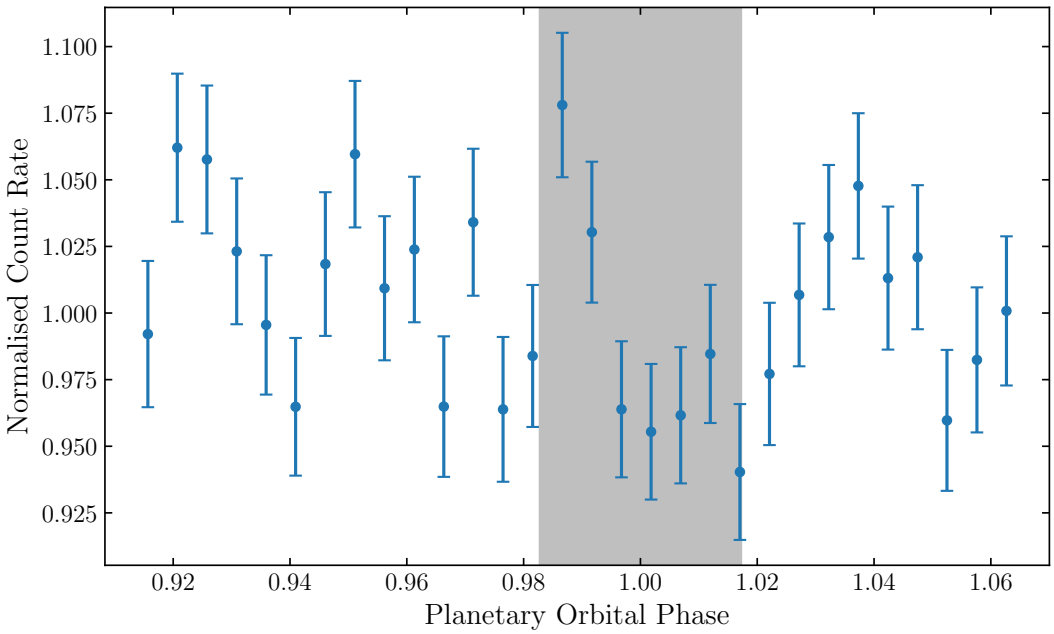


Figure 6.8: As Fig. 6.5, but for the hard band (0.60–1.20 keV) only.

energies. Combining spectra extracted from each of the observations, I plotted the cumulative counts as a function of energy, as shown in Fig. 6.6. Using this, I split the data into two energy bands with a roughly equal number of counts in each. The soft band light curve (0.166–0.60 keV), plotted in Fig. 6.7, shows a clear transit signal, with the expected W-shaped profile. The hard band (0.60–1.20 keV), plotted in Fig. 6.8, is noisier like the light curve for the full energy range, and shows the same dip and rise starting during the optical transit seen for the full energy range of 0.166–1.20 keV. I decided to fit a transit model to the soft and hard bands simultaneously. This process is described in Section 6.4.3, but first I introduce the model used in the fit.

### 6.4.2 Coronal model

X-ray emission from stars is dominated by that from the corona, as I introduced in Section 1.3. This emission is optically thin, resulting in a characteristic limb-brightened appearance, instead of the limb-darkening seen at optical wavelengths. The result of this is a W-shaped light curve, like that seen in Fig. 6.7, in contrast to the U-shaped transits typically observed in optical, NIR, and NUV wavelengths (for example, Figs. 1.1 & 3.8). This W-shaped profile is expected in X-rays (e.g. Llama and Shkolnik, 2015; Marin and Grosso, 2017, and as explained in Section 1.3).

I chose to model the transit with an exponentially decaying coronal density profile, with 3D radial symmetry. This resulting coronal emission flux, $f_{\rm X}$, is described as

$$f_{\rm X}(r) = \begin{cases} f_{\rm X}(0)\exp(\frac{-2r}{H}), & \text{for } r > R_*. \\ 0, & \text{for } r < R_*. \end{cases} \tag{6.1}$$

The factor of two in the exponent comes from $f_{\rm X}$ being proportional to $n_e^2$, the square of the election number density. $r$ is the radial distance from the stellar centre, and $R_*$ is the stellar radius (to the photosphere edge). $H$ is the pressure scale height of the corona. Assuming an isothermal plasma, this is equal to the electronic density height (e.g. Marin and Grosso, 2017). Under the isothermal assumption, $H$ is given by

$$H = \frac{2k_B T}{\mu m_H g}, \tag{6.2}$$

where $k_B$ is the Boltzmann constant, T is the temperature of the plasma, $\mu$ is the mean particle weight, and $m_H$ is the mass of the hydrogen atom. $g$ is the surface gravity of the star, given by $GM_*/R_*^2$.

This profile was projected into two dimensions, where the geometry considered is given in Fig. 6.9, and numerically integrated along the line of sight. This calculation was performed at 10001 points in $x$ stretching out radially on the projection. The line of sight integral is given by

$$I(z,x) = \begin{cases} 2I(0,x)\int_0^\infty \exp\left(\frac{-2}{H}\sqrt{z^2+x^2}\right)\, dz, & \text{for } x > R_*, \\ I(0,x)\int_{\sqrt{R_*^2-x^2}}^\infty \exp\left(\frac{-2}{H}\sqrt{z^2+x^2}\right)\, dz, & \text{for } x < R_*. \end{cases} \tag{6.3}$$

The resulting array was normalised such that a total intensity of unity is gained radially in the projection. An array of these 10001 integration results were passed as a custom limb darkening law in the BATMAN code (Kreidberg, 2015). BATMAN's coordinate system is defined between $x = 0$, at the centre of the stellar disc, and $x = 1$. Usually $x = 1$ corresponds to the edge of the photospheric disc, but I instead set $x = 1$ to be three pressure scale heights beyond the edge of the stellar disc, as shown in Fig. 6.9. For each $x$ examined by BATMAN during a calculation, a linear interpolation of the surrounding integration values was performed to estimate the relative brightness of the corona at that $x$ for the current model being considered.

### 6.4.3 Fitting the light curves

I ran an MCMC fit (see Section 2.5) to the binned, folded soft and hard band light curves simultaneously using the EMCEE code (Foreman-Mackey et al., 2013). For the

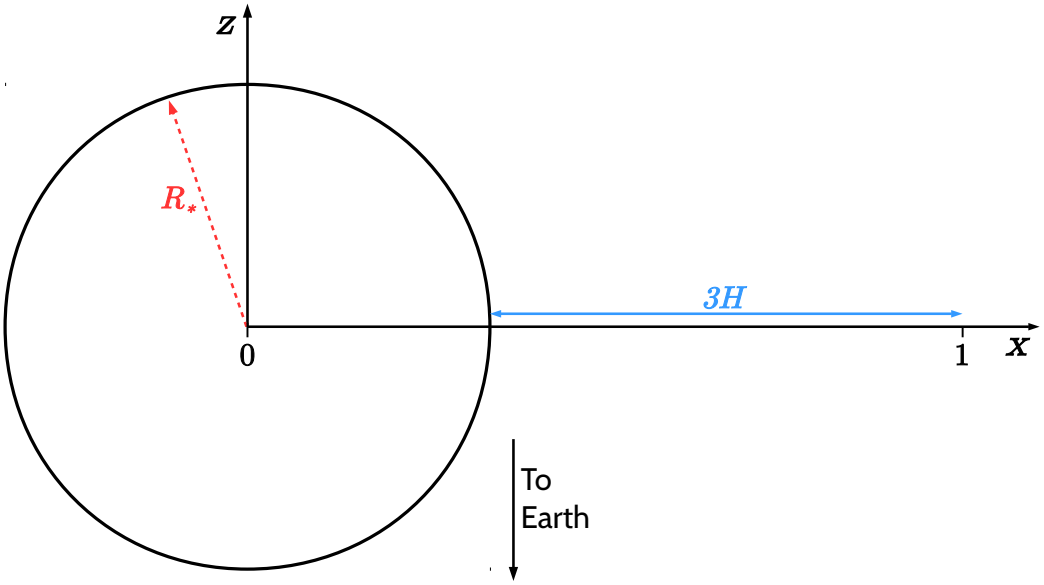


Figure 6.9: The considered geometry of the coronal profile.

fits, I opted to use 200 phase bins as opposed to the 30 that has been used for display purposes in some of the presented figures. The fitted parameters were the coronal scale height, the planetary X-ray absorption radius in each energy band ($R_{\mathrm{X,\ soft}}$ and $R_{\mathrm{X,\ hard}}$), a temporal offset in the transit centre time ($t_0$), and a normalisation offset to assess the out-of-transit level of the data in each energy band ($N_{\mathrm{soft}}$ and $N_{\mathrm{hard}}$). This is necessary because the normalisation process (described in Section 6.4.1) used the average of all of the data between 0.9131 and 1.0652 in phase. Thus, dips in the count rate associated with the transit signal will force this average to lie between the out-of-transit and in-transit level. $H$ and $t_0$ were forced to be the same across both the soft and hard band fits. In reality, $H$ may well have an energy dependence due to the higher energies being dominated by higher temperatures. However, since a single temperature emits across a wide range of energy, this dependence of $H$ with photon energy may well be rather weak. Moreover, given how noisy the hard band light curve is, it was difficult to constrain any dependence from this data alone, and so fitting $H$ across both datasets was deemed the best solution. Furthermore, an asymmetry in the material distribution likely affects both bands similarly, and so linking $t_0$ makes sense. Each parameter was given a uniform prior. $R_{\mathrm{X}}$ was limited to be in the range $0 < R_{\mathrm{X}} < R_*$. $t_0$ was forced to lie between 0.985 and 1.015 to prevent it moving off to unrealistic values, and visual inspection of Fig. 6.7 shows it to be within this range. The overall value of the model for each phase bin was calculated by considering the model at 21 separate points spaced evenly within the

phase range and averaging over them. This was done because the model can vary significantly across a single bin, and so sampling it in numerous places within each bin and taking the average should help the model better reflect the binned data, which is also averaged across those same phases. The fit was run with 20 walkers, each taking 3500 steps, the first 500 of which were discarded as burn-in. Inspection of the chains, shown in Fig. 6.10, found that this was sufficient for them to have converged successfully.

With $H$ and $t_0$ now fixed to their best fit values, I ran the MCMC fit for another 3500 samples, again discarding the first 500. This fit left only the absorption radii and offsets in each band free to explore their parameter spaces. It does not necessarily give the absolute depth and, in particular, errors, which requires $H$ and $t_0$ to be free. The process instead gives a much better assessment of how the depth varies with energy, and is a common method in analysing optical transmission spectra (e.g. Sing et al., 2012; Kirk et al., 2017; Louden et al., 2017b; Evans et al., 2018).

I show the soft and hard band light curves again in Figs. 6.11 and 6.12; this time together with the model given by the best fit parameters found by the MCMC. The two versions are with the 200 and 30 phase bins, respectively. The best fit parameters inferred from both fits are displayed along with their 1-$\sigma$ uncertainties in Table 6.3, with the overplotted model in both cases being that from the second MCMC fit ('$H$ and $t_0$ fixed' in Table 6.3). The model from the initial fit was almost identical visually. Contour plots and histograms associated with the samples drawn are shown in the corner plots in Figs. 6.13 and 6.14, and these depict a number of correlations present between the model parameters. $H$ correlates with both absorption radii, $R_{\mathrm{X,soft}}$ and $R_{\mathrm{X,hard}}$. This makes sense, as increasing $H$ spreads the coronal emission over a larger area on the sky, and so a larger absorber would be required to produce the same depth. It seems that this correlation is the reason that the errors on $R_{\mathrm{X,soft}}$ are surprisingly (given the relative quality of the two light curves) as large as $R_{\mathrm{X,hard}}$. In the second fit, where $H$ is held constant, the errors for $R_{\mathrm{X,soft}}$ are smaller than for $R_{\mathrm{X,hard}}$, as expected. The absorption radii also correlate with their bands' respective normalisation offsets. Again, this makes sense: raising the baseline out-of-transit would require a larger absorber in order to produce the required depth.

The hard band light curve is visually much noisier than the soft band, and the best fit model overlaid in Fig. 6.12 is clearly not as good a fit to the hard data as it is for the soft. This is particularly the case for the first half of the light curve, and could well be the result of low amplitude flares which would be more important

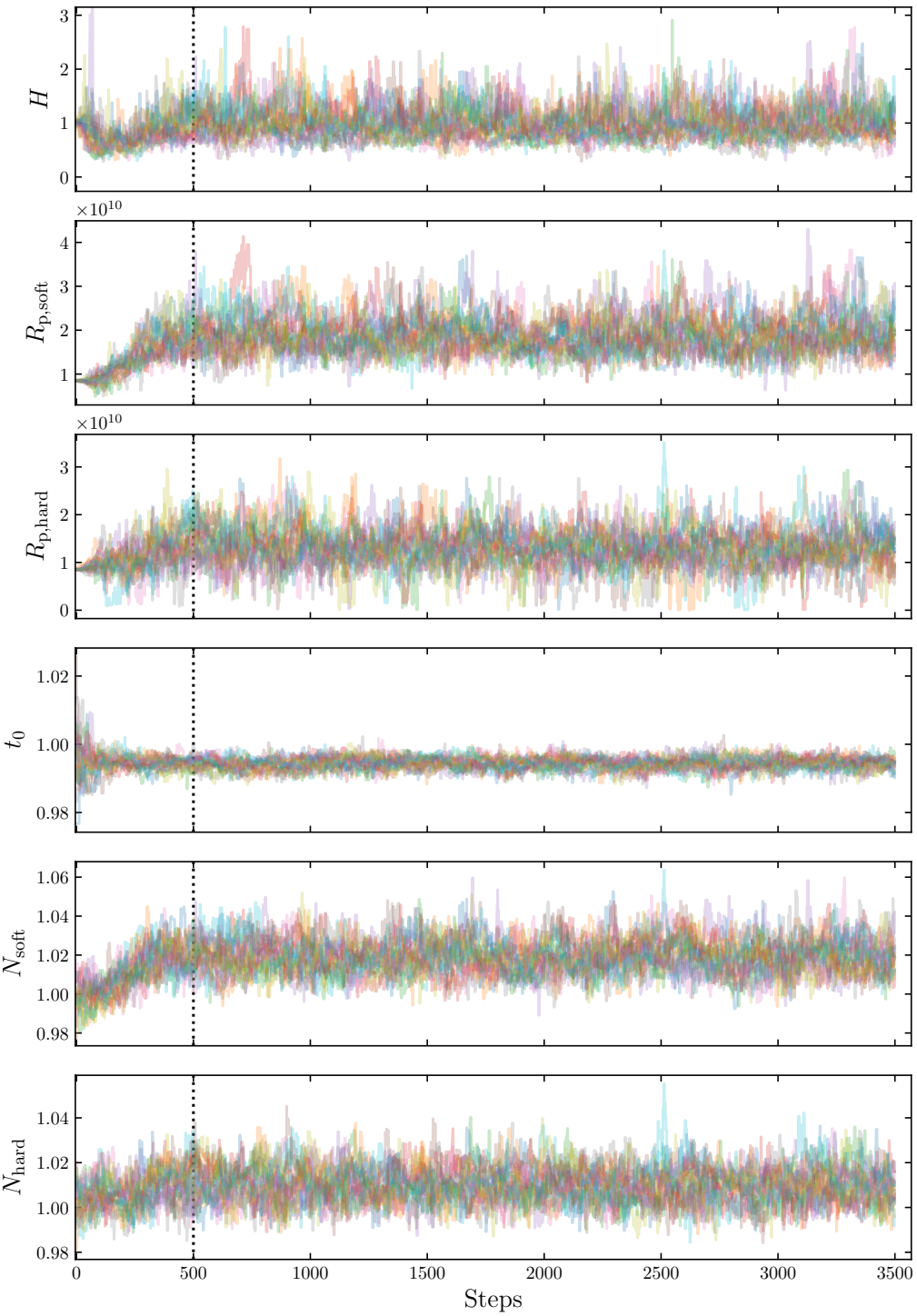


Figure 6.10: Visualisation of the chains for each parameter in the first MCMC fit. Each walker's 3500 steps are displayed as a separate line. The black dotted line at 500 steps shows the extent of the burn-in; the samples to the left of this line were discarded for the final parameter estimation.

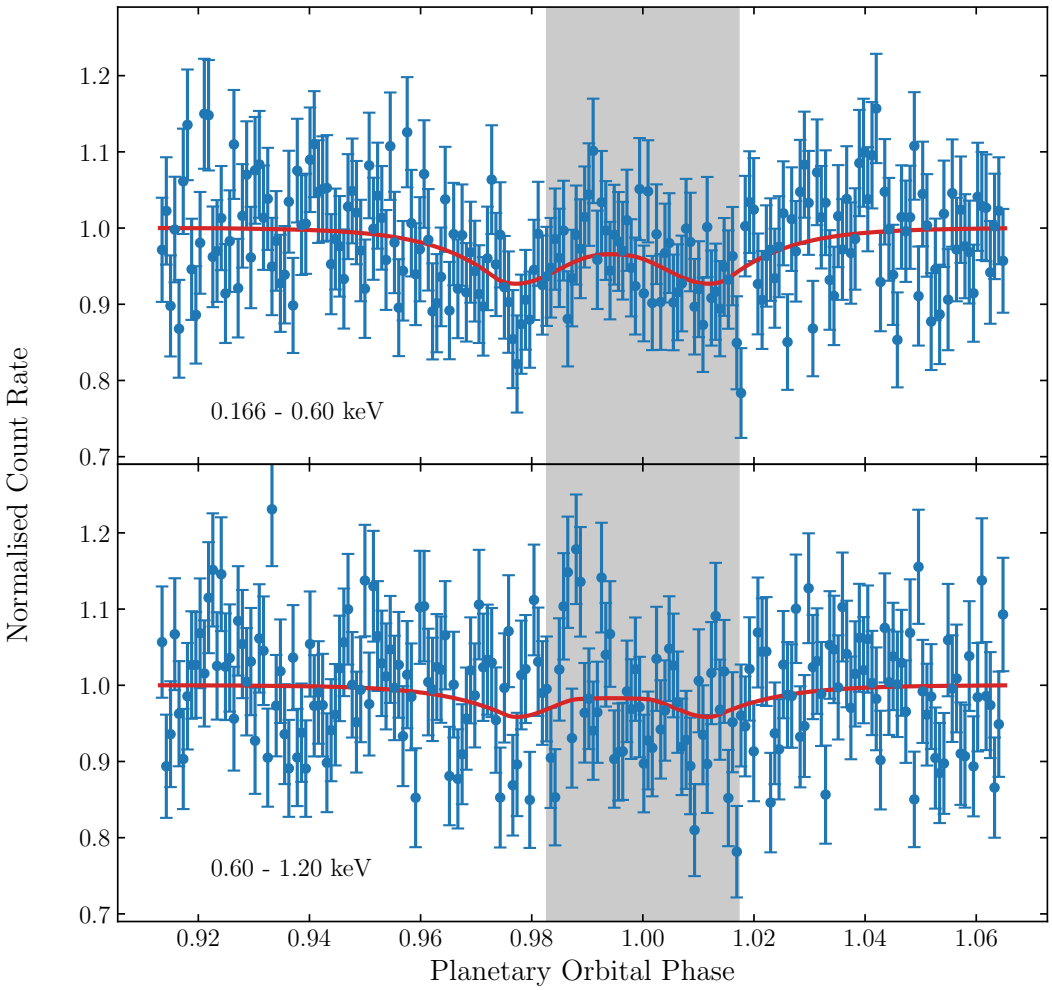


Figure 6.11: Light curves for the soft (0.166–0.60 keV; top panel) and hard (0.60–1.20 keV; bottom panel) energy bands. Overplotted are the results of the second MCMC fit, where $H$ and $t_0$ were fixed to their best fit values from the first fit (see text and Table 6.3). The data here is plotted using 200 phase bins; this is the cadence to which the data was fitted with the MCMCs.

in harder X-rays. In order to determine if this was biasing the fit parameters, I ran a fit to the soft band data only. This yielded values for all of the parameters that agreed with the fits to both energy bands simultaneously to well within the uncertainties. The uncertainties themselves were also of very similar size to those obtained by the fit to both energy ranges. I discuss the energy dependence in the context of these fits further in Section 6.6.

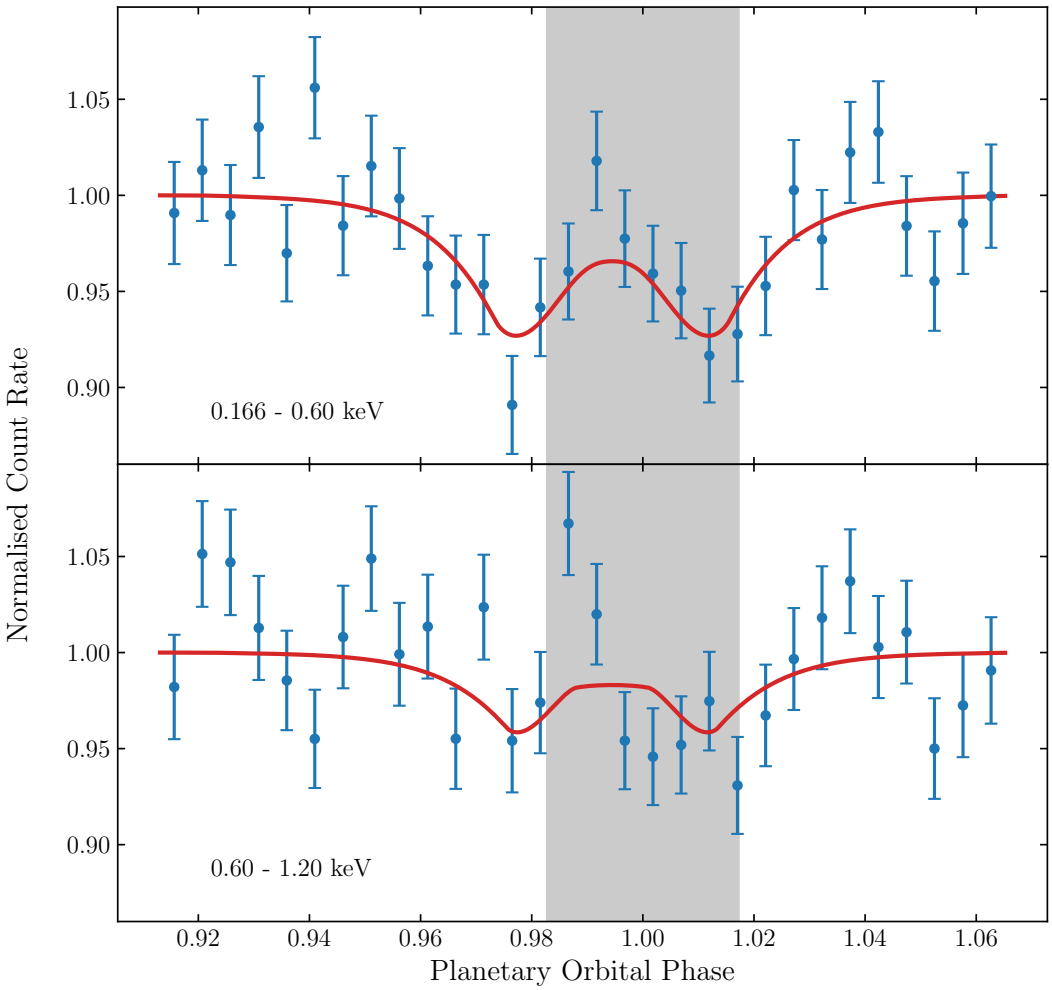


Figure 6.12: As Fig. 6.11, but with 30 phases bins instead of 200 for a clearer view of the data.

## 6.5 X-ray transmission spectroscopy

Further to the investigations of the light curves and comparisons of the soft and hard energy bands in Section 6.4, above, I also investigated the transit signal as a function of energy by employing a similar method to that used for HD 219134b in Section 4.5.5. Spectra of HD 189733, combined across all twenty observations, were compared in and out-of-transit. The 'in-transit' phases were set to those where the fitted 0.166–0.60 keV model, with the normalisation offset removed, was lower than 0.96. This focussed down on the areas of the model towards the maximum extent of the two dips. As there was a lack of phases within $0.9131 < \phi < 1.0652$ totally out-of-transit, I instead set the "out-of-transit" phases to be those where the fitted model

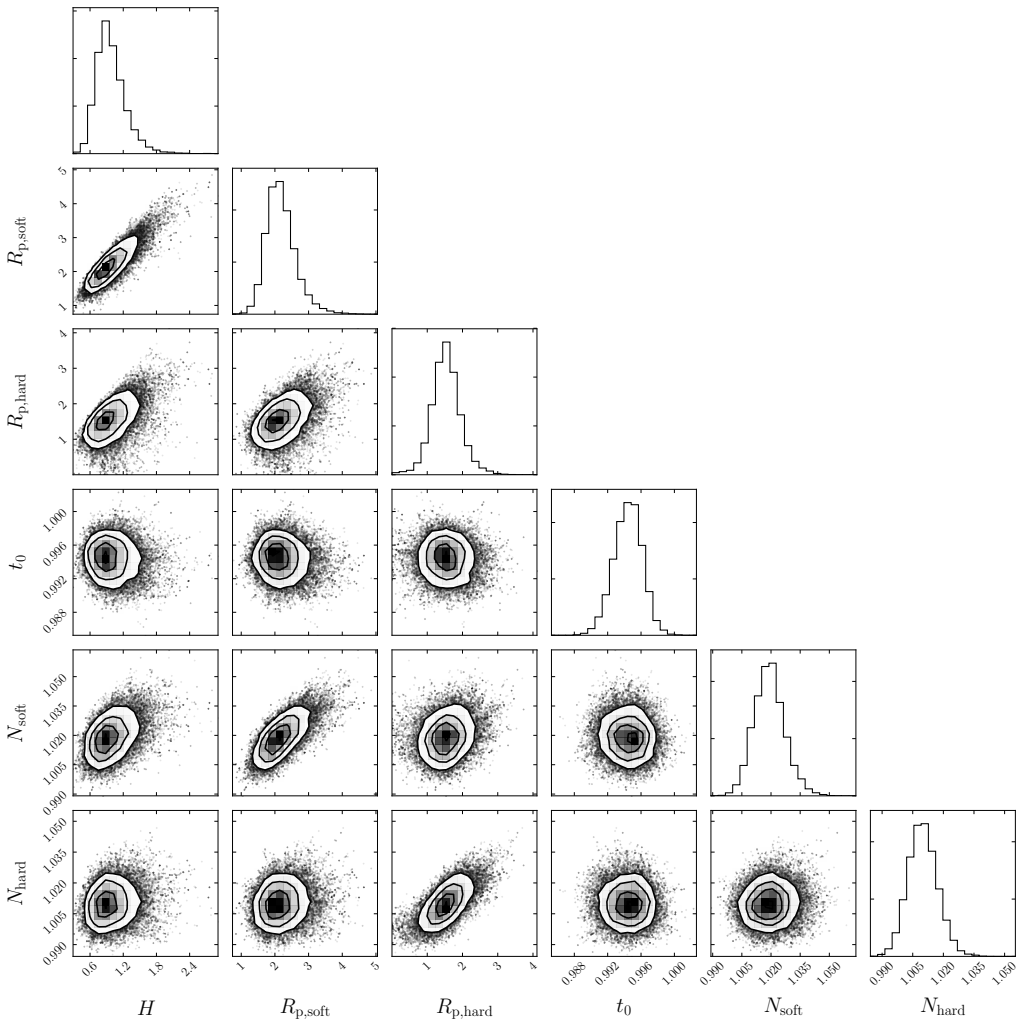


Figure 6.13: Corner plot displaying 2-D contour plots and 1-D histograms of the samples drawn by the first MCMC fit, with $H$ and $t_0$ linked across the soft and hard band models.

exceeded 0.9975. This gives total in-transit phases coverage of 0.0424, and 0.0429 for the corresponding out-of-transit phases. I highlight these phase definitions, overlaid on the best model soft band model, in the schematic in Fig. 6.15.

In and out-of-transit spectra were extracted for each of the separate observations and combined together using the FTOOLS routine ADDSPEC. Although this handled the source counts correctly, the background spectra did not combine as they should have. To counter this issue, I reran the combination of the background spectra with an explicit call to MATHPHA, one of the tasks ADDSPEC internally calls. This correctly combined the background spectra. The SPECGROUP command, part

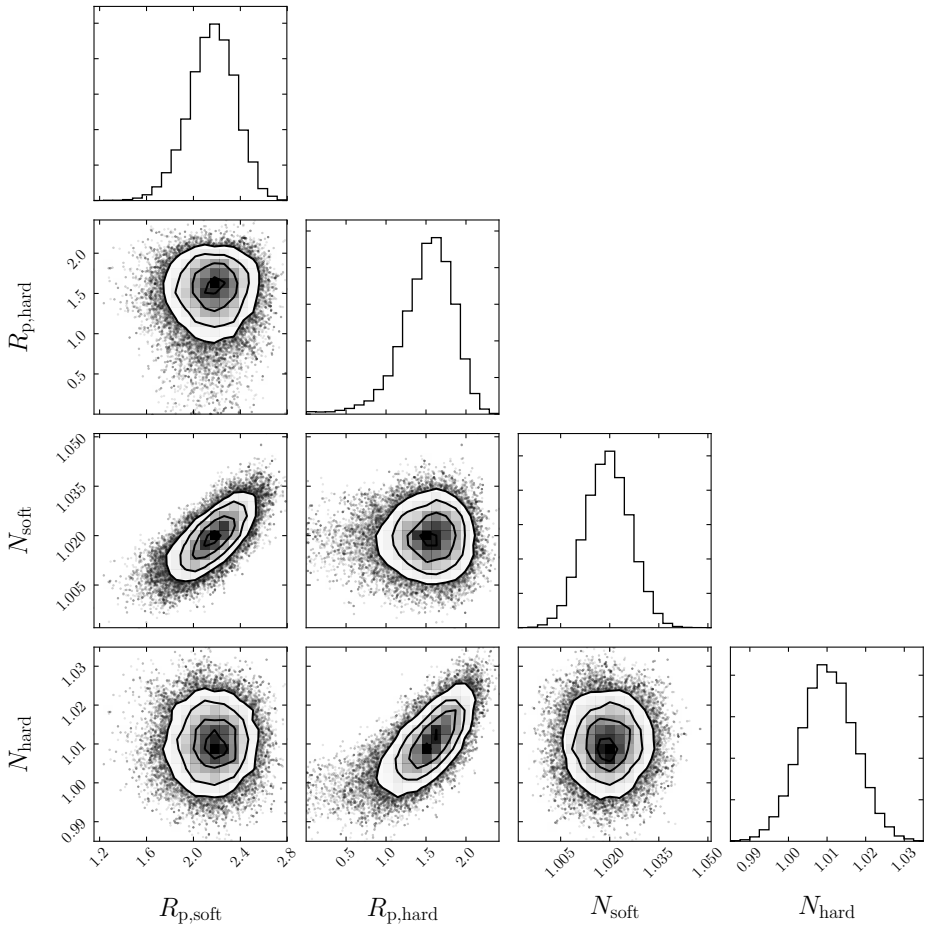


Figure 6.14: As Fig. 6.13, but for the second MCMC with $H$ and $t_0$ fixed to their best fit values from the first fit.

of the SAS package, was then used to split the spectra up into predefined energy bins.

I did this process three times, splitting the data into two, three and four energy bins. Each time, I chose energy ranges such that the total counts were split roughly evenly across the spectral bins. The extracted spectra were plotted and examined first using XSPEC. I display the in-out spectra for two, three and four spectral bins in Figs. 6.16, 6.17 and 6.18, respectively. Interested in how their count rates compared, I took the ratio of the out-of-transit data to that in-transit, as shown in Figs. 6.19, 6.20 and 6.21. Two horizontal lines are also plotted on these figures. The first is at a ratio of 1, for where there was would be no change in the count rate. The second is at the depth one would expect if $R_{\rm X} = R_{\rm opt}$, holding $H$ and $t_0$ at their best fit values determined from the soft and hard fits in Section 6.4.3.

Table 6.3: Results for the simultaneous soft (0.166–0.60 keV) and hard (0.60–1.20 keV) band MCMC fits. The '$H$ and $t_0$ linked' section refers to the first fit performed, where $H$ and $t_0$ were left free to vary, but linked across soft and hard bands. The '$H$ and $t_0$ fixed' section refers to the second fit, where $H$ and $t_0$ were fixed to their best-fit value determined from the first fit. $R_\mathrm{p}$ refers to the radius of the planet measured optically (Table 6.1).

| Parameter | Symbol | Fitted value | | Units |
|---|---|---|---|---|
| | | $H$ & $t_0$ linked | $H$ & $t_0$ fixed | |
| Coronal scale height | $H$ | $0.94^{+0.28}_{-0.21}$ | Fixed | $R_*$ |
| Soft absorp. radius | $R_\mathrm{X,soft}$ | $\left(1.82^{+0.39}_{-0.30}\right) \times 10^{10}$ | $\left(1.85^{+0.19}_{-0.17}\right) \times 10^{10}$ | cm |
| | | $2.13^{+0.46}_{-0.36}$ | $2.17^{+0.22}_{-0.20}$ | $R_\mathrm{p}$ |
| Hard absorp. radius | $R_\mathrm{X,hard}$ | $\left(1.30^{+0.33}_{-0.31}\right) \times 10^{10}$ | $\left(1.32^{+0.23}_{-0.29}\right) \times 10^{10}$ | cm |
| | | $1.53^{+0.38}_{-0.36}$ | $1.55^{+0.27}_{-0.33}$ | $R_\mathrm{p}$ |
| Transit centre | $t_0$ | $0.9945^{+0.0016}_{-0.0018}$ | Fixed | Phase |
| Soft norm. offset | $N_\mathrm{soft}$ | $1.0190^{+0.0079}_{-0.0076}$ | $1.0193 \pm 0.0069$ | |
| Hard norm. offset | $N_\mathrm{hard}$ | $1.0097^{+0.0074}_{-0.0069}$ | $1.0102^{+0.0071}_{-0.0069}$ | |

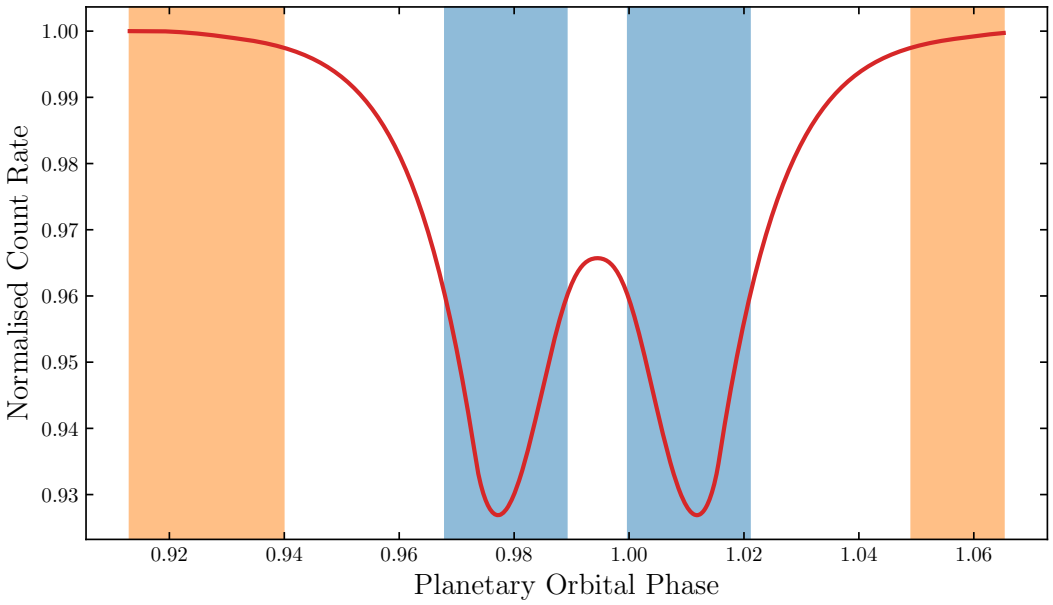


Figure 6.15: Plot showing the definition of the phases for in- and out-of-transit in the transmission spectroscopy investigations. The orange shaded regions are treated as out-of-transit, while the blue regions are treated as in-transit.

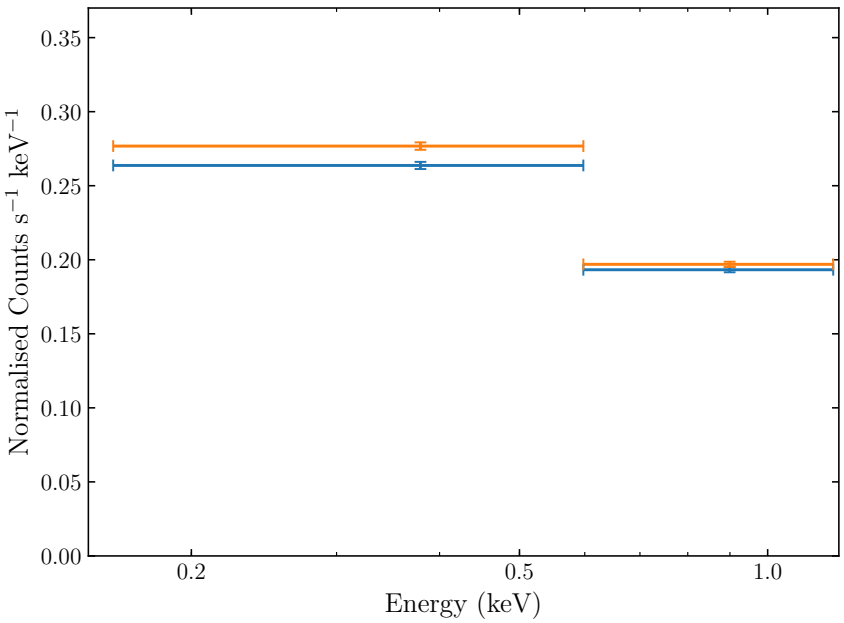


Figure 6.16: Spectra for the in-transit (blue) and out-of-transit (orange) data across all twenty observations, split into two energy bins. The definition of in and out-of-transit in this context is given in the main text.

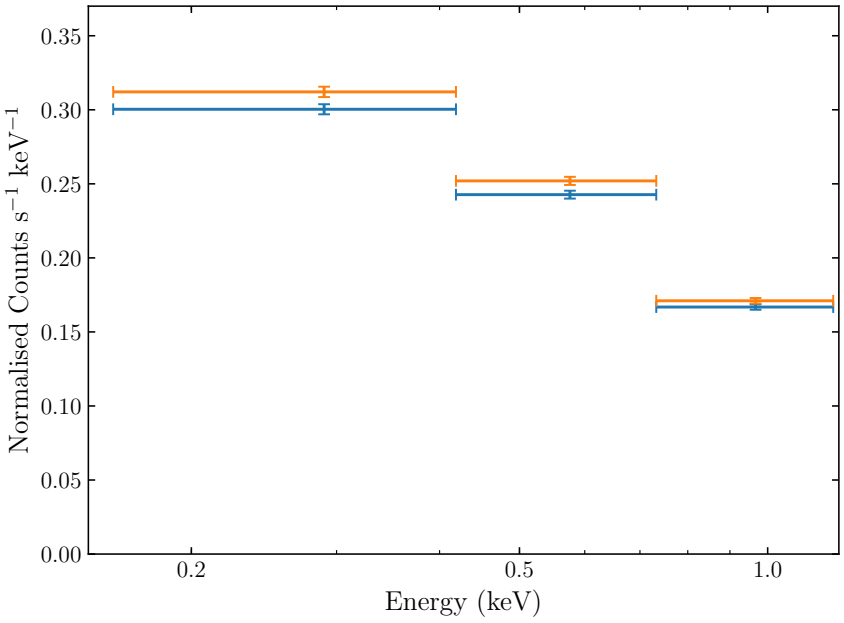


Figure 6.17: As Fig. 6.16, but with three energy bins.

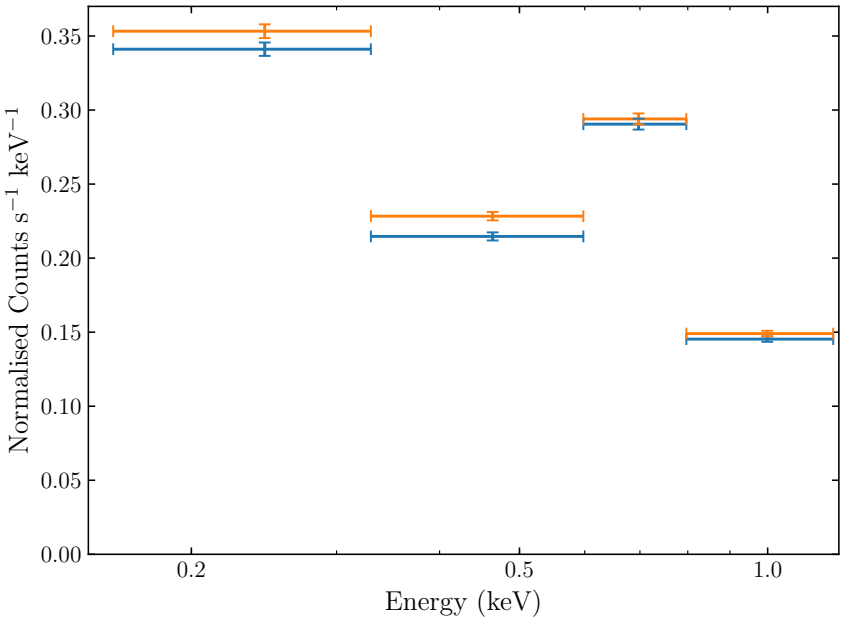


Figure 6.18: As Fig. 6.16, but with four energy bins.

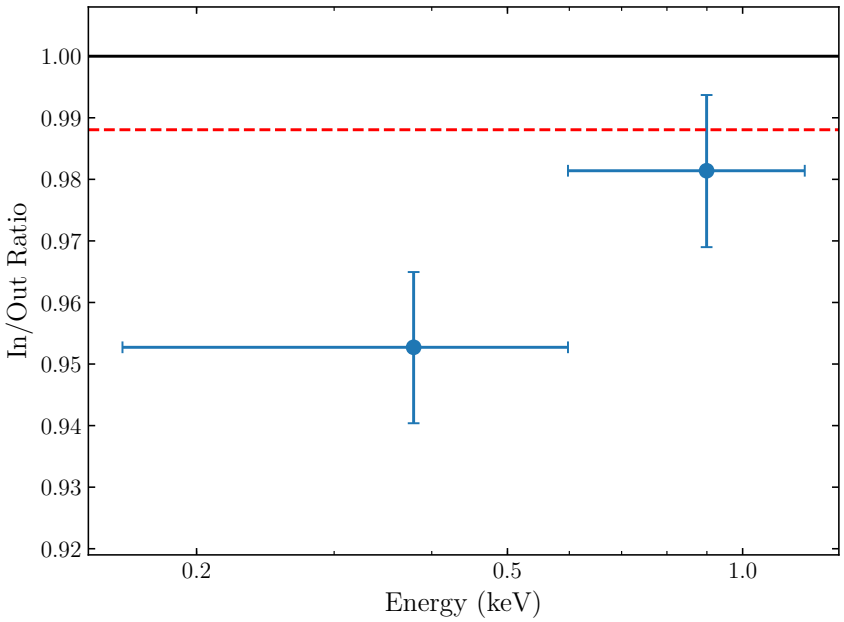


Figure 6.19: Ratio of the in and out-of-transit spectra shown in Fig. 6.16. The solid black line is for a ratio of 1. The dashed red line is that expected for an absorber size equal to the size of the planet optically, assuming the best fit $H$ and $t_0$ from Section 6.4.3.

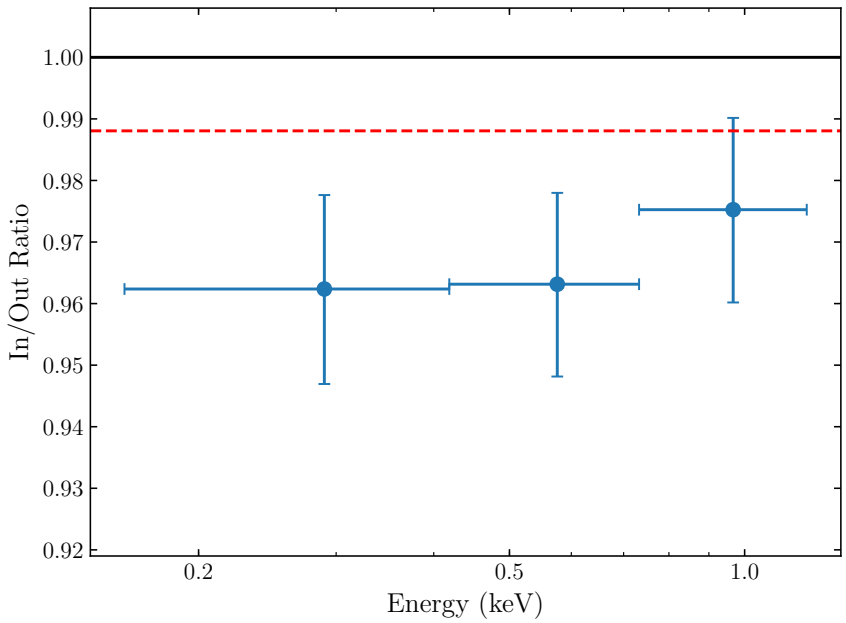


Figure 6.20: As Fig. 6.19, but with three energy bins.

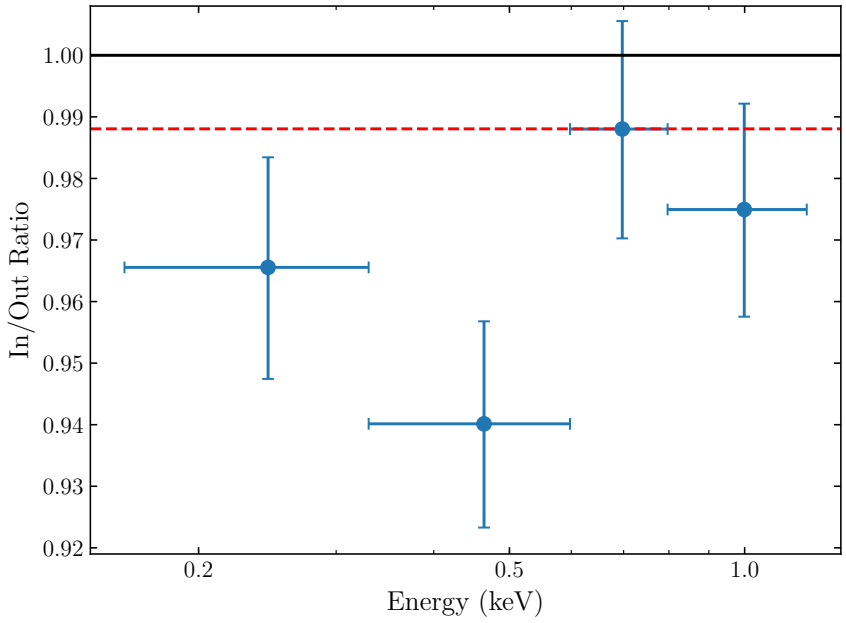


Figure 6.21: As Fig. 6.19, but with four energy bins.

Splitting the data like this into just two bins shows a similar result to that seen in the light curves and model fits in Section 6.4.3, above. In this case, the softer band has a clearly deeper transit than the harder energies. Splitting the data up into more bins obviously increases the error size, making differences between bands harder to pick out. With three roughly even count bins, the ratios can be considered constant across all three, with a hint of decreased transit depth in the hardest bin. Interestingly, there is more variation again when the data was split into four bins. The harder energies again have shallower depths, but it is the second softest bin (0.33–0.60 keV) and not the softest bin (0.166–0.33 keV) that gives the deepest transit in this case.

## 6.6 Discussion

The phase-folded, soft band light curve displayed in Figs. 6.7 and 6.12 represents the first unambiguous detection of the X-ray transit of a planet across its host star. My light curves remain relatively noisy despite averaging across twenty separate primary transits, particularly for the harder energies. However, the expected double dip transit profile is clearly detected in the soft energy band, caused by the optically-thin coronal emission dominating the X-ray output of the star. The transit is also seen to extend well beyond the optical transit, both before and after. This is perhaps not unexpected because the coronal emission extends well beyond the photospheric stellar disc. However, some other features - not least the transit depth, and apparent temporal offset - are more surprising. I now discuss some of the key findings and limitations of my MCMC model fits to the data, as well as the investigation into the transit depth as a function of energy.

### 6.6.1 Size of the absorbing region

One of the most visually striking features of the soft band light curve is the depth of the two dips in count rate, up to around 10%. Moreover, when 200 phase bins are used to plot the data (Fig. 6.11), the count rate for a few bins in the minima dip down to as much as 20% below the baseline. For comparison, the optical transit depth is 2.47% (Baluev et al., 2015).

According to the best-fit model, the minima of the two dips in the soft band are at a transit depth of 7.3%. This agrees well with the inferences of Poppenhaeger et al. (2013), who determined that their noisier folded light curve gave a depth of 6–8%. However, choosing any single combination of six of their seven observations varied the depth anywhere between 2 and 9%. My depth is consistent with the upper

end of this range. It should also be noted that the light curves in the Poppenhaeger et al. (2013) study covered the energy range 0.2–2.0 keV. The single *XMM-Newton* observation in their study would have been affected by contamination from the third background source, although their six Chandra observations have sufficient spatial resolution to fully separate out the three sources.

In their section 4.1, Poppenhaeger et al. (2013) discuss two possible scenarios for why the X-ray transit is deeper than in the optical. These are: (1) an inhomogeneous corona, and (2) an extended planetary atmosphere of escaping material. Given the long temporal baseline of my data (8 years including the 2007 observations, 2 years excluding it), and the relative symmetry of the data in the soft band, the former clearly cannot be explained by a single active region. Instead, scenario 1 would rely on the stellar latitudes crossed by the planet being considerably above average in terms of activity level over a sustained period of time. Poppenhaeger et al. (2013) concluded that this scenario is unlikely as observations of spot crossing events (e.g. Pont et al., 2007; Sing et al., 2011) show the transit path of HD 189733b does not appear to have a significantly larger spot coverage compared to the rest of the star. The temporal offset I find for the transit centre, which I discuss in more detail in Section 6.6.2, corroborates this inference. For the transit to appear early under the assumption that only the disc of the planet itself is absorbing, the temporally-averaged area of greatest activity along the transit path must also be offset from the centre of the stellar disc. The spin-orbit obliquity between the planet and the star is negligible (Triaud et al., 2009; Cegla et al., 2016), meaning the planet transit path covers similar stellar latitudes all the way across. This, combined with the fact that I am averaging over twenty separate observations spread out over such a long baseline, and as such a wide range of spin phases, means such an offset is a very unlikely circumstance. Even a large persistent active region would therefore be smoothed out in the average light curve. Note, however, I do not rule out there being inhomogeneity in the coronal structure generally, particularly within the individual observations (see Section 6.6.3).

Scenario 2 requires a region of absorbing material extending beyond the planet's optically-measured disc. This is more plausible, not least because multiple species have been detected escaping the planet's atmosphere (see Chapter 1 and Section 6.2). The second MCMC fit, holding $H$ and $t_0$ constant, yields an X-ray absorption radius of $2.17^{+0.22}_{-0.20}$ times the optical radius of the planet, $R_{\rm p}$, in the soft energy band. Thus, the absorbing region is larger than the planet at a significance of almost 6-$\sigma$, though it should be noted that this relies on a fixed value of $H$, which correlates with $R_{\rm X}$ in both bands when left free (Fig. 6.13). In the fit with $H$ free,

$R_{\rm X,soft}$ is still larger than $R_{\rm p}$ with a significance of over 3-$\sigma$ (See Table 6.3).

The results imply that the absorbing region in soft X-rays is about four times the area of the planetary disc, as projected onto the sky. I display this visually in Fig. 6.22, which compares the best fit absorption region and the disc of the planet as measured optically. These are plotted together with the best fitting coronal model. Both this schematic and the MCMC fit assumes the absorption region is circular when projected onto the sky, and 100% opaque. In reality, neither of these are likely true. The planet itself will be opaque, but the opacity of material escaping or in the extended atmosphere will depend on the column density of the material, which will vary across the absorption region. The circular assumption is likely to be a simplification too, especially if a substantial fraction of the absorbing material is now unbound to the planet. I discuss further the nature of this absorbing material in Section 6.6.2, below.

In the hard band, the best fit absorption radius is not statistically significantly different from the optical radius of the planet; the significance of the larger radius in this band is slightly less than 2-$\sigma$. Holding $H$ and $t_0$ constant, the relative absorption radii in the two bands are highly suggestive of a difference between the two bands. As the two bands are sensitive to different species, a difference between the bands would be indicative of the species present in the absorbing region. However, the significance of this difference is just below 3-$\sigma$.

### 6.6.2 Early transit

Although the transit appears relatively symmetric, the centre of the transit is offset. The best fit value of $t_0$ in the MCMC fit, $0.9945^{+0.0016}_{-0.0018}$ equates to the transit being $1060^{+310}_{-340}$ s, or $17.6^{+5.6}_{-5.1}$ min, early. This implies that the large absorbing region inferred from the deep transit in Section 6.6.1 is leading the planet as it transits across the star. I show the physical scale of this offset in Fig. 6.22, where only the tail end of this region overlaps with the planetary disc. The planet is very much still one of the primary opacity sources in generating the transit in X-rays, but the 'centre of the absorption' clearly leads the planet. I note specifically that all twenty observations have been successfully corrected to the Solar System barycentre using the SAS task BARYCEN (see also Section 2.3), and so this cannot be contributing to the offset.

This offset shows my X-ray transit is sensitive to a different region of material than typically probed by Ly $\alpha$. A large planetary tail being driven away from the planet at high velocity by, and through charge exchange with, the stellar wind was invoked to explain the observations of a deep transit with a long egress in Ly $\alpha$

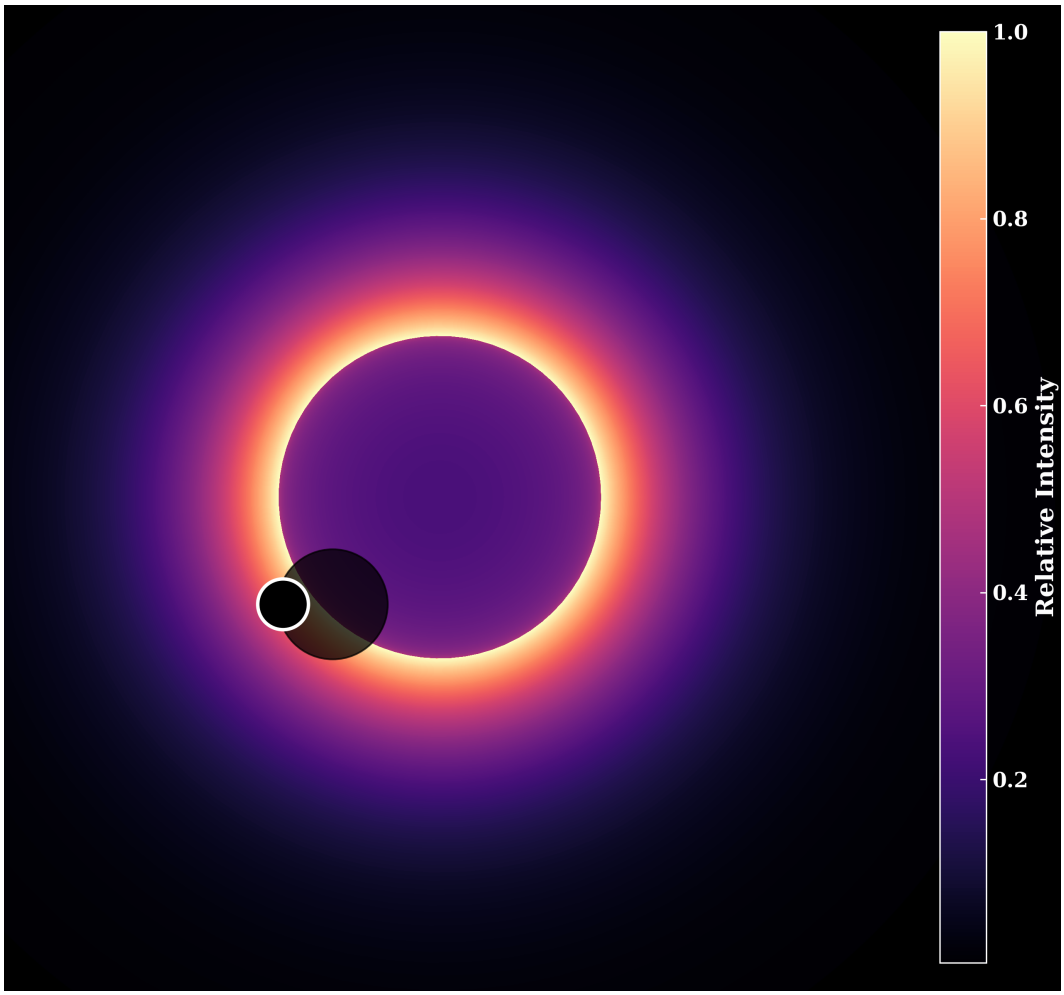


Figure 6.22: Schematic showing how the best-fitting coronal model varies - the colour bar shows the relative intensity of the coronal emission from different regions according to the best-fit model. Overplotted are the planet (smaller, solid black circle with white outline) and the best-fitting absorption region in the soft band (larger, translucent circle). The two are offset from one another in phase according to the MCMC fit, with the absorber leading the planet as they transit the star.

(Lecavelier des Etangs et al., 2012; Bourrier and Lecavelier des Etangs, 2013). Potentially, my transit observations could be probing lower velocity material escaping or residing in the extended atmosphere that is invisible to Ly $\alpha$ because of ISM absorption.

An early transit would not be without precedent, even for HD 189733b. Possible signatures of early, pre-optical transit absorption have been identified in FUV lines for the ionised species S III and N V (Bourrier et al., 2013, Bourrier et al., in prep). While these variations could be of stellar origin, they could be produced by a bow shock ahead of the planet. Similarly, Cauley et al. (2015) identified excess absorption pre-transit in optical observations of the first few Balmer lines, consistent with a bow shock. This occurred up to two hours before the planet transit. While this is too early to be produced by the same region of material that we are probing, it suggests that there could be significant regions of escaping material leading the planet, as required by my data.

As a further example, one can also look to the NUV transit of WASP-12b. Here, the planet showed a deeper transit with an early ingress when observed in the NUV by *HST* (Fossati et al., 2010; Haswell et al., 2012). Two suggestions were proposed to explain this bias towards early transits. The planet could have filled and overflowed its Roche lobe (Li et al., 2010), and now unbound mass is transferred to the star (Lai et al., 2010). Alternatively, the early ingress was also suggested to again result from a bow shock in front of the planet along its orbital path where the stellar wind interacts with escaping material at the edge of planetary magnetosphere (Vidotto et al., 2010; Llama et al., 2011). Further observations of WASP-12b suggested the early ingress feature might not present all the time (Haswell et al., 2012; Copperwheat et al., 2013; Nichols et al., 2015). Vidotto et al. (2011) concluded that variations in shock features in transit light curves should be common, and only in the case of a circularised planet whose orbital axis is perfectly aligned with the stellar spin should the bow shock be steady. Alternatively, Haswell (2018) invokes fig. 9 of Carroll-Nellenback et al. (2017) to propose that the variability of WASP-12b's ingress can be explained by patchy material that has been lost by the planet as part of a hydrodynamic outflow and is now dispersed around its orbital path. With my observations averaging over twenty primary transits, I suggest that my early ingress feature is more permanent and thus less likely to be explained in this latter way. Unlike WASP-12b, HD 189733b is circularised and the spin-orbit obliquity between the planet and the star is negligible (Triaud et al., 2009; Cegla et al., 2016), and so a bow shock feature could be more steady over time.

I conclude that a bow shock scenario is a plausible explanation for the early

transit seen in my data. Further investigation aiming to identify possible species involved in producing the absorption seen, as well as detailed physical modelling of the planetary outflow, will be able to probe this theory further.

### 6.6.3 Analysis of the coronal model

In this section, I assess the merits and drawbacks of the coronal model I have applied in my fits to the light curves.

Coronal emission of the Sun is highly structured, as was highlighted by the image of the X-ray Sun in Fig 1.10. Signatures of activity are present at optical wavelengths too, but affect stellar brightness in these bands by only a small fraction. Active regions dominate the X-ray emission. Given that a magnetic dynamo is thought to act in other late-type stars (see Section 1.3), similarly structure is likely present for those stars too. Llama and Shkolnik (2015) suggest that for a star like the Sun, stellar activity could result in the radii of planets and their atmospheres in X-rays being wrong by up to 50%. HD 189733 is a relatively active K dwarf (e.g. Wright et al., 2004; Shkolnik et al., 2008, Chapter 7), and certainly more active than the Sun. One of the primary reasons for averaging across as many as twenty primary transits was to have the best shot at averaging over fluctuations in coronal emission both spatially within the individual observations, and temporally across multiple epochs. A similar isothermal, exponentially decaying corona was used to model the quiescent emission a theoretical study of the HD 189733b X-ray transit by Marin and Grosso (2017). However, considering only the quiescent emission and with it only dependent on radius are simplifications, even when averaging over so many observations.

Despite this, the exponential coronal model does provide a good fit to the data, especially in the soft band, as demonstrated by the $\chi^2_{\rm red}$ value of 1.09. In the hard band, the lesser quality of fit is more down to the noisiness of the data, particularly in the first half of the folded light curve. While mathematically the fit across both bands is acceptable, it does not necessarily mean that the model, and thus the determined values of the parameters, is the most accurate physical description of the observations.

The determined value of the coronal scale height, $H$, is $0.94^{+0.28}_{-0.21}\,\mathrm{R}_*$, as shown in Table 6.3. Rearranging Equation 6.2, I can input this fitted value and estimate the coronal temperature. I assume $\mu = 1.27$, which was also the value used by Marin and Grosso (2017). This accounts for a small but not insignificant fraction of helium in the corona. I obtain a value for the temperature of $\left(1.46^{+0.44}_{-0.39}\right) \times 10^7\,\mathrm{K}$. The equivalent energy is $1.26^{+0.38}_{-0.34}\,\mathrm{keV}$. These values seem a little high, considering

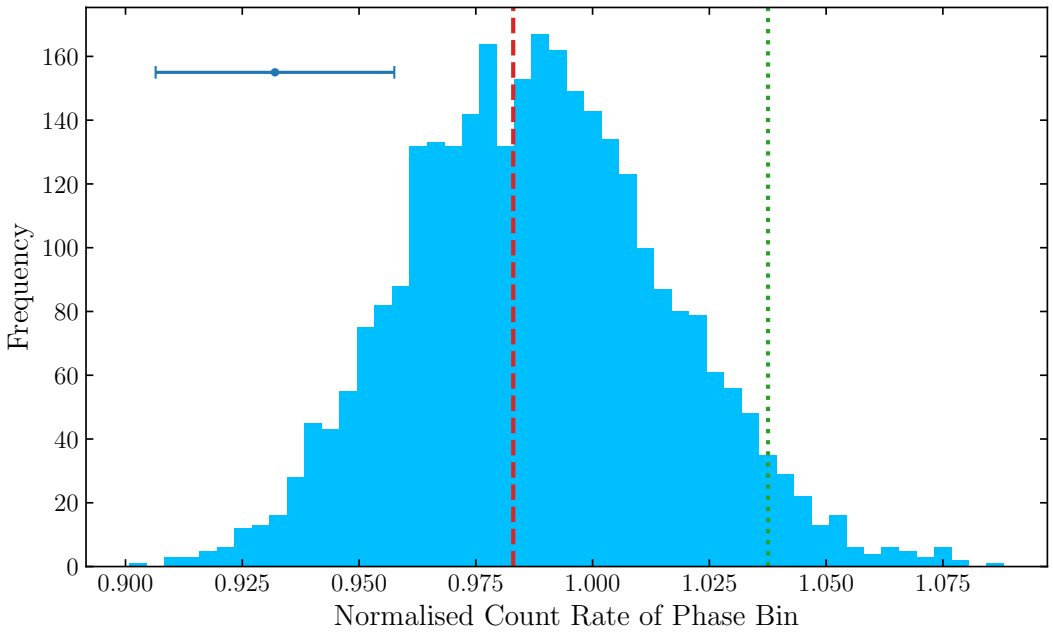


Figure 6.23: Normalised count rates of the phase bin at 0.992, taking 3000 random combinations of any twenty of the twenty observations and allowing repeats. The red dashed line represents the value of the fitted model at this phase, while the green dashed line represents the value in the actual soft band light curve in Figs. 6.7 and 6.12. The errorbar in the top left hand corner represents the average uncertainty in each count rate measurement.

the softness of the source, as highlighted by the fitted temperatures I find in Section 7.4.3. The result is within 2-$\sigma$ of the highest of the three fitted temperatures, and well within 3-$\sigma$ of the middle temperature. Given the simplicity of the model, this is a reasonable result.

From a visual point of view, the model does less well in the minima, slightly underestimating the depth of the transit at these points. The drop to the minima along the ingress in the soft band in Fig. 6.11 is quite sudden. This could be caused by either an extra, unconsidered coronal effect, such as a range of scale heights reflecting the range of temperatures. Alternatively, it could be telling us something about the shape of the absorbing region: if material is escaping and is interacting with the stellar wind, the region is likely more complex than the simple circular disc it is modelled as here. For instance, maybe we are looking along an extended structure in the deeper minima, but viewing it more from the side in the second, slightly shallower minima. In any case, this is evidence of higher order structure that the model I have applied is not able to reproduce.

In both bands, the model also seems to underestimate how much the data

rises back up in between the two minima. In the model, the rise is to perhaps about half the maximum transit depth, whereas the data points rise all the way back up to the out-of-transit baseline at its highest point. I examined this further through a bootstrapping technique. I took the twenty observations and, allowing for repeats, randomly selected an observation twenty times. These were combined and the count rate in the phase bin at 0.992 (i.e. the phase bin with the highest count rate during the transit in the soft band light curve in Figs. 6.7 and 6.12) was noted. 3000 iterations of this process were performed, with a histogram of the results plotted in Fig. 6.23. The distribution of results points to the actual data being biased towards higher values by a small minority, perhaps just one or two, of the observations. The centre of the distribution lines up well with the model result. This is highly suggestive that the model's failure to rise back up enough with the data mid transit is caused by residual effects of stellar variability that even averaging over twenty primary transits cannot fully remove. On the positive side, this investigation suggests that the level of the model in this phase bin is reasonable.

Overall, the main advantage of my model is in its simplicity. Not considering extra coronal structure or a more complex shape for the absorbing region ensures the number of parameters required to fit the light curve is small. Indeed, the quality of data even across twenty transits is probably not that conducive to adding in much more complexity. Even in the model I have used, there are multiple correlated parameters, and adding further complexity comes with the risk of just introducing further degeneracies that are not able to be broken given the quality of data.

### 6.6.4 Spectroscopy

The analysis in Section 6.5 corroborates the deeper transit in the soft band. This is when comparing both to the harder energy bands and the transit depth that would be expected for an absorbing region of size $R_{\rm X} = R_{\rm p}$. When the same process is applied with three and four energy bins, the results are less striking, particularly for three bins. In that case, the three ratios are consistent with each other. Splitting into four does hint at species in the 0.33–0.60 keV dominating the soft band absorption.

The method is potentially biased towards giving deeper soft band transits, as the phases used to define what constituted in and out-of-transit was based on the best fit model to the soft band fit in Section 6.4.3. Therefore, the method is perhaps optimised for minimising ratios at softer energies, and harder energies could preferentially show deeper transits (or smaller ratios) with a different choice of phases. Of course, the noisiness of hard band data presented here makes determining transit signals in it tough, but the ratios obtained using this method are likely

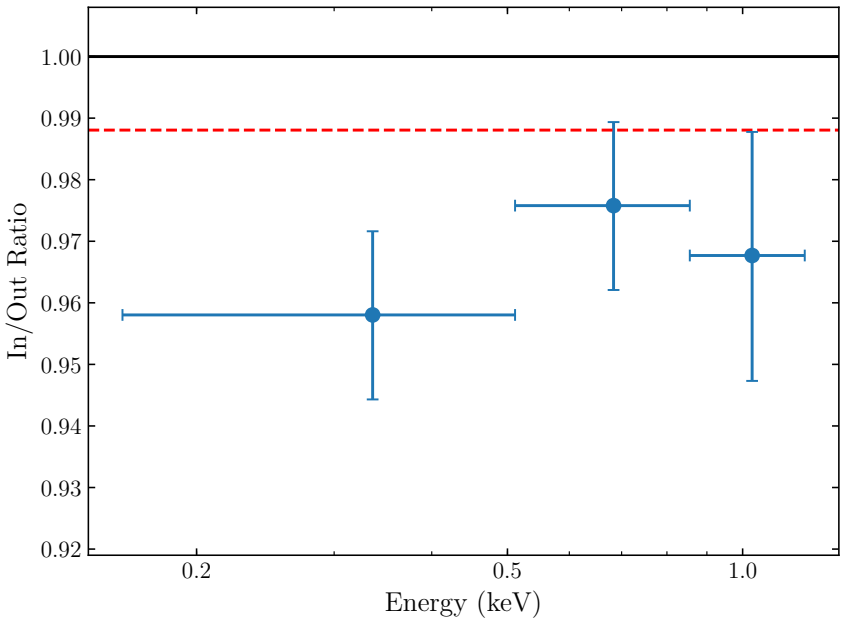


Figure 6.24: As Fig. 6.20, but splitting the data evenly by energy.

somewhat sensitive to the phase definition used.

The choice of where to split the data in terms of energy is also relevant. I chose to split the data into roughly equally sized bins in terms of counts, as I had done for the light curves in Section 6.4. For a comparison, I again split the data into three bins, but this time into roughly equal-sized energy ranges. This gives energy ranges of 0.16–0.51, 0.51–0.85, and 0.85–1.2 keV, as opposed to the 0.16–0.42, 0.42–0.73, and 0.73–1.2 keV used for the equal count split. The resulting ratios, displayed in Fig. 6.24, are somewhat different than before. While the three are still consistent with each other, it is the middle bin that now shows a hint of having a shallower transit. This suggests that the ratios obtained using this method are also somewhat sensitive to the energy ranges the data are split into.

## 6.7 Conclusions

I have successfully detected the X-ray transit of HD 189733b across its host star. At the soft X-ray energies, the expected double dip transit profile is evident in the data. Visual inspection of the soft band light curves reveal a much deeper transit than would be expected from the planet disc alone, as measured optically. Subsequent fitting of the light curves placed the soft band depth at 7.3%, consistent with the depth suggested by Poppenhaeger et al. (2013) to explain their noisier data. Fitting

also confirmed the transit centre to be $17.6^{+5.6}_{-5.1}$ min early, another feature of the transit that was visually apparent in the soft band light curve.

The soft band additionally appears to have a deeper transit than the harder energies, and when the data is refitted with $H$ and $t_0$ held constant, in order to explore the relative depth of the two bands, the two depths show clear evidence of being different. Splitting the data up into energy ranges based on equal counts and taking the ratio of the in and out-of-transit does corroborate this finding further; the soft-hard difference is apparent when splitting into two and four bins. Further investigations showed the relative depths between the in-out ratios are somewhat sensitive to both the exact phase and energy definitions used.

As regards the nature of the absorbing material, the deeper transit suggests that there is an absorbing region of material escaping the planet evident in the soft band, in addition to the planet disc itself. This agrees with previous observations at Ly $\alpha$ wavelengths and of some metal lines that indicate material escaping or residing in an extended atmosphere. The majority of this absorbing region appears to be leading the planet in its orbital path around the star. A possible explanation is that the transit is probing a bow shock where the escaping material is meeting the stellar wind, an interpretation previously applied to early ingresses seen for both this planet and WASP-12b in various optical, NUV, and FUV observations. With more complex modelling, if applied carefully, this idea might be able to be explored further.

# Chapter 7

# X-ray flares, activity, and SPI in the HD 189733 system

## 7.1 Introduction

The interest in the HD 189733 system in X-rays goes well beyond transits. In Section 1.4, I introduced the idea that hot Jupiters are thought to be massive enough while having small enough separations to potentially induce magnetic or tidal effects on their host stars. As previously mentioned in Chapter 6, HD 189733 hosts an M dwarf stellar companion on a wide orbit, in addition to its hot Jupiter. This makes the system an excellent target for probing possible SPI (see Section 1.4), as the wide binary companion should be far enough apart from the close K dwarf-hot Jupiter pair that it is unaffected in terms of its activity.

The Poppenhaeger et al. (2013) study looking at the X-ray transit also took advantage of the superior spatial resolution of *Chandra* to detect HD 189733B in X-rays. Poppenhaeger and Wolk (2014) used the measured X-ray luminosities to estimate ages for the two stellar components. For the planet host HD 189733A, they compared the X-ray luminosity to those of young K stars in the Hyades (Stelzer and Neuhäuser, 2001), and those in the field (Schmitt and Liefke, 2004), and approximated an X-ray-derived-age in the region of 1–2 Gyr. For the companion HD 189733B, they compared $L_X$ to that for field M stars (Schmitt and Liefke, 2004), and to M dwarfs in the Galactic old disc and halo (Micela et al., 1997), approximating an X-ray-age of 5–10 Gyr. Poppenhaeger and Wolk (2014) interpreted this, and a similar result for CoRoT-2AB, as evidence of spinning up or inhibition of the spin down of the host star due to tidal interactions, thus maintaining the activity level above that of a typical star of its age.

Shkolnik et al. (2008) also claimed evidence of SPI for HD 189733 in chromospheric observations. Their data suggested that the mean absolute deviation of the Ca K line residuals is phased with the orbital period of the planet. Cauley et al. (2018) also found evidence of Ca K line residuals phasing with the orbit in one of their analysed epochs. However, none of the other five epochs they investigated exhibited a similar signal, and so the existence of these signatures remains highly questionable.

The series of papers by Pillitteri et al. (2010, 2011, 2014) claimed the timing of X-ray flares to be linked to the orbital phase of the planet. Light curves for three *XMM-Newton* observations, in 2009, 2011 and 2012 all revealed X-ray flares just after the secondary eclipse of the planet between planetary orbital phases, $\phi$, 0.52 and 0.65. Despite the small number statistics and strongly biased phase coverage, they interpreted this as evidence of the coronal activity being phased with planetary motion. FUV observations of the system with *HST* presented by Pillitteri et al. (2015) also found an increase in line fluxes during phases 0.50–0.63. They interpreted these X-ray/FUV results as escaping planetary material being accreted by the star, about 70–90° in front of the planet along its orbit. However, spectropolarimetry observations of the system by Fares et al. (2010) showed no clear magnetic SPI between the star and planet. The study found activity indicators were predominately modulated with stellar rotation. Route (2019) assessed the quality of the evidence for SPI across multiple wavelengths from X-ray through to radio, concluding that the previously claimed phasing of various activity indicators with the orbital period of the planet are not statistically significant, and that some or all of the claims may be explained by insufficient sampling of the star's activity, and not SPI.

In this Chapter, I use archival observations with *Swift*, and all 25 observations of the system with *XMM-Newton* to further investigate stellar activity, X-ray flares, and the possibility of SPI signatures in the HD 189733 system.

## 7.2 Observations

### 7.2.1 *Swift*

I analysed archival observations of the HD 189733 system taken with the X-ray Telescope (XRT) on the *Swift* spacecraft over nine years from June 2008 through July 2017. I define 12 separate epochs within this period, as outlined in Table 7.1. Of these, the epoch 8 data were previously analysed by Lecavelier des Etangs et al. (2012) and Pillitteri et al. (2014). X-ray variability within the epoch was observed, including a flare on the host star 9 hr before the primary transit of the planet.

Table 7.1: Details of the *Swift* observations. The listed exposure times are for the XRT instrument.

| Epoch | Observation IDs | No. of Obs | Start Time (TT) | Finish Time (TT) | Exp. Time (ks) | Elapsed Time (ks) |
|---|---|---|---|---|---|---|
| 1 | 00036406001 | 1 | 2008-06-08 06:48 | 2008-06-08 18:13 | 3.98 | 41.1 |
| 2 | 00036406002 – 00036406003 | 2 | 2008-07-18 09:08 | 2008-07-19 09:22 | 1.68 | 87.2 |
| 3 | 00036406004 | 1 | 2008-12-03 01:07 | 2008-12-03 12:38 | 4.77 | 41.5 |
| 4 | 00036406005 – 00036406006 | 2 | 2009-02-23 12:42 | 2009-02-26 19:26 | 7.92 | 283.4 |
| 5 | 00036406007 | 1 | 2009-11-29 14:41 | 2009-11-29 18:01 | 1.16 | 12.0 |
| 6 | 00036406008 | 1 | 2009-12-25 23:49 | 2009-12-26 04:50 | 1.42 | 18.1 |
| 7 | 00036406009 | 1 | 2010-02-21 00:21 | 2010-02-22 03:52 | 15.10 | 99.1 |
| 8 | 00036406010 – 00036406017 | 8 | 2011-09-07 07:49 | 2011-09-08 11:28 | 21.99 | 99.5 |
| 9 | 00092203001 | 1 | 2015-04-23 09:48 | 2015-04-23 19:50 | 11.00 | 36.1 |
| 10 | {00036406018 – 00036406023}<br>{00033910001 – 00033910013} | 18 | 2015-07-29 07:45 | 2015-08-04 15:42 | 7.91 | 547.0 |
| 11 | 00036406024 | 1 | 2016-07-01 10:27 | 2016-07-01 18:53 | 7.62 | 30.4 |
| 12 | 00036406025 – 00036406033 | 9 | 2017-07-31 00:45 | 2017-07-31 04:31 | 5.44 | 13.6 |

I obtained light curves for the observations using the online tools for building data products described in Evans et al. (2007, 2009). Three different energy ranges were investigated: 0.3–3.0 keV (the "full" dataset), 0.3–1.0 keV ("soft"), and 1.0–3.0 keV ("hard"). Throughout our investigations, I bin the data per observational snapshot, where one snapshot corresponds to a single *Swift* orbits-worth of data.

As for *XMM-Newton* (see Chapter 6 and below), the PSFs of the X-ray three sources (the two binary components and the background source) overlap in the *Swift* images. In Section 6.3, I determined that the M dwarf companion only makes a significant contribution to the flux when flaring, and confirmed that the background X-ray source is only relevant above about 1.2 keV (see also, Poppenhaeger et al., 2013). The extraction radius used by the online tool depends on the uncorrected count rate in an initial 30 arcsec radius circle, centred on the output from XRTCENTROID, an FTOOL task (Evans et al., 2007). Examination of output files from the process confirmed that the final extraction radius was 15 arcsec.

### 7.2.2 *XMM-Newton*

The HD 189733 system has been observed on 25 occasions by *XMM-Newton* between April 2007 and April 2015. These are the twenty observations covering primary transits used in Chapter 6, together with five further observations that do not cover transits. These five non-transit observations all cover some portion of phases between $\phi = 0.40$ and $\phi = 0.76$, around and just after the secondary eclipse. The full set of observations are listed in Table 7.2. As mentioned in Chapter 6, all of the primary transit observations were taken in small window mode with the thin optical blocking filter. The five extra, non-transit observations were made with the EPIC cameras in prime full window mode with the medium blocking filter.

All *XMM-Newton* data used in this study were reduced using the Scientific Analysis System (SAS 15.0.0), following the standard procedure.

## 7.3 *Swift* Results

I examined the *Swift* data from a number of different angles to explore stellar variation and, in particular, flaring. These included scanning the data for phasing with the planetary orbit and stellar rotation, as well as performing a search for additional, previously unreported flares.

Table 7.2: Details of the *XMM-Newton* observations. Twenty of them are the same observations used to detect the transit in Chapter 6.

| No. | Observation IDs | Start Time (TT) | Finish Time (TT) | Exp. Time (s) |
|---|---|---|---|---|
| 1 | 0506070201 | 2007-04-17 14:06:31 | 2007-04-18 05:20:49 | 54858 |
| 2 | 0600970201 | 2009-05-18 21:15:54 | 2009-05-19 07:37:49 | 37315 |
| 3 | 0672390201 | 2011-04-30 23:14:20 | 2011-05-01 10:06:12 | 39112 |
| 4 | 0690890201 | 2012-05-07 18:24:32 | 2012-05-08 11:29:48 | 61516 |
| 5 | 0692290201 | 2013-05-09 20:16:00 | 2013-05-10 07:09:38 | 39218 |
| 6 | 0692290301 | 2013-11-03 07:54:13 | 2013-11-03 18:12:33 | 37100 |
| 7 | 0692290401 | 2013-11-21 00:58:40 | 2013-11-21 12:38:40 | 42000 |
| 8 | 0744980201 | 2014-04-05 05:05:20 | 2014-04-05 18:25:20 | 48000 |
| 9 | 0744980301 | 2014-05-02 01:22:25 | 2014-05-02 10:44:05 | 33700 |
| 10 | 0744980401 | 2014-05-13 01:55:22 | 2014-05-13 13:02:01 | 39999 |
| 11 | 0744980501 | 2014-05-15 09:57:00 | 2014-05-15 18:50:20 | 32000 |
| 12 | 0744980601 | 2014-05-17 14:21:12 | 2014-05-17 23:14:32 | 32000 |
| 13 | 0744980801 | 2014-10-17 16:08:26 | 2014-10-18 02:25:06 | 37000 |
| 14 | 0744980901 | 2014-10-19 20:38:36 | 2014-10-20 06:11:56 | 34400 |
| 15 | 0744981001 | 2014-10-22 01:39:14 | 2014-10-22 12:44:14 | 39900 |
| 16 | 0744981101 | 2014-10-24 06:15:47 | 2014-10-24 17:05:47 | 39000 |
| 17 | 0744981301 | 2014-11-08 20:16:34 | 2014-11-09 05:53:14 | 34600 |
| 18 | 0744981201 | 2014-11-11 00:37:26 | 2014-11-11 12:50:46 | 44000 |
| 19 | 0744981401 | 2014-11-13 06:46:05 | 2014-11-13 15:39:25 | 32000 |
| 20 | 0744980701 | 2014-11-15 09:48:00 | 2014-11-15 20:38:00 | 39000 |
| 21 | 0748391401 | 2015-04-03 03:30:49 | 2015-04-03 16:40:49 | 47400 |
| 22 | 0744981501 | 2015-04-13 02:37:23 | 2015-04-13 15:14:03 | 45400 |
| 23 | 0744981601 | 2015-04-17 12:34:55 | 2015-04-17 23:58:15 | 41000 |
| 24 | 0744981701 | 2015-04-19 19:06:26 | 2015-04-20 05:39:46 | 38000 |
| 25 | 0748391501 | 2015-04-23 06:17:15 | 2015-04-23 18:30:35 | 44000 |

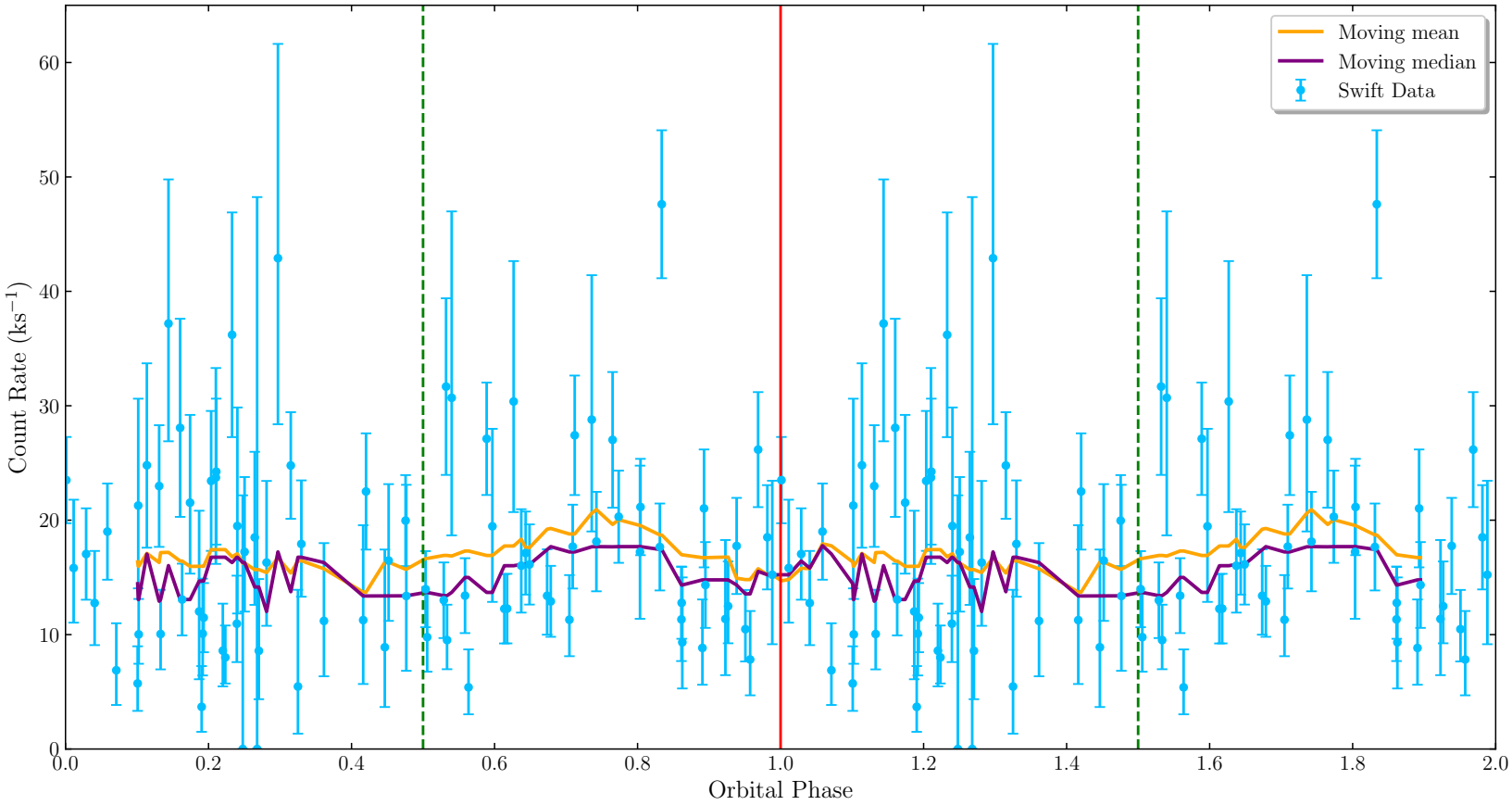


Figure 7.1: Light curve over the full energy range for HD 189733 in *Swift* data between June 2008 and July 2017, phase folded on the orbital period of the planet. The primary and secondary transits are marked with the red solid and green dashed lines, respectively. The moving mean and median, calculated with a phase window of 0.20, are also overplotted.

### 7.3.1 Entire data analyses

Fig. 7.1 shows the light curve of the data from across the full temporal range available. The light curve is binned by snapshot, a property of the data related to *Swift*'s low Earth orbit only allowing it to take data for part of its orbit. The data plotted between $\phi = 1$ and $\phi = 2$ is exactly the same as that from the first half of the plot, repeated to aid the eye in picking out any variation, particularly either side of the planetary transit. Overplotted are the moving median and mean, each calculated with a window size of $\phi = 0.20$ around each phase ($\phi = 0.10$ either side). The moving averages, especially the mean hint at some variability around $\phi = 0.8$, possibly biased by the September 2011 flare. To test this further, I binned the data in eight equally-sized phase bins (0–0.125, 0.125–0.25, 0.25–0.375 etc.) with and without the flare, and calculated the weighted mean. I plot both cases in Figs. 7.2 and 7.3. Assuming a constant model at the level of the weighted mean, I calculated the $\chi^2$ of both iterations of the binned data. The flare does indeed have a large effect. With the flare included $\chi^2_{\rm red} = 2.65$ giving a p-value of 0.0098, but without the flare $\chi^2_{\rm red} = 1.10$ and the p-value is 0.359. This not only demonstrates the effect of the flare, but also shows there is no statistically significant phasing of the *Swift* data with the orbital period of the planet.

Fig. 7.4 displays the Lomb-Scargle periodogram of the *Swift* data. This was plotted using the ASTROPY (Astropy Collaboration et al., 2013; Price-Whelan et al., 2018) implementation, and the associated false alarm probabilities that are plotted employ the code's built-in method taken from Baluev (2008). Three frequencies of interest are highlighted: those associated with the planetary orbital period, $P_{\rm orb}$, of 2.218575200 d (Baluev et al., 2015), and the equatorial and polar stellar rotational periods ($P_{\rm rot}$) of 11.94 and 16.53 d, respectively (Fares et al., 2010). The periodogram reveals little evidence of any periodic features in the data at these frequencies of interest. Indeed, no peaks exceed the 5% false alarm probability level.

Also of interest is any potential long term variability, perhaps due to an activity cycle like the 11 year Solar cycle. Fig. 7.5 displays the weighted average count rate, averaged over each epoch of observations. All observations within each 10 days of each other were combined with one another. Again, I performed a test of the data against a constant model equal to the weighted mean. The resulting $\chi^2_{\rm red}$ is 2.67, giving a p-value of 0.00192, and ruling out the constant model with 99.8% confidence. In this case, removing the September 2011 flare does not remove the statistical significance of the variability. Indeed, the $\chi^2_{\rm red}$ with the flare removed is 3.01, giving an even smaller p-value of 0.00051. This confirms that although it is difficult looking to pick out any visually obvious periodic signatures akin to an

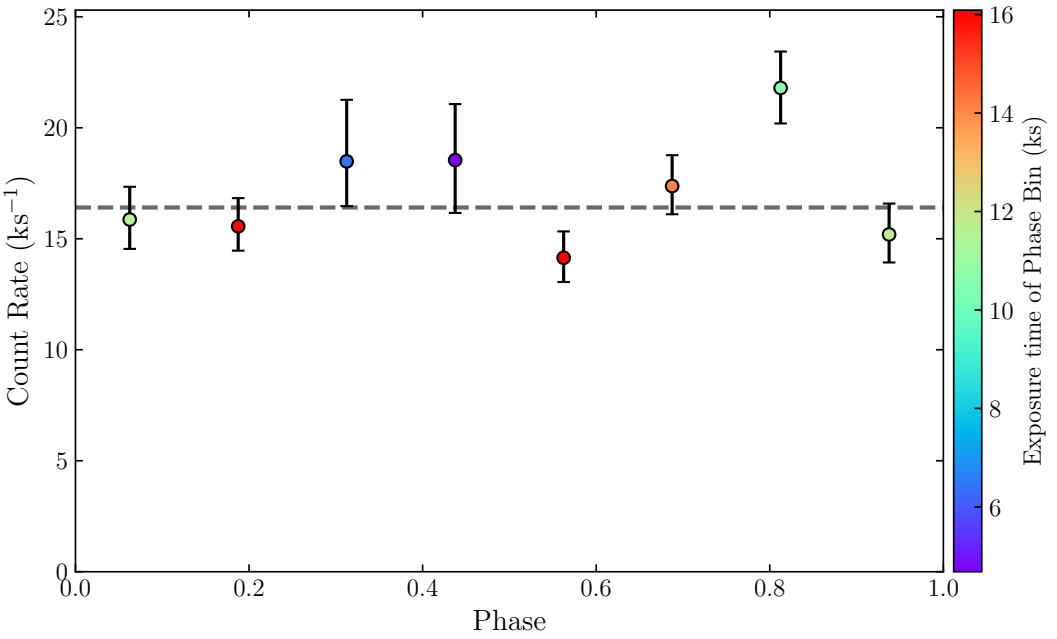


Figure 7.2: Average count rate for each phase bin of the *Swift* data. Each point is coloured according to the total exposure time at that epoch. The grey dashed line is the weighted mean of all of the points.

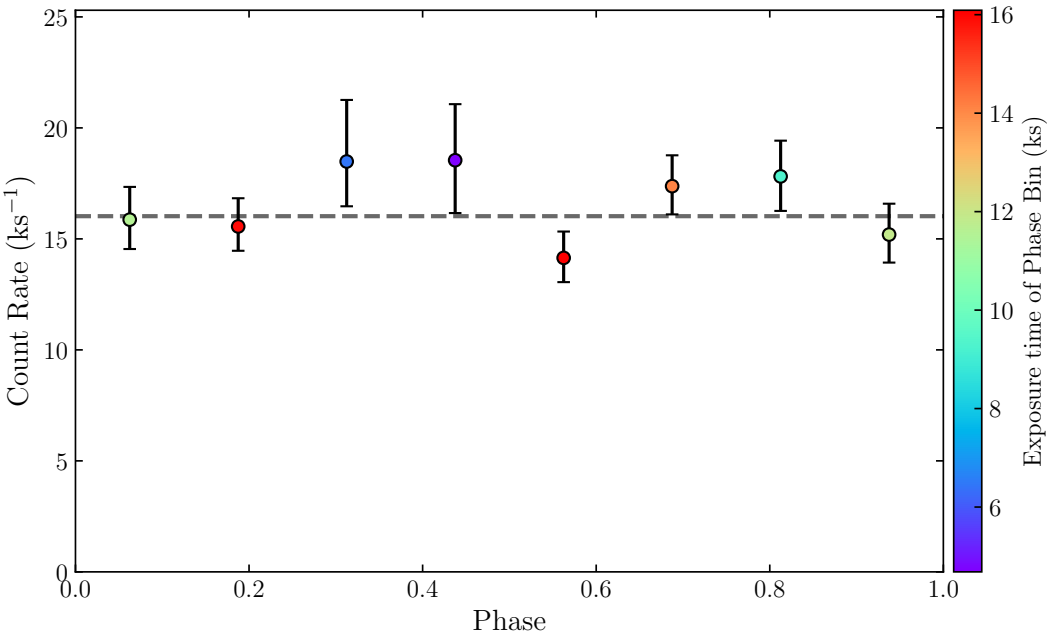


Figure 7.3: As Fig 7.2, but with the September 2011 flare excluded.

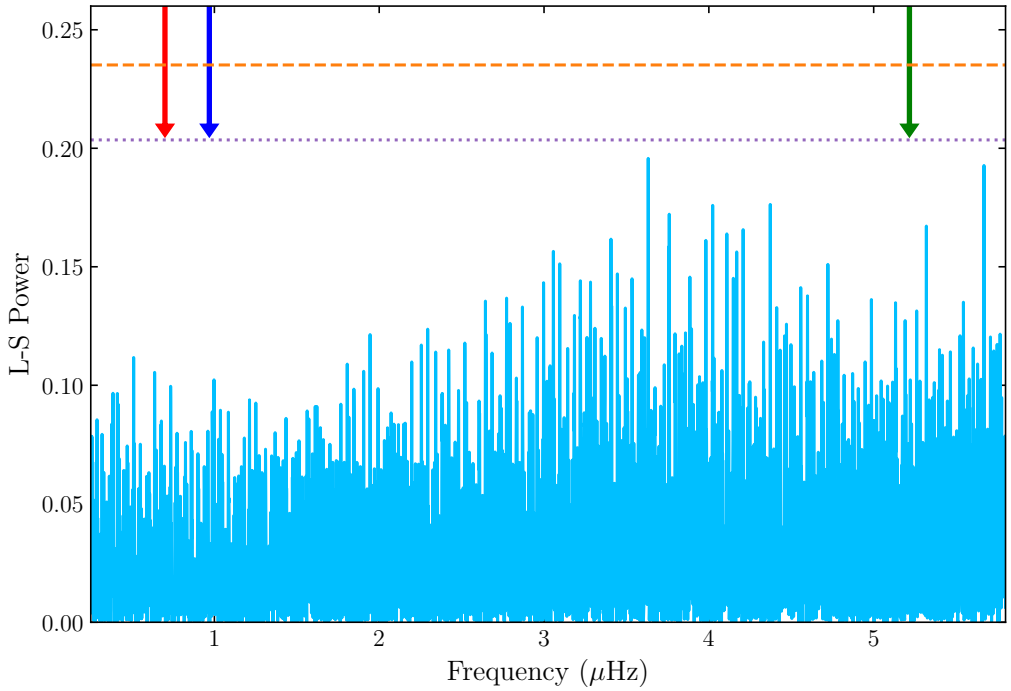


Figure 7.4: Lomb-Scargle periodogram for the *Swift* snapshots over the full energy range. Arrows indicate the frequencies associated with (l to r): polar $P_{\rm rot}$ (red); equatorial $P_{\rm rot}$ (blue); $P_{\rm orb}$ (green). The purple dotted and orange dashed lines represent the 5% and 1% false alarm probabilities.

activity cycle, the *Swift* data is variable between the defined epochs. I explore the more sensitive *XMM-Newton* data in this context in Section 7.4.3.

### 7.3.2 Search for additional flares

Lecavelier des Etangs et al. (2012) noted a strong flaring event in the *Swift* observation on 7 September 2011, during epoch 8 as defined in Table 7.1. Pillitteri et al. (2014) also mentioned the event in their own flaring analysis, although, curiously, they mistakenly place the event at $\phi = 0.2$ (see, for example, their fig. 9), despite also (correctly) stating elsewhere the assertion from Lecavelier des Etangs et al. (2012) that it occurred about 9 hours before the primary transit. This corresponds to $\phi = 0.834$. The snapshot corresponding to the flare has the highest single snapshot count rate across all of the *Swift* data, at $0.0476 \pm 0.0065\,{\rm s}^{-1}$. I performed a search across the rest of the observations to determine if any additional flares can be unambiguously identified.

The most obvious property to look at is the count rates, and so I took the top decile of snapshots using this measure. This gives eight snapshots, which I label

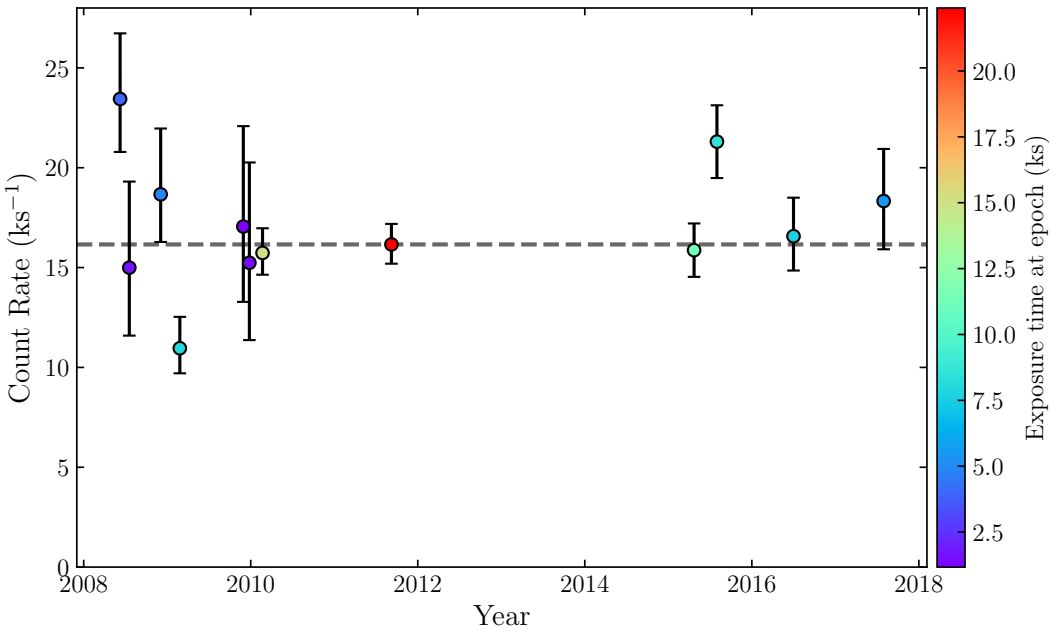


Figure 7.5: As Fig. 7.2, but with the average count rate at each of the defined epochs (see table 7.1) in *Swift* data.

as S1 through S7(a/b), in addition to the known flare F1. Details of these snapshots are given in Table 7.3. Two snapshots from 31 July 2017 are listed as 7a and 7b. These are consecutive snapshots, spaced only 15 minutes apart, and could be related to the same event. In contrast, the two snapshots for 8 June 2008 are listed as S1 and S2 are considered separate events, as they are almost five hours apart with two snapshots in between that have a lower count rate.

Stars often exhibit a hardening of their high-energy spectrum at epochs associated with flares (see Section 1.3.3). Therefore, the first test of these highest count rate snapshots was to look at their hardness ratio, $HR$, where I have defined $HR$ as

$$HR = \frac{H - S}{H + S}. \tag{7.1}$$

$H$ is the count rate in the hard band, defined as 1.0 to 3.0 keV, and $S$ is the soft count rate, defined for energies between 0.3 to 1.0 keV. Fig. 7.6 displays the hardness ratios of the snapshots. Although the error bars of some points extend to $|HR| > 1$, such values are unphysical. The point furthest to the right is the known flare, while the next points immediately leftward in the top panel are the candidate snapshots; their $HR$ values are given in Table 7.3. Three of the nine, including the known flare, have positive values of $HR$, which indicates an epoch with more X-rays from the

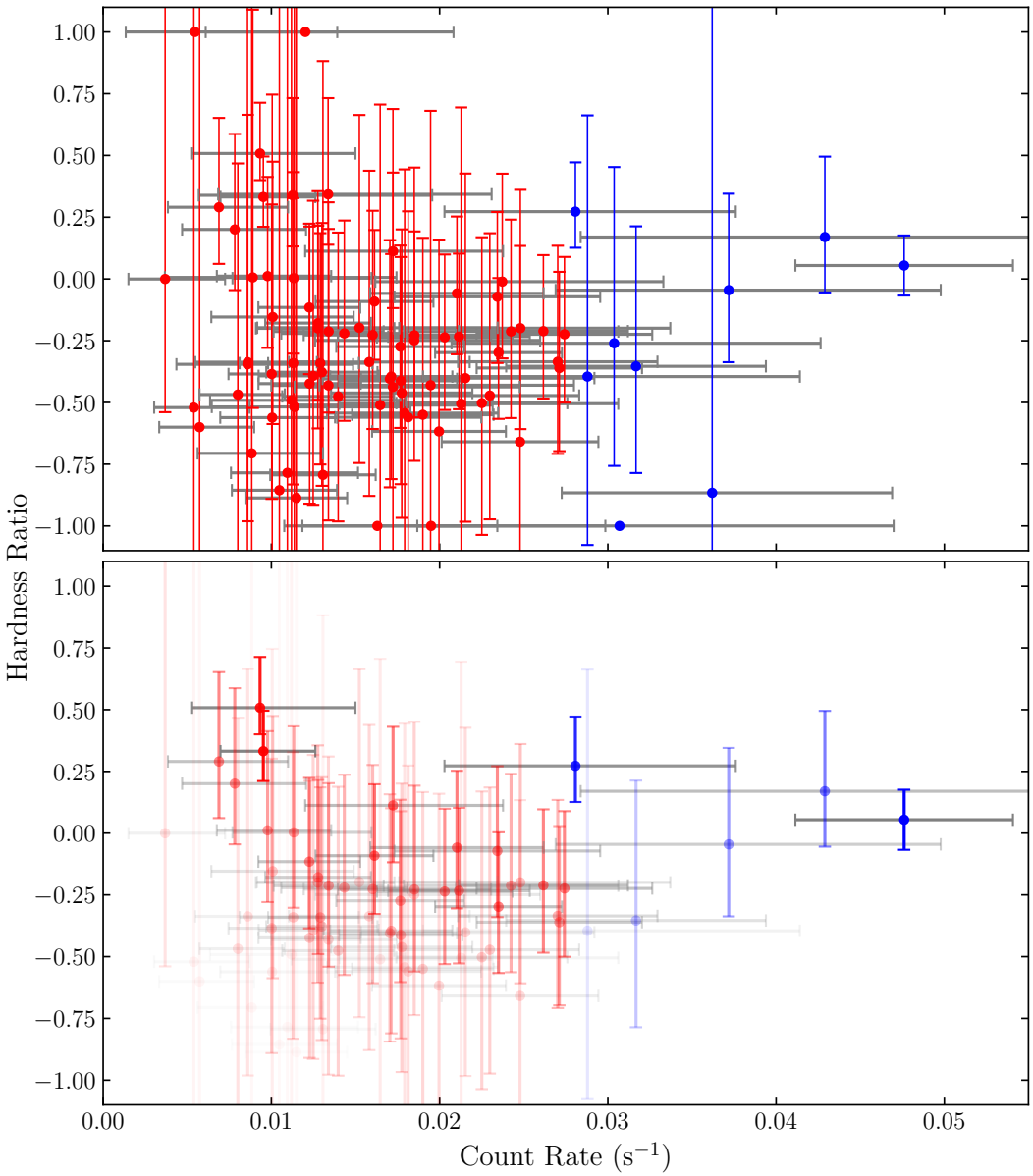


Figure 7.6: Top panel: hardness ratio against count rate for all snapshots in the *Swift* data. The blue points are the snapshots listed in Table 7.3. Bottom panel: the same data with an exposure cut of 500 s applied and the transparency of the points inversely proportional to the size of the hardness ratio error bars.

Table 7.3: Properties of the top decile (by count rate) of snapshots in the *Swift* data. The full, soft, and hard energy bands are 0.3–3.0 keV, 0.3–1.0 keV, and 1.0–3.0 keV, respectively.

| Label | Date | Phase | Exp. (s) | Full CR ($ks^{-1}$) | $S$ ($ks^{-1}$) | $H$ ($ks^{-1}$) | $HR$ |
|---|---|---|---|---|---|---|---|
| F1 | 07-09-2011 | 0.834 | 1434 | $47.6 \pm 6.5$ | $22.5 \pm 4.4$ | $25.1 \pm 4.7$ | $0.05 \pm 0.12$ |
| S1 | 08-06-2008 | 0.144 | 504 | $37^{+13}_{-10}$ | $19.4^{+9.3}_{-7.1}$ | $17.8^{+9.4}_{-6.9}$ | $-0.05^{+0.39}_{-0.29}$ |
| S2 | 08-06-2008 | 0.233 | 484 | $36^{+10}_{-9}$ | $34^{+10}_{-9}$ | $2.4^{+3.9}_{-1.9}$ | $-0.9^{+2.8}_{1.4}$ |
| S3 | 03-12-2008 | 0.297 | 511 | $43^{+19}_{-15}$ | $18^{+13}_{-9}$ | $25^{+15}_{-11}$ | $0.17^{+0.33}_{-0.22}$ |
| S4 | 23-02-2009 | 0.627 | 308 | $30^{+12}_{-10}$ | $19^{+10}_{-7}$ | $11.2^{+8.2}_{-5.5}$ | $-0.26^{+0.71}_{-0.50}$ |
| S5 | 21-02-2010 | 0.160 | 644 | $28.1^{+9.5}_{-7.9}$ | $10.2^{+6.2}_{-4.5}$ | $17.9^{+7.7}_{-6.0}$ | $0.27^{+0.20}_{-0.15}$ |
| S6 | 01-07-2016 | 0.736 | 622 | $29^{+13}_{-10}$ | $20^{+11}_{-8}$ | $8.7^{+8.3}_{-5.0}$ | $-0.40^{+1.06}_{-0.68}$ |
| S7a | 31-07-2017 | 0.532 | 924 | $31.7 \pm 7.7$ | $21.4^{+6.9}_{-5.7}$ | $10.2^{+5.4}_{-4.0}$ | $-0.35^{+0.57}_{-0.43}$ |
| S7b | 31-07-2017 | 0.540 | 213 | $31^{+16}_{-12}$ | $31^{+16}_{-12}$ | 0 | $-1$ |

harder band than soft. This is in contrast to the majority of points, which tend to cluster between $HR = -0.25$ and $HR = -0.75$, their negative values indicating a snapshot dominated by softer X-rays.

In the bottom panel of Fig. 7.6, I applied an exposure cut of 500 s to the data, and weighted each point's transparency by the magnitude of its hardness ratio error bars. Points with longer exposure times tend to be better constrained in both count rate and $HR$, and weighting the transparency in this way aids the eye in picking out these best constrained points from the background.

S3 and S5 show the best evidence of being harder snapshots than the main cluster of points in Fig. 7.6. Both have $HR$ values consistent with the known flare, F1, with S5 showing a hint of being even harder. S1 also has a $HR$ value that agrees with F1, although its large uncertainties on both its $HR$ and its count rate mean it is also consistent with the main cluster of points. The other snapshots all are consistent with no hardening of their count rates.

It is interesting to note the few relatively well constrained points in the top left, with a count rate about $10\,ks^{-1}$ and $HR$ =0.25–0.50, meaning they are particularly hard snapshots. The data covers the energy range 0.3–3.0 keV, and thus contamination by the background source is possible. These snapshots are therefore likely the result of the planet host star being particularly X-ray quiet, and thus the harder background source being more prominent, leading to a more positive value of $HR$.

I also investigated the $\sigma$-significance of each snapshot. That is, how many $\sigma$

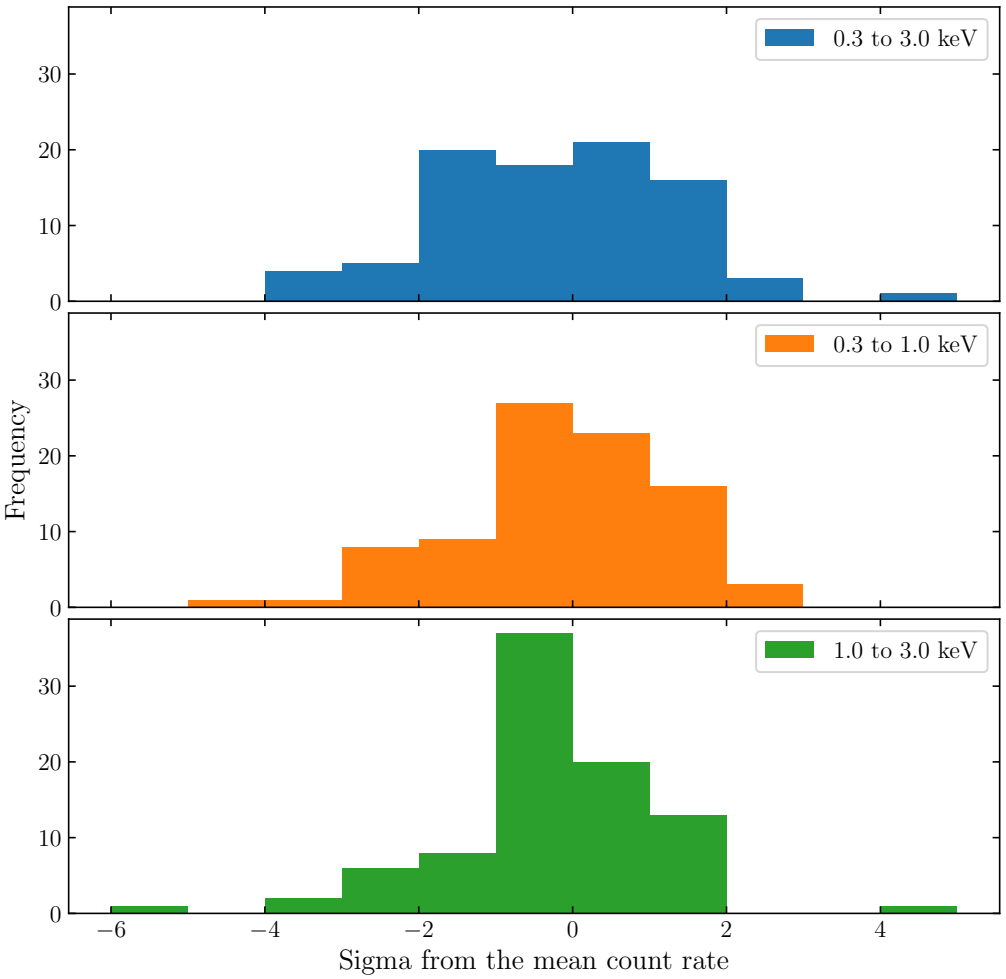


Figure 7.7: Histograms outlining the $\sigma$-significance (as defined in the main text) of each snapshot in the three energy ranges: 0.3–3.0 keV (top), 0.3–1.0 keV (middle), and 1.0–3.0 keV (bottom).

from the mean count rate does each snapshot lie. As can be seen in Fig. 7.7, F1 is the only snapshot that is greater than $3\sigma$ above the mean count rate in any energy range investigated, doing so for both the harder energy range and the full 0.3 to 3.0 keV range. Thus F1 is the only snapshot that can be unambiguously regarded as a flare. The other snapshots tested here have count rates that are not high enough and/or well enough constrained to be regarded equivalently.

I conclude that S3 and S5 are the best candidates flare snapshots among those tested, showing similar hardening to F1. Had the exposure times for these snapshots been longer, their count rates and $HR$ may have been constrained well enough to declare them as flares with confidence. It may also be that these snapshots

represent an observation of the star on its way back down to quiescence, with the peak of the flare occurring during the gap between the previous snapshot and the candidate.

### 7.3.3 Flare Position Analysis

The M-star binary companion HD 189733B has previously been assumed relatively quiet in X-rays, with Poppenhaeger et al. (2013) providing the only fully resolved detection at these wavelengths. However, given the discovery of flares from the stellar companion in the *XMM-Newton* data (see Sections 6.3 and 7.4.2), I performed a positional analysis on the known *Swift* flare, labelled F1 above. XRTCENTROID, part of the HEASOFT software package, was employed to fit each individual snapshot of epoch 8 (see Table 7.1). The calculated centroid was then compared to the position of each of the three X-ray sources in the region. An average of the positions of these three sources was used as the initial position guess in XRTCENTROID, along with a box half-width of 1 arcmin. Figs. 7.8 and 7.9 show the results of this analysis, for the full and hard energy ranges, respectively. I omitted the soft band for this analysis as the flare snapshot is not significantly higher in that energy band (Fig. 7.7). A slight shift in the centroid can be seen towards the primary in the flare snapshot, and away from both the companion and the background X-ray source. This is perhaps clearer in the harder energies, and suggests the flare indeed emanated from the planet host.

## 7.4 *XMM-Newton* Results

The primary foci of the *XMM-Newton* analyses were to examine the flares and possible activity cycle signatures in the data for the planet host star. However, as part of assessing the contamination in Chapter 6, I discovered three flares unambiguously originating from the stellar companion HD 189733B instead. I described the method used to split the three sources into their constituent parts in Section 6.3.

### 7.4.1 Planet host star flares

Three flares emanating from the planet host star in observations 2, 3, and 4 (see Table 7.2) of the *XMM-Newton* data were previously identified by Pillitteri et al. (2010, 2011, 2014). Their timing, all peaking between $\phi = 0.52$ and $\phi = 0.65$, were interpreted as evidence for phasing of the stellar activity with the orbital period of the planet. I used my contamination assessment method to confirm that the three flares identified by the Pillitteri papers indeed originated from the planet host

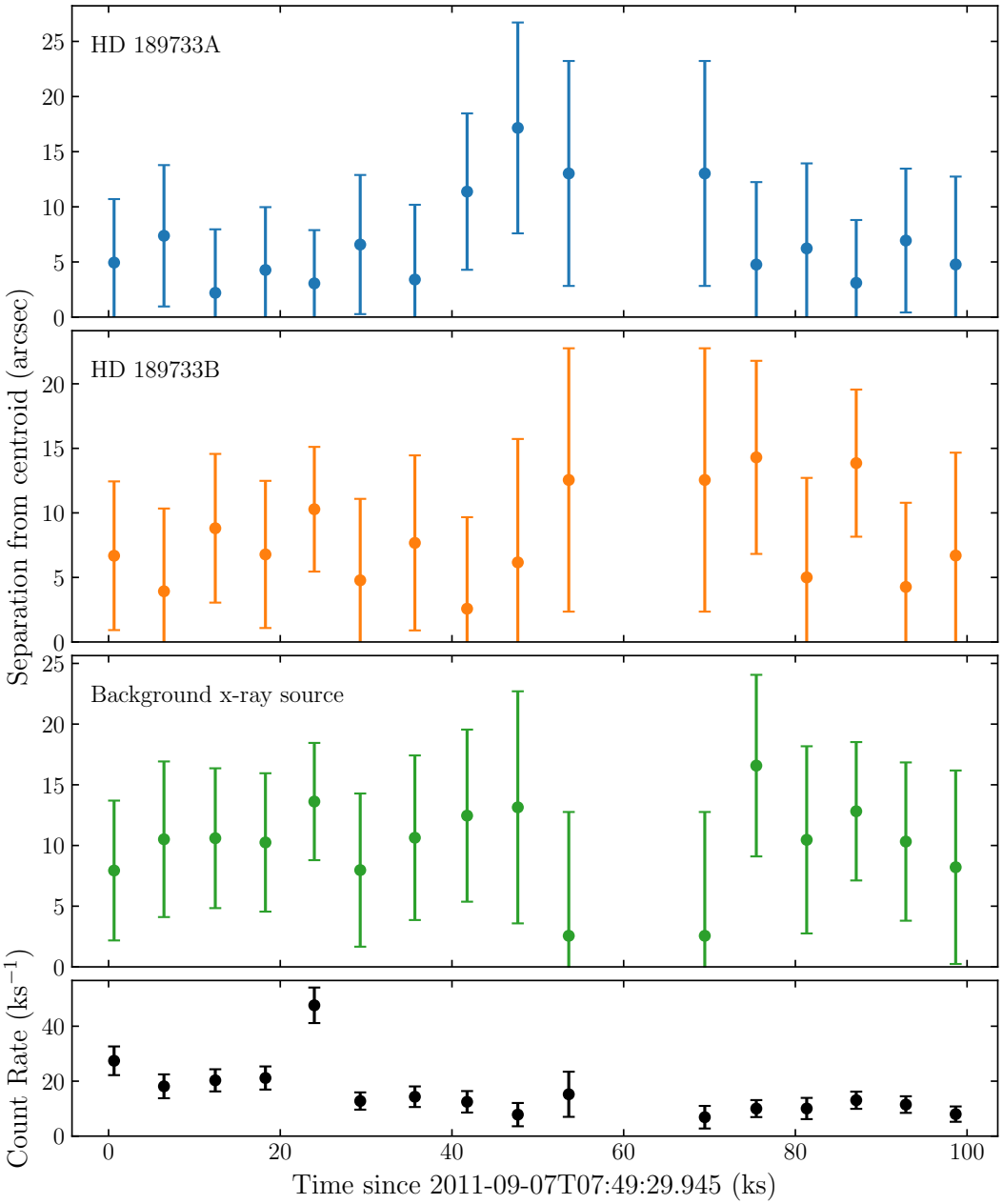


Figure 7.8: Distance of each of the three objects from the position calculated by XRTCENTROID for each snapshot in the energy range 0.3–3.0 keV. Top panel: centroid distance from HD 189733 A. Upper-middle panel: centroid distance from HD 189733 B. Lower-middle panel: centroid distance from the background X-ray source. Bottom panel: count rate for each snapshot in the energy range 0.3–3.0 keV. The flare F1 is the fifth snapshot from the left.

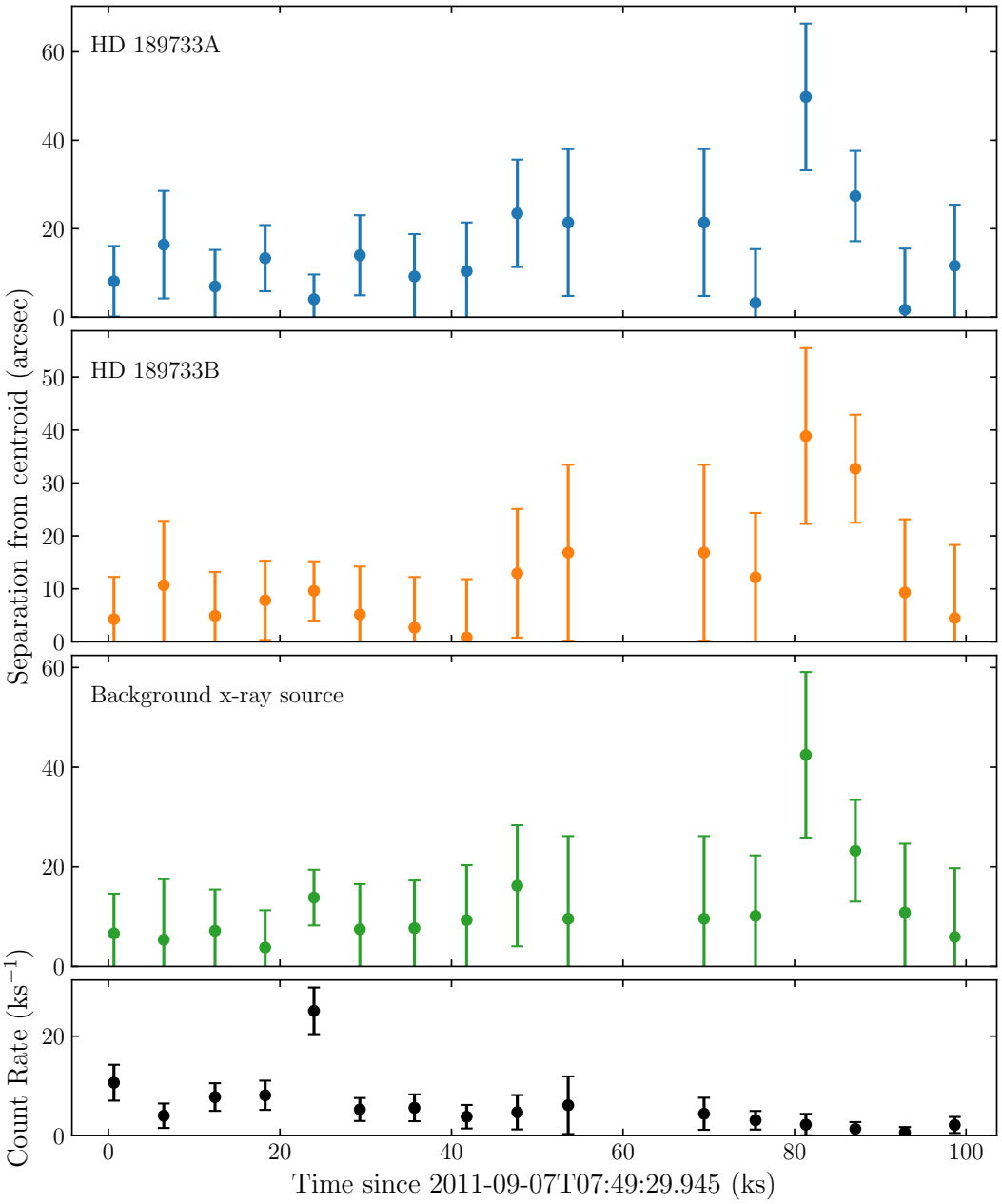


Figure 7.9: As Fig. 7.8 but for the hard band, 1.0–3.0 keV.

star, as previously assumed, with Fig. 7.10 showing the light curves for both stars A and B in each observation. In this figure, as well as Figs. 7.11 and 7.12, the count rate for star B seems to be consistently below zero in some of the observations after the contamination method is applied. This could result from inaccuracies in the astrometry of the *XMM-Newton* data, which is typically on the order of a few arcseconds (Watson et al., 2009). However, the errors this introduces are not so important here, since my primary goal in these figures is to identify flaring periods and not to accurately assess the quiescent flux levels.

Searching through the new observations analysed here, I find a new flare from the planet host within observation 12 on 17 May 2014. The light curves of both stars during this observation are shown in Fig. 7.11. The light curves are plotted for 0.166–1.2 keV; the cutoff at 1.2 keV is where the third, background X-ray source becomes important (see Section 6.3). This newly identified flare was particularly strong, with the flux peaking at around three times the flux either side of the flare. Examination of the three previously observed flares in Fig. 7.10 shows that all three peaked at or less than twice the surrounding quiescent flux level within their respective observations.

The data assessed here also includes two new non-primary transit observations taken with *XMM-Newton* in April 2015. These probe similar phases to those of the flares identified in the Pillitteri papers. Despite some low-amplitude variability, there are no clear flares in either observation.

### 7.4.2 Stellar companion flares

When I assessed the contamination of the planet host star by the stellar companion and background third source in Section 6.3, I indeed found the companion to be quiet in X-rays at almost all times. However, I also identified three X-ray flares that clearly emanated from the companion as opposed to the planet host. These were observed on 3 Nov 2013, 11 Nov 2014, and 15 Nov 2014. Their light curves are displayed in Fig. 7.12. The first was the strongest of the three, reaching a peak count rate greater than the 17 May 2014 primary star flare. This flare is therefore the strongest flare detected in the system, for either star, by *XMM-Newton*.

I re-assess the evidence for the X-ray-derived age for the companion being older, and therefore indicative of SPI between HD 189733b and its host star, in Section 7.5.2.

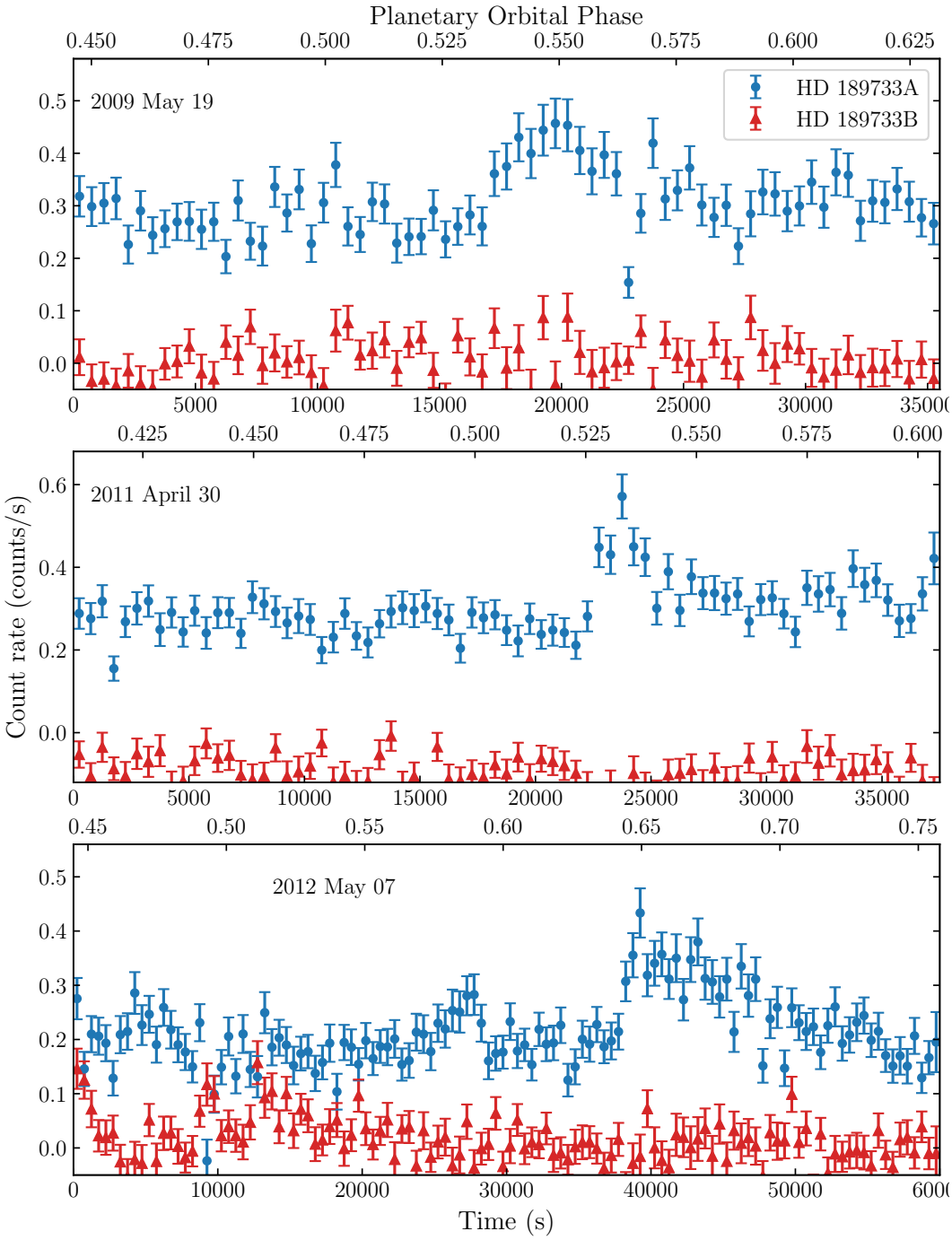


Figure 7.10: 0.166–1.2 keV light curve for the three observations with flares identified by Pillitteri et al. (2010, 2011, 2014), for HD 189733A (blue circles) and HD 189733B (red triangles).

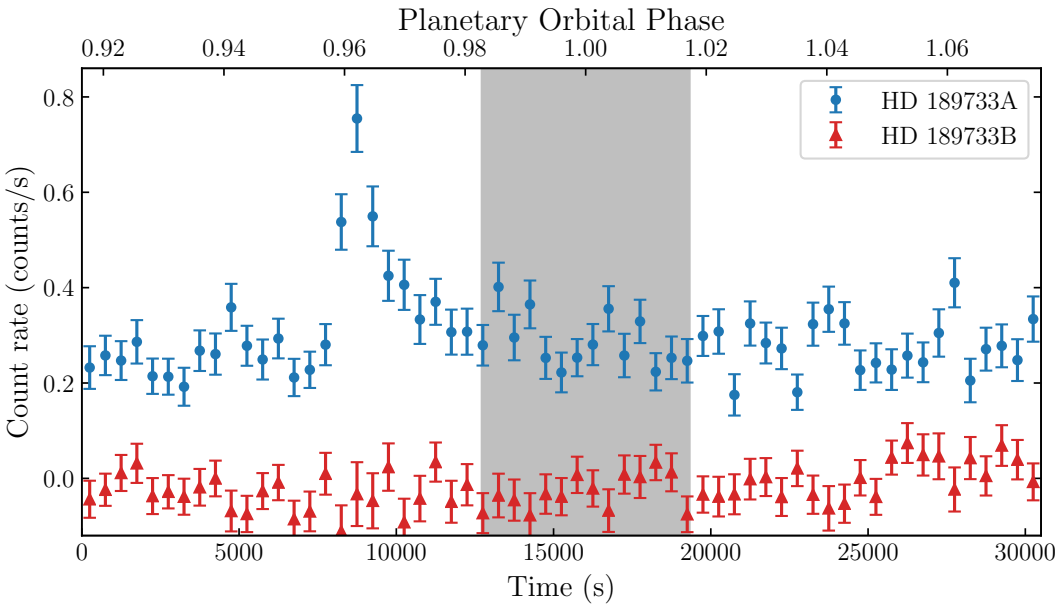


Figure 7.11: As Fig. 7.10, but for the newly identified flare on 17 May 2014. The grey shaded region depicts the primary transit of HD 189733b.

### 7.4.3 X-ray Spectra

I analysed the X-ray spectra for all 25 observations simultaneously, using XSPEC. I restricted the data to be below 1.2 keV to avoid significant contamination from the background source, and removed all flares from both the planet host star and HD 189733B. The latter means that I also avoid any significant contamination from the stellar companion.

As in Chapters 3, 4, and 5, I fitted optically-thin plasma models (Smith et al., 2001), but with a few key differences to the method. Firstly, I require a third temperature component. All three temperatures were linked across all 25 observations, but their associated normalisations were allowed to vary between observations. Second, in order to obtain a good fit to all spectra simultaneously, I used an APEC model variant in XSPEC called 'VAPEC'. This allowed me to free up the abundances associated with individual species separately. I freed up C, N, O, Ne, and Fe; these are all elements relevant for the FIP effect (see Section 1.3.2), with the first four all being high FIP elements. All other species were kept fixed at Solar values (Asplund et al., 2009). The freeing up of certain abundances like this yields a far superior spectral fit to either fixing all species at solar, or allowing the abundance of all species to vary together by the same amount. I give the temperatures and abundances obtained by the spectral fit along with their 1-$\sigma$ uncertainties in Table 7.4, while the fluxes are

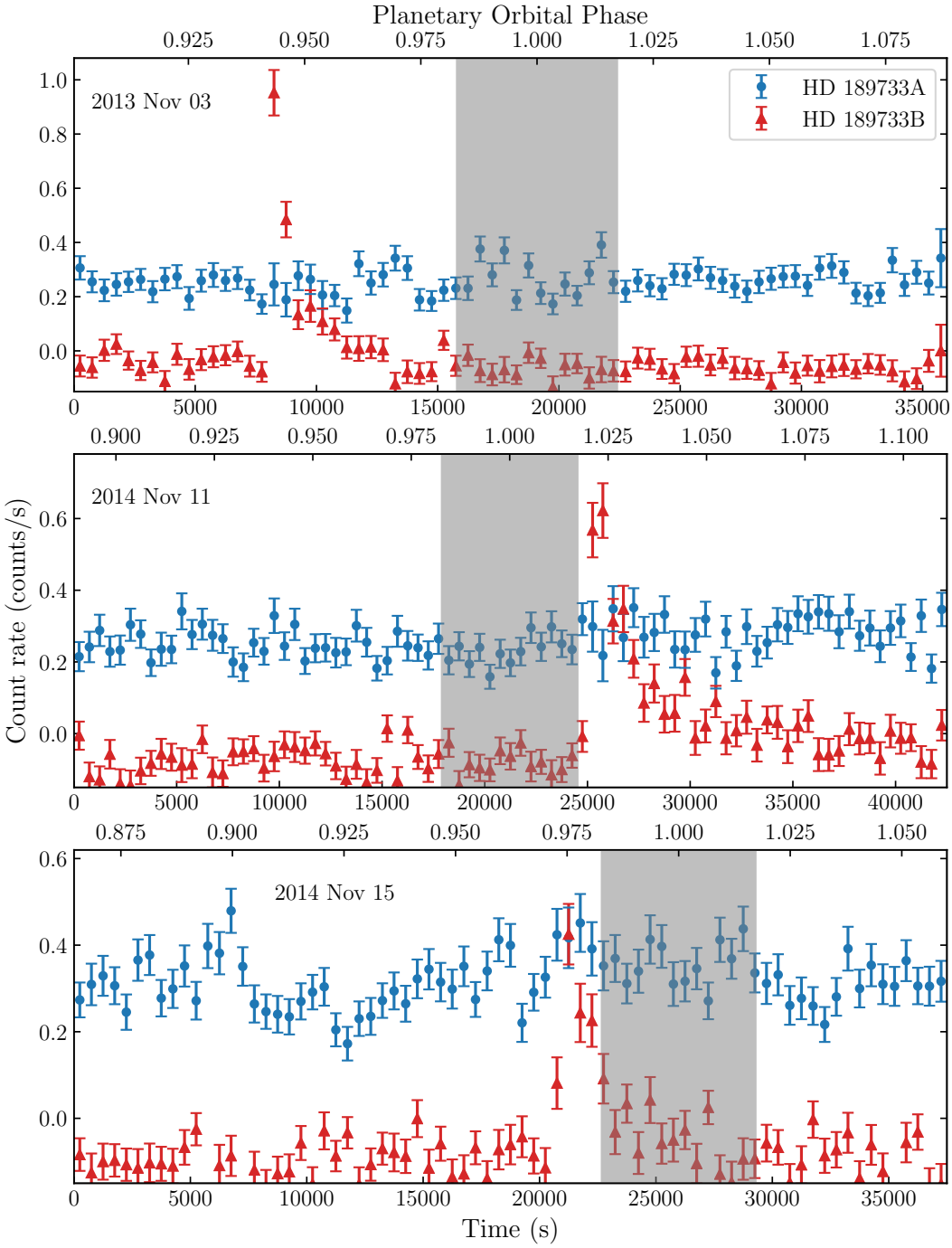


Figure 7.12: As Figs. 7.10 and 7.11, for the three observations from 3 Nov 2013 (top), 11 Nov 2014 (middle), and 15 Nov 2014 (bottom). Each light curve shows a flare from the stellar companion HD 189733B.

Table 7.4: Best fit parameters for the simultaneous fit to spectra from all 25 observations. The temperatures were forced to be the same across the observations. The abundance values are with respect to the Solar photosphere values of Asplund et al. (2009).

| Parameter | Symbol | Value | Unit |
|---|---|---|---|
| Temperature 1 | $kT_1$ | $0.1160^{+0.0039}_{-0.0027}$ | keV |
| Temperature 2 | $kT_2$ | $0.411^{+0.013}_{-0.011}$ | keV |
| Temperature 3 | $kT_3$ | $0.781^{+0.013}_{-0.025}$ | keV |
| Carbon abund. | C | $2.11^{+0.16}_{-0.17}$ | Solar |
| Nitrogen abund. | N | $4.60^{+0.18}_{-0.35}$ | Solar |
| Oxygen abund. | O | $2.16^{+0.09}_{-0.17}$ | Solar |
| Neon abund. | Ne | $0.95^{+0.20}_{-0.17}$ | Solar |
| Iron abund. | Fe | $0.730^{+0.030}_{-0.082}$ | Solar |
| FIP bias | $F_{\rm bias}$ | $0.527^{+0.033}_{-0.023}$ | |

displayed in Table 7.5. In Fig. 7.13, I show a corner plot of the samples drawn for the temperatures and freed-up coronal abundances in a 400,000-step MCMC.

To investigate the FIP effect (see Section 1.3.2) in HD 189733, I applied equation 1.12, for each of the four high FIP species. Given HD 189733's measured metallicity, [Fe/H] $= -0.03 \pm 0.04$ (Bouchy et al., 2005), I set the photospheric abundances to Solar values (Asplund et al., 2009). I calculate a value for $F_{\rm bias}$ of $0.527^{+0.033}_{-0.023}$, indicative of a strong inverse FIP effect, usually found for young, very active stars (Wood et al., 2012; Laming, 2015). The inverse FIP effect was first seen by Brinkman et al. (2001) for HR 1099, and their fig. 4 shows a clear, tight trend of abundance increasing with FIP. Here, my plot of abundance vs. FIP (Fig. 7.14) shows an increase from Fe up to N, but Ne is completely inconsistent with an increase with FIP. Evidence of coronal abundance enhancements or depletions not simply just being linked with the FIP date back over two decades though (e.g. Schmelz et al., 1996), and it is important too to remember that I have not measured these abundances using higher resolution spectra that resolve individual lines, which would likely be more accurate. Interestingly, my findings are also in stark disagreement with an assessment of the FIP effect for HD 189733 by Poppenhaeger et al. (2013). They found $F_{\rm bias} = -0.41$, although they only assessed the abundances of neon and oxygen. My value of iron is consistent with theirs at a 1-$\sigma$ level, but my neon and oxygen abundances are not at all compatible with theirs. There are more spectra here, and the *XMM-Newton* EPIC-pn spectra are of better quality than the *Chandra* ACIS-S spectra analysed by Poppenhaeger et al. (2013), as they have many more counts present: the count rates in my observations using the 15 arcsec extraction are typically $0.3\,{\rm s}^{-1}$, a factor of six larger than in the *Chandra* observations (see

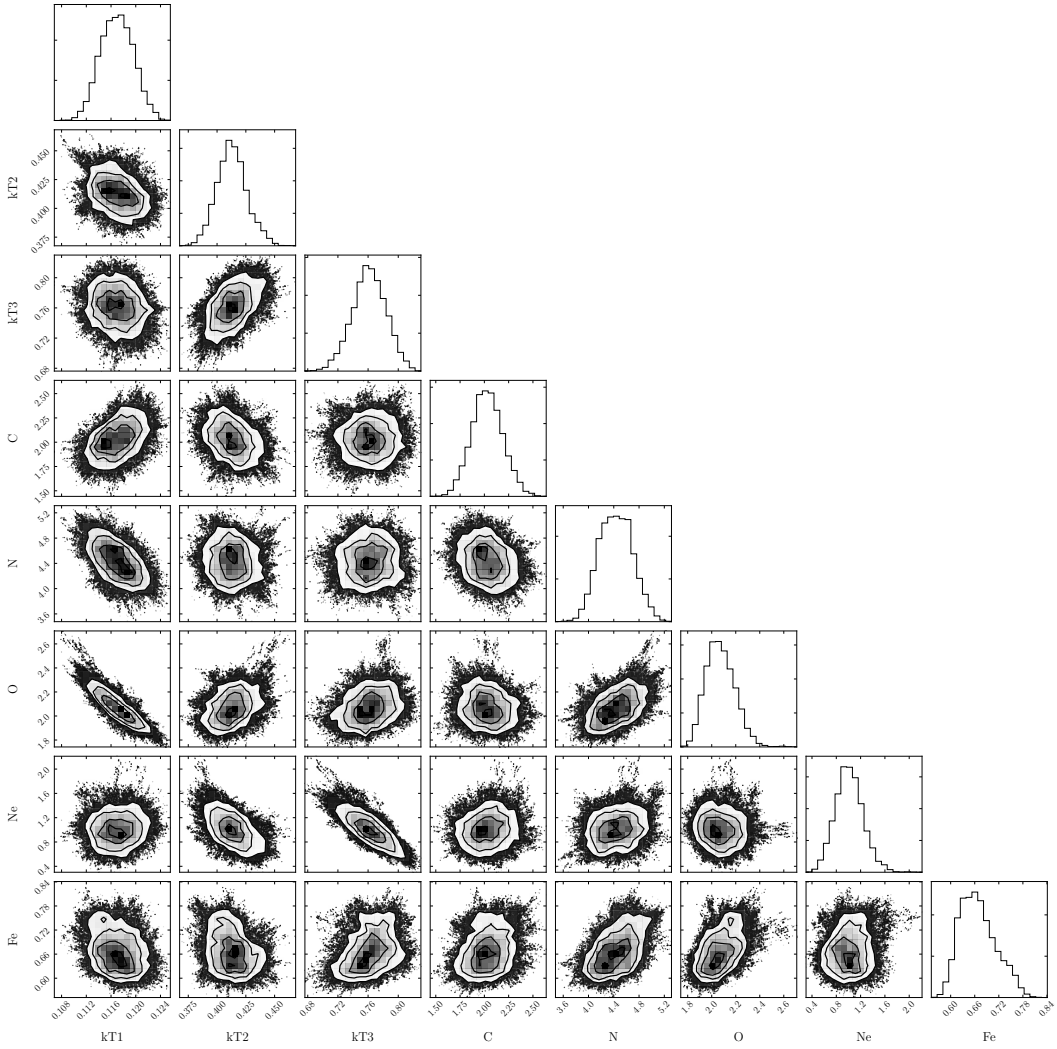


Figure 7.13: Corner plot displaying the 2-D contour plots and 1-D histograms of the samples drawn for the temperatures and coronal abundances by an MCMC exploration of the parameter space around the spectral fit.

Table 7.5: Quiescent unabsorbed fluxes at Earth obtained for each observation in the 0.2–2.4 keV band. For the dates corresponding to each observation number, see Table 7.2.

| Obs No. | Emission Measures | | | Unabsorbed $F_{\mathrm{X},\oplus}$ |
|---|---|---|---|---|
| | Temp. 1 | Temp. 2 | Temp. 3 | |
| | | ($\times 10^{50}\,\mathrm{cm}^{-3}$) | | ($\times 10^{-13}\,\mathrm{erg\,s^{-1}\,cm^{-2}}$) |
| 1 | $2.482^{+0.286}_{-0.172}$ | $2.886^{+0.198}_{-0.352}$ | $2.260^{+0.526}_{-0.134}$ | $3.615^{+0.043}_{-0.042}$ |
| 2 | $3.221^{+0.248}_{-0.325}$ | $2.810^{+0.266}_{-0.351}$ | $3.975^{+0.564}_{-0.219}$ | $4.708^{+0.051}_{-0.108}$ |
| 3 | $2.807^{+0.311}_{-0.322}$ | $3.435^{+0.331}_{-0.351}$ | $3.507^{+0.535}_{-0.285}$ | $4.640^{+0.049}_{-0.103}$ |
| 4 | $2.199^{+0.143}_{-0.101}$ | $1.963^{+0.133}_{-0.247}$ | $2.083^{+0.375}_{-0.835}$ | $2.931^{+0.032}_{-0.038}$ |
| 5 | $2.920^{+0.211}_{-0.278}$ | $2.990^{+0.291}_{-0.267}$ | $2.690^{+0.359}_{-0.164}$ | $4.057^{+0.039}_{-0.084}$ |
| 6 | $2.654^{+0.236}_{-0.299}$ | $3.185^{+0.344}_{-0.334}$ | $2.601^{+0.425}_{-0.218}$ | $4.001^{+0.053}_{-0.079}$ |
| 7 | $3.018^{+0.186}_{-0.269}$ | $3.032^{+0.368}_{-0.254}$ | $3.012^{+0.504}_{-0.218}$ | $4.274^{+0.055}_{-0.052}$ |
| 8 | $3.016^{+0.260}_{-0.315}$ | $2.550^{+0.328}_{-0.254}$ | $3.218^{+0.435}_{-0.210}$ | $4.122^{+0.065}_{-0.046}$ |
| 9 | $2.918^{+0.301}_{-0.215}$ | $3.552^{+0.245}_{-0.336}$ | $2.595^{+0.558}_{-0.149}$ | $4.303^{+0.089}_{-0.070}$ |
| 10 | $2.763^{+0.261}_{-0.255}$ | $3.223^{+0.363}_{-0.217}$ | $3.090^{+0.378}_{-0.247}$ | $4.310^{+0.056}_{-0.061}$ |
| 11 | $3.146^{+0.215}_{-0.237}$ | $2.726^{+0.382}_{-0.419}$ | $4.780^{+0.691}_{-0.284}$ | $5.024^{+0.086}_{-0.063}$ |
| 12 | $3.140^{+0.319}_{-0.275}$ | $2.864^{+0.442}_{-0.512}$ | $3.661^{+0.611}_{-0.157}$ | $4.551^{+0.094}_{-0.071}$ |
| 13 | $3.170^{+0.286}_{-0.335}$ | $2.443^{+0.201}_{-0.297}$ | $4.071^{+0.530}_{-0.211}$ | $4.542^{+0.103}_{-0.096}$ |
| 14 | $3.000^{+0.106}_{-0.318}$ | $2.935^{+0.435}_{-0.183}$ | $3.602^{+0.429}_{-0.408}$ | $4.503^{+0.024}_{-0.093}$ |
| 15 | $3.109^{+0.361}_{-0.273}$ | $4.253^{+0.271}_{-0.375}$ | $3.695^{+0.656}_{-0.159}$ | $5.283^{+0.106}_{-0.077}$ |
| 16 | $2.997^{+0.156}_{-0.378}$ | $2.806^{+0.377}_{-0.196}$ | $3.607^{+0.156}_{-0.378}$ | $4.437^{+0.054}_{-0.074}$ |
| 17 | $2.578^{+0.257}_{-0.263}$ | $2.661^{+0.280}_{-0.509}$ | $2.895^{+0.587}_{-0.120}$ | $3.845^{+0.048}_{-0.058}$ |
| 18 | $2.822^{+0.267}_{-0.312}$ | $2.817^{+0.357}_{-0.331}$ | $3.275^{+0.432}_{-0.170}$ | $4.210^{+0.066}_{-0.085}$ |
| 19 | $2.865^{+0.253}_{-0.401}$ | $3.824^{+0.394}_{-0.326}$ | $7.588^{+0.573}_{-0.172}$ | $4.972^{+0.064}_{-0.087}$ |
| 20 | $2.914^{+0.117}_{-0.309}$ | $3.726^{+0.568}_{-0.967}$ | $3.725^{+0.353}_{-0.241}$ | $4.942^{+0.056}_{-0.029}$ |
| 21 | $3.295^{+0.242}_{-0.390}$ | $4.107^{+0.393}_{-0.328}$ | $5.288^{+0.739}_{-0.251}$ | $6.011^{+0.093}_{-0.057}$ |
| 22 | $2.826^{+0.163}_{-0.308}$ | $4.080^{+0.506}_{-0.258}$ | $3.068^{+0.470}_{-0.301}$ | $4.773^{+0.042}_{-0.067}$ |
| 23 | $3.083^{+0.253}_{-0.255}$ | $3.194^{+0.367}_{-0.437}$ | $4.503^{+0.693}_{-0.233}$ | $5.110^{+0.067}_{-0.078}$ |
| 24 | $3.255^{+0.211}_{-0.365}$ | $3.545^{+0.412}_{-0.133}$ | $4.200^{+0.457}_{-0.295}$ | $5.216^{+0.068}_{-0.093}$ |
| 25 | $3.861^{+0.151}_{-0.322}$ | $2.959^{+0.484}_{-0.260}$ | $5.222^{+0.638}_{-0.451}$ | $5.652^{+0.053}_{-0.076}$ |

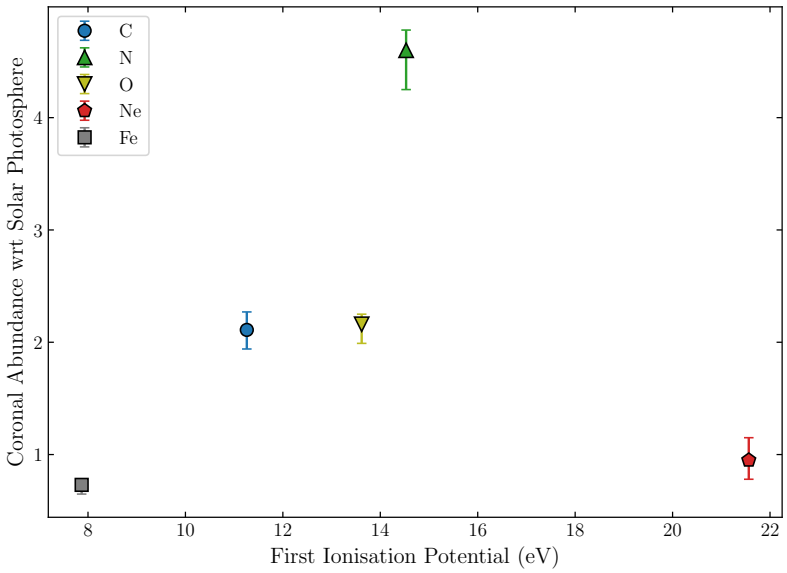


Figure 7.14: Corner plot displaying the 2-D contour plots and 1-D histograms of the samples drawn for the temperatures and coronal abundances by an MCMC exploration of the parameter space around the spectral fit.

their fig. 4). Fixing the abundances at their values and refitting the *XMM-Newton* spectra yields a very poor fit, with $\chi^2 = 5709$ and a p-value of 0. For comparison, my best fit has $\chi^2 = 635$ and a p-value of 0.07. Altogether, this gives me confidence in my fitted abundances over theirs.

### Long-term activity variations

I plot the measured fluxes obtained above as a function of time in Figs. 7.15 and 7.16. The latter is a zoomed in version of the former, focussing on the best populated time range, that between May 2013 and April 2015. Examining the fluxes in this way permits an investigation of long-term variations that may be present in the *XMM-Newton* data, similar to that carried out in Section 7.3, for the *Swift* data.

I also tried to split the observations into nine distinct, 'epoch' groups based on date: April 2007 (1 observation), May 2009 (1), April 2011 (1), May 2012 (1), May 2013 (1), November 2013 (2), Spring 2014 (5), Autumn 2014 (8), April 2015 (3). I then averaged the flux across all of the observations within each epoch. Where an epoch contained more than one observation, the individual fluxes for each observation were weighted by their corresponding exposure times. The resulting plot of fluxes for each epoch is shown in Fig 7.17.

Examining these figures shows that there is evidence of substantial variability

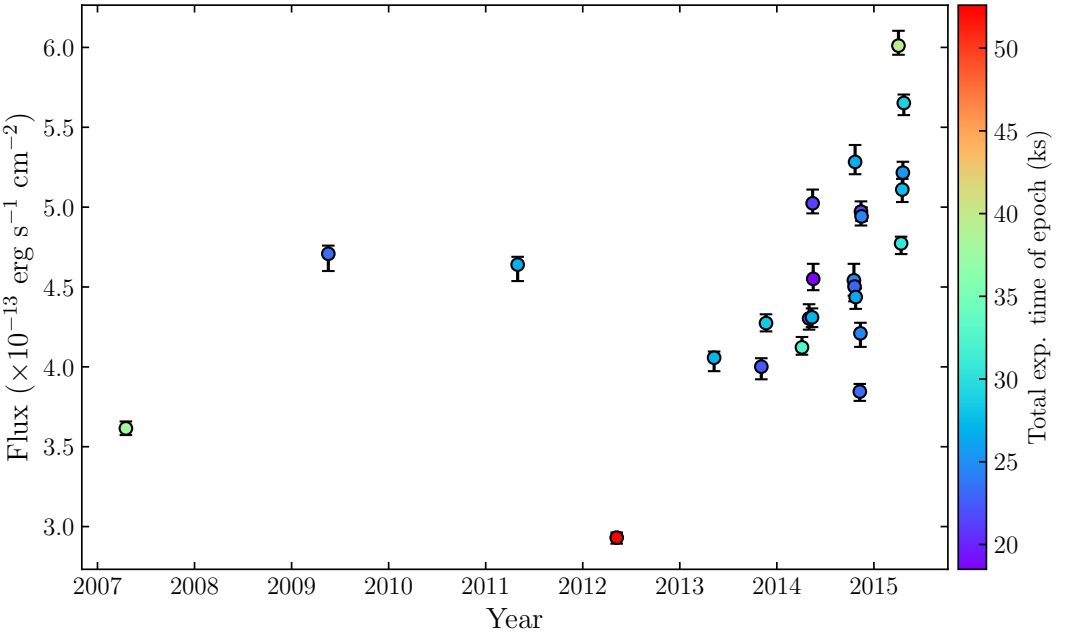


Figure 7.15: Unabsorbed fluxes measured from each *XMM-Newton* observation. The points are coloured according to their total live exposure time.

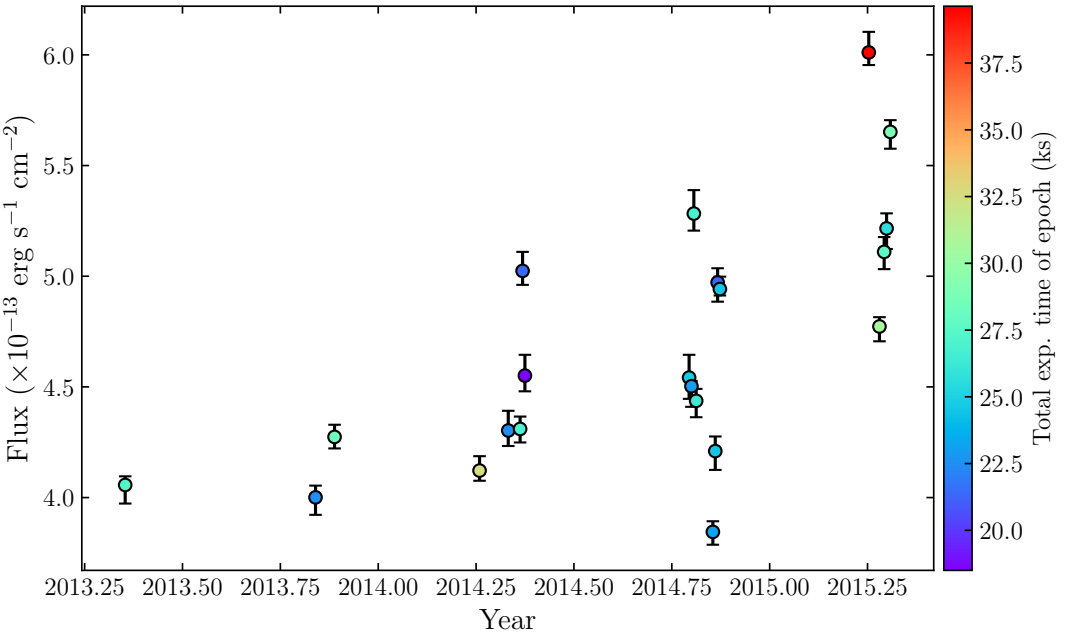


Figure 7.16: As Fig. 7.15, but zoomed into the time period May 2013 to April 2015.

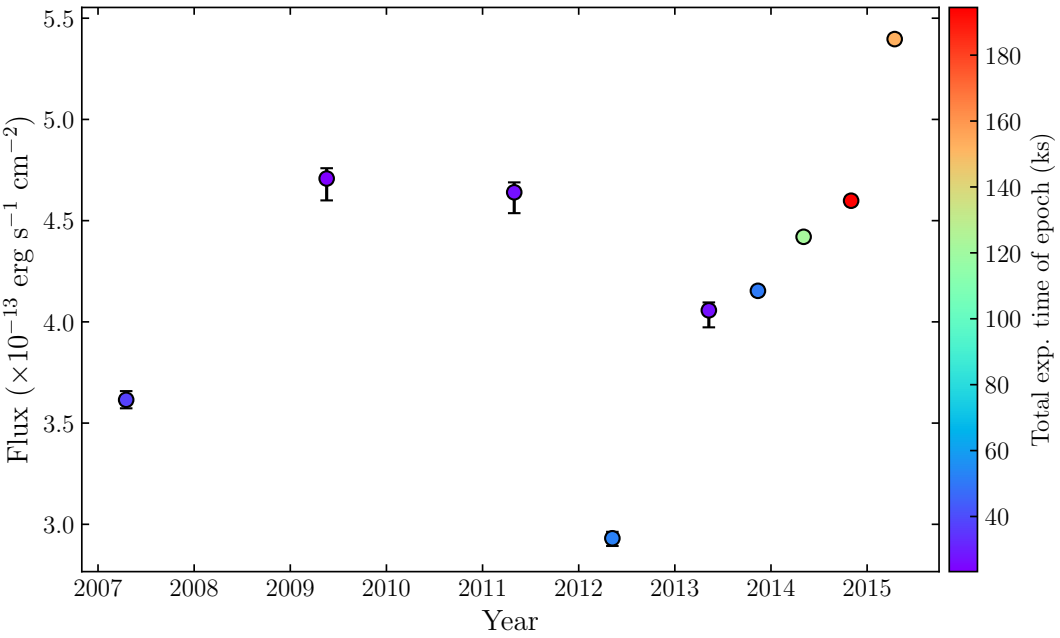


Figure 7.17: Fluxes for each defined epoch (see main text) in the XMM-Newton data. Errors on those epochs with more than a single observation are too small to be visible.

in the quiescent X-ray emission of the star. Fig. 7.5 hinted at this in the *Swift* data, but here the superior precision of *XMM-Newton* and longer exposure times make a big difference. The first four observations show significant variation between them, although the 2009 and 2011 observations are compatible within their uncertainties. The 2012 flux is particularly low, an interesting fact given the observation also contained a (removed) flare from the planet host. One would perhaps expect the presence of active regions associated with the origin of the flare to still shine bright at the out of flare times. Looking at the period where the sampling is greatest - the time period covered by the zoomed in plot in Fig. 7.16 - is particularly interesting as there is evidence for a more structured long term variation. The maximum flux appears to increase substantially across the time period, as does the spread of fluxes within each defined epoch. When these observations are binned into one point per epoch in Fig. 7.17, the average flux at each epoch is also seen to increase over this period. However, given the above this is being driven by the increase in the maximum flux rather than an increased flux at all times. I assess the implications of these long term variation findings further in Section 7.5.1, below.

## 7.5 Discussion

### 7.5.1 Activity of the planet host star

#### Phasing with the orbital period

Pillitteri et al. (2010, 2011, 2014) point to three flares observed up to 8 hr after the secondary eclipse at three different epochs as evidence of phasing of the coronal emission with the planet's orbit. As is evidenced in the significances listed in table 3 of one of their own papers (Pillitteri et al., 2014), their claim is not at all statistically significant. Despite this, with the extra data analysed here it was worth checking if the data showed any evidence of such a phasing. Putting those three Pillitteri flares together with the new *XMM-Newton* flare from the planet host (Section 7.4.1 & Fig. 7.11), and the known *Swift* flare, I assessed whether the distribution of flares and exposure time in orbital phase are significantly different. I performed a two-sample Kolmogorov-Smirnov (KS) test of the two, yielding a KS statistic of 0.439 and a p-value of 0.215. This means that the null hypothesis of the two being drawn from the same distribution cannot be rejected, and so there is no statistically significant phasing of the observed flares with orbital period. Additionally, this conclusion persists when including the two best candidate *Swift* flares from Section 7.3.2 (p-value = 0.361), and when testing only the *XMM-Newton* data (p-value = 0.332).

The nine year baseline *Swift* data were also searched for evidence of any phasing of the quiescent X-ray flux with orbital period in Section 7.3.1. With the known flare removed, the $\chi^2$ tests performed also showed no significant phasing of the quiescent X-ray flux with orbital period. I did not analyse the *XMM-Newton* data in this way due to the heavily uneven phase coverage of these data, which are clustered around the primary transit and secondary eclipse.

This lack of evidence for the phasing of HD 189733A's X-ray emission with orbital period, either in quiescent flux or the timing of flares, agrees with the findings of a multi-wavelength assessment of HD 189733 by Route (2019). That study attributed the previous claims of activity phased with the orbital period to "inadequately-sampled intrinsic stellar activity from an active star, rather than star-planet interactions."

#### Phasing with the stellar rotation

The periodogram analysis in Fig. 7.4 reveals no significant peak around the corresponding frequencies. However, the *Swift* data are sampled very unevenly and very sparsely, with the epochs of observations noticeably spread out across the nine year

baseline. This possibly affects the ability to see periodic features on the timescale of interest (12–16 d), should any actually exist. Active regions typically come and go on timescales of less than a few stellar rotations. Since these will not always spring up in the same place, modulation of brightness due to them is in that sense only quasi-periodic over the full nine year baseline of the observations.

**Signatures of long term activity cycle**

In examining the observation-to-observation variations in count rates and fluxes in *Swift* and *XMM-Newton*, I uncovered evidence of long baseline variation in the X-ray emission of HD 189733A.

The count rates measured from the *Swift* observations are not of high enough precision to pick out specific structure in any long term variations. The data are good enough to rule out a constant count rate across the nine year baseline with 98% confidence, but not good enough to say much more given the significant, but somewhat erratic scatter. Long term variation in the *XMM-Newton* data appears more structured, particularly in the highly sampled two year period between May 2013 and April 2015.

In Fig. 1.14, I plotted the daily averaged X-ray fluxes for the Sun at Earth in the 0.2–2.4 keV band, spanning a little over one 11 year cycle. Significant higher order variation is seen in addition to the main activity cycle, and is of higher amplitude towards Solar maximum. This is similar to that apparent in Fig. 7.16 for HD 189733, where the average and maximum flux increases over the two year period, but so does the spread of fluxes. Similar increases in higher order variation towards the maximum of the Solar activity cycle have also been observed in sunspot number (e.g. Fig. 1.13), and at various wavelengths including radio (F10.7 index: e.g. Svalgaard and Hudson, 2010), NUV (S-index: e.g. Egeland et al., 2017; Meunier, 2018), MUV (Mg II index: e.g. Woods et al., 2018) and EUV (e.g. Solomon et al., 2010). This indeed suggests our flux changes could be indicative of a coronal activity cycle.

Unfortunately, while they hint at even higher amplitudes to the variation, the first four observations between 2007 and 2012 are too sparsely sampled to be able to infer much more about the underlying properties of the variation. The difference between the lowest (2012) and highest (03 April 2015) is a factor of two, much lower than the factor of 5 or 6 difference between Solar minimum and maximum in the slightly broader ROSAT energy band (Judge et al., 2003, and Fig.1.14). However, the coronal activity cycle measured by *XMM-Newton* for 61 Cyg A, a moderately K5V much closer in spectral type to HD 189733, only varies by a factor or two or three (Hempelmann et al., 2006; Robrade et al., 2012). This means that

a similar difference between the maximum and minimum flux found for HD 189733 in our observations is a plausible amplitude of the cycle, but I cannot be sure if the variation extends beyond that observed given the large fraction of the eight year baseline that is not sampled.

Taken altogether, the data suggest that I am probing the long term, magnetic activity cycle of HD 189733. While the increase across the well sampled two year period suggests the activity cycle is likely as least twice as long as this, further observations are required to uncover the values of key properties of the cycle, such as its period and amplitude.

#### X-ray-age of HD 189733A

Using the relations of Jackson et al. (2012), I estimated HD 189733A's X-ray-age using the measured *XMM-Newton* fluxes (Table 7.5). As in previous chapters, I double the flux in order to estimate the 0.1–2.4 keV band flux from the observed 0.2–2.4 keV band. Applying the relations to the highest and lowest fluxes yield age estimates of $0.41^{+0.33}_{-0.37}$ Gyr and $0.68^{+0.55}_{-0.63}$ Gyr, respectively. This places the likely X-ray-age of HD 189733A at a few hundred Myr, perhaps up to about a Gyr - the lower end of the Poppenhaeger and Wolk (2014) range. The strong inverse FIP effect observed in Section 7.4.3 is also indicative of a young, active star.

### 7.5.2 Activity of the M star companion

The measured quiescent flux of the stellar companion is almost two orders of magnitude lower than the primary ($\log L_{\rm X} = 26.67$; Poppenhaeger et al., 2013). Poppenhaeger and Wolk (2014) claimed the X-ray-age derived from this value disagrees with that derived from the primary, and that this is evidence of a tidal interaction between the primary star and the planet that has maintained the spin rate at a higher level than expected for its age.

The estimation of X-ray-ages of the two components was made by comparing the X-ray luminosity of each star to the observed ranges for stars of similar spectral type at different ages. For HD 189733A, this involved comparing to the ranges in $L_{\rm X}$ encompassed by both young K stars in the Hyades (Stelzer and Neuhäuser, 2001), and field K stars (Schmitt and Liefke, 2004). The star's $L_{\rm X}$ is a little below the range of the former and towards the higher end of the latter, and on that basis approximated an X-ray-age of 1–2 Gyr. For the companion HD 189733B, they compared $L_{\rm X}$ to the rather large ranges (in both $L_{\rm X}$ and age) encompassed by field M stars (Schmitt and Liefke, 2004), and old disc/halo M dwarfs (Micela et al., 1997),

approximating the age to be 5–10 Gyr. This analysis by Poppenhaeger and Wolk (2014) is rather crude and the ages obtained are, at best, approximations. It is particularly curious that the study makes no comparison of HD 189733B to younger stars as they do for HD 189733A, given they are trying to rule out its X-ray-age being younger.

I detected three flares in the 25 *XMM-Newton* observations, with two of these spaced just four days apart. Additionally, in detecting star B with *Chandra*, Poppenhaeger et al. (2013) also identified a possible flare in one of their six light curves, as well as other possible flare-like variation in some of their other light curves. However, the count rate was too low to characterise the events further. Altogether, this means that across a total observation time of 804 ks (9.3 d) with *XMM-Newton* and *Chandra*, there are a minimum of four flares for HD 189733B, corresponding to a rate of $0.43\,\mathrm{d}^{-1}$. Four flares is also the same number observed for the planet host across these data, and this casts doubt on the conclusion that one star is active and the other inactive. The largest flare detected across the *XMM-Newton* data was also one of the companion flares. Rates of X-ray flares for a relatively large sample of stars were measured by Pye et al. (2015), making use of the 2XMM serendipitous source catalogue. My flare rate is several orders of magnitude larger than their full sample of 504 stars, and an order of magnitude larger than those stars observed to flare at least once. However, that survey encompasses a wide range of stellar types from F to mid-M, across which the flare properties of stars may change significantly. The authors did not attempt to split the stars up by spectral type given the smaller number of stars in their flaring sample. A comparison of HD 189733B's flaring rate to a substantial sample of similar-type stars would be desirable, but such a sample has not yet been explored.

Unfortunately, the Jackson et al. (2012) relations I used for HD 189733A are not applicable to stars later than mid-to-late K-type; HD 189733B was determined to be of spectral type M3.5–M5 by Bakos et al. (2006). Some recent studies have explored the X-ray-rotation relationship for fully convective M dwarfs (Stelzer et al., 2016; Wright and Drake, 2016; Wright et al., 2018; González-Álvarez et al., 2019). I applied the Wright et al. (2018) relations to estimate a spin period from the $L_\mathrm{X}/L_\mathrm{bol}$, taking the measured *Chandra* 0.25–2.0 keV $L_\mathrm{X}$ of $4.7 \times 10^{26}\,\mathrm{erg\,s^{-1}}$ (Poppenhaeger et al., 2013), and yielding $P_\mathrm{rot} = 40.9^{+7.5}_{-7.8}\,\mathrm{d}$. These uncertainties do not take into account the scatter of the sample around the fitted relations though, and in reality may be two or three times larger than this. In comparison, the rotation periods of stars of similar spectral type in the Pleiades (Rebull et al., 2016; Stauffer et al., 2016), Blanco-1 (Gillen et al., submitted), Hyades (Douglas et al., 2016), and Praesepe

(Douglas et al., 2017), measured with either *K2* or NGTS, all show rotation periods $< 20$ d, with the vast majority $< 10$ d. These young open clusters all range in age 100–800 Myr. Additionally, Newton et al. (2016) found that 5 Gyr old mid M dwarfs have rotation periods of about 100 d, and that those up towards 10 Gyr old commonly have rotation periods up to 140 d. Together, this all suggests an intermediate age for HD 189733B, between 1 and a couple of Gyr. However, without an actual measured value of $P_{\rm rot}$, this is a very tentative estimate. Despite the hints, the evidence for an age difference remains rather weak, with the uncertainties on both components' age estimates, particularly that of star B, meaning that identical X-ray-ages cannot be ruled out.

## 7.6 Conclusions

I have investigated a few different aspects of stellar activity within the HD 189733 planetary system, using X-ray observations from *Swift* and *XMM-Newton*. The baselines across which the observations from both are spread out are long: nine years for *Swift*, and eight years for *XMM-Newton*.

I found no evidence of the star's X-ray activity being phased with the planet's orbit. No significantly increased emission is observed at any orbital phase when looking at the *Swift* data as a whole, and the distribution of flares identified across both telescopes' data is consistent with the distribution of exposure time with phase. The latter point remains true when looking solely at the *XMM-Newton* data, or when the two best candidate flares identified in the *Swift* data are also included. These two best candidate flares may have have been unambiguously observed as flares had their exposure times been longer, allowing a better constraint on their count rates and hardness ratios.

The estimated age of HD 189733A based on its relationship with $L_{\rm X}/L_{\rm bol}$ is around 500 Myr, with the uncertainties allowing for a much younger star, but also one that could be a little over a Gyr old. The $F_{\rm bias}$ of HD 189733A, together with its rotation period and activity also seem highly indicative of a young, active star. The *XMM-Newton* fluxes also hint at a multi-year activity cycle for HD 189733A, but the sampling outside the 2013–2015 epoch is too sparse to derive values for its period or amplitude.

The X-ray-age of HD 189733B is very uncertain. Three new *XMM-Newton* flares, together with those hinted at in the previous *Chandra* data, imply a flare rate of just under one every two days. This presents a challenge to the previous claims that the X-ray-age is consistent with a 5–10 Gyr old star. Furthermore,

the rotation period estimated from its *Chandra* X-ray luminosity points to a star considerably younger than this previous estimate, perhaps as young as 1 Gyr, placing it within the possible range of X-ray-ages of the primary. A direct measurement of $P_{\rm rot}$ for HD 189733B is desirable and would provide more insight to the system's age. However, at present, the uncertainties on the ages of the two stars means that the possibility of star A being spun-up by its hot Jupiter are much weaker than previously claimed.

# Chapter 8

# Conclusions and future outlook

In this thesis, I have presented analyses of various X-ray observations of exoplanetary systems. I will briefly summarise the main results of the work, before discussing future avenues to explore going forward.

## 8.1 Summary of the thesis

Across Chapters 3–5, I presented observations of 12 stars made predominately with *XMM-Newton*, and also *ROSAT* and *Swift*. The planets ranged in size from rocky bodies slightly larger than Earth right up to Jupiter-size. In each case, the detected emission was explored through light curve and spectral analysis, and the XUV irradiation of each planet was characterised from the derived fluxes, and estimates of the resulting mass loss rates were made. As part of these investigations, I derived new relations for extrapolating X-ray flux to the unobservable EUV band, using Solar *TIMED/SEE* data, and compared the results to other nearby stars. In the analysis of WASP-80b (Section 3.5.2), I made the first successful detection of a transit with the OM onboard *XMM-Newton*. The NUV transit depth showed a hint of being shallower than measured optically.

In Chapters 4 and 5, the observations analysed are for systems hosting planets in radius-period space close to either the Neptunian desert or the photoevaporation valley. The first TESS planet, $\pi$ Men c, is likely undergoing mass loss at a greater rate than both the similar-sized HD 97658b, and GJ 436b, where the escaping atmosphere is readily detectable in Ly $\alpha$. Although HD 219134b/c are likely stripped of any H/He envelope they may have been born with, I observe a hint of a transit-like feature for planet b in my X-ray light curve. The planets in Praesepe are thought to be old enough (800 Myr) to have passed the epoch of most intense irradiation

and evaporation, but my relations for EUV reconstruction suggest more than half of the EUV irradiation they will experience up to 5 Gyr is actually still to come. The importance of this depends on the role of EUV vs. X-rays in driving mass loss, which is still not certain.

In Chapter 6, I analysed 20 *XMM-Newton* observations of HD 189733b, making the first unambiguous detection of an X-ray transit. The expected double-dip transit shape was successfully identified at softer energies, with the model fit revealing an absorber leading the planet in its orbit, and which has a radius twice that of the planet measured optically. The large absorbing region corroborates previous inferences of an extended atmosphere of material around the planet. The transit shows evidence of an energy dependence, with the soft band transit deeper than the hard band, although the hard band light curve suffers from greater red noise.

In Chapter 7, I analyse the HD 189733 planetary system in the context of stellar activity and possible star-planet interaction signatures, making use of all *XMM-Newton* and *Swift* observations of the system. The fluxes derived from a simultaneous fit to all 25 *XMM-Newton* EPIC-pn spectra show evidence of a long-term activity cycle for the planet host HD 189733A, which is also seen to exhibit a strong inverse FIP effect, typically seen for young, active stars. The evidence for X-ray signatures of SPI in the system, specifically in relation to the phasing of activity with the planet's orbit and the relative X-ray-derived age of the two stellar components, appears much weaker than previously claimed. In addition to a fourth *XMM-Newton* flare for HD 189733A, I identify three flares emanating from HD 189733B, the M-type stellar companion.

## 8.2 Future work

One of the main limitations of my lifetime mass loss estimates is the use of a constant radius. This could perhaps be improved a little by using a constant density instead, but even that prescription would not be suitable for planets either side of the photoevaporation valley. For those planets, the radius is strongly dependant on the envelope mass fraction, where just a couple of percent H/He by mass can double the radius (Owen and Wu, 2017). Thus, the density would substantially change if this is removed by photoevaporation. Instead, a possible alternative approach would be to employ an evolution code wherein the mass loss prescription is an input to the process. As an example, the stellar evolution code MESA has been previously adapted for use with both giant (Paxton et al., 2013), and sub-Neptune-sized planets (Chen and Rogers, 2016). With a proper account of the radius change that such a

code would provide, the evolution of planets could be better constrained.

A few of the planets I present X-ray observations for should be well suited to probing their atmospheres for direct evidence of the predicted escape, despite such observations not yet having been made. The recent discovery of $\pi$ Men c has provided the single best target for characterising a super-Earth atmosphere, and I predict the G-type host star's Ly $\alpha$ flux should be greater than either GJ 436 or HD 97658. WASP-80 might also be a good target. Given its 3 % deep transit, Ly $\alpha$ or helium observations should be able to probe its atmospheric escape. A Ly $\alpha$ snapshot of WASP-80 showed that large transits could be detected (Salz, 2015). A large extended atmosphere has already been detected for HAT-P-11b using observations of the 10830 Å He line (Allart et al., 2018; Mansfield et al., 2018), and the system should also be very amenable to Ly $\alpha$ observations. HD 219134 would also be interesting to probe, given the system's brightness and the hint of transit-like features in X-rays presented here, even though planets b and c likely do not retain a H/He envelope, given their density. The Praesepe planets are likely more difficult to probe because of their relatively large distance, especially in Ly $\alpha$, though K2-100 might be a good target for He observations, which can be performed out to larger distances.

For investigating the evidence of shallower NUV transits than in the optical for WASP-80b and a few other planets, more observations are required to confirm the features. The relatively low precision of the *XMM-Newton* OM means it is not the best probe of this; the OM would be a better instrument for planets with a much deeper NUV transit, as was the original idea for observing the planets with fast mode transit coverage in Chapter 3. For investigating shallower transits, observations from a larger telescope that can provide more precise photometry is required. Most desirable would be to observe multiple transits across the NUV and optical/IR simultaneously. By observing both wavelength ranges simultaneously, both instrumental effects and differing stellar activity between epochs can be eliminated as potential causes of the difference in transit depth. Such observations could be possible with simultaneous multi-band photometery provided by instruments like ULTRACAM or HiPERCAM. The former has been used for planet transit observations in the past (Copperwheat et al., 2013; Bento et al., 2014; Kirk et al., 2016).

It would be desirable to extend the work done on the Praesepe system to even younger planets, where the X-ray emission is still saturated and the greatest rate of mass loss is still ongoing. In order to do this, more (transiting) planets in young open clusters and stellar associations need to be discovered, in addition to the handful provided by *K2*. K2-33b is a very young (11 Myr) planet somewhat larger than Neptune in the Upper Scorpius subgroup of the Scorpius-Centaurus OB

association (Mann et al., 2016), and would be a exciting system to target in X-rays.

For investigating the relative activity-derived-ages in the HD 189733 system, one important extra piece of the puzzle would be the measurement of a rotation period for HD 189733B. This could be input into rotation-age and X-ray-rotation relationships to yield more information of the activity-age of the star, for comparison with HD 189733A. Alternatively, age estimations for both components via other methods may also be useful. If both are shown to be young via these methods, it would weaken the case for SPI even further.

Now that the X-ray transit of HD 189733 has been successfully detected, it could be possible to split the 20 observations up in other ways. Examples of this would be to examine the transit as a function of time, or perhaps observation brightness. The latter case could be interesting from the point of view of whether the mass loss is observed to be greater when the X-ray irradiation is greater. As seen from the investigations of the transit as a function of energy in this work however, splitting up the data into more than a couple of groups leaves the uncertainties on the depth much larger, and conclusions more uncertain. More complex modelling of the transit could help constrain the nature of the absorbing material further, though as I explained in Section 6.6.3, such work is likely to encounter degeneracies between models.

As regards X-ray transits of other targets, GJ 436b and possibly $\pi$ Men c provide the next best targets for detection. GJ 436b is an attractive prospect given its very deep Ly $\alpha$ transit, although feasibility studies I have performed using the noise level of the existing *XMM-Newton* observations highlight the difficulty of detecting transits even if 15–20 primary transits are observed, unless they are very deep. Similarly, $\pi$ Men c is a very small planet compared to HD 189733b, for which the X-ray transit detection was expensive in terms of observing time. However, if $\pi$ Men c also shows deep Ly $\alpha$ transits, it too could be a possible target to probe next, given its relatively bright host. One also hopes for a HD 189733-like system to be found by TESS, and such a planet could also have its X-ray transit probed. If these potential targets are not suitable for X-ray transit detection, HD 189733b may prove the only system amenable to such detections with the current generation of X-ray telescopes. *ATHENA* is currently under development at ESA as the second large class mission of the Cosmic Visions programme (Nandra et al., 2013), with launch planned for the 2030s. This mission may enable the observation of X-ray transits of some of these next-best target planets.

# Bibliography


Agol E. and Fabrycky D.C., 2018. *Transit-Timing and Duration Variations for the Discovery and Characterization of Exoplanets*, 7.

Agol E. et al., 2010. *ApJ*, 721:1861–1877.

Allart R. et al., 2018. *Science*, 362:1384–1387.

Allart R. et al., 2019. *arXiv e-prints*, arXiv:1901.08073.

Arnaud K.A., 1996. In G.H. Jacoby and J. Barnes, editors, *Astronomical Data Analysis Software and Systems V*, volume 101 of *Astronomical Society of the Pacific Conference Series*, 17.

Asplund M. et al., 2009. *ARA&A*, 47:481–522.

Astropy Collaboration et al., 2013. *A&A*, 558:A33.

Astudillo-Defru N. et al., 2017. *A&A*, 600:A13.

Auvergne M. et al., 2009. *A&A*, 506:411–424.

Awiphan S. et al., 2016. *MNRAS*.

Ayres T.R., 2009. *ApJ*, 696:1931–1949.

Ayres T.R., 2014. *AJ*, 147:59.

Ayres T.R. and Linsky J.L., 1980. *ApJ*, 241:279–299.

Ayres T.R. et al., 2008. *ApJL*, 678:L121.

Bakos G. et al., 2004. *PASP*, 116:266–277.

Bakos G.Á. et al., 2002. *PASP*, 114:974–987.

Bakos G.Á. et al., 2006. *ApJ*, 641:L57–L60.

Bakos G.Á. et al., 2010. *ApJ*, 710:1724–1745.

Baliunas S.L. et al., 1995. *ApJ*, 438:269–287.

Ballester G.E. and Ben-Jaffel L., 2015. *ApJ*, 804:116.

Baluev R.V., 2008. *MNRAS*, 385:1279–1285.

Baluev R.V. et al., 2015. *MNRAS*, 450:3101–3113.

Baraffe I. et al., 2004. *A&A*, 419:L13–L16.

Baraffe I. et al., 2005. *A&A*, 436:L47–L51.

Baraffe I. et al., 2006. *A&A*, 450:1221–1229.

Barros S.C.C., Demangeon O., and Deleuil M., 2016. *A&A*, 594:A100.

Batalha N.M. et al., 2010. *ApJ*, 713:L109–L114.

Beaugé C. and Nesvorný D., 2013. *ApJ*, 763:12.

Béky B. et al., 2014. *ApJ*, 788:1.

Bell Burnell J., 2017. *Nature Astronomy*, 1:831–834.

Ben-Jaffel L., 2007. *ApJL*, 671:L61–L64.

Ben-Jaffel L., 2008. *ApJ*, 688:1352–1360.

Ben-Jaffel L. and Ballester G.E., 2013. *A&A*, 553:A52.

Ben-Jaffel L. and Sona Hosseini S., 2010. *ApJ*, 709:1284–1296.

Benedict G.F. et al., 2002. *ApJL*, 581:L115–L118.

Benedict G.F. et al., 2006. *AJ*, 132:2206–2218.

Bento J. et al., 2014. *MNRAS*, 437:1511–1518.

Benz A.O., 2008. *Living Reviews in Solar Physics*, 5:1.

Benz A.O. and Güdel M., 2010. *ARA&A*, 48:241–287.

Berger E. et al., 2001. *Nature*, 410:338–340.

Bergfors C. et al., 2013. *MNRAS*, 428:182–189.

Berghoefer T.W. et al., 1997. *A&A*, 322:167–174.

Berta-Thompson Z.K. et al., 2015. *Nature*, 527:204–207.

Beth A. et al., 2016. *Icarus*, 280:415–423.

Biddle L.I. et al., 2014. *MNRAS*, 443:1810–1820.

Boller T. et al., 2016. *A&A*, 588:A103.

Bonfanti A., Ortolani S., and Nascimbeni V., 2016. *A&A*, 585:A5.

Booth R.S. et al., 2017. *MNRAS*, 471:1012–1025.

Borucki W.J. and Summers A.L., 1984. *Icarus*, 58:121–134.

Borucki W.J. et al., 2010. *Science*, 327:977.

Bouchy F. et al., 2005. *A&A*, 444:L15–L19.

Bourrier V., Ehrenreich D., and Lecavelier des Etangs A., 2015. *A&A*, 582:A65.

Bourrier V. and Lecavelier des Etangs A., 2013. *A&A*, 557:A124.

Bourrier V. et al., 2013. *A&A*, 551:A63.

Bourrier V. et al., 2016. *A&A*, 591:A121.

Bourrier V. et al., 2017a. *A&A*, 597:A26.

Bourrier V. et al., 2017b. *A&A*, 599:L3.

Bourrier V. et al., 2017c. *A&A*, 602:A106.

Bourrier V. et al., 2018a. *A&A*, 620:A147.

Bourrier V. et al., 2018b. *Nature*, 553:477–480.

Bowyer S. and Malina R.F., 1991. *Advances in Space Research*, 11:205–215.

Bowyer S. et al., 1996. *ApJS*, 102:129.

Boyajian T.S. et al., 2012. *ApJ*, 757:112.

Bradt H., 2003. *Astronomy Methods*. Cambridge University Press.

Bradt H.V.D., Ohashi T., and Pounds K.A., 1992. *ARA&A*, 30:391–427.

Brandt T.D. and Huang C.X., 2015. *ApJ*, 807:24.

Brinkfeldt K. et al., 2006. *Icarus*, 182:439–447.

Brinkman A.C. et al., 2001. *A&A*, 365:L324–L328.

Brogi M. et al., 2016. *ApJ*, 817:106.

Brown D.J.A. et al., 2011. *MNRAS*, 415:605–618.

Brown T.M. and Morrow C.A., 1987. *ApJL*, 314:L21–L26.

Burnight T., 1949. *Phys. Rev.*, 76:165.

Burrows D.N. et al., 2005. *SSRv*, 120:165–195.

Cameron R.H., Dikpati M., and Brandenburg A., 2017. *SSRv*, 210:367–395.

Carrington R.C., 1859. *MNRAS*, 20:13–15.

Carroll-Nellenback J. et al., 2017. *MNRAS*, 466:2458–2473.

Carter J.A. et al., 2009. *ApJ*, 696:241–253.

Cash W., 1979. *ApJ*, 228:939–947.

Cassan A. et al., 2012. *Nature*, 481:167–169.

Catalano S. et al., 1996. In K.G. Strassmeier and J.L. Linsky, editors, *Stellar Surface Structure*, volume 176 of *IAU Symposium*, 403.

Catling D.C. and Kasting J.F., 2017. *Escape of Atmospheres to Space*, 129–168. Cambridge University Press.

Cauley P.W., Redfield S., and Jensen A.G., 2017. *AJ*, 153:217.

Cauley P.W. et al., 2015. *ApJ*, 810:13.

Cauley P.W. et al., 2018. *AJ*, 156:262.

Cauley P.W. et al., 2019. *AJ*, 157:69.

Cecchi-Pestellini C., Ciaravella A., and Micela G., 2006. *A&A*, 458:L13–L16.

Cecchi-Pestellini C. et al., 2009. *A&A*, 496:863–868.

Cegla H.M. et al., 2016. *A&A*, 588:A127.

Chabrier G. and Baraffe I., 1997. *A&A*, 327:1039–1053.

Chadney J.M. et al., 2015. *Icarus*, 250:357–367.

Chadney J.M. et al., 2017. *A&A*, 608:A75.

Chamberlain J.W., 1963. *Planetary & Space Sci.*, 11:901–960.

Charbonneau D. et al., 2000. *ApJL*, 529:L45–L48.

Charbonneau D. et al., 2002. *ApJ*, 568:377–384.

Charbonneau P., 2010. *Living Reviews in Solar Physics*, 7:3.

Chen H. and Rogers L.A., 2016. *ApJ*, 831:180.

Claret A., 2000. *A&A*, 363:1081–1190.

Claret A. and Bloemen S., 2011. *A&A*, 529:A75.

Clark B.J.M. et al., 2018. *Publications of the Astronomical Society of the Pacific*, 130:034401.

Copperwheat C.M. et al., 2013. *MNRAS*, 434:661–670.

Coustenis A. et al., 1998. In R. Rebolo, E.L. Martin, and M.R. Zapatero Osorio, editors, *Brown Dwarfs and Extrasolar Planets*, volume 134 of *Astronomical Society of the Pacific Conference Series*, 296.

Crossfield I.J.M. et al., 2019. *Research Notes of the American Astronomical Society*, 3(1):24.

Cuntz M., Saar S.H., and Musielak Z.E., 2000. *ApJL*, 533:L151–L154.

Currie M.J. et al., 2014. In N. Manset and P. Forshay, editors, *Astronomical Data Analysis Software and Systems XXIII*, volume 485 of *Astronomical Society of the Pacific Conference Series*, 391.

Cutri R.M. et al., 2003. *VizieR Online Data Catalog*, 2246.

Delfosse X. et al., 1998. *A&A*, 331:581–595.

Deming D., Louie D., and Sheets H., 2019. *PASP*, 131(1):013001.

Dommanget J. and Nys O., 2002. *VizieR Online Data Catalog*, 1274.

Dorman B., Nelson L.A., and Chau W.Y., 1989. *ApJ*, 342:1003–1018.

Dorn C. and Heng K., 2018. *ApJ*, 853:64.

Douglas S.T. et al., 2016. *ApJ*, 822(1):47.

Douglas S.T. et al., 2017. *ApJ*, 842(2):83.

Durney B.R., De Young D.S., and Roxburgh I.W., 1993. *SolPhys*, 145:207–225.

Duvall Jr. T.L., Harvey J.W., and Pomerantz M.A., 1986. *Nature*, 321:500.

Dziembowski W.A., Goode P.R., and Libbrecht K.G., 1989. *ApJL*, 337:L53–L57.

Eaton N., Draper P.W., and Allan A., 2009. *Starlink User Note*, 45.

Edlén B., 1943. *Z. fur Astrophysik*, 22:30.

Egeland R., 2018. *ApJ*, 866:80.

Egeland R. et al., 2017. *ApJ*, 835:25.

Eggleton P.P. and Tokovinin A.A., 2008. *MNRAS*, 389:869–879.

Ehrenreich D. and Désert J.M., 2011. *A&A*, 529:A136.

Ehrenreich D. et al., 2008. *A&A*, 483:933–937.

Ehrenreich D. et al., 2012. *A&A*, 547:A18.

Ehrenreich D. et al., 2015. *Nature*, 522:459–461.

Ekenbäck A. et al., 2010. *ApJ*, 709:670–679.

Erkaev N.V. et al., 2007. *A&A*, 472:329–334.

Erkaev N.V. et al., 2016. *MNRAS*, 460:1300–1309.

Evans P.A. et al., 2007. *A&A*, 469:379–385.

Evans P.A. et al., 2009. *MNRAS*, 397:1177–1201.

Evans T.M. et al., 2018. *AJ*, 156(6):283.

Fabrycky D. and Tremaine S., 2007. *ApJ*, 669:1298–1315.

Fares R. et al., 2010. *MNRAS*, 406:409–419.

Favata F. and Micela G., 2003. *Space Science Reviews*, 108:577–708.

Favata F. et al., 2008. *A&A*, 490:1121–1126.

Feigelson E.D. et al., 2004. *ApJ*, 611:1107–1120.

Folsom C.P. et al., 2018. *MNRAS*, 481:5286–5295.

Foreman-Mackey D., 2016. *The Journal of Open Source Software*, 24.

Foreman-Mackey D. et al., 2013. *PASP*, 125:306.

Fossati L. et al., 2010. *ApJ*, 714:L222–L227.

Fossati L. et al., 2017. *A&A*, 598:A90.

France K. et al., 2016. *ApJ*, 820:89.

Fressin F. et al., 2013. *ApJ*, 766:81.

Fulton B.J. and Petigura E.A., 2018. *AJ*, 156:264.

Fulton B.J. et al., 2017. *AJ*, 154:109.

Gaia Collaboration et al., 2018. *A&A*, 616:A1.

Galli A. et al., 2008. *Planetary & Space Sci.*, 56:807–811.

Gandolfi D. et al., 2018. *ArXiv e-prints*, arXiv:1809.07573.

Gatewood G. et al., 1992. *AJ*, 104:1237–1247.

Gaudi B.S. et al., 2017. *Nature*, 546:514–518.

Gehrels N. et al., 2004. *ApJ*, 611(2):1005–1020.

Ghezzi L. et al., 2010. *ApJ*, 720:1290–1302.

Giacconi R. et al., 1962. *Physical Review Letters*, 9:439–443.

Giacconi R. et al., 1979. *ApJ*, 230:540–550.

Gillon M. et al., 2016. *Nature*, 533:221–224.

Gillon M. et al., 2017a. *Nature*, 542:456–460.

Gillon M. et al., 2017b. *Nature Astronomy*, 1:0056.

Gilman P.A., 1983. *ApJS*, 53:243–268.

Ginzburg S., Schlichting H.E., and Sari R., 2016. *ApJ*, 825:29.

Ginzburg S., Schlichting H.E., and Sari R., 2018. *MNRAS*, 476:759–765.

González-Álvarez E. et al., 2019. *arXiv e-prints*.

Grigis P.C. and Benz A.O., 2004. *A&A*, 426:1093–1101.

Güdel M., 2004. *A&ARv*, 12:71–237.

Güdel M., Guinan E.F., and Skinner S.L., 1997. *ApJ*, 483:947–960.

Güdel M. and Nazé Y., 2009. *A&A Rev.*, 17:309–408.

Guillot T., 1999. *Science*, 286.

Günther H.M. et al., 2012. *ApJ*, 750:78.

Gupta A. and Schlichting H.E., 2018. *arXiv e-prints*.

Hale G.E. and Nicholson S.B., 1925. *ApJ*, 62:270.

Hale G.E. et al., 1919. *ApJ*, 49:153.

Hartkopf W.I. and McAlister H.A., 1984. *PASP*, 96:105–116.

Hastings W.K., 1970. *Biometrika*, 57(1):97–109.

Haswell C.A., 2010. *Transiting Exoplanets*. Cambridge University Press.

Haswell C.A., 2018. *WASP-12b: A Mass-Losing Extremely Hot Jupiter*, 97. Springer International Publishing.

Haswell C.A. et al., 2012. *ApJ*, 760:79.

Heise J. et al., 1975. *ApJL*, 202:L73–L76.

Helled R., Lozovsky M., and Zucker S., 2016. *MNRAS*, 455:L96–L98.

Helled R. et al., 2011. *ApJ*, 726:15.

Hempelmann A. et al., 2006. *A&A*, 460:261–267.

Henden A.A. et al., 2012. *Journal of the American Association of Variable Star Observers (JAAVSO)*, 40:430.

Henry G.W. et al., 2000. *ApJL*, 529:L41–L44.

Henry G.W. et al., 2011. *ArXiv e-prints*.

Hodgson R., 1859. *MNRAS*, 20:15–16.

Hoffleit D. and Jaschek C., 1991. *The Bright star catalogue*.

Høg E. et al., 2000. *A&A*, 355:L27–L30.

Holmström M. et al., 2008. *Nature*, 451:970–972.

Howe A.R. and Burrows A., 2015. *ApJ*, 808:150.

Howell S.B. et al., 2014. *PASP*, 126:398.

Huang C.X. et al., 2018. *ArXiv e-prints*, arXiv:1809.05967.

Huber K.F., Czesla S., and Schmitt J.H.M.M., 2017a. *A&A*, 597:A113.

Huber K.F., Czesla S., and Schmitt J.H.M.M., 2017b. *A&A*, 600:C1.

Hünsch M. et al., 1999. *A&As*, 135:319–338.

Ionov D.E., Pavlyuchenkov Y.N., and Shematovich V.I., 2018. *MNRAS*, 476:5639–5644.

Jackson A.P., Davis T.A., and Wheatley P.J., 2012. *MNRAS*, 422:2024–2043.

Jackson R.J. and Jeffries R.D., 2010. *MNRAS*, 407:465–478.

Jansen F. et al., 2001. *A&A*, 365:L1–L6.

Jao W.C. et al., 2018. *ApJ*, 861:L11.

Jardine M. and Unruh Y.C., 1999. *A&A*, 346:883–891.

Jeans J., 1925. *The Dynamical Theory of Gases*. Cambridge University Press.

Jensen A.G. et al., 2012. *ApJ*, 751:86.

Jin S. and Mordasini C., 2018. *ApJ*, 853:163.

Jin S. et al., 2014. *ApJ*, 795:65.

Johnson M.C. et al., 2016. *ApJ*, 821:74.

Johnson M.C. et al., 2018. *AJ*, 155:100.

Johnstone C.P. and Güdel M., 2015. *A&A*, 578:A129.

Johnstone C.P. et al., 2015. *A&A*, 577:A122.

Jones H.R.A. et al., 2002. *MNRAS*, 333:871–875.

Jordi K., Grebel E.K., and Ammon K., 2006. *A&A*, 460:339–347.

Judge P.G., Solomon S.C., and Ayres T.R., 2003. *ApJ*, 593:534–548.

Kalberla P.M.W. et al., 2005. *A&A*, 440:775–782.

Kane S.R. and Anderson K.A., 1970. *ApJ*, 162:1003.

Kashyap V.L., Drake J.J., and Saar S.H., 2008. *ApJ*, 687:1339-1354.

Kirk J. et al., 2016. *MNRAS*, 463:2922–2931.

Kirk J. et al., 2017. *MNRAS*, 468:3907–3916.

Kirk J. et al., 2018. *MNRAS*, 474:876–885.

Klimchuk J.A., 2006. *SolPhys*, 234:41–77.

Knutson H.A. et al., 2011. *ApJ*, 735:27.

Knutson H.A. et al., 2014. *ApJ*, 794:155.

Koen C. et al., 2010. *MNRAS*, 403:1949–1968.

Konacki M. et al., 2003. *Nature*, 421:507–509.

Koskinen T.T. et al., 2013. *Icarus*, 226:1678–1694.

Kreidberg L., 2015. *PASP*, 127:1161.

Kreidberg L. and Oklopčić A., 2018. *Research Notes of the American Astronomical Society*, 2:44.

Kreidberg L. et al., 2014. *Nature*, 505:69–72.

Kubyshkina D. et al., 2018a. *A&A*, 619:A151.

Kubyshkina D. et al., 2018b. *ApJL*, 866:L18.

Kulow J.R. et al., 2014. *ApJ*, 786:132.

Kupka F. and Montgomery M.H., 2002. *MNRAS*, 330:L6–L10.

Kurokawa H. and Kaltenegger L., 2013. *MNRAS*, 433:3239–3245.

Kurokawa H. and Nakamoto T., 2014. *ApJ*, 783:54.

Lai D., Helling C., and van den Heuvel E.P.J., 2010. *ApJ*, 721:923–928.

Laming J.M., 2015. *Living Reviews in Solar Physics*, 12:2.

Lammer H. et al., 2003. *ApJ*, 598:L121–L124.

Lammer H. et al., 2009. *A&A*, 506:399–410.

Lanotte A.A. et al., 2014. *A&A*, 572:A73.

Lavie B. et al., 2017. *A&A*, 605(31340):L7. ISSN 0004-6361.

Lecavelier Des Etangs A., 2007. *A&A*, 461:1185–1193.

Lecavelier Des Etangs A. et al., 2010. *A&A*, 514:A72.

Lecavelier des Etangs A. et al., 2012. *A&A*, 543:L4.

Lehmer O.R. and Catling D.C., 2017. *ApJ*, 845:130.

Li S.L. et al., 2010. *Nature*, 463:1054–1056.

Libralato M. et al., 2016. *MNRAS*, 463:1780–1796.

Limber D.N., 1958. *ApJ*, 127:387.

Lin D.N.C., Bodenheimer P., and Richardson D.C., 1996. *Nature*, 380:606–607.

Linsky J.L., Fontenla J., and France K., 2014. *ApJ*, 780:61.

Linsky J.L. et al., 2010. *ApJ*, 717:1291–1299.

Lippincott S.L., 1974. *AJ*, 79:974–978.

Livingston J.H. et al., 2018. *ArXiv e-prints*.

Llama J. and Shkolnik E.L., 2015. *ApJ*, 802:41.

Llama J. et al., 2011. *MNRAS*, 416:L41–L44.

Lopez E.D. and Fortney J.J., 2013. *ApJ*, 776:2.

Louden T., Wheatley P.J., and Briggs K., 2017a. *MNRAS*, 464:2396–2402.

Louden T. et al., 2017b. *MNRAS*, 470:742–754.

Lucy L.B. and White R.L., 1980. *ApJ*, 241:300–305.

Luger R. et al., 2016. *AJ*, 152:100.

Luger R. et al., 2017. *ArXiv e-prints*.

Lundkvist M.S. et al., 2016. *Nature Communications*, 7:11201.

Maggio A. et al., 1987. *ApJ*, 315:687–699.

Maggio A. et al., 2015. *ApJL*, 811:L2.

Mancini L. et al., 2014. *A&A*, 562:A126.

Mandel K. and Agol E., 2002. *ApJ*, 580:L171–L175.

Manduca A., Bell R.A., and Gustafsson B., 1977. *A&A*, 61:809–813.

Mann A.W. et al., 2016. *AJ*, 152:61.

Mann A.W. et al., 2017. *AJ*, 153:64.

Mansfield M. et al., 2018. *ApJ*, 868:L34.

Marin F. and Grosso N., 2017. *ApJ*, 835:283.

Marois C. et al., 2008. *Science*, 322:1348.

Marois C. et al., 2010. *Nature*, 468:1080–1083.

Martin R.G. and Livio M., 2012. *MNRAS*, 425:L6–L9.

Martin R.G., Livio M., and Palaniswamy D., 2016. *ApJ*, 832:122.

Martinez C.F. et al., 2019. *arXiv e-prints*.

Matsakos T. and Königl A., 2016. *ApJ*, 820:L8.

Mayor M. and Queloz D., 1995. *Nature*, 378:355–359.

Mayor M. et al., 2009. *A&A*, 493:639–644.

Mazeh T., Holczer T., and Faigler S., 2016. *A&A*, 589:A75.

Metropolis N. et al., 1953. *J. Chem. Phys.*, 21:1087–1092.

Meunier N., 2018. *A&A*, 615:A87.

Micela G., 2002. In B. Montesinos, A. Gimenez, and E.F. Guinan, editors, *The Evolving Sun and its Influence on Planetary Environments*, volume 269 of *Astronomical Society of the Pacific Conference Series*, 107.

Micela G., Pye J., and Sciortino S., 1997. *A&A*, 320:865–877.

Micela G. et al., 1985. *ApJ*, 292:172–180.

Mittag M. et al., 2017. *A&A*, 600:A119.

Mohanty S. and Basri G., 2003. *ApJ*, 583:451–472.

Monet D.G. et al., 2003. *AJ*, 125:984–993.

Morley C.V. et al., 2015. *ApJ*, 815:110.

Morris B.M. et al., 2017. *ArXiv e-prints*.

Motalebi F. et al., 2015. *A&A*, 584:A72.

Moutou C. et al., 2003. *A&A*, 405:341–348.

Murray-Clay R.A., Chiang E.I., and Murray N., 2009. *ApJ*, 693:23–42.

Nandra K. et al., 2013. *arXiv e-prints*.

Neff J.E. and Simon T., 2008. *ApJ*, 685:478–488.

Newton E.R. et al., 2016. *ApJ*, 821:93.

Newton E.R. et al., 2017. *ApJ*, 834:85.

Nichols J.D. et al., 2015. *ApJ*, 803:9.

Norris C.M. et al., 2017. *A&A*, 605:A45.

Nortmann L. et al., 2018. *Science*, 362:1388–1391.

Noyes R.W., Weiss N.O., and Vaughan A.H., 1984. *ApJ*, 287:769–773.

Nutzman P. and Charbonneau D., 2008. *PASP*, 120:317.

Obermeier C. et al., 2016. *AJ*, 152:223.

Odert P. et al., 2019. *arXiv e-prints*.

Oja T., 1993. *A&As*, 100:591.

Oklopčić A., 2019. *arXiv e-prints*.

Oklopčić A. and Hirata C.M., 2018. *ApJ*, 855:L11.

Öpik E.J., 1963. *Geophysical Journal*, 7:490–506.

Orlando S. et al., 2017. *A&A*, 605:A19.

Owen J.E., 2018. *arXiv e-prints*.

Owen J.E. and Alvarez M.A., 2016. *ApJ*, 816:34.

Owen J.E. and Jackson A.P., 2012. *MNRAS*, 425:2931–2947.

Owen J.E. and Lai D., 2018. *MNRAS*.

Owen J.E. and Wu Y., 2013. *ApJ*, 775:105.

Owen J.E. and Wu Y., 2016. *ApJ*, 817:107.

Owen J.E. and Wu Y., 2017. *ApJ*, 847:29.

Pace G., 2013. *A&A*, 551:L8.

Pagano I. et al., 2009. *Earth Moon and Planets*, 105:373–378.

Pallavicini R. et al., 1981. *ApJ*, 248:279–290.

Parker E.N., 1955. *ApJ*, 122:293.

Parker E.N., 1963. *Interplanetary dynamical processes.*

Parks G.K. and Winckler J.R., 1969. *ApJL*, 155:L117.

Paxton B. et al., 2011. *ApJS*, 192:3.

Paxton B. et al., 2013. *The Astrophysical Journal Supplement Series*, 208(1):4.

Paxton B. et al., 2015. *ApJS*, 220:15.

Pease D.O., Drake J.J., and Kashyap V.L., 2006. *ApJ*, 636:426–431.

Penz T., Micela G., and Lammer H., 2008a. *A&A*, 477:309–314.

Penz T. et al., 2008b. *Planet. Space Sci.*, 56:1260–1272.

Pepper J. et al., 2007. *PASP*, 119:923–935.

Pepper J. et al., 2017. *AJ*, 153:177.

Perdelwitz V. et al., 2018. *A&A*, 616:A161.

Perryman M., 2011. *The Exoplanet Handbook*. Cambridge University Press.

Perryman M., 2018. *The Exoplanet Handbook*. Cambridge University Press.

Perryman M. et al., 2014. *ApJ*, 797:14.

Pickles A.J., 1998. *PASP*, 110:863–878.

Pillitteri I. et al., 2010. *ApJ*, 722:1216–1225.

Pillitteri I. et al., 2011. *ApJ*, 741:L18.

Pillitteri I. et al., 2014. *ApJ*, 785:145.

Pillitteri I. et al., 2015. *ApJ*, 805:52.

Pizzolato N. et al., 2003. *A&A*, 397:147–157.

Pollacco D.L. et al., 2006. *PASP*, 118:1407–1418.

Pollack J.B. et al., 1996. *Icarus*, 124:62.

Pont F., 2009. *MNRAS*, 396:1789–1796.

Pont F. et al., 2007. *A&A*, 476:1347–1355.

Pope B.J.S., Parviainen H., and Aigrain S., 2016. *MNRAS*, 461:3399–3409.

Poppenhaeger K., Robrade J., and Schmitt J.H.M.M., 2010. *A&A*, 515:A98.

Poppenhaeger K., Schmitt J.H.M.M., and Wolk S.J., 2013. *ApJ*, 773:62.

Poppenhaeger K. and Wolk S.J., 2014. *A&A*, 565:L1.

Pottasch S.R., 1963. *ApJ*, 137:945.

Preibisch T. and Feigelson E.D., 2005. *ApJS*, 160:390–400.

Price-Whelan A.M. et al., 2018. *AJ*, 156:123.

Pye J.P. et al., 2015. *A&A*, 581:A28.

Raghavan D. et al., 2006. *ApJ*, 646:523–542.

Ramírez I., Allende Prieto C., and Lambert D.L., 2013. *ApJ*, 764:78.

Randich S. et al., 1996. *A&A*, 305:785.

Rauer H. et al., 2014. *Experimental Astronomy*, 38:249–330.

Reale F., Peres G., and Orlando S., 2001. *ApJ*, 557:906–920.

Rebull L.M. et al., 2016. *AJ*, 152:113.

Redfield S. and Linsky J.L., 2000. *ApJ*, 534:825–837.

Redfield S. and Linsky J.L., 2008. *ApJ*, 673:283-314.

Redfield S. et al., 2008. *AJLl*, 673:L87.

Reinhold T., Reiners A., and Basri G., 2013. *A&A*, 560:A4.

Ribas I. et al., 2005. *ApJ*, 622:680–694.

Ricker G.R. et al., 2015. *Journal of Astronomical Telescopes, Instruments, and Systems*, 1(1):014003.

Rizzuto A.C. et al., 2018. *ArXiv e-prints*.

Robrade J. and Schmitt J.H.M.M., 2009. *A&A*, 497:511–520.

Robrade J., Schmitt J.H.M.M., and Favata F., 2012. *A&A*, 543:A84.

Route M., 2019. *ApJ*, 872:79.

Rubenstein E.P. and Schaefer B.E., 2000. *ApJ*, 529:1031–1033.

Rutledge R.E. et al., 2000. *ApJL*, 538:L141–L144.

Salz M., 2015. *Escaping atmospheres of hot extrasolar gas planets*. Ph.D. thesis, Universität Hamburg.

Salz M. et al., 2015a. *A&A*, 576:A42.

Salz M. et al., 2015b. *A&A*, 576:A21.

Salz M. et al., 2016a. *A&A*, 585:L2.

Salz M. et al., 2016b. *A&A*, 586:A75.

Salz M. et al., 2018. *A&A*, 620:A97.

Sanz-Forcada J., Stelzer B., and Metcalfe T.S., 2013. *A&A*, 553:L6.

Sanz-Forcada J. et al., 2010. *A&A*, 511:L8.

Sanz-Forcada J. et al., 2011. *A&A*, 532:A6.

Sato B. et al., 2005. *ApJ*, 633:465–473.

Scandariato G. et al., 2013. *A&A*, 552:A7.

Schatzman E., 1962. *Annales d'Astrophysique*, 25:18.

Schlawin E. et al., 2010. *ApJL*, 722:L75–L79.

Schmelz J.T. et al., 1996. *ApJ*, 473:519.

Schmitt J.H.M.M., 1997. *A&A*, 318:215–230.

Schmitt J.H.M.M. and Liefke C., 2004. *A&A*, 417:651–665.

Schmitt J.H.M.M. et al., 1990. *ApJ*, 365:704–728.

Schneider J. et al., 1998. In R. Rebolo, E.L. Martin, and M.R. Zapatero Osorio, editors, *Brown Dwarfs and Extrasolar Planets*, volume 134 of *Astronomical Society of the Pacific Conference Series*, 241.

Schrijver C.J., Mewe R., and Walter F.M., 1984. *A&A*, 138:258–266.

Schröder C. and Schmitt J.H.M.M., 2007. *A&A*, 475:677–684.

Schwabe H., 1844. *Astronomische Nachrichten*, 21:233.

Seager S., 2010. *Exoplanet Atmospheres: Physical Processes*. Princeton University Press.

Seager S., Deming D., and Valenti J.A., 2009. *Astrophysics and Space Science Proceedings*, 10:123.

Seager S. and Sasselov D.D., 2000. *ApJ*, 537:916–921.

Shematovich V.I., Ionov D.E., and Lammer H., 2014. *A&A*, 571:A94.

Shkolnik E., Walker G.A.H., and Bohlender D.A., 2003. *ApJ*, 597:1092–1096.

Shkolnik E. et al., 2005. *ApJ*, 622:1075–1090.

Shkolnik E. et al., 2008. *ApJ*, 676:628–638.

Simon T. et al., 2002. *ApJ*, 579:800–809.

Sing D.K. et al., 2011. *MNRAS*, 416:1443–1455.

Sing D.K. et al., 2012. *MNRAS*, 426(2):1663–1670.

Sing D.K. et al., 2016. *Nature*, 529:59–62.

Singh K.P., White N.E., and Drake S.A., 1996. *ApJ*, 456:766.

Skrutskie M.F. et al., 2006. *AJ*, 131:1163–1183.

Skumanich A., 1972. *ApJ*, 171:565.

Smith R.K. et al., 2001. *ApJ*, 556:L91–L95.

Soderblom D.R., 2010. *ARA&A*, 48:581–629.

Solomon S.C. et al., 2010. *GeoRL*, 37:L16103.

Soubiran C. et al., 2008. *A&A*, 480:91–101.

Southworth J., 2010. *MNRAS*, 408:1689–1713.

Spake J.J. et al., 2018. *Nature*, 557:68–70.

Spiegel E.A. and Zahn J.P., 1992. *A&A*, 265:106–114.

Stauffer J. et al., 2016. *AJ*, 152:115.

Stelzer B. and Neuhäuser R., 2001. *A&A*, 377:538–556.

Stelzer B. et al., 2016. *MNRAS*, 463:1844–1864.

Stökl A., Dorfi E., and Lammer H., 2015. *A&A*, 576:A87.

Strüder L. et al., 2001. *A&A*, 365:L18–L26.

Svalgaard L. and Hudson H.S., 2010. In S.R. Cranmer, J.T. Hoeksema, and J.L. Kohl, editors, *SOHO-23: Understanding a Peculiar Solar Minimum*, volume 428 of *Astronomical Society of the Pacific Conference Series*, 325.

Szabó G.M. and Kálmán S., 2019. *arXiv e-prints*.

Szabó G.M. and Kiss L.L., 2011. *ApJ*, 727:L44.

Takeda G. et al., 2007. *ApJS*, 168:297–318.

Tanaka Y., Inoue H., and Holt S.S., 1994. *PASJ*, 46:L37–L41.

Tanner A.M., Gelino C.R., and Law N.M., 2010. *PASP*, 122:1195.

Telleschi A. et al., 2005. *ApJ*, 622:653–679.

Testa P., 2010. *Proceedings of the National Academy of Science*, 107:7158–7163.

Testa P., Saar S.H., and Drake J.J., 2015. *Philosophical Transactions of the Royal Society of London Series A*, 373:20140259–20140259.

Tian F. et al., 2005. *ApJ*, 621:1049–1060.

Torres G., 2007. *ApJ*, 671:L65–L68.

Tremblin P. and Chiang E., 2013. *MNRAS*, 428:2565–2576.

Triaud A.H.M.J. et al., 2009. *A&A*, 506:377–384.

Triaud A.H.M.J. et al., 2013. *A&A*, 551:A80.

Triaud A.H.M.J. et al., 2015. *MNRAS*, 450:2279–2290.

Tsurutani B.T. et al., 2003. *Journal of Geophysical Research (Space Physics)*, 108:1268.

Turner J.D. et al., 2016. *MNRAS*, 459:789–819.

Turner J.D. et al., 2017. *MNRAS*, 472:3871–3886.

Turner M.J.L. et al., 2001. *A&A*, 365:L27–L35.

Ulmschneider P., Theurer J., and Musielak Z.E., 1996. *A&A*, 315:212–221.

Unruh Y.C., Solanki S.K., and Fligge M., 1999. *A&A*, 345:635–642.

Vaiana G.S., 1983. In J.O. Stenflo, editor, *Solar and Stellar Magnetic Fields: Origins and Coronal Effects*, volume 102 of *IAU Symposium*, 165–185.

Valenti J.A. and Fischer D.A., 2005. *ApJS*, 159:141–166.

Van Doorsselaere T., Shariati H., and Debosscher J., 2017. *ApJS*, 232:26.

Van Eylen V. et al., 2018. *MNRAS*, 479:4786–4795.

Van Grootel V. et al., 2014. *ApJ*, 786:2.

van Leeuwen F., 2007. *A&A*, 474:653–664.

van Saders J.L. et al., 2016. *Nature*, 529:181–184.

Vaughan A.H., Preston G.W., and Wilson O.C., 1978. *PASP*, 90:267–274.

Vidal-Madjar A. et al., 2003. *Nature*, 422:143–146.

Vidal-Madjar A. et al., 2004. *ApJ*, 604:L69–L72.

Vidal-Madjar A. et al., 2008. *ApJL*, 676:L57.

Vidal-Madjar A. et al., 2013. *A&A*, 560:A54.

Vidotto A.A., Jardine M., and Helling C., 2010. *ApJL*, 722:L168–L172.

Vidotto A.A., Jardine M., and Helling C., 2011. *MNRAS*, 414:1573–1582.

Vilhu O., 1984. *A&A*, 133:117–126.

Vilhu O. and Walter F.M., 1987. *ApJ*, 321:958–966.

Voges W. et al., 1999. *A&A*, 349:389–405.

Vogt S.S. et al., 2015. *ApJ*, 814:12.

Volkov A.N. et al., 2011. *ApJL*, 729:L24.

Walker G.A.H. et al., 2008. *A&A*, 482:691–697.

Walsh B.M. et al., 2014. *Space Weather*, 12:387–394.

Wambsganss J., 1997. *MNRAS*, 284:172–188.

Wargelin B.J. et al., 2017. *MNRAS*, 464:3281–3296.

Watson A.J., Donahue T.M., and Walker J.C.G., 1981. *Icarus*, 48:150–166.

Watson M.G. et al., 2009. *A&A*, 493(1):339–373.

Weisskopf M.C. et al., 2000. In J.E. Truemper and B. Aschenbach, editors, *X-Ray Optics, Instruments, and Missions III*, volume 4012 of *SPIE*, 2–16.

West R.G. et al., 2018. *arXiv e-prints*, arXiv:1809.00678.

Wheatley P.J. et al., 2017. *MNRAS*, 465:L74–L78.

Wheatley P.J. et al., 2018. *MNRAS*, 475:4476–4493.

White N.E. et al., 1990. *ApJ*, 350:776–795.

Williams D.M., 2003. *American Journal of Physics*, 71:1198–1200.

Wilms J., Allen A., and McCray R., 2000. *ApJ*, 542:914–924.

Wilson O.C., 1978. *ApJ*, 226:379–396.

Winn J.N., 2018. *Planet Occurrence: Doppler and Transit Surveys*, 195. Springer International Publishing.

Winn J.N. et al., 2017. *AJ*, 154:60.

Wolfgang A., Rogers L.A., and Ford E.B., 2016. *ApJ*, 825:19.

Wolszczan A., 1994. *Science*, 264:538–542.

Wolszczan A. and Frail D.A., 1992. *Nature*, 355:145–147.

Wolter H., 1952. *Annalen der Physik*, 445:94–114.

Wood B.E., Laming J.M., and Karovska M., 2012. *ApJ*, 753:76.

Wood B.E. et al., 1994. *ApJS*, 93:287–307.

Woods T.N. et al., 2005. *Journal of Geophysical Research (Space Physics)*, 110:A01312.

Woods T.N. et al., 2018. *SoPh*, 293:76.

Wright J.T. et al., 2004. *ApJS*, 152:261–295.

Wright N.J. and Drake J.J., 2016. *Nature*, 535:526–528.

Wright N.J. et al., 2011. *ApJ*, 743:48.

Wright N.J. et al., 2018. *MNRAS*, 479:2351–2360.

Wu C.J., Ip W.H., and Huang L.C., 2015. *ApJ*, 798:92.

Wu Y. and Lithwick Y., 2013. *ApJ*, 772:74.

Yan F. and Henning T., 2018. *Nature Astronomy*, 2:714–718.

Yan M., Sadeghpour H.R., and Dalgarno A., 1998. *ApJ*, 496:1044–1050.

Yelle R.V., 2004. *Icarus*, 170:167–179.

Youngblood A. et al., 2016. *ApJ*, 824:101.

Zurlo A. et al., 2018. *MNRAS*, 480:35–48.